

5. SITE 959¹

Shipboard Scientific Party²

HOLE 959A

Date occupied: 9 January 1995
Date departed: 12 January 1995
Time on hole: 2 days, 19 hr, 45 min
Position: 3°37.659'N, 2°44.112'W
Bottom felt (drill pipe measurement from rig floor, m): 2102.0
Distance between rig floor and sea level (m): 11.29
Water depth (drill pipe measurement from sea level, m): 2090.7
Total depth (from rig floor, m): 2582.7
Penetration (m): 480.7
Number of cores (including cores having no recovery): 52
Total length of cored section (m): 480.7
Total core recovered (m): 456.2
Core recovery (%): 94.9
Oldest sediment cored:
Depth (mbsf): 480.9
Lithology: claystone
Age: Oligocene
Measured velocity (km/s): 1.927 at Section 159-959A-47X-2, 60 cm

HOLE 959B

Date occupied: 12 January 1995
Date departed: 13 January 1995
Time on hole: 15 hr, 00 min
Position: 3°37.657'N, 2°44.135'W
Bottom felt (drill pipe measurement from rig floor, m): 2101.5
Distance between rig floor and sea level (m): 11.29
Water depth (drill pipe measurement from sea level, m): 2090.2
Total depth (from rig floor, m): 2285.9
Penetration (m): 184.4
Number of cores (including cores having no recovery): 20
Total length of cored section (m): 184.4
Total core recovered (m): 192.53
Core recovery (%): 104.4
Oldest sediment cored:
Depth (mbsf): 184.4

Lithology: nannofossil chalk
Age: Miocene
Measured velocity (km/s): 1.635 at Section 159-959B-20H-4, 109 cm

HOLE 959C

Date occupied: 13 January 1995
Date departed: 14 January 1995
Time on hole: 20 hr, 45 min
Position: 3°37.669'N, 2°44.116'W
Bottom felt (drill pipe measurement from rig floor, m): 2102.2
Distance between rig floor and sea level (m): 11.29
Water depth (drill pipe measurement from sea level, m): 2090.9
Total depth (from rig floor, m): 2281.8
Penetration (m): 179.6
Number of cores (including cores having no recovery): 20
Total length of cored section (m): 179.6
Total core recovered (m): 187.34
Core recovery (%): 104.3
Oldest sediment cored:
Depth (mbsf): 179.6
Lithology: nannofossil chalk
Age: Miocene
Measured velocity (km/s): N/A

HOLE 959D

Date occupied: 14 January 1995
Date departed: 24 January 1995
Time on hole: 10 days, 5 hr, 30 min
Position: 3°37.656'N, 2°44.149'W
Bottom felt (drill pipe measurement from rig floor, m): 2102.0
Distance between rig floor and sea level (m): 11.29
Water depth (drill pipe measurement from sea level, m): 2090.7
Total depth (from rig floor, m): 3260.9
Penetration (m): 1158.9
Number of cores (including cores having no recovery): 78
Total length of cored section (m): 741.10
Total core recovered (m): 429.03
Core recovery (%): 57.9
Oldest sediment cored:
Depth (mbsf): 1158.9
Lithology: claystone and siltstone

¹Masle, J., Lohmann, G.P., Clift, P.D., et al., 1996. *Proc. ODP, Init. Repts.*, 159: College Station, TX (Ocean Drilling Program).

²Shipboard Scientific Party is given in the list preceding the Table of Contents.

Age: Early Cretaceous

Measured velocity (km/s): 3.737 at Section 159-959D-76R-1, 48 cm

Comments: Drilled 0.0–417.8 mbsf.

Principal results: After the transit from Dakar, a single-channel seismic survey was made across the three primary proposed sites. Crossing lines were shot over each location for comparison with the pre-cruise site survey. Beacons were dropped over each site in turn during the survey. Hole 959A was spudded at 0100 hr on 10 January. APC cores were taken until refusal at 180.1 mbsf, when the XCB was deployed, resulting in further penetration to 479.9 mbsf. Following a jet-in test, Holes 959B and 959C were APC cored until refusal at 184.4 and 179.6 mbsf, respectively. Hole 959D was a rotary (RCB) cored hole. The upper 417.8 mbsf was washed down prior to resuming coring shortly above the depth achieved in Hole 959A. Good hole conditions and recovery resulted in the decision to deepen this hole beyond the 900 mbsf originally planned, and thus dispense with the need for a cased reentry Hole 959E. Slow penetration rates and low recovery caused the termination of this hole at 1158.9 mbsf. Logging was then attempted. Although lowering of the tool string was initially prevented by bridges in the upper part of the hole, all three standard logs were run over the lower half of the hole. The hole was plugged and the pipe tripped, with the bottom-hole assembly (BHA) reaching the drill floor at 0530 hr on 24 January.

Five lithologic units were recognized (see Appendix A). Lithologic Unit I (Holocene to middle Miocene; 0–208 mbsf) comprises a mixture of nanofossil ooze and foraminifer ooze, which alternate from laminated to bioturbated intervals. The upper 23 mbsf (Pleistocene) is darker due to increased pyrite and organic matter contents. Lithologic Unit II comprises 599.3 m (208.0–812.3 mbsf) of alternating siliceous and calcareous sediment, divided into three subunits. Subunit IIA (lower Oligocene to lower Miocene) comprises interbedded nanofossil chalk, diatomite, and clay. A black, middle Oligocene chert layer at 430–440 mbsf is designated Subunit IIB. Subunit IIC (lower Oligocene to upper Paleocene) comprises micrite chalk and porcellanite. Lithologic Unit III (upper Paleocene to lower Coniacian) comprises 231.0 m of black claystone (812.3–1043.3 mbsf). Black claystone with nanofossils occurs at both the top and base of the unit. The Cretaceous/Tertiary boundary could not be identified in the sediment or by using microfossils. Even palynomorphs were poorly preserved. Lithologic Unit IV (lower Turonian to lower Coniacian; 1043.3–1081.7 mbsf) comprises 38.4 m of sandy limestone, sandy dolomite, and calcareous sandstone. Lithologic Unit V (upper Albian; 1081.7–1158.9 mbsf) comprises quartz sandstone and silty claystone.

Most of the sediments cored in Holes 959A–959C are shallow dipping. At 0–47 mbsf dips are high due to drilling disturbance. A slight increase in dip value with depth (from 2°–4° at 48–70 mbsf, to 4°–15° by 400 mbsf) was observed in Hole 959A. In Hole 959D, bedding dips are relatively shallow from 420 to 600 mbsf but increase to 20°–30° between 960 and 1000 mbsf, before decreasing to 6°–15° between 1035 and 1044 mbsf. This change corresponds to the top of lithologic Unit IV. An abrupt increase in bedding dip (51°–83°) was recorded over the interval 1112–1140 mbsf. Geographically oriented bedding dip directions from Holes 959A and 959B indicate trends toward the north-northwest and northwest, respectively. Microfaults appear at 92 mbsf in Hole 959A and occur within most of the sequence below this level. Anastomosing normal faults with seams of fine-grained material along fault planes and minor associated reverse faults are a distinctive structural feature of the diatomites of lithologic Unit II. These faults are postdated by sharply defined planar normal faults. Reorientation of the cores in Holes 959A and 959B shows a series of northeast-dipping normal faults and a conjugate set dipping northwest and southeast, respectively. Several types of vein geometry and infills were observed in Hole 959D, including barite, calcite, quartz, dolomite, and kaolinite. Two or three generations of vein growth were observed. Veins occur as tension gashes, irregular veinlets, septarian-type networks, and along faults. Many are slickensided and display evidence of shearing.

At Site 959 we recovered Pleistocene to Albian deposits. A nearly complete Neogene section with diverse calcareous microfossils is present in the upper 350 m (seafloor to Section 159-959A-37X-CC). Oligocene rocks were recovered between Sections 159-959A-37X-CC and 52X-CC

(351–480 mbsf) and 159-959D-1R-CC to 13R-CC (417–532 mbsf). Upper Eocene to upper Paleocene siliceous rocks were found between Sections 159-959D-14R-CC and 43R-CC. Between Sections 159-959D-45R-CC and 65R-CC only agglutinated foraminifers and pollens were found, of probable Late Cretaceous age. An unconformity likely spans much of the Paleocene. Sparse nanofossils between Sections 159-959D-65R-CC and 74R-CC indicate a Santonian-Albian age. Rocks between Sections 159-959D-74R-CC and 78R-CC are barren of siliceous and calcareous microfossils.

Whole-core magnetic susceptibility measurements show a low susceptibility from the seafloor to about 50 mbsf in Holes 959A–959C, and a gradual increase from 50 to 162 mbsf. A low susceptibility from about 162 mbsf to the bottom of each hole corresponds to an increase in clay content. Susceptibility measurements from Hole 959D show a low susceptibility from 417.8 to 1100 mbsf, and a slight rise beneath this depth, in the sandstones of lithologic Unit IV. Remanence intensity is generally low (0.1–1.0 mA/m) at 0–50 mbsf. Between 50 and 162 mbsf it reaches 10–50 mA/m, where a drilling induced effect dominates. Stepwise demagnetization to 25 mT indicates the presence of additional high coercivity components, but these could not be resolved aboard ship. Below 162 mbsf NRM intensity is low, generally <1 mA/m. Cores 159-959A-1H through 4H yielded reversals in declination from which a preliminary magnetostratigraphic interpretation could be made to the base of the Matuyama reverse polarity chron, and more tentatively to the base of the Gauss normal polarity chron. This magnetostratigraphy indicates a sedimentation rate of about 7 m/m.y. since 3.5 Ma.

Interstitial water analyses reflect the influence of organic matter degradation at 0–200 mbsf. Methanogenesis is seen below the sulfate-reducing zone. Profiles of Ca, Mg, Mn, and alkalinity indicate carbonate precipitation within the zone of sulfate reduction. Carbonate dissolution and recrystallization is suggested by Sr, Ca, and alkalinity trends below 150 mbsf. Dissolved silica concentrations are high where sediments rich in biogenic silica are recrystallizing and exhibit minima in portions of the section with negligible silica content. Uptake of potassium by clay minerals is likely to be responsible for a systematic decrease in pore-fluid potassium concentrations with increasing depth in the sediment.

Organic carbon contents range from 0.1 to 5.45 wt%, and carbonate carbon ranges from 0 to 83 wt%. Fluctuations in these values correlate with lithology, although highly variable organic and carbonate carbon patterns within lithologic units demonstrate changes in paleoenvironmental conditions and/or different degrees of diagenetic overprint. Continuous input from terrestrial sources during the Pliocene–Pleistocene is indicated by generally intermediate to low carbonate contents (25–55 wt%) and elevated C/N ratios (10–20). Carbonate and organic carbon profiles in Miocene and Oligocene interbeds of TOC-rich diatomites and porcellanites indicate carbonate dissolution due to degradation of labile organic matter. Thermally immature organic matter (T_{\max} 400°–420°C) is characteristic for diatomites and porcellanites. The highest TOC contents were measured in Upper Cretaceous black claystones. A dominant African terrestrial source of the organic matter is shown by high C/N ratios and intermediate hydrogen indices (150–250 mgHC/gTOC). Very high contents of thermally overmature (T_{\max} 465°–485°C) organic matter were found at the bottom of Hole 959D. C_1/C_{2+} ratios indicate that thermogenic processes had occurred in the geologic past, as anticipated before the cruise.

The physical properties data at Site 959 are heterogeneous, reflecting variations in consolidation, age, and lithology. The most important discontinuities occur at 150 mbsf, 456 mbsf, and 750 mbsf. The discontinuity at 150 mbsf does not correspond to a change in lithology. At 456 mbsf, the change coincides with a change from nanofossil chalk and clay to chert. The discontinuity at 750 mbsf occurs in an interval with no change in lithology, but a noted increase in clay and decrease in opal. The scatter in values of physical properties is generally very narrow, suggesting that few small-scale heterogeneities exist in sediments at Site 959 (especially in lithologic Units I to III).

Downhole measurements were successfully conducted in the lower part of Hole 959D (395–1077 mbsf). The logs are of excellent quality throughout the logged sequence despite limited borehole washout near the

top (405–425 mbsf) and bottom (1025–1045 mbsf) of the logged interval. Initial comparison between log and core data shows good correlation for natural gamma-ray and velocity measurements. Preliminary interpretation of the FMS data shows bedding planes dipping consistently north-northwest with increasing dips downhole (from 20° at 550 mbsf to >40° at 850 mbsf).

BACKGROUND AND OBJECTIVES

Site 959 is located in 2100 m water depth on a small plateau that extends just north of the top of the Côte d'Ivoire-Ghana Marginal Ridge (CIGMR) on the southern shoulder of the Deep Ivorian Basin (DIB) (Fig. 1). Both features, the CIGMR and DIB, were generated as a consequence of Early Cretaceous rifting of the northern South Atlantic. However, the CIGMR is believed to have been influenced by additional tectonic and thermal processes related to active transform motion. This occurred first between the African and Brazilian borderlands, and then between the evolving, extensional DIB and the southern, newly created, bordering oceanic crust (Masclé and Blarez, 1987).

The sedimentary cover at Site 959 is thought to have recorded the different stages of development of both the extensional basin and the bordering marginal ridge. In effect this means the sediment record of this site spans the DIB's syn-rift and post-rift periods and the Marginal Ridge's syn-transform and subsequent vertical behavior (Basile et al., 1993).

Crustal thicknesses beneath the Basin and the Marginal Ridge are identical and indicate a Moho depth on the order of 22 km, which in turn implies that extension has been rather homogeneous across the whole region (Sage, 1994). At Site 959 the total sediment thickness is about 3000 m, of which 1550 m comprises the syn-tectonic (syn-rift and syn-transform) sequences according to seismic refraction data (see Basile et al., this volume).

Single-channel and multichannel seismic (MCS) reflection profiles across the northern slope of the Marginal Ridge (Figs. 2 and 3) show an acoustic sequence made up of six main units; the deepest one, Unit A, has a mean interval velocity of 3.5 km/s and can be correlated with the syn-rift deposits of the DIB (Basile et al., 1993). According to observations and sampling made during submersible dives EN 8, 9, 10, and 12 of the *Equanaute* cruise (Masclé et al., 1993, 1994), this unit is likely to be made of a wedge, approximately 1500

m thick, of intensively faulted and folded clastic sediments of deltaic environment. The age of Unit A is presumed to be Early Cretaceous (Barremian to early Albian). Unit A appears as acoustic basement on single-channel seismic profiles, and is characterized on MCS lines close to Site 959 by strongly diffractive and irregular reflectors, showing some local continuity. Unit A can also be detected beneath most of the Marginal Ridge itself, including its southern slope. We believe that its specific diffractive seismic pattern results from both its lithology (successive deltaic to pro-deltaic deposits with limited lateral extension) and from its intensely fractured nature.

Unit B unconformably overlies Unit A and shows a comparable diffractive pattern but with more internal continuity. Although Unit B is clearly a post-rift deposit with respect to the DIB, it is believed to have also recorded parts of the syn-transform deformational history of the bordering Marginal Ridge. At Site 959 the mean seismic velocity of 3.5 km/s suggests that Unit B is up to 450 m thick. In composition, Unit B was expected to be of clastic character since it appears to have been deposited during, and as a result of, active tectonism on the CIGMR.

The youngest seismic units seen at Site 959 are clearly characterized by well layered reflectors suggesting relatively regular sedimentation. Unit C lies unconformably on underlying units along the northern slope of the Marginal Ridge, where it appears to have filled a series of small bordering basins. Subsequent Units D through F are almost horizontal in the DIB and show a progressive pinching out against the CIGMR; this has been interpreted to be due to coeval Marginal Ridge uplift, at least until the time of deposition of Unit E. The total thickness of Units C through F is estimated to be 1100 m.

Objectives

Transform Margin Evolution

The primary goals at Site 959 were to ascertain the composition, age, and nature of deformation of the sediments and acoustic basement in the DIB and on the CIGMR, as well as to chart their vertical motion through time. The long-term objective is to better understand the different structural, thermal, and sedimentary processes that are operative at the transform margin before (Unit A), during (chiefly Unit B and potentially Units C–D), and after active transform tectonism.

New constraints on the timing of the end of extensional deformation within the DIB, in the initiation of oceanic accretion, as well as the timing of transform activity and uplift and subsidence history of the marginal ridge, were anticipated from the drilling.

Continuous coring was also aimed at determining the ages and facies of sediments within the active transform margin. A precise definition of the origin of onlaps and toplaps seen along the northern slope of the Marginal Ridge (tectonic-isostatic events vs. paleoceanographic fluctuations) was also targeted. Finally a thermo-mechanical model of transform margin is anticipated using the diagenetic history of sediments during and after tectonic activity, and the past thermal regime deduced from fission track analysis. The site is also expected to have suffered heating caused by the vicinity of adjacent young oceanic lithosphere.

Microtectonic observations, paleostress measurements, tilting history, and paleomagnetic controls from Units A and B will be used concurrently to define the tectonic regime and the evolution of the transform margin during its early development.

Surface and Intermediate Water Paleoceanography

Site 959 is the primary paleoceanographic site of Leg 159. Because of its hemipelagic sedimentation rate and its location on the Marginal Ridge near the top of the continental rise, Site 959 was expected to contain a high-resolution stratigraphic record isolated from disturbance by turbidity flows coming from the continental shelf and

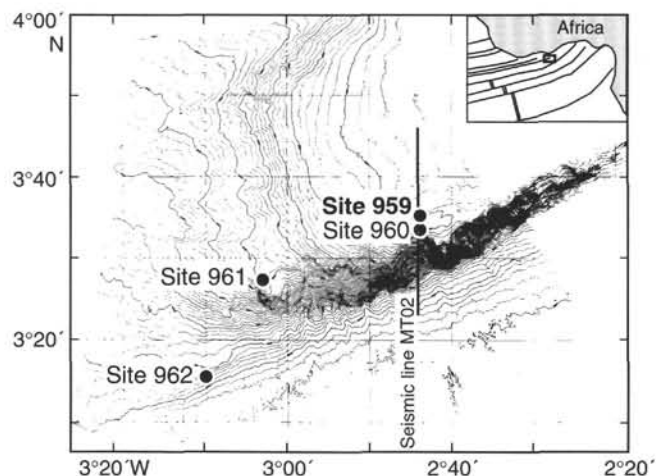


Figure 1. Location of Leg 159 sites on a swath bathymetric map (*Equamarge* II cruise, 1988; Masclé et al., 1989) of the Côte d'Ivoire-Ghana Marginal Ridge and surroundings (bathymetry is in meters; contour interval 50 m).

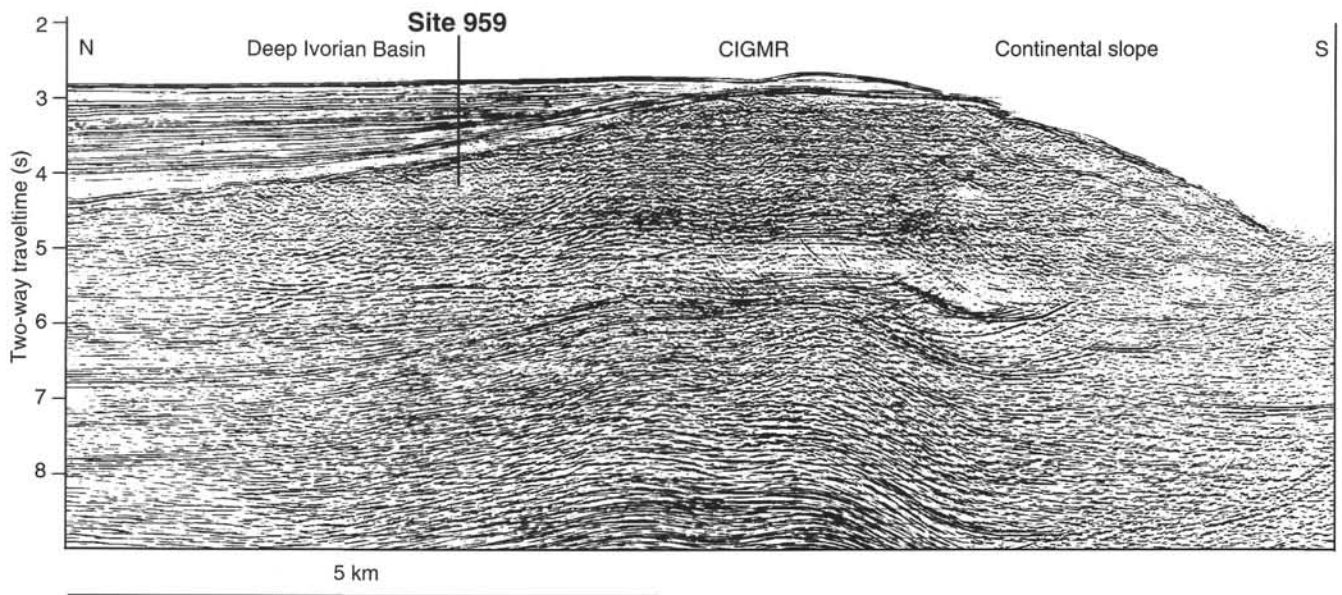


Figure 2. Migrated MCS section of Line MT02 (*Equasis* cruise, 1990; Mascle et al., 1995) showing location of Site 959.

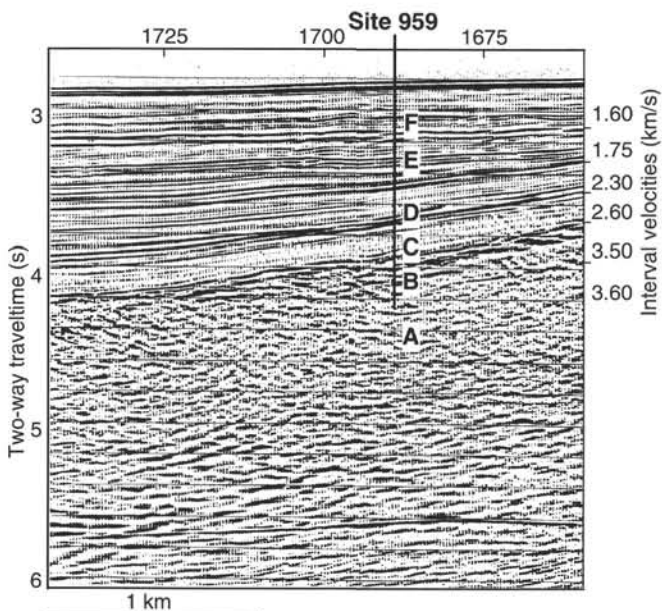


Figure 3. Enlargement of MCS section showing the main seismic units penetrated at Site 959.

slope and discontinuities from local slumping and soft-sediment deformation. Furthermore, its bathymetric position, at a relatively shallow depth (2 km), offered the possibility of recovering carbonate sediments relatively unaltered by dissolution and fossil benthic foraminifers formed under the influence of past intermediate waters. We planned to use the expanded, carbonate-rich section anticipated at this site to improve the resolution of tropical biostratigraphies and paleoclimate histories and to use the benthic foraminifers to document past changes in the character of intermediate waters. Site 959 also offered the possibility of sampling shallow-water sediments formed on the Marginal Ridge during the Cretaceous, helping to characterize the geometry and oceanography of the evolving seaway between the North and South Atlantic.

OPERATIONS

ODP Leg 159 began when SEDCO/BP 471 (*JOIDES Resolution*) arrived dockside in Dakar, Senegal, at 0700 hr on 3 January 1995. The vessel had just completed a drydocking period in Falmouth, England, so there were no logistical or repair activities to be accomplished in Dakar. All resupply was handled in Falmouth, limiting Dakar activities to technical crew change and the boarding of the scientific party. All personnel were aboard ship by 1200 hr on 4 January 1995. Sailing clearances were obtained and the last line was away at 1430 hr. Once the ship was clear of the Dakar breakwater, the captain set a southeasterly course for Site 959 (see Fig. 1, "Underway Geophysics" chapter, this volume).

Dakar to Site 959

A newly cleaned hull and favorable weather conditions helped the *JOIDES Resolution* to make excellent time en route to the operating area for Site 959 (proposed site IG-1). The Guinea Current, flowing southeasterly off the west coast of Africa at a speed of up to 1.5 knots, helped the vessel to achieve an average speed of 13.2 knots for the transit. Due to recent reports of an increase in piracy off the west coast of Africa, the vessel kept 35–40 nautical miles away from the coastline while in transit to the operating area.

While en route to the operating area we decided to spend up to 24 hr conducting a pre-site seismic survey of all three primary drill sites (proposed sites IG-1, IG-2, and IG-3) and to pre-deploy positioning beacons at each site (see "Underway Geophysics" chapter, this volume). The waypoint for the start of surveying activities was reached at 1600 hr on 8 January 1995. Approximately 8 hr were spent conducting a 3.5-kHz single-channel seismic survey of each primary proposed drill site. A duplication of the original pre-cruise survey line across each site was accomplished in addition to a second, roughly perpendicular, crossing line to aid in locating the site as accurately as possible. The risk of hydrocarbons in this area made the accurate positioning of the drill sites, using the pre-cruise multichannel seismic survey, imperative. Our survey aimed to reproduce the previously revealed structure and permit accurate locations of the sites.

At 0045 hr on 9 January 1995 beacon SN 1242 (Datasonics Model 354B, 15 kHz, 208 db) was deployed at Site 962 (proposed site IG-

3). At 0945 hr that same day, beacon SN 1248 (Datasonics Model 354B, 14.5 kHz, 208 db) was deployed at Site 961 (proposed site IG-2). After completion of the 3.5-kHz seismic survey of the "IG" operating area, the last beacon (Datasonics Model 354B, 15 kHz, 208 db, SN 779) was dropped on location at 1630 hr on 9 January at Site 959 (proposed site IG-1).

Site 959 (Proposed Site IG-1)

Site 959 lies on the continental slope off the southwest coast of Ghana, approximately 130 nautical miles southeast of Abidjan in 2100 m of water. Initial plans called for multiple holes at this site beginning with triple advanced hydraulic piston coring (APC) to approximately 200 mbsf, or to APC refusal. The third APC hole was to be deepened to approximately 300 mbsf or greater if the XCB coring system was yielding satisfactory results. The APC/XCB coring was to be followed by a single bit RCB hole to a depth of approximately 900 mbsf, or until a satisfactory casing point was located for the deep coring effort on the following hole. The final hole at this site was projected to be cored to 1600 mbsf. To accomplish this it was anticipated that a full reentry cone installation, including a 10-3/4 in. surface casing string to approximately 870 mbsf, would be required.

Hole 959A

The APC/XCB bottom hole assembly (BHA) was made up with a non-magnetic drill collar and a new Security 11-7/16 inch S86F bit (SN 479055). The BHA was run in the hole, and at 0100 hr on 10 January, the first APC core was shot from a depth of 2101.0 m. Mud-line was established at 2102.0 m, (according to the direct pipe measurement (DPM). The corrected precision depth recorder (PDR) reading normalized to driller's datum was 2106.4 m. APC coring advanced through a greenish gray nannofossil ooze until a refusal depth of 180.1 mbsf (Core 159-959A-19H). The APC cored section recovered 188.69 m or 104.3% of the interval cored (Table 1). The cores were oriented beginning with Core 159-959A-3H, and three successful Adara temperature tool measurements were taken at 85.1 mbsf (Core 159-959A-9H), 132.6 mbsf (Core 159-959A-14H), and 180.1 mbsf (Core 159-959A-19H). Data from the first Adara temperature measurement, attempted at a depth of 37.6 m (Core 159-959A-4H), was considered suspect due to apparent movement of the cutting shoe.

The extended core barrel (XCB) was then deployed to give the scientific party the opportunity to evaluate the quality of the piston cores from Hole 959A before APC coring resumed at Holes 959B and 959C. During XCB coring a second positioning beacon was deployed as a back up to the primary beacon. At 2025 hr on 10 January beacon SN 1245 (Datasonics Model 354B, 17 kHz, 208 db) was deployed. When this beacon would not command off at the seafloor, the primary (initial) beacon was turned off and positioning continued using the backup beacon for the remainder of the time at this site. The XCB core barrel was dropped and XCB coring advanced from 180.1 mbsf to 479.9 mbsf. The cored interval was 299.8 m with 267.51 m recovered (89.2%).

Hydrocarbons (Hole 959A)

Gas chromatograph (GC3) and Natural Gas Analyzer (NGA) analysis on Core 159-959A-50X indicated the presence of long-chain hydrocarbons up to C_6 and higher. The results are shown in Table 2.

The data suggesting the presence of long-chain hydrocarbons in Core 159-959A-50X were considered suspect for several reasons. Normal trends associated with the approach to a hydrocarbon reservoir were absent. Unusual chemical bonding as well as a variety of complex and substituted hydrocarbon chains were prevalent, indicating a non-equilibrium environment. This was considered inconsistent with the normal occurrence of hydrocarbons and more likely to indicate a recent, artificially induced, phenomenon. A burnt smell asso-

ciated with the XCB cutting shoes was detected in Cores 159-959A-49X through 51X. Levels of total organic carbon (TOC) were identified in the sediments sufficient to yield higher long-chain hydrocarbons if adequate heat was applied. It was therefore suggested the long-chain hydrocarbons were produced as a result of extreme frictional heating by the XCB cutting shoes during the coring process. To confirm this theory a single APC core (159-959A-52H) was taken to a depth of 480.7 mbsf as the last core of the hole. The APC advanced 0.8 m and recovered 0.74 m. Head-space analysis of the core indicated that the hole was within acceptable hydrocarbon limits. A methane/ethane ratio of 1120/1 was established, and on three of four samples there was no detectable ethane (Table 3). No hydrocarbons above C_3 were identified.

Hole 959A was terminated at 480.7 mbsf due to poor recovery with the XCB coring system and in favor of spudding the scheduled single bit RCB hole to reach the deeper objectives. The APC/XCB coring systems recovered 456.20 m or 94.9% of the section cored on Hole 959A. The bit cleared the seafloor at 1215 hr on 12 January, ending Hole 959A.

Hole 959B

Hole 959B was spudded at 1300 hr on 12 January after the vessel was offset 15 m due north of Hole 959A. The first APC core was shot from a depth of 2097.0 m to stagger the cored interval from Hole 959A. Mud line was established at 2101.5 m (DPM). APC coring advanced through the same greenish gray nannofossil ooze as cored in Hole 959A until reaching a refusal depth of 184.4 mbsf (Core 159-959B-20H) (see Table 1). The APC-cored section recovered 192.53 m or 104.4% of the interval penetrated. The cores were oriented beginning with Core 159-959B-3H, and successful Adara temperature measurements were taken at 43.0 mbsf (Core 159-959B-5H), 81.0 mbsf (Core 159-959B-9H), and 138.0 mbsf (Core 159-959B-15H). At 0315 hr on 13 January the bit cleared the seafloor ending Hole 959B.

Jet-in Test

Prior to spudding Hole 959C the vessel was offset 15 m north and 30 m east of Hole 959B. This was the planned location for the reentry cone installation for Hole 959E. A successful jet-in test was conducted to aid in establishing the amount of 16-in. casing to be made up to the reentry cone. Jet-in testing lasted one hour and penetrated to 72 mbsf using up to 40 strokes per minute (spm).

Hole 959C

Hole 959C was spudded at 0630 hr 13 January after the vessel was offset 30 m west of the jet-in location, which corresponds to a location 15 m north of Hole 959B. The first APC core was shot from a depth of 2094.0 m to stagger the cored interval from Holes 959A/B. Mud line was established at 2101.2 m (DPM). APC coring advanced until reaching a refusal depth of 179.6 mbsf (Core 159-959C-20H) (see Table 1). The APC-cored section recovered 187.34 m or 104.3% of the interval cored. As in the two previous holes, the cores were oriented beginning with Core 159-959C-3H. No Adara temperature measurements were attempted on this hole. Upon completion of the third set of APC coring, the drill string was tripped back to the drill floor of the ship so that the APC/XCB BHA could be changed to that required for rotary (RCB) coring. At 2400 hr on 13 January the bit cleared the rig floor ending Hole 959C.

Hole 959D

During make up of an RCB BHA and mechanical bit release, the vessel was offset 60 m south and 30 m west of Hole 959C. This placed Hole 959D to the south and west of Holes 959A-959C. The

Table 1. Site 959 coring summary.

Core	Date (Jan. 1995)	Time (UTC)	Depth (mbsf)	Length cored (m)	Length recovered (m)	Recovery (%)	Core	Date (Jan. 1995)	Time (UTC)	Depth (mbsf)	Length cored (m)	Length recovered (m)	Recovery (%)			
159-959A-							9H	13	1135	68.8-78.3	9.5	10.13	106.6			
1H	10	0115	0.0-9.1	9.1	9.08	99.8	10H	13	1205	78.3-87.8	9.5	9.90	104.0			
2H	10	0200	9.1-18.6	9.5	9.89	104.0	11H	13	1235	87.8-97.3	9.5	10.13	106.6			
3H	10	0300	18.6-28.1	9.5	10.04	105.7	12H	13	1305	97.3-106.8	9.5	10.03	105.6			
4H	10	0430	28.1-37.6	9.5	10.34	108.8	13H	13	1340	106.8-116.3	9.5	9.95	105.0			
5H	10	0515	37.6-47.1	9.5	10.00	105.2	14H	13	1410	116.3-125.8	9.5	10.07	106.0			
6H	10	0610	47.1-56.6	9.5	9.95	105.0	15H	13	1440	125.8-135.3	9.5	9.98	105.0			
7H	10	0700	56.6-66.1	9.5	10.09	106.2	16H	13	1510	135.3-144.8	9.5	9.98	105.0			
8H	10	0730	66.1-75.6	9.5	9.92	104.0	17H	13	1545	144.8-154.3	9.5	9.98	105.0			
9H	10	0815	75.6-85.1	9.5	9.50	100.0	18H	13	1635	154.3-163.8	9.5	9.98	105.0			
10H	10	0900	85.1-94.6	9.5	10.05	105.8	19H	13	1715	163.8-173.3	9.5	8.86	93.2			
11H	10	0945	94.6-104.1	9.5	9.98	105.0	20H	13	1800	173.3-179.6	6.3	6.33	100.0			
12H	10	1030	104.1-113.6	9.5	10.10	106.3	Coring totals:						179.6	187.34	104.3	
13H	10	1100	113.6-123.1	9.5	9.98	105.0	159-959D-									
14H	10	1200	123.1-132.6	9.5	9.60	101.0	***Drilled from 0.0 to 417.8 mbsf***									
15H	10	1245	132.6-142.1	9.5	9.88	104.0	1R	14	2100	417.8-427.3	9.5	8.48	89.2			
16H	10	1315	142.1-151.6	9.5	9.92	104.0	2R	14	2300	427.3-436.8	9.5	0.28	3.0			
17H	10	1400	151.6-161.1	9.5	9.45	99.5	3R	15	0050	436.8-446.4	9.6	0.21	2.1			
18H	10	1500	161.1-170.6	9.5	10.04	105.7	4R	15	0220	446.4-455.8	9.4	0.39	4.2			
19H	10	1600	170.6-180.1	9.5	10.14	106.7	5R	15	0345	455.8-465.3	9.5	0.11	1.2			
20X	10	1730	180.1-189.1	9.0	9.74	108.0	6R	15	0530	465.3-469.3	4.0	0.09	2.3			
21X	10	1830	189.1-198.6	9.5	9.75	102.0	7R	15	0730	469.3-475.0	5.7	0.17	3.0			
22X	10	1935	198.6-207.6	9.0	9.29	103.0	8R	15	0930	475.0-484.6	9.6	1.34	13.9			
23X	10	2020	207.6-216.6	9.0	9.60	106.0	9R	15	1045	484.6-494.2	9.6	7.50	78.1			
24X	10	2105	216.6-225.8	9.2	9.94	108.0	10R	15	1135	494.2-503.8	9.6	3.32	34.6			
25X	10	2145	225.8-235.5	9.7	9.79	101.0	11R	15	1240	503.8-513.6	9.8	1.78	18.1			
26X	10	2220	235.5-245.1	9.6	9.81	102.0	12R	15	1330	513.6-523.2	9.6	4.92	51.2			
27X	10	2300	245.1-254.8	9.7	9.84	101.0	13R	15	1425	523.2-532.8	9.6	5.13	53.4			
28X	10	2350	254.8-264.4	9.6	9.91	103.0	14R	15	1530	532.8-542.4	9.6	3.08	32.1			
29X	11	0100	264.4-274.0	9.6	9.83	102.0	15R	15	1640	542.4-552.1	9.7	1.17	12.0			
30X	11	0210	274.0-283.7	9.7	9.77	101.0	16R	15	1735	552.1-561.8	9.7	5.17	53.3			
31X	11	0325	283.7-293.3	9.6	9.25	96.3	17R	15	1830	561.8-571.4	9.6	8.13	84.7			
32X	11	0430	293.3-303.0	9.7	9.12	96.1	18R	15	1945	571.4-580.9	9.5	7.32	77.1			
33X	11	0540	303.0-312.6	9.6	9.48	98.7	19R	15	2015	580.9-590.6	9.7	0.74	7.6			
34X	11	0710	312.6-322.2	9.6	9.74	101.0	20R	15	2210	590.6-600.2	9.6	4.54	47.3			
35X	11	0825	322.2-331.8	9.6	9.77	102.0	21R	15	2330	600.2-609.7	9.5	9.13	96.1			
36X	11	0945	331.8-341.5	9.7	10.01	103.2	22R	16	0100	609.7-619.3	9.6	9.40	97.9			
37X	11	1100	341.5-351.2	9.7	9.81	101.0	23R	16	0220	619.3-629.0	9.7	7.95	81.9			
38X	11	1215	351.2-360.8	9.6	9.90	103.0	24R	16	0335	629.0-638.7	9.7	9.55	98.4			
39X	11	1315	360.8-370.5	9.7	9.85	101.0	25R	16	0500	638.7-648.3	9.6	6.97	72.6			
40X	11	1415	370.5-380.2	9.7	9.83	101.0	26R	16	0645	648.3-658.0	9.7	9.07	93.5			
41X	11	1530	380.2-389.8	9.6	9.77	102.0	27R	16	0815	658.0-667.6	9.6	9.89	103.0			
42X	11	1630	389.8-399.2	9.4	9.64	102.0	28R	16	0945	667.6-677.2	9.6	9.79	102.0			
43X	11	1800	399.2-408.5	9.3	9.86	106.0	29R	16	1110	677.2-686.9	9.7	6.56	67.6			
44X	11	1915	408.5-418.1	9.6	9.71	101.0	30R	16	1230	686.9-696.6	9.7	8.78	90.5			
45X	11	2040	418.1-427.7	9.6	9.90	103.0	31R	16	1400	696.6-706.2	9.6	7.15	74.5			
46X	11	2215	427.7-437.4	9.7	9.83	101.0	32R	16	1515	706.2-715.9	9.7	4.26	43.9			
47X	11	2350	437.4-447.0	9.6	3.24	33.7	33R	16	1640	715.9-725.5	9.6	3.32	34.6			
48X	12	0130	447.0-456.6	9.6	0.47	4.9	34R	16	1825	725.5-735.2	9.7	7.26	74.8			
49X	12	0340	456.6-466.3	9.7	0.36	3.7	35R	16	2000	735.2-744.9	9.7	9.94	102.0			
50X	12	0630	466.3-475.9	9.6	0.26	2.7	36R	16	2215	744.9-754.5	9.6	6.29	65.5			
51X	12	0815	475.9-479.9	4.0	0.24	6.0	37R	17	0015	754.5-764.2	9.7	5.03	51.8			
52H	12	1000	479.9-480.7	0.8	0.74	92.5	38R	17	0200	764.2-773.8	9.6	0.96	10.0			
Coring totals:				480.7	456.20	94.9	39R	17	0320	773.8-783.5	9.7	7.20	74.2			
159-959B-							40R	17	0450	783.5-793.0	9.5	8.71	91.7			
1H	12	1315	0.0-5.0	5.0	4.89	97.8	41R	17	0630	793.0-802.6	9.6	8.68	90.4			
2H	12	1400	5.0-14.5	9.5	9.90	104.0	42R	17	0745	802.6-812.3	9.7	4.13	42.6			
3H	12	1440	14.5-24.0	9.5	9.93	104.0	43R	17	0915	812.3-821.9	9.6	9.65	100.0			
4H	12	1515	24.0-33.5	9.5	9.88	104.0	44R	17	1045	821.9-831.6	9.7	9.97	103.0			
5H	12	1600	33.5-43.0	9.5	10.01	105.3	45R	17	1200	831.6-841.3	9.7	1.11	11.4			
6H	12	1630	43.0-52.5	9.5	9.84	103.0	46R	17	1345	841.3-850.9	9.6	1.86	19.4			
7H	12	1700	52.5-62.0	9.5	9.88	104.0	47R	17	1515	850.9-860.6	9.7	0.84	8.7			
8H	12	1730	62.0-71.5	9.5	9.98	105.0	48R	17	1710	860.6-870.2	9.6	8.13	84.7			
9H	12	1815	71.5-80.0	9.5	10.25	107.9	49R	17	1840	870.2-879.9	9.7	8.70	89.7			
10H	12	1850	80.0-90.5	9.5	10.03	105.6	50R	17	2000	879.9-889.2	9.3	7.63	82.0			
11H	12	1920	90.5-100.0	9.5	9.81	103.0	51R	17	2200	889.2-898.8	9.6	9.57	99.7			
12H	12	1950	100.0-109.5	9.5	9.90	104.0	52R	18	0515	898.8-908.5	9.7	5.44	56.1			
13H	12	2020	109.5-119.0	9.5	10.09	106.2	53R	18	0715	908.5-918.1	9.6	10.16	105.8			
14H	12	2045	119.0-128.5	9.5	10.06	105.9	54R	18	0845	918.1-927.8	9.7	4.19	43.2			
15H	12	2130	128.5-138.0	9.5	9.96	105.0	55R	18	1015	927.8-937.4	9.6	9.93	103.0			
16H	12	2200	138.0-147.5	9.5	9.99	105.0	56R	18	1145	937.4-947.1	9.7	9.94	102.0			
17H	12	2235	147.5-157.0	9.5	10.06	105.9	57R	18	1315	947.1-956.8	9.7	6.81	70.2			
18H	12	2320	157.0-166.5	9.5	10.04	105.7	58R	18	1530	956.8-966.5	9.7	4.82	49.7			
19H	13	0020	166.5-175.5	9.0	9.13	101.0	59R	18	1715	966.5-976.1	9.6	7.27	75.7			
20H	13	0230	175.5-184.4	8.9	8.90	100.0	60R	18	1900	976.1-985.8	9.7	7.61	78.4			
Coring totals:				184.4	192.53	104.4	61R	18	2100	985.8-995.4	9.6	5.40	56.2			
159-959C-							62R	18	2310	995.4-1005.0	9.6	4.77	49.7			
1H	13	0700	0.0-2.3	2.3	2.31	100.0	63R	19	0100	1005.0-1014.7	9.7	9.29	95.8			
2H	13	0730	2.3-11.8	9.5	9.90	104.0	64R	19	0240	1014.7-1024.1	9.4	8.04	85.5			
3H	13	0810	11.8-21.3	9.5	9.78	103.0	65R	19	0430	1024.1-1033.7	9.6	9.88	103.0			
4H	13	0845	21.3-30.8	9.5	9.91	104.0	66R	19	0630	1033.7-1043.3	9.6	9.68	101.0			
5H	13	0925														

Table 1 (continued).

Core	Date (Jan. 1995)	Time (UTC)	Depth (mbsf)	Length cored (m)	Length recovered (m)	Recovery (%)
72R	20	0045	1091.2–1100.8	9.6	5.31	55.3
73R	20	0410	1100.8–1110.5	9.7	2.79	28.7
74R	20	0730	1110.5–1120.2	9.7	2.73	28.1
75R	20	1100	1120.2–1129.8	9.6	1.94	20.2
76R	20	1430	1129.8–1139.5	9.7	2.62	27.0
77R	20	1730	1139.5–1149.2	9.7	2.57	26.5
78R	20	2150	1149.2–1158.9	9.7	9.56	98.5
Coring totals:				741.1	429.03	57.9
Drilled:				417.8		
Total:				1158.9		

Table 2. Gas chromatograph (GC3) and Natural Gas Analyzer (NGA) analysis on Core 159-959A-50X.

	Depth (mbsf)	C ₁	C ₂	Ratio	C ₃	IC ₄	NC ₄	IC ₅	NC ₆	IC ₆
GC3	475.9	11935	132	90	60	6	11	483	0	0
NGA	475.9	620	172	4	224	58	112	110	43	26

Note: All data indicated in ppm.

Table 3. Methane/ethane ratio from Core 159-959A-52H.

Core	Depth (mbsf)	C ₁	C ₂	Ratio	C ₃
159-959A-52H	480.7	1345	0	0	0
52H	480.7	346	0	0	0
52H	480.7	4479	4	1120	2
52H	480.7	5271	0	0	0

reentry Hole 959E was planned for spudding to the northeast, thus maximizing the separation between the site's two projected deepest holes, Holes 959D and 959E, at 900 m and 1600 m, respectively. The RCB wireline core barrels were spaced out and the drill string was run in the hole. Hole 959D was spudded with a center bit in place at 0645 hr 14 January. Because Hole 959A was located within 30 m of Hole 959D, the water depth (2102 m DPM) from that hole was used in this case as well. After drilling ahead for 11.75 hr at an average rate of penetration (ROP) of 38 m/hr, the center bit barrel was recovered and an RCB core barrel was pumped to bottom. Continuous RCB coring was initiated at 1830 hr 14 January at a depth of 417.8 mbsf, approximately 63 m above the depth at which APC/XCB coring was terminated in Hole 959A. Although it was hoped that the RCB coring system would get better recovery through this interval than the XCB system did, this proved not to be the case. As this interval was also an area of concern due to the hydrocarbon indications in Hole 959A, particular attention was paid to the headspace analysis of the RCB cores as the hole approached the termination depth of Hole 959A. No hydrocarbons higher than C₃ were identified and even these were in trace amounts. Methane/ethane ratios were also well within accepted limits. This seemed to confirm the idea that high temperatures generated from XCB cutting shoes during the coring process caused artificial hydrocarbon indications.

When Hole 959D reached the target depth of 900 mbsf, a wiper trip was made with the drill string to 100 mbsf and showed that hole stability was excellent. There was no evidence of fill, drag, overpull, abnormal torque, or pump pressure to indicate any existing or impending downhole problem. No rotation of the pipe was required during the trip; however, after the trip there was 15 m of debris at the bottom of the hole. The decision was made to continue coring ahead.

Core recovery and the rate of penetration (ROP) were excellent. It was theorized that if Hole 959D could be deepened to the target stratigraphic depth (approximately 1600 mbsf) then that would eliminate the need for setting a reentry cone and 10-3/4 in. surface casing string. This in turn would save much hardware and operating time. Should the depth objective of 1600 mbsf not be reached in this hole, then it was planned to recover the lowermost part of the section at a second site (Site 960), proposed site IG-1bis, the planned alternate to IG-1. This plan maximized coring time and also allowed a larger quantity of the deepest sediments (seismic Unit A) to be cored rather than requiring time-consuming coring of the overlying relatively thick (450 m) sediments of seismic Unit B.

As depth of the hole increased beyond 1000 mbsf, coring was interrupted on several occasions to wait for hydrocarbon analysis. The black shale sediments then being cored tended to yield peaks in the hydrocarbon analysis; the levels dropped off dramatically in sandstone interbeds. Below Core 159-959D-64R (1024.1 mbsf) higher hydrocarbons (NC₄ to IC₅) were detected in trace amounts. Cores 159-959D-65R (1033.7 mbsf) and 66R (1043.3 mbsf) had 6 and 10 ppm C₆, respectively, with 6.6% methane and a methane-ethane ratio 82:1. Analysis of Core 159-959D-67R (1053.0 mbsf) was more favorable, and yielded only 0.59% to 0.88% methane and a ratio of 40:1. The quantity of NC₄ and IC₅ dropped by 66%, and no C₆ was detected.

RCB coring continued for six days, with recovery reaching an average of 57.9% (Table 1). Recovery of black shales and siltstones was excellent, even exceeding 100% at times. This was tempered by poor recovery (<10%) in the fractured sandstones and in areas where chert was present. As far downhole as 745 mbsf, penetration rates were surprisingly good and ranged from 19 to 38 m/hr. Zones of accelerated penetration rate (6–7 min/core) and minimal recovery (3%–6%) at 450–480 mbsf were associated with chert recovery.

Hole 959D was terminated at 1158.9 mbsf due to increasingly poor ROP and the continued occurrence of thick black shale intervals with associated hydrocarbon spikes. Headspace analysis on Core 159-959D-78R yielded a C₁/C₂ ratio of 30, the same as Core 159-959D-77R. Ethane was measured at only 3%, and C₃, NC₄, and IC₄ were present in trace amounts. No higher hydrocarbon chains were present. The hydrocarbon situation had minimal impact on the decision to terminate Hole 959D. Instead the major scientific objectives had been accomplished, and since the ROP had been steadily decreasing (Core 159-959D-78R took 200 min to cut 9.7 m of unconsolidated black shale), it was decided that the remaining objectives would likely be better attained at the alternate proposed IG-1bis site.

Logging (Hole 959D)

After termination of drilling, a 30-barrel Sepiolite mud pill was circulated from the bottom up and a second wiper trip was made to 100 mbsf. Hole stability continued to be excellent, and there was no evidence of any existing or impending downhole problem. Two wireline runs were made to release the mechanical bit release (MBR) and subsequently shift the sleeve back down to close off the dog windows in the side of the MBR top connector. The hole was displaced with 400 barrels of Sepiolite mud, and the pipe was tripped to 99.5 mbsf in preparation for logging operations. Due to the anticipated hole conditions the Conical Side Entry Sub (CSES) was not picked up.

After rigging of the Schlumberger logging sheaves, the first suite of tools was assembled. Run No. 1, referred to as the Quad combination (see "Downhole Measurements" section, this chapter), was run into the hole, but was only able to reach 120 mbsf or approximately 20 m below the end of the pipe. It was suggested that the sticky clays recovered in this portion of the hole were swelling due to hydration and causing blockage. The logging tools were recovered and the CSES was picked up to allow the drill pipe to be lowered past the restriction. The drill string was lowered to 390 mbsf before encounter-

ing a restriction, which proved impassable without the ability to rotate the pipe. Because the logs in the lower portion of the hole were of the top priority the pipe was tripped back, the CSES was removed, and the top drive was picked up. With rotation the string was lowered to 423 mbsf, and the Quad combination logging string was run into the hole before stopping at 548 mbsf, or 125 m beyond the end of the pipe. This portion of the hole was then logged.

All indications were that the hole remained in good condition, as the drill pipe was not encountering any drag or resistance during the lowering process. Because of this it was theorized that the hole might be slightly deviated from the vertical and have a rugose wall due to the interbedded formations. Lack of centralization of the logging tools would allow them to lie on the low side of the hole and tend to hang up on downhole ledges. To try to circumvent this problem a meter-long, rubber "hole finder" was installed on the bottom of the logging suite in place of the LDEO temperature tool. After recovering the logging tools, the top drive was again picked up and the pipe was run farther into the hole to 567 mbsf. The top drive was set back and the second run (#2) with the Quad combination tools was made. This time a depth of 1081 mbsf was reached, within 78 m of the total depth of the hole. Logs were obtained from this interval up to the pipe at 567 mbsf. The next logging run (#3) was made with the Formation MicroScanner and Natural Gamma Tool (FMS/NGT). These tools reached a depth of 938 mbsf and logs were obtained from that depth up to the drill pipe at 538 mbsf. The final logging run (#4) was made with the geochemical tool string (GST, ACT, CNTG, and NGTC). These tools reached a depth of 927 mbsf, and logs were obtained from that point up to the drill pipe at 538 mbsf. This concluded logging operations for Hole 959D. After rigging down the last suite of tools and the logging sheaves, preparations were begun for the plugging and abandonment of the hole.

Plug and Abandonment (Hole 959D)

Because Hole 959D was located on a continental slope, the hole was filled with 117 barrels of 10 ppg weighted mud and capped with a 20-barrel cement plug. The drill string was pulled out of the hole and after clearing the mud line the pipe was flushed with seawater to remove any residual cement. During the trip the primary and backup positioning beacons were commanded to release. The primary beacon (SN 779) was recovered in short order; however, the backup beacon (SN 1245) apparently failed to release and was not observed at the surface. Tripping of the drill string was then resumed and the MBR top connector reached the rig floor at 0530 hr, thus completing Hole 959D.

SITE GEOPHYSICS

Site Survey

During the seismic survey shot at the beginning of Leg 159 two seismic lines were acquired across proposed site IG1 (Site 959). Full details of the acquisition of these single-channel seismic data are given in the "Underway Geophysics" chapter (this volume). The seismic survey across Site 959 included a northeast-southwest trending line (IG1-1), parallel to *Equasis* multichannel seismic (MCS) Line MT05, and a north-south trending line (IG1-2), which is coincident with *Equasis* MCS Line MT02 (Fig. 4). Shooting Line IG1-2 coincident with the previously acquired MCS Line MT02 allowed us to verify the site location from the real-time display of the data and assure that the acoustic beacon was deployed at the correct location. These considerations are particularly important at this site because the geological setting allows for possible hydrocarbon accumulations where the deeper sedimentary layers pinch-out against the acoustic basement slope to the south. Therefore, accurate site location was important to maximize safety, as recommended by the JOIDES Pollution Prevention and Safety Panel (PPSP). In addition, the single and multichannel seismic data already available had been acquired prior to full GPS

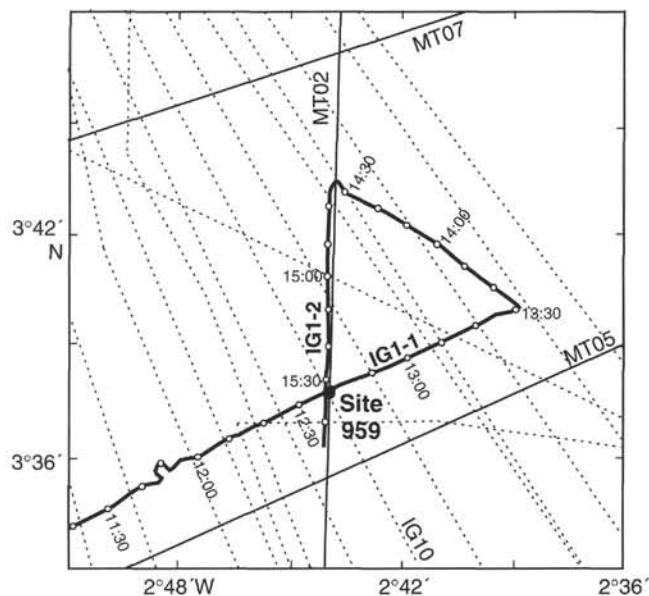


Figure 4. Track chart showing the single-channel seismic data collected over Site 959 together with previous seismic surveys in the area. Dashed lines correspond to single-channel data collected during the *Equamarge II* 1988 program; solid lines denote multichannel lines acquired during the *Equasis* survey of 1990. Site 959 was selected at the intersection of MCS Line MT02 and single-channel Line IG10.

satellite coverage of this area, so it was necessary to check for any possible positioning errors of these older data. However, despite these uncertainties, lines MT02 and IG1-2 show excellent agreement.

Although the single-channel seismic data are less penetrative than the multichannel data already available, acoustic basement and several intra-sediment reflectors can still be distinguished on these data. Following basic processing (mute, 10–100 Hz bandpass filter) and re-display of these data, the sedimentary column in the Deep Ivorian Basin north of the Côte d'Ivoire-Ghana Marginal Ridge can be divided into Units A through F as discussed in the "Background and Objectives" section, this chapter (Fig. 5).

Integration of Seismic Profiles with Observations from the Site

Although downhole velocity logs were obtained at Hole 959D between 550 and 1050 mbsf, the initial conversions from two-way traveltime (TWT) to depth for prominent reflectors were computed using the vertical velocities measured by either the Digital Sound Velocimeter or the Hamilton Frame Velocimeter (see "Physical Properties" section, "Explanatory Notes" chapter, this volume). The depth estimates of the major reflectors are summarized in Table 4, and the tie of Site 959 to the two crossing single-channel seismic lines (IG1-1 and IG1-2) and multichannel Line MT02 is shown in Figure 6.

Reflector R1: 0.20 s TWT Below Seafloor

Reflector R1 is seen most clearly on MCS Line MT02 where it correlates with the top of seismic Unit E ("Background and Objectives" section, this chapter), although on the single-channel lines, IG1-1 and IG1-2, this horizon can barely be discerned (Fig. 6). The computed depth for this reflector is 180 mbsf. From the lithostratigraphy of Site 959 the transition from lithologic Units I to II (i.e., the transition from largely nannofossil ooze to predominantly siliceous facies) lies at a depth of 208 mbsf. The dominant frequency of the water-gun seismic source used is 40 Hz, which corresponds to a wavelength of 40 m at velocities of 1.6 km/s. Within the resolution of the

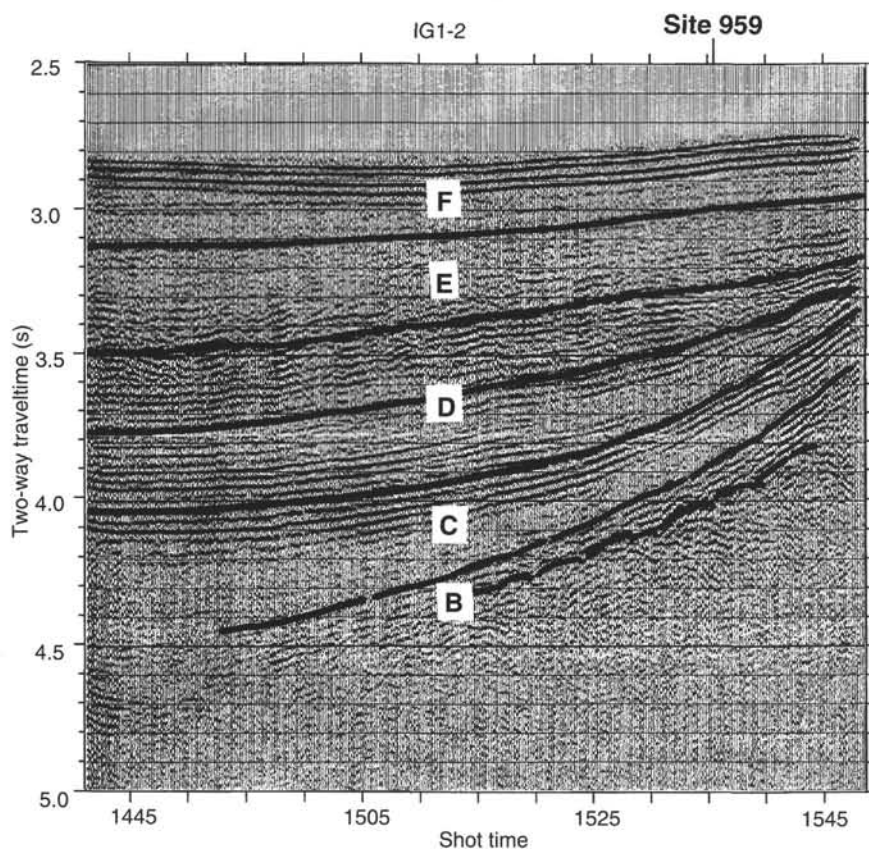


Figure 5. Single-channel seismic reflection Line IG1-2 (see Fig. 4 for location). Traces have been filtered from 10 to 100 Hz. Uppercase letters (B–F) indicate seismic units.

Table 4. Depth of reflectors at Site 959.

Reflector	Top of unit	Time (s TWT)	Computed depth (mbsf)	Origin of reflector*
R1	E	0.20	180	Transition from nanfossil ooze (Unit I) to siliceous facies (Unit II)
R2	D	0.54	430	Chert; top of Subunit IIB
R3		0.65	530	?Within Subunit IIC
R4	C	0.90	750	Increased carbonate content; transition from porcellanite to chalk at base Subunit IIC
R5	B	1.13	980	Dolomite and barite toward the base of Unit III
R6	A	1.24	1130	Sandstone and siltstone beds; Unit V

Note: * See "Lithostratigraphy" section, this chapter.

seismic signal, Reflector R1 can therefore be considered to represent the interface between lithologic Units I and II. The sedimentary section above Reflector R1 is acoustically transparent, showing no reflections.

Reflector R2: 0.54 s TWT Below Seafloor

Reflector R2 corresponds to the top of lithologic Subunit IIB, which comprises black chert and claystone. The computed depth for this reflector is 430 mbsf. This horizon lies toward the top of a region of increased reflectivity compared with the largely transparent sediments above (Fig. 6). The underlying sediments show well layered, slightly undulating, reflectors that may be disturbed by small faults. Reflector R2 corresponds to the top of seismic Unit D.

Reflector R3: 0.65 s TWT Below Seafloor

Although Reflector R3 is seen as a relatively large amplitude, clear, reflector on the seismic sections (Fig. 6), there is no obvious lithologic explanation for this event, which lies within lithologic Subunit IIC at a computed depth of 530 mbsf. However, this depth interval does show a slight variation in the sediment physical properties, with a small increase in bulk density and a corresponding decrease in porosity (see Fig. 60). This reflector lies within seismic Unit D.

Reflector R4: 0.90 s TWT Below Seafloor

Reflector R4 is a strong and continuous event on the seismic reflection profiles that separates a unit exhibiting well layered reflections from an underlying transparent unit (Fig. 6). The computed depth of this reflector is 750 mbsf. This is located toward the base of lithologic Unit II and coincides with a small increase in carbonate content, giving a change in lithologic constituents from porcellanite with clay to porcellanite nanfossil chalk (see "Lithostratigraphy" section, this chapter). The effect of this increase in carbonate content can also be observed in the physical properties data, which show a sharp decrease in porosity at this depth (see Fig. 60). Reflector R4 corresponds to the top of seismic Unit C.

Reflector R5: 1.13 s TWT Below Seafloor

Reflector R5, computed depth 980 mbsf, corresponds to the first occurrence of barite and dolomite within claystone toward the base of lithologic Unit III (995 mbsf). This is slightly above the top of lithologic Unit IV (which corresponds to seismic Unit B) and the resolution of these two separate events is probably beyond that of a seismic wavelength (at this depth, where the velocity is approximately 2.0 km/s, the wavelength of the seismic signal is on the order of 50

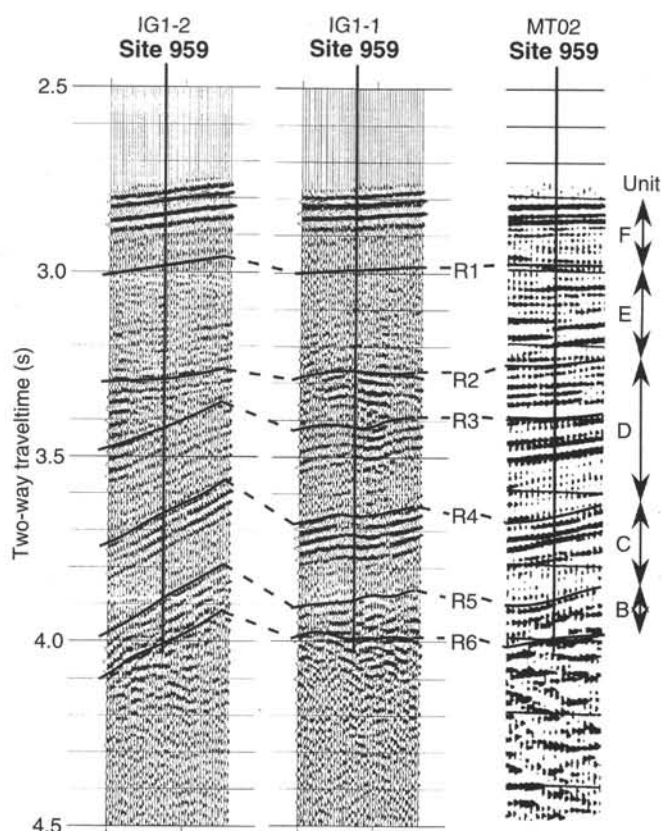


Figure 6. Ties of the principal reflectors observed on single-channel seismic Lines IG1-1 and IG1-2, and multichannel Line MT02 to Site 959.

m). Reflector R5 marks the top of a zone of strong, relatively discontinuous, reflectors (Fig. 6).

Reflector R6: 1.24 s TWT Below Seafloor

Reflector R6, which is hyperbolic in character, has the appearance of acoustic basement. Comparison with sediments recovered from Hole 959D indicates alternating layers of sandstones and silty claystones within lithologic Unit V. This interval appears to be marked by a sharp increase in compressional-wave velocity. The computed depth of Reflector R6 (1130 mbsf) is slightly below the top of lithologic Unit V (1082 mbsf), which corresponds to the top of seismic Unit A.

In Situ Temperature Measurements

The ADARA tool was deployed to obtain in situ temperature measurements in Hole 959A. The components of the thermal tool are located in the coring shoe of the advanced piston corer, and the ADARA depth therefore is based on the sub-bottom depth of the base of the APC core barrel. Measurements were taken at 37.6, 85.1, 132.6, and 180.1 mbsf. However, the measurement obtained at 37.6 mbsf was omitted from the dataset as the temperature profile did not show a normal decay toward equilibrium. During deployment the tool was held at the mud line for several minutes to equilibrate to the bottom temperature, before being lowered down the drill string prior to coring. After insertion of the tool, the temperatures were measured at 5-s intervals for 10–15 min before the core was withdrawn. This procedure provides a sufficiently long transient record for reliable extrapolation of the steady state temperature (Fig. 7). Sub-bottom temperatures were extrapolated from synthetic curves that were constructed to fit the transient temperature data.

The temperatures obtained were then plotted against depth (Fig. 8). The slope of a linear least squares fit of the temperature against

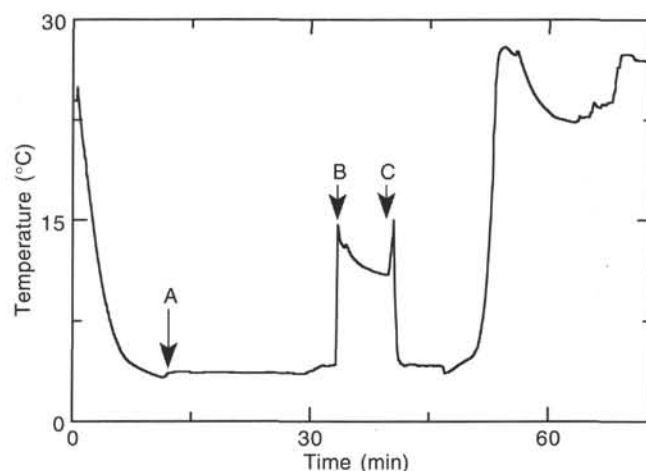


Figure 7. ADARA deployment at 132.6 mbsf in Hole 959A. Observed temperature as a function of time. Between A and B the tool is equilibrating to the bottom water temperature. B marks the insertion point, following which the temperature decays toward thermal equilibrium, before the core is withdrawn (C). Core 159-959A-14H.

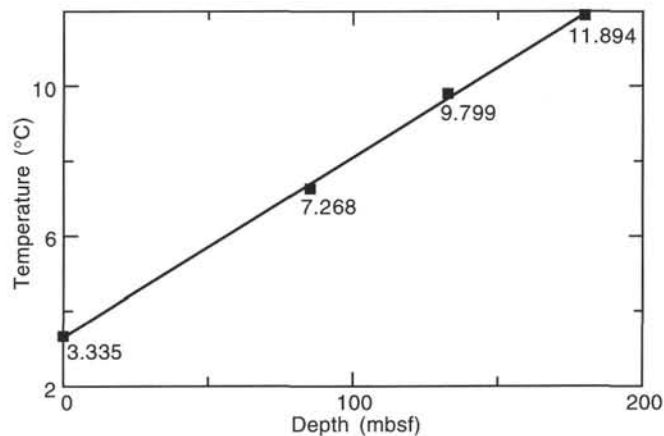


Figure 8. Linear least squares curve of temperature vs. depth for Hole 959A.

depth yields an estimate of a geothermal gradient of $0.048^{\circ}\text{C}/\text{m}$ (99% confidence level) in the upper 180 mbsf of Hole 959A.

Using the thermal conductivity data obtained (see “Physical Properties” section, this chapter) an estimate can be made of the heat flow at this site. The mean value of thermal conductivity is $1.17 \text{ W m}^{-1}\text{C}^{-1}$, which, when multiplied with the geothermal gradient, gives a heat flow value of 0.056 W m^{-2} from 0 to 180 mbsf at Hole 959A.

LITHOSTRATIGRAPHY

Introduction

Site 959 was drilled in 2090.7 m of water, on the Côte d’Ivoire-Ghana Marginal Ridge as discussed in the “Operations” section (this chapter). A total of 1158.9 m of the stratigraphic section was cored in four holes.

We divided the sediment into five lithologic units (Fig. 9; Table 5). Going downsection, lithologic Unit I, Holocene to lower Miocene, comprises 208.0 m of dominantly calcareous sediment with two end-member sediment components: nannofossil ooze (grading downhole into nannofossil chalk), and foraminifer ooze (grading downhole into foraminifer chalk). These components alternate from lighter (more foraminifer-rich) to darker beds, and from laminated to bioturbated intervals. This unit was divided into two lithologic sub-

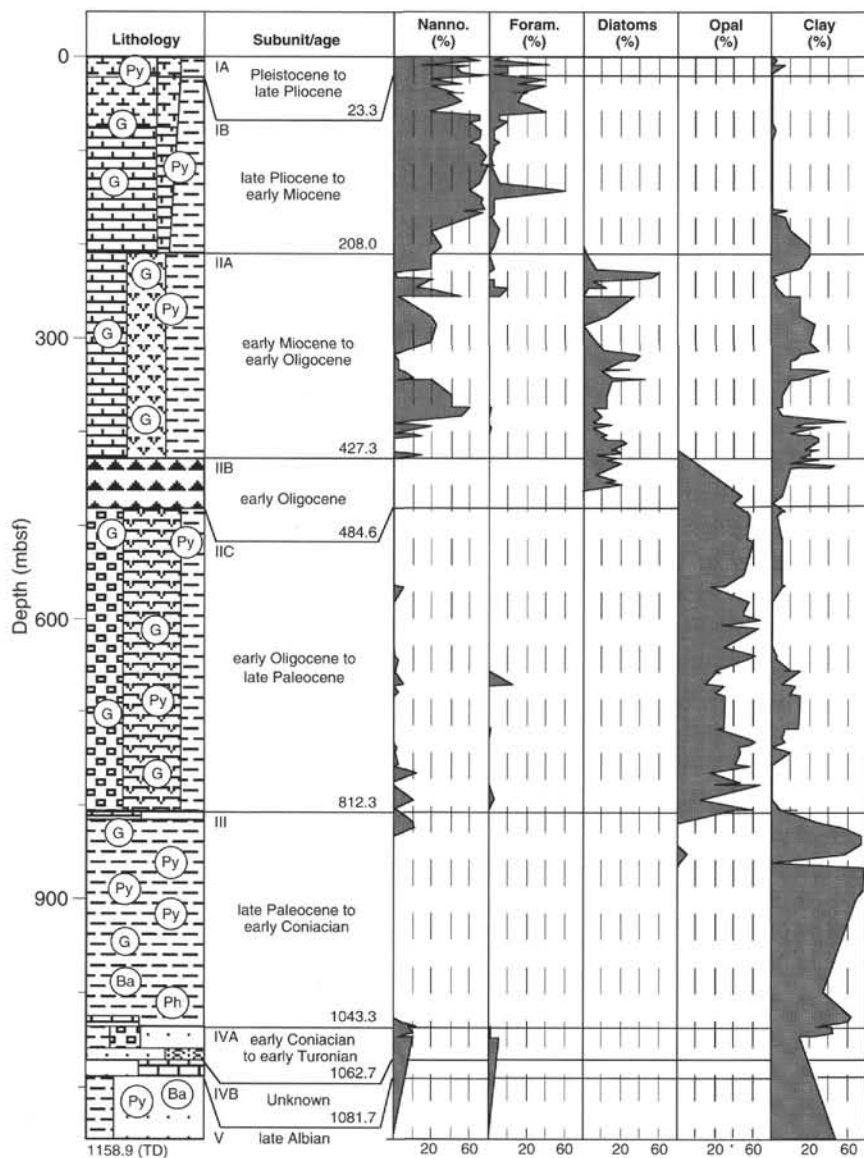


Figure 9. Stratigraphic column for Site 959.

units because the upper 23 m (Pleistocene to late Pliocene age) has a darker color resulting from increased pyrite and organic matter levels. Lithologic Unit II comprises 599.3 m of alternating siliceous and calcareous sediment. We divided this unit into three lithologic subunits based upon the preservation of the siliceous microfossils. The upper lithologic subunit, IIA, comprises interbedded nannofossil chalk, diatomite, and clay, and ranges from early Miocene to early Oligocene in age. A black, middle early Oligocene age chert layer between 430 and 440 mbsf was designated lithologic Subunit IIB. Beneath this layer in lithologic Subunit IIC, nannofossils are poorly preserved and siliceous microfossils are not preserved. The sediment of Subunit IIC comprises micrite chalk and porcellanite and ranges from early Oligocene to late Paleocene in age. Lithologic Unit III comprises 231.0 m of black claystone, ranges in age from late Paleocene to early Coniacian, and has minor black claystone with nannofossils occurring at both the top and base of the unit. The Cretaceous/Tertiary boundary was not observed because of the absence of calcareous and siliceous fossils, and could not be identified using palynomorphs because of their poor preservation. Lithologic Unit IV comprises 38.4 m of sandy limestone, sandy dolomite, calcareous sandstone, and limestone of early Coniacian to early Turonian and unknown age. Lithologic Unit V comprises quartz sandstone and silty claystone of late Albian age.

Description of Lithologic Units

Unit I

Description: Nannofossil ooze and chalk, foraminifer nannofossil ooze and chalk, and nannofossil ooze and chalk with clay

Interval: Sections 159-959A-1H-1, 0 cm, through 23X-1, 40 cm; 159-959B-1H-1, 0 cm, through 20H-CC, 33 cm (TD); and 159-959C-1H-1, 0 cm, through 20H-CC, 26 cm (TD)

Depth: 0–208.0 mbsf, Hole 959A; 0–184.4 mbsf, Hole 959B; 0–179.6 mbsf, Hole 959C

Age: Pleistocene to early Miocene

Unit I comprises nannofossil ooze and chalk, foraminifer ooze and chalk, and nannofossil ooze or chalk with clay. The color varies from light to dark gray, and the bedding varies from centimeter-scale laminations to massive when intensely bioturbated. This lithologic unit was divided into two subunits based on variation in color. Subunit IA, Pleistocene to late Pliocene in age, comprises distinctly darker nannofossil and/or foraminifer ooze because of elevated levels of organic matter and pyrite, and Subunit IB, late Pliocene to early Miocene in age, comprises lighter nannofossil and/or foraminifer ooze that grades downward into nannofossil and/or foraminifer chalk. This subunit bears a distinctly laminated interval with glauconitic hard-

Table 5. Lithologic units for Site 959.

Unit	Subunit	Cored interval	Depth interval (mbsf)	Thickness (m)	Lithology	Age (Epoch)
I	A	159-959A-1H, 0 cm, to 3H-4, 15 cm	0–23.3	23.3	Nannofossil/foraminifer ooze, dark gray (more pyrite)	Pleistocene to late Pliocene
		159-959B-1H, 0 cm, to 4H-1, 60 cm 159-959C-1H, 0 cm, to 4H-3, 60 cm	0–24.6 0–24.9	24.6 24.9		
	B	159-959A-3H-4, 15 cm, to 23X-1, 40 cm 159-959B-4H-1, 60 cm, to 20H-CC, 33 cm (TD) 159-959C-4H-3, 60 cm, to 20H-CC, 26 cm (TD)	23.3–208.0 24.6–184.4 24.9–179.6	184.7 Base not reached Base not reached	Nannofossil/foraminifer ooze, nannofossil/foraminifer chalk with thin glauconite beds (clayey nannofossil chalk and nannofossil clay in the lower 60 m of Hole 959A)	late Pliocene to early Miocene
II	A	159-959A-23X-1, 40 cm, to 49X-CC, 0 cm	208.0–456.6	247.5	Interbedded diatomite with nannofossil chalk and clay (chert at 430 mbsf in Hole 959A)	early Miocene to early Oligocene
		159-959D-1R-1, 0 cm, to 1R-6, 95 cm (base)	417.8–427.3	9.5 (top not recovered)		
	B	159-959A-49X-CC, 0 cm, to 52X-CC, 3 cm (TD) 159-959D-2R-1, 0 cm, to 8R-CC, 17 cm (base)	456.6–480.7 427.3–484.6	24.1 57.3	Chert and claystone	middle early Oligocene
	C	159-959D-9R-1, 0 cm, to 42R-CC, 21 cm (base)	484.6–812.3	327.7	Porcellanite, with micrite and some clay	early Oligocene to late Paleocene
III		159-959D-43R-1, 0 cm, to 66R-CC, 38 cm (base)	812.3–1043.3	231	Black claystone, minor claystone with nannofossils	late Paleocene to early Coniacian
IV	A	159-959D-67R-1, 0 cm, to 68R-CC, 15 cm (base)	1043.3–1062.7	19.4	Sandy limestone, sandy dolomite, and calcareous sandstone	early Coniacian to early Turonian
	B	159-959D-69R-1, 0 cm, to 70R-1, 43 cm (base)	1062.7–1081.7	19.0	Limestone	Unknown
V		159-959D-71R-1, 0 cm, to 78R-CC, 20 cm (TD)	1081.7–1158.9	77.2	Quartz sandstone and silty claystone	late Albian

Note: TD = total depth

grounds and coarser foraminifer sand layers. Clay content gradually increases downhole.

Subunit IA

Description: Nannofossil ooze, foraminifer nannofossil ooze, and nannofossil ooze with clay

Interval: Sections 159-959A-1H-1, 0 cm, through 3H-4, 15 cm; 159-959B-1H-1, 0 cm, through 4H-1, 60 cm; and 159-959C-1H-1, 0 cm, through 4H-3, 60 cm

Depth: 0–23.3 mbsf, Hole 959A; 0–24.6 mbsf, Hole 959B; 0–24.9 mbsf, Hole 959C

Age: Pleistocene to late Pliocene

Subunit IA comprises nannofossil ooze and foraminifer ooze as end-member types of sediment, with various admixtures of the two forming interbeds. Increased abundance of foraminifers (e.g., 50%–65% vs. 15%–20%) gives the sediment a lighter color over 10- to 80-cm intervals. Boundaries between lighter and darker intervals are gradational, usually as a result of bioturbation. Disseminated pyrite occurs throughout this subunit, with local concentrations in burrows. Bioturbation is slight to moderate. Large, oval holothurian burrows (up to 4 cm across) are present, but most burrows are 1 cm across, and horizontal to subhorizontal. In intervals with slight bioturbation, original laminae are visible (e.g., see core photograph for Core 159-959A-2H, this volume). Laminae also vary in color from lighter and more foraminifer rich, to darker and more coccolith rich. Several scoured contacts were observed (e.g., in core photograph for Core 159-959A-1H-4, 10–15 cm), and these may account, in part, for the variation in thickness among the three holes. There is usually a millimeter-thick lag of foraminifers above the scoured contacts.

The dark color of this subunit separates it from the sediment below. No significant compositional variation visible in smear slides accompanies this color change, except for a slightly higher level of pyrite in Subunit IA. Organic carbon levels also are higher as discussed in the “Organic Geochemistry” section, this chapter.

Subunit IB

Description: Nannofossil ooze and chalk, foraminifer nannofossil ooze and chalk, and nannofossil chalk with clay

Interval: Sections 159-959A-3H-4, 15 cm, through 23X-1, 40 cm; 159-959B-4H-1, 60 cm, through 20H-CC, 33 cm (TD); and 159-959C-4H-3, 60 cm, through 20H-CC, 26 cm (TD)

Depth: 23.3–208.0 mbsf, Hole 959A; 24.6–184.4 mbsf, Hole 959B; 24.9–179.6 mbsf, Hole 959C

Age: late Pliocene to early Miocene

Subunit IB was separated from the overlying subunit on the basis of a sharp color change from darker to lighter gray, which corresponds to reduced levels of organic carbon and pyrite. There is no significant variation in the principal components—nannofossils, foraminifers, and minor clay—from the overlying subunit. Nannofossil ooze and foraminifer ooze (as well as various admixtures of these two end members), gradually consolidate downhole to become nannofossil chalk and foraminifer chalk. We placed the change from ooze to chalk at approximately 75 mbsf, corresponding to a reduction in porosity and water content (see “Physical Properties” section, this chapter). This depth also corresponds (within 5 m) to the first downhole appearance of glauconitic hardgrounds.

There is a gradual increase in clay content downhole. Sediment from the lower 60 m of Hole 959A is clayey nannofossil chalk and nannofossil clay. This is accompanied by a relative decrease in foraminifer abundance. The increase in clay content is visible as a sharp but temporary decrease in CaCO₃ content of the sediment from Hole 959A, beginning at approximately 160 mbsf (see “Organic Geochemistry” section, this chapter), a gradual increase in natural gamma-ray background radiation (see “Physical Properties” section, this chapter), and a change in magnetic properties (see “Paleomagnetism” section, this chapter).

Color variations in this subunit, occurring over 10- to 80-cm intervals, reflect the relative abundance of nannofossils (darker intervals) and foraminifers (lighter intervals). A green band, caused by

enrichment in glauconitic (?) pellets, occurs, below at 65.6 mbsf in Hole 959A (65.2 mbsf in Hole 959B; 62.6 mbsf in Hole 959C). The occurrence of color bands increases downhole, and they form part of a distinct color banding that persists to the base of the subunit. The color bands comprise three distinct lithologies: a light gray green nannofossil chalk with foraminifers, generally overlain by a medium brown gray foraminifer nannofossil chalk, overlain by a glauconite nannofossil chalk. The bands locally form distinct 1-cm-thick laminae (Fig. 10), or in other places, form color bands up to 5 cm thick that grade into one another and are somewhat mixed by bioturbation. These laminae or color band triplets form beds 10 to 150 cm thick and are separated by moderately to highly bioturbated intervals of foraminifer nannofossil chalk. Locally, the foraminifer- and glauconite-enriched beds have sharp contacts: a sharp lower contact for the former, and a sharp upper contact for the latter. The foraminifer-enriched beds with a sharp basal contact appear to be foraminifer-sand lags formed by bottom current winnowing. The glauconite-enriched laminae with a sharp upper contact are hardgrounds representing brief hiatuses in deposition (Fig. 10). Between 135 and 140 mbsf, the hardgrounds have been oxidized to a rusty brown color. The green material may be a glauconitic smectite or a 7Å (berthierine) green clay. XRD analysis of the bulk sediment shows both a broad peak at 14Å and a peak at 7Å in this sediment (Fig. 11).

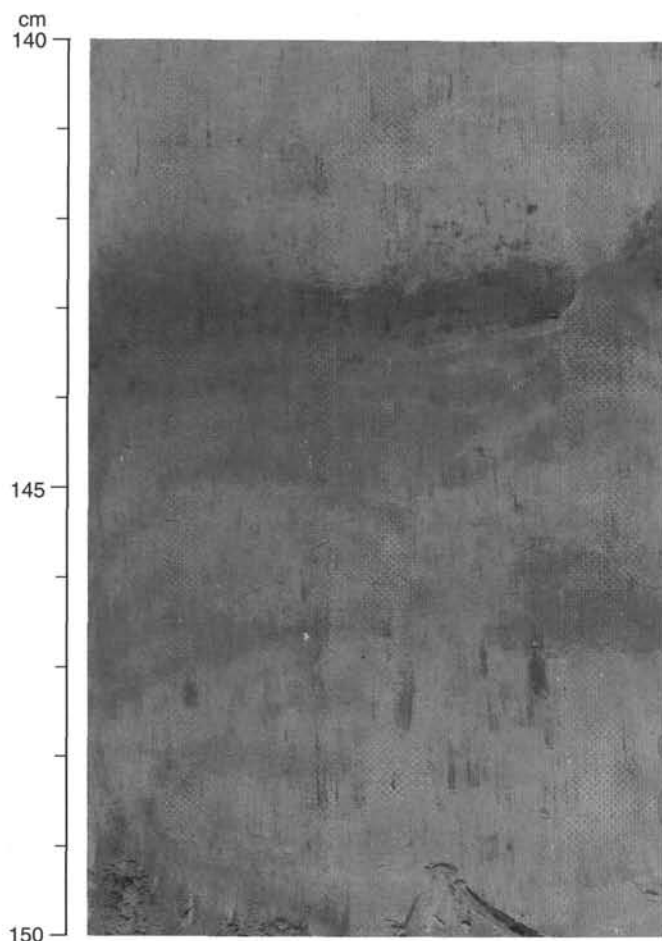


Figure 10. Section 159-959A-18H-4, 140–150 cm; characteristic color banding or laminae of parts of lithologic Subunit IB. The light color is nannofossil chalk; the medium color is enriched in foraminifers (foraminifer nannofossil chalk); and the dark color is enriched in glauconite pellets (glauconite nannofossil chalk). These laminated triplets form beds up to 1.5 m thick and alternate with moderately to highly bioturbated nannofossil chalk.

The bioturbated intervals between the banded or laminated intervals attest to a thriving, albeit temporary, benthic community, which included *Planolites*, *Thalassinoides*, *Ophiomorpha*, and *Zoophycos*. *Chondrites* rarely occurs in darker intervals. In some parts of the core, the sediment is faintly mottled, and appears to be thoroughly mixed by bioturbation (see core photograph for Core 159-959A-13H in "Cores" section, this volume). Pyrite is scattered as black specks throughout the sediment and is locally concentrated in burrows. Other burrows have been partly replaced by green material, and still others have been replaced by dolomite, identified by XRD as well as visually in smear slides. The first downhole occurrence of dolomite is in Core 159-959B-10H at approximately 85 mbsf.

The color bands or laminae persist to the base of Holes 959B and 959C, but are not present in Hole 959A below Core 159-959A-20H. This depth marks the change from APC to XCB coring, so that drilling disturbance may account for the loss. In the lowest part of this lithologic unit (Core 159-959A-21X to Section 159-959A-23X-1, 40 cm), alternations between dark and light sediment, all of it bioturbated, recur. But here the dark color arises from increased clay levels and the light color from increased nannofossil levels. Foraminifer abundance decreases to less than 5% of the sediment. The base of the lithologic unit occurs at the top of the first downhole occurrence of diatomite.

Unit II

Description: Diatomite, chert, and porcellanite

Interval: Sections 159-959A-23X-1, 40 cm, through 52X-CC, 3 cm (TD), and 159-959D-1R-1, 0 cm, through 42R-CC, 21 cm

Depth: 208.0–480.7 mbsf, Hole 959A; 417.8–812.3 mbsf, Hole 959D

Age: early Miocene to late Paleocene

The sediments of lithologic Unit II are dominated by siliceous biogenic phases and their diagenetic products and include diatomite, porcellanite, and chert. The upper boundary of this unit was defined by the first occurrence of diatoms as a major biogenic component. This contrasts with the nannofossil and foraminifer oozes and chalks of lithologic Unit I, where diatoms, although present as a subordinate component, do not comprise a distinctive lithology. In lithologic Unit II, diatoms, radiolarians, and other siliceous components can constitute more than 90% of the biogenic pelagic grains (although generally these average about 40%). This lithology is distinctive in appearance and unambiguous upon close examination. In addition to diatoms and

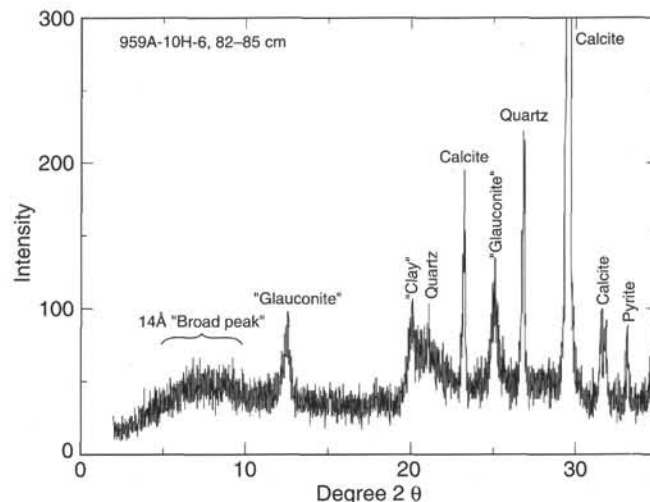


Figure 11. X-ray diffractogram of the green material of lithologic Subunit IB shows a weak smectite peak (14Å) at about 8° 2θ, and a 7Å peak around 12.4° 2θ. The latter may be detrital kaolinite or authigenic berthierine.

radiolarians, Unit II was characterized by the abundance of other siliceous components, including spicules and silicoflagellates as well as diagenetic lithologies such as chert and porcellanite. Note that the definitive recognition of this unit was based upon the dominance of siliceous components over calcareous nannofossils and zooplankton. Furthermore, the preservation of these primary skeletal materials varies downcore. In general, with increasing depth, siliceous skeletal remains are progressively transformed to opal-CT. This was observed as the development of isotropic particles as a major component of the finest size fraction. Continuing diagenesis of opaline phases is locally manifested in the formation of chert and porcellanite, which dominate in the lower part of this unit (Subunits IIB and IIC, respectively). The lower boundary of lithologic Unit II, and the upper boundary of lithologic Unit III, is marked by a transition to black claystones and minor dark gray claystones with nannofossils.

Subunit IIA

Description: Diatomite interbedded with nannofossil chalk and clay
Interval: Sections 159-959A-23X-1, 40 cm, through 49X-CC, 0 cm, and 159-959D-1R-1, 0 cm, through 1R-6, 95 cm
Depth: 208.0–456.6 mbsf, Hole 959A; 417.8–427.3 mbsf, Hole 959D
Age: early Miocene to early Oligocene

Lithologic Subunit IIA is characterized by a marked increase in the abundance of siliceous microfauna and flora as the primary biogenic component. This subunit is dominated by the presence of diatoms with associated siliceous faunas and floras (silicoflagellates, spicules, and radiolarians). Varying contributions of clay and nannofossils lead to an overall pattern of interbedded or alternating lithologies present throughout this interval (e.g., nannofossil chalk, diatom nannofossil chalk, clayey diatom nannofossil chalk, diatomite with clay, clayey diatomite, and claystone with diatoms). These alternations, with individual lithologies ranging in thickness from 10 to 80 cm, are manifested as changes in the sediment color, from light to dark, from light gray and brown to dark gray, to black. In general, lithologies dominated by diatoms and siliceous phases represent the darker lithology, whereas the addition of clays and/or calcareous microfaunas produces the lighter interbedded lithology.

Over the stratigraphic range of this subunit, lithologies exhibit an overall progression from calcareous (diatom nannofossil chalk in Cores 159-959A-23X through 34X), to siliceous (clayey diatomite in Cores 159-959A-34X through 37X), to calcareous (diatomite with nannofossils in Cores 159-959A-37X through 41X), to clay rich (diatom clay/claystone in Cores 159-959A-42X through 49X). Diatoms, unlike other siliceous microfossils, are present throughout the interval, varying only in abundance relative to other contributing components. When present, foraminifers and radiolarians are commonly fragmented and corroded or remain only as pyritized relicts. Spicules remain as a minor component in all siliceous lithologies, presumably reflecting their refractory nature during the diagenetic alteration of opaline silica.

Pyrite is present as a common associated mineral phase, generally occurring as fine clay to silt-sized framboids disseminated throughout lithologic Subunit IIA. Pyrite is also present locally as concretions that range in size from 5 to 15 mm (e.g., in Section 159-959A-34X-6) or concentrated within burrow traces. In addition to pyrite, dolomite or siderite may be developed as local replacement phases in burrows within nannofossil-rich intervals.

Disruption of primary bedding by bioturbation is evident throughout this subunit, although it is best expressed near gradational contacts between overlying and underlying lithologies, which provide a color contrast for the expression of burrow structures. Trace fossils include *Zoophycos*, *Chondrites*, and *Planolites*. *Chondrites* is most abundant in the lower part of diatomite beds and is gradually replaced upward by *Zoophycos* (see Fig. 12, Section 159-959A-26X-3, 110–130 cm).

Structures suggesting bed-load transport of sediment are rare. Although laminated intervals are common, particularly within the diat-

omite lithologies, little evidence of deposition by density or turbidity currents is present. A notable exception is the occurrence of a crudely graded bed of lithoclasts at Section 159-959A-33X-1, 80–105 cm (Fig. 13). At this interval, sand-sized intraclasts of the dominant lithologies, foraminifers and glauconite-bearing peloids, are deposited in thin beds exhibiting evidence of cross stratification and grading.

Subunit IIB

Description: Black chert and claystone
Interval: Sections 159-959A-49X-CC, 0 cm, through 52X-CC, 3 cm (TD), and 159-959D-2R-1, 0 cm, through 8R-CC, 17 cm
Depth: 456.6–480.7 mbsf, Hole 959A; 427.3–484.6 mbsf, Hole 959D
Age: middle early Oligocene

Lithologic Subunit IIB was characterized by the occurrence of black, translucent chert, which is interbedded with dark gray to black claystone and clayey diatomite. Little fabric of the primary lithology is preserved within the replacing chert except for vague traces reflective of bioturbational structures. Pyrite occurs abundantly throughout this interval as nodules replacing burrows within the clay-rich lithologies. Organic matter is disseminated throughout the diatomites and claystones, occurring as discrete fragments of plant material making up to 20% of the bulk sediment based on visual estimates. The poor recovery of this interval most likely reflects the alternation of brittle chert layers with ductile clayey lithologies. Large intervals were condensed by drilling operations with retrieval of only sporadic cobblesized fragments of chert and drilling lags of pyrite nodules (Fig. 14, Section 159-959D-52R-1, 20–38 cm).

The upper boundary of Subunit IIB was defined as the first occurrence of chert and the decrease in preserved siliceous microfossils. Clayey diatomite is also present in the upper part of this subunit. The lower boundary is marked by the last occurrence of chert (except for minor chert at the base of Subunit IIC) and a change to porcellanite and clayey porcellanite below.

Subunit IIC

Description: Porcellanite, with micrite and clay
Interval: Sections 159-959D-9R-1, 0 cm, through 42R-CC, 21 cm
Depth: 484.6–812.3 mbsf
Age: early Oligocene to late Paleocene

Lithologic Subunit IIC consists of porcellanite characterized by the development of opaline lepispheres formed from the diagenetic alteration of siliceous microfossils. As a result, this interval is virtually barren of all siliceous flora and fauna. The top of this interval was defined as the last occurrence of chert and the first occurrence of porcellanite. The lower boundary was defined as the last occurrence of porcellanite that coincides with the transition to black micritic and nannofossil claystones.

Porcellanite of Subunit IIC occurs with a distinctive color banding ranging from 10 cm to 2.5 m thick, which reflects variation in the organic matter and pyrite content, and in the degree of bioturbation. In addition, lighter bands/beds possess higher abundances of zeolites, which occur disseminated throughout the matrix as well as replacing calcareous microfossils. Most burrow traces appear flattened due to compaction, which imparts a laminated bedding fabric to much of this lithology (e.g., Cores 159-959D-13R through 15R). Most of these laminae, which range in thickness from 1 to 5 mm, are discontinuous and appear lenticular.

Pyrite and organic debris are abundant throughout this subunit and are responsible for the dark coloration of most lithologies. In addition to disseminated pyrite framboids, local concretionary growth in burrows accentuates these features. Laminae are differentially compacted over these early formed structures.

Significant variation is present in the lithologic constituents of the porcellanites over the stratigraphic range of this subunit. The upper part is interbedded with clay-rich lithologies (e.g., clayey porcellanite and porcellanite with clay). Micrite occurs at various levels within

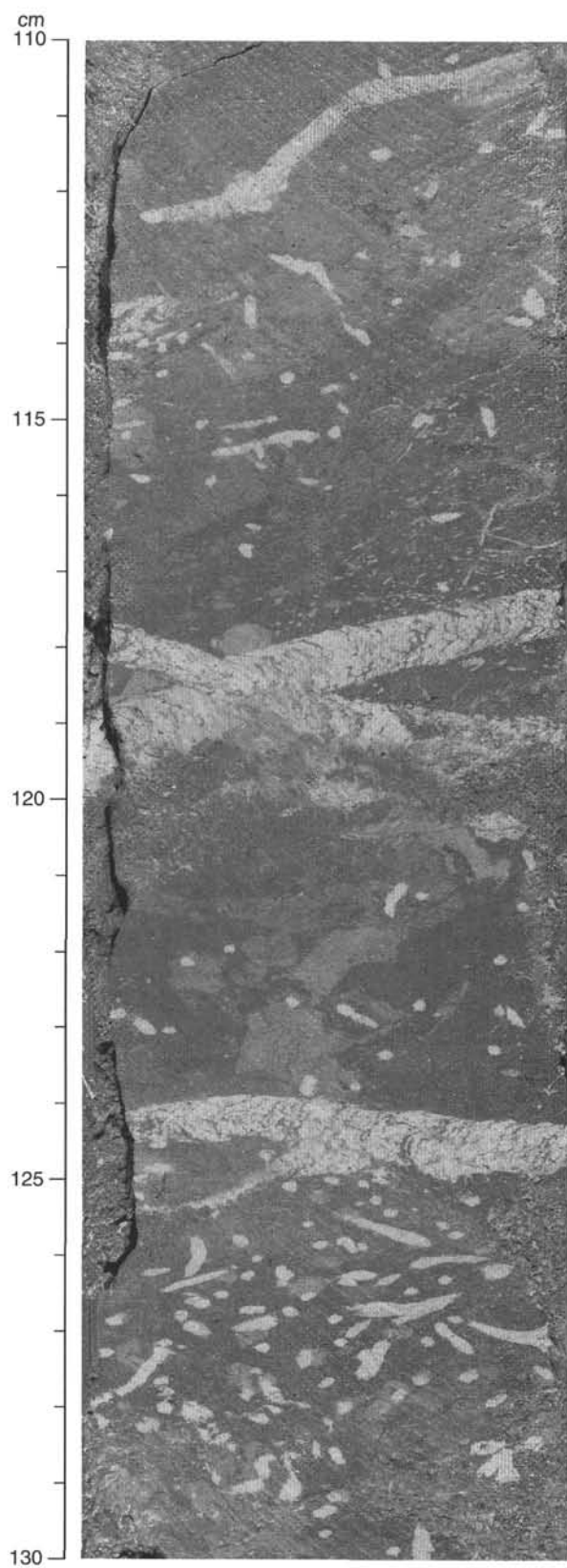


Figure 12. Section 159-959A-26X-3, 110–130 cm; *Chondrites* and *Zoophycos* burrows in diatomite with clay characteristic of bioturbation within the siliceous lithology of lithologic Subunit IIA.

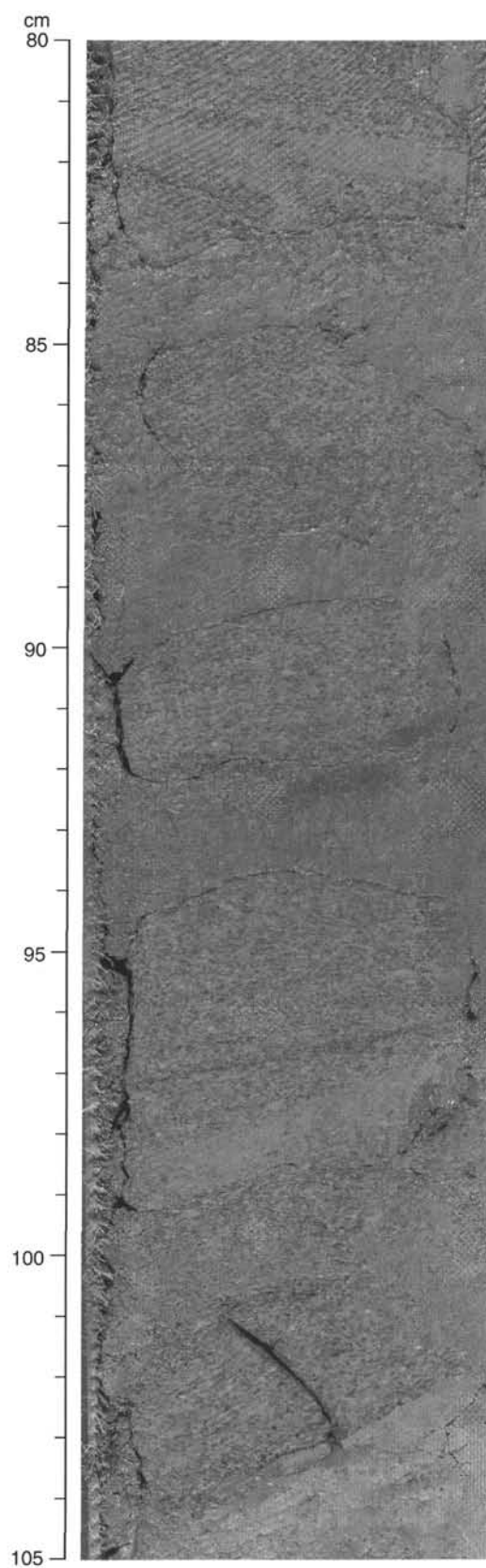


Figure 13. Section 159-959A-33X-1, 80–105 cm; intraclastic sandstone composed of glauconite-bearing peloids. Intraclasts of dominant lithologies exhibit crude graded bedding and cross stratification. Such features are interpreted as grain-flow or density-flow deposits.

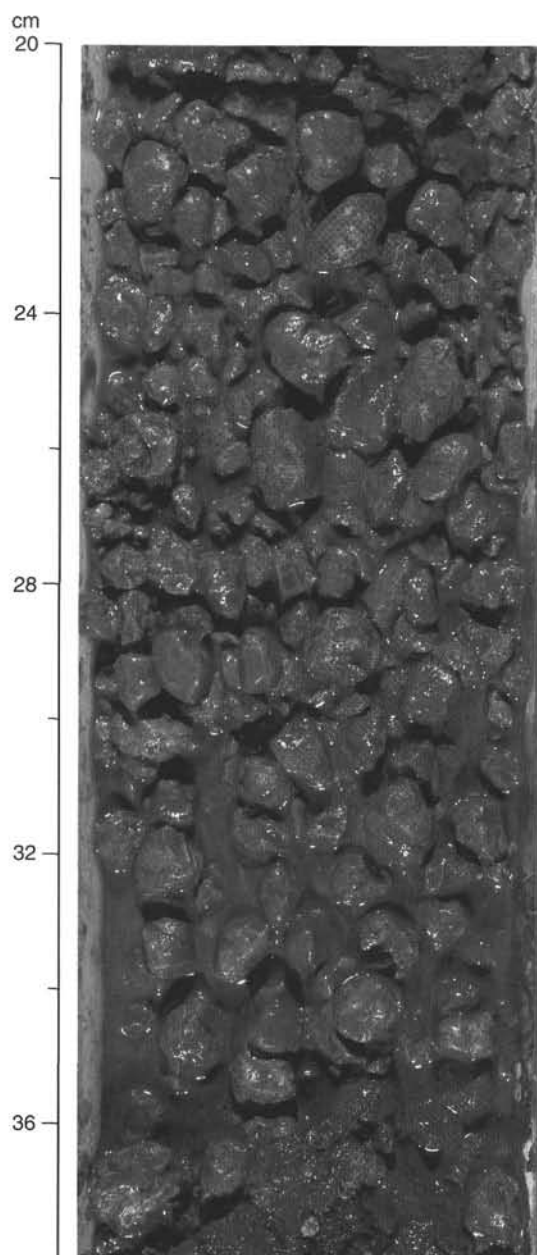


Figure 14. Section 159-959A-52H-1, 20–38 cm; pyrite nodule interval produced as a residual lag during drilling of lower part of lithologic Subunit IIB.

this subunit, but systematically increases in the lower part. At this level (Cores 159-959D-21R through 42R) the increasing carbonate content of these lithologies is best characterized as the change from porcellanite with clay to porcellanite with micrite, and subsequently to porcellanite nannofossil chalk. This downhole trend to increased carbonate content is gradational and continues across the lower boundary of Subunit IIC.

Unit III

Description: Black claystone and claystone with nannofossils
 Interval: Sections 159-959D-43R-1, 0 cm, through 66R-CC, 38 cm
 Depth: 812.3–1043.3 mbsf
 Age: late Paleocene to early Coniacian

The upper 19.3 m of lithologic Unit III consists of alternating beds of upper Paleocene claystone, nannofossil claystone, and micrite claystone. Lighter colored carbonate-bearing intervals are greenish gray (5GY 5/1 to 7GY 4/1) and occur in the upper 12.6 m of the unit. The claystone is greenish gray to black (2.5G 3/1 to 5PB N2.5); the dark color arises from higher pyrite concentrations (up to 10%). Abundant white specks in the lighter intervals are foraminifers, which have been replaced by zeolite or barite. Between 824.9 and 831.6 mbsf, lighter greenish gray claystone alternates with black claystone, and the darker layers increase in abundance downward in Core 159-959D-44R. The interval is slightly to moderately bioturbated with *Planolites*, *Zoophycos*, composite burrows, and *Chondrites*, with the latter more abundant in the darker intervals.

The interval from 831.6 to 898.2 mbsf is dominated by grayish black (N1 to N2) massive claystone, which alternates with massive to faintly laminated lighter gray (N4 to 5Y 5/1) claystone. The lighter color is related to a lower content of organic matter and pyrite, which are abundant in the black claystone (Core 159-959D-50R). This interval is early Paleocene to Maastrichtian in age, and is slightly to moderately bioturbated. Discontinuous burrows define laminations, and some *Zoophycos* burrows are still visible. Barite occurs in Cores 159-959D-46R and 51R.

In Cores 159-959D-52R through 55R (898.5 to 937.4 mbsf), which are Maastrichtian in age, the following lithologies are present: black (N1 to N3) to dark olive gray (5G 2/1 to 10Y 3/1) claystone, dark gray to black (5G 3/1) glauconite claystone with pyrite, and medium gray to black (2.5G 3/0) claystone with pyrite. Disseminated pyrite, barite, and glauconite occur, with glauconite pellets concentrated along thin laminae in some intervals. Most of the laminae are discontinuous and interrupted by slight to moderate bioturbation. *Zoophycos* and other burrows are infilled with pyrite and other disseminated minerals (Fig. 15). A few zeolite spherules are present.

The interval from 937.1 to 995.4 mbsf (Cores 159-959D-56R through 61R) contains numerous microfaults with slickensides (see “Structural Geology” section, this chapter). The structural shear in Cores 159-959D-58R through 60R is indicated by the stretching and folding of burrows, such as *Chondrites* and *Zoophycos* (Fig. 16). The slightly to moderately bioturbated interval consists of dark gray to medium gray (N3 to N4) claystone, and dark brown to black (5B 4/1 to 10G 2.5/1) claystone with pyrite. Many burrows are filled with pyrite or barite (Fig. 17), and several of the microfaults are lined with barite. Glauconite occurs as a minor component in the claystone with pyrite. Rectangular spots containing calcite occur from 987.8 to 991.0 mbsf in Core 159-959D-61R. Preliminary palynological studies suggest a Maastrichtian age for Cores 159-959D-56R through 58R, but there are no fossil dates for the lower part of the interval, which is inferred to be Campanian.

Faintly laminated to massive claystone is the dominant lithology from 995.4 to 1033.7 mbsf. The sediment is dark gray to black (N4 to 7PB 2/0) and has some slightly coarser grained intervals, which contain clasts of shell fragments and some claystone flakes, barite, and dolomite (Fig. 18). Disseminated pyrite occurs throughout, but some pyrite enrichment occurs as laminae and fracture fills. The coarser grained intervals show some fining-upward characteristics, and the graded beds are 40 to 50 cm thick. Plant debris occurs in the laminated portions. Slight to moderate bioturbation interrupts the fine laminations in the claystone, but recognizable burrows such as *Zoophycos* occur in the nonlaminated intervals. A bed of granule-sized conglomerate occurs as a minor lithology in Section 159-959D-65R-6 (1020–1022 mbsf; Fig. 19). The conglomerate grades into sand-sized sediment in its upper part, which has a gradational contact with the claystone. The clasts are dominantly rounded carbonate fragments, shell fragments, plant debris associated with glauconite, and some calcite. The maximum clast size is 3 mm. Kaolinite and calcite fill some small cracks (2–4 mm diameter) in Sections 159-959D-62R-1 and 2 (Fig. 20), and 159-959D-63R-2 and 4. The last core in this interval (Core 159-959D-65R) was dated as Santonian. No fossil dates are available for Cores 159-959D-62R through 64R.

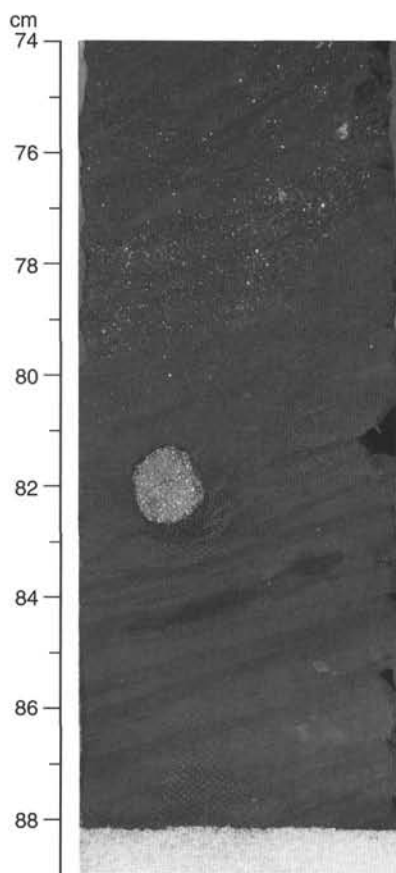


Figure 15. Section 159-959D-54R-1, 74–89 cm; black claystone locally bioturbated with *Zoophycos* and *Planolites* in lithologic Unit III. Note the larger burrow filled with pyrite at 82–84 cm. Bright grains from 74 to 80 cm are euhedral pyrite crystals.

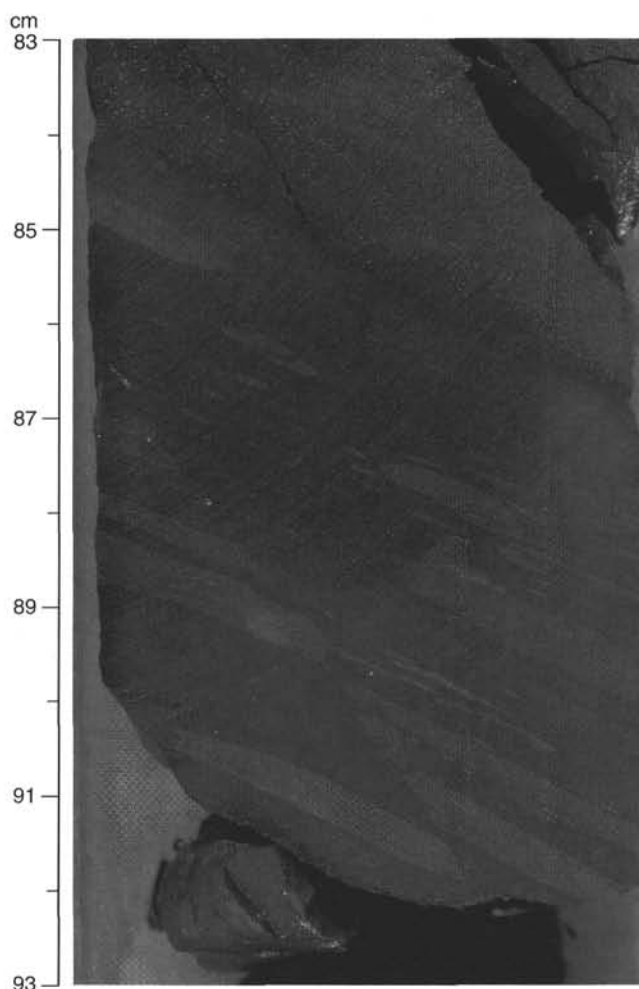


Figure 16. Section 159-959D-60R-5, 83–93 cm; bioturbated interval from lithologic Unit III, with normal faults cutting across the burrows. Light specks between 82 and 84 cm are foraminifers, replaced by barite.

Carbonate-bearing lithologies reappear in the lowermost portion of lithologic Unit III (1033.7–1043.3 mbsf, Core 159-959D-66R). This dark gray (N3/1) interval is slightly bioturbated and contains an alternating sequence of nanofossil claystone with glauconite, nanofossil claystone, and laminated claystone with nanofossils. Microfaults are present in Sections 159-959D-66R-3 and 5. Phosphatic hardgrounds, with brown and black nodules up to 2 cm in diameter in a clayey matrix, occur in Sections 159-959D-66R-4 and 7 (Fig. 21). Some of the nodules are composites with previous generations of phosphate nodules incorporated within them. A phosphatic conglomerate in Section 159-959D-66R-6 was apparently formed by the erosion of hardgrounds similar to those in Sections 159-959D-66R-4 and 7 (Fig. 22). These phosphate nodules are crudely bedded and not cemented to one another, but float in a clayey matrix and grade upward into a laminated interval. A hardground in Section 159-959D-66R-CC represents a stage boundary with Santonian fossils above and early Coniacian fossils below.

Unit IV

Description: Sandy limestone, sandy dolomite, calcareous sandstone, and limestone
 Interval: Sections 159-959D-67R-1, 0 cm, through 7R-1, 43 cm (TD)
 Depth: 1043.3–1081.7 mbsf
 Age: early Coniacian to early Turonian, and older

Lithologic Unit IV comprises dominantly sandy limestone, sandy dolomite, calcareous sandstones, and limestones. The upper bound-

ary of this unit was defined by the first occurrence of quartz-sand-rich limestone and dolomite beneath the succession of phosphatic hardgrounds, or the slightly redeposited equivalents of these features. This unit was divided into two subunits based upon the compositional differences in major lithologies, such as quartz content, and such major sedimentary characteristics as types of bedding. Lithologic Subunit IVA is dominated by fine-grained, massive to faintly laminated sandy limestone and sandy dolomite. Lithologic Subunit IVB consists of a distinctive 19-m-thick limestone.

Subunit IVA

Description: Sandy limestone, sandy dolomite, and calcareous sandstone
 Interval: Sections 159-959D-67R-1, 0 cm, through 68R-CC, 15 cm
 Depth: 1043.3–1062.7 mbsf
 Age: early Coniacian to early Turonian

Subunit IVA consists of beds of olive gray (10Y 3/1) to dark gray (N3) sandy dolomite and light gray (10Y 5/10) sandy limestone and calcareous sandstone. The sandy dolomite varies locally from faintly laminated to highly bioturbated bedding. Dolomite content increases with increased bioturbation. The poorly sorted sandy limestone (Sections 159-959D-67R-2, 130–150 cm, and 159-959D-67R-CC, 0–15 cm) contains abundant foraminifers and nanofossils (see Fig. 23) and dispersed fragments of bivalve shells with quartz sand content

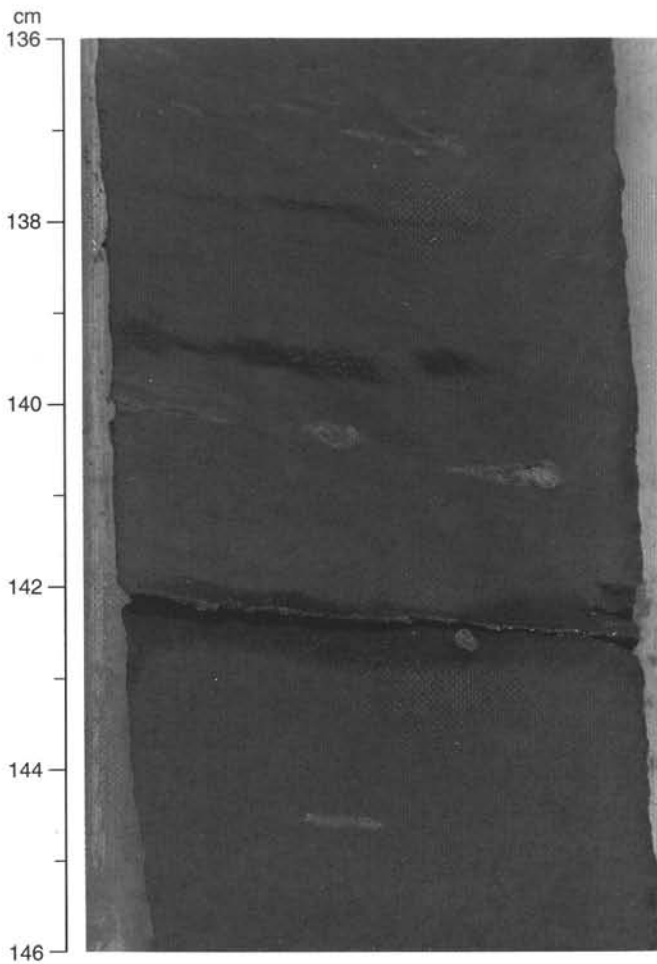


Figure 17. Section 159-959D-60R-4, 136–146 cm. Burrows in lithologic Unit III are filled with barite and appear sheared by compaction.

varying from 10% to 20%. In Core 159-959D-68R, poorly sorted massive to crudely laminated calcareous sandstones are associated with thin conglomerate beds. Clasts include phosphatic pebbles and glauconitic rip-up clasts intermixed with quartz and carbonate sand.

Subunit IVB

Description: Limestone
 Interval: Sections 159-959D-69R-1, 0 cm, through 70R-1, 43 cm
 Depth: 1062.7–1081.7 mbsf
 Age: Unknown

Subunit IVB consists entirely of light-colored (5Y 5/1) limestone and dolomitic limestone with some quartz sandy limestone. The limestones consist of skeletal and intraclastic wackestones, packstones, and grainstones with abundant skeletal fragments, for example, red algae and mollusks (Core 159-959D-69R). In some intervals clasts are lithified and cemented within a darker micritic matrix. Quartz sand content varies from 0% to 50%. Brownish sedimentary layers in wackestones are due to disseminated dolomite (Section 159-959D-69R, 65–70 cm). The lower part of this subunit contains less or no quartz sand intermixed with the carbonate components (Core 159-959D-70R).

Unit V

Description: Quartz sandstone and silty claystone
 Interval: Sections 159-959D-71R-1, 0 cm, through 78R-CC, 20 cm (TD)

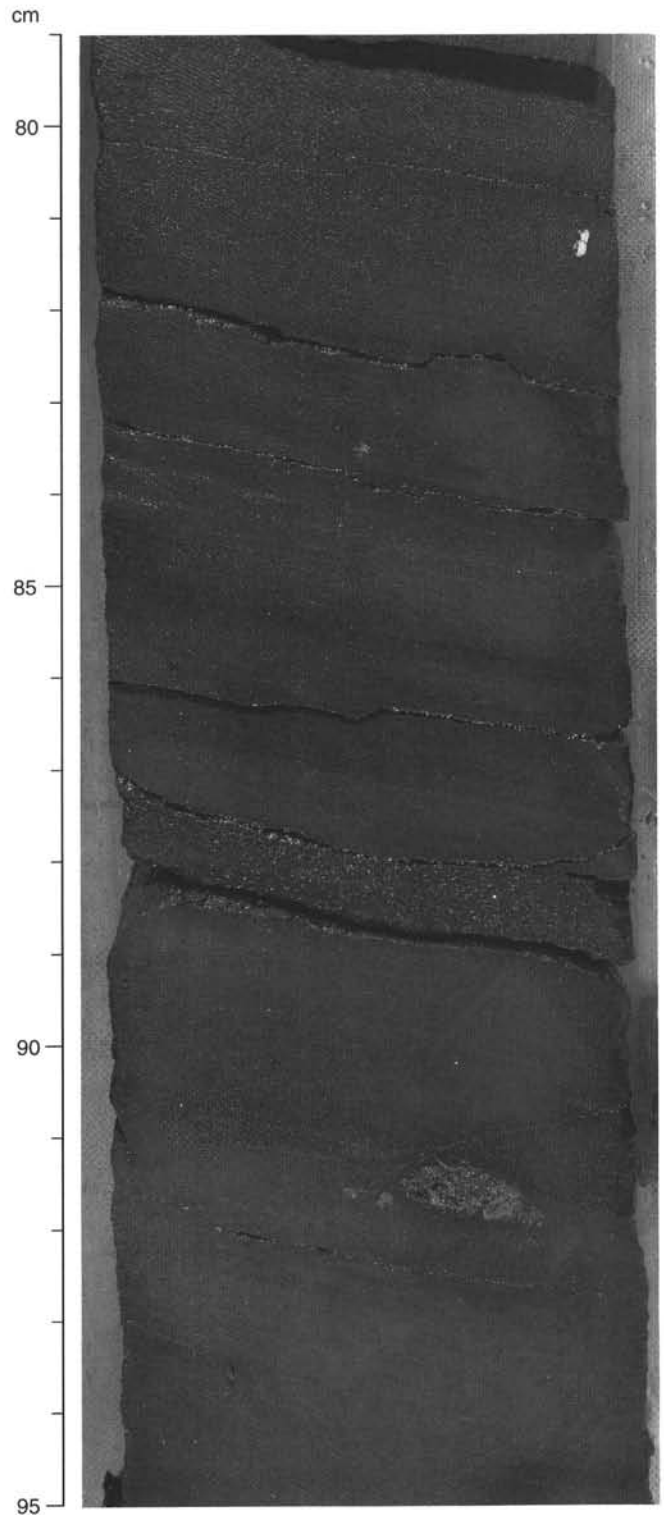


Figure 18. Section 159-959D-63R-4, 79–95 cm; succession of size-graded beds in lithologic Unit III. For example, the bed at 87–88 cm comprises a basal sand-rich lithology that grades upward to parallel laminated siltstone.

Depth: 1081.7–1158.9 mbsf
 Age: late Albian

This unit is dominated by medium gray (N4 to N5) to light gray (N6 to N7) sandstones embedded with fine-grained darker gray (N2) clay-rich sediments. Fine-grained portions are mostly converted to a

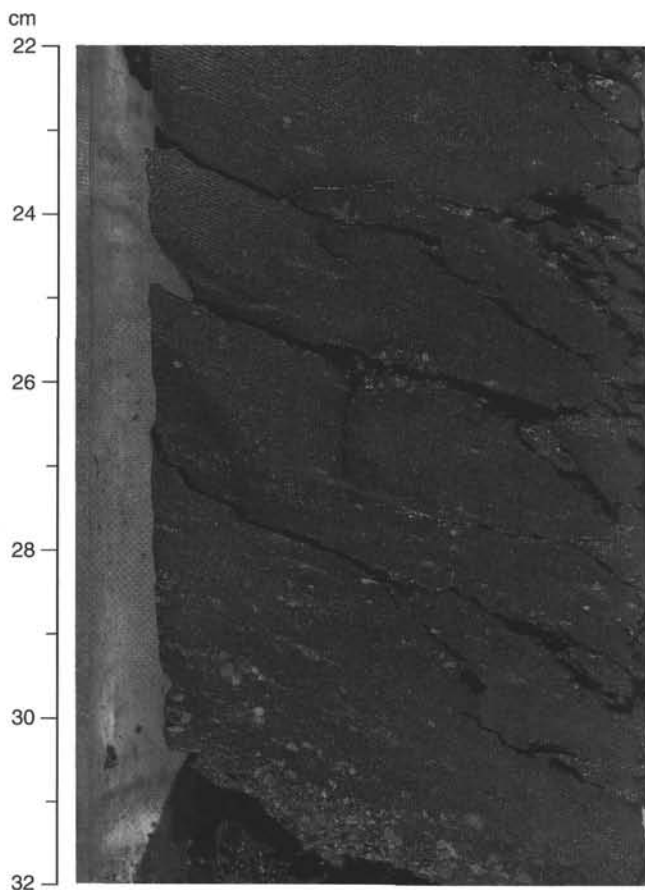


Figure 19. Section 159-959D-64R-6, 22–32 cm; graded conglomerate bed in lithologic Unit III. The clasts comprise dolomite, quartz, and glauconite.

mixture of siltstone and silty claystone fragments with loose silt and clay due to drilling disturbance. Sandstones in the upper part of this subunit (from Cores 159-959D-71R through 72R) are poorly sorted and mostly parallel or crudely laminated. Massive sandstones (Sections 159-959D-71R-1, 65–127 cm, and CC, 0–16 cm) show some water-escape structures, in which coarser sand is injected upward into the overlying sand. Kaolinized feldspar occurs within intergranular pores.

The interval from 1091.2 to 1149.2 mbsf (Cores 159-959D-72R through 77R) is dominated by medium gray (N4), fine- to medium-grained sandstone. Typically the sandstone is parallel-laminated or cross-laminated, with foreset laminae showing relatively low-angle, crosscutting relationships (Fig. 24). Some of the laminae are slightly curved upward, showing small-scale hummocky and swale bedforms. In Core 159-959D-73R, intervals of parallel laminated sandstone show a fining-upward trend within laminae with sandstone beds only 2 to 4 cm thick. Their lower contacts are sharp, whereas the upper contacts are commonly rippled. In Section 159-959D-74R-2, sandstones are trough cross-bedded with curved, erosional lower set contacts (Fig. 25). Between sandy beds there are dark gray (N3) silty claystones or finely laminated clayey siltstones. The fine-grained portions are highly brecciated and disturbed by drilling. Syn-sedimentary convolution and slump folds occur at Section 159-959D-74R-2, 19–32 cm, and 159-959D-75R-1, 30–56 cm, respectively. Quartz content in the sandstones is high, up to 60% of the total components. Silty sandstones and claystones have a significant component of plant debris (up to 40%). As a minor lithology, a breccia occurs in Section 159-959D-72R-3, 120–127 cm. Breccia fragments consist of angular laminated sandstone embedded within a silty sand-

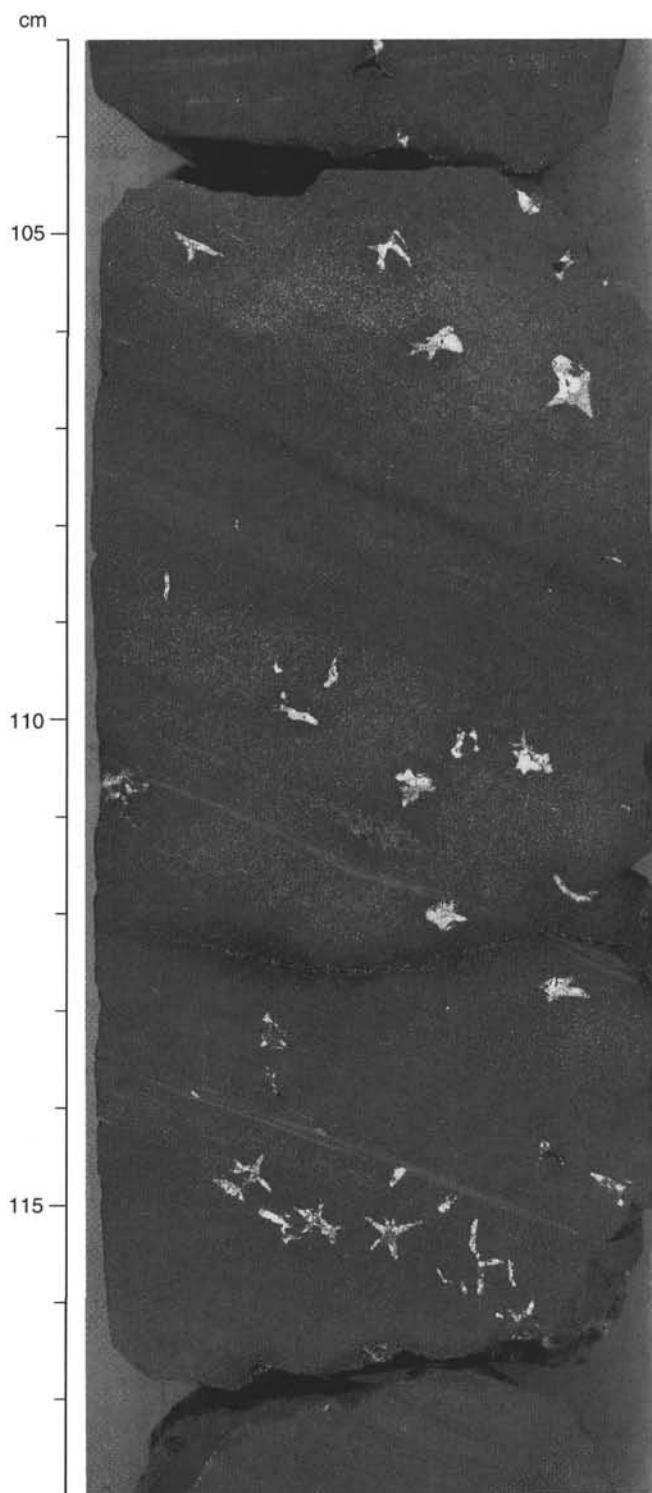


Figure 20. Section 159-959D-62R-2, 103–118 cm; mineralized veins in lithologic Unit III filled with calcite and kaolinite.

stone matrix. Kaolinite and carbonate fill some veins in Section 159-959D-73R-1, 125–132 cm.

The interval from 1149.2 to 1158.9 mbsf (Core 159-959D-78R) lacks sandstone beds and the major lithology is a fine-grained, dark gray (N3) siltstone and claystone. This interval is highly brecciated by drilling and contains some dispersed fragments of laminated, fine-grained sandstone.

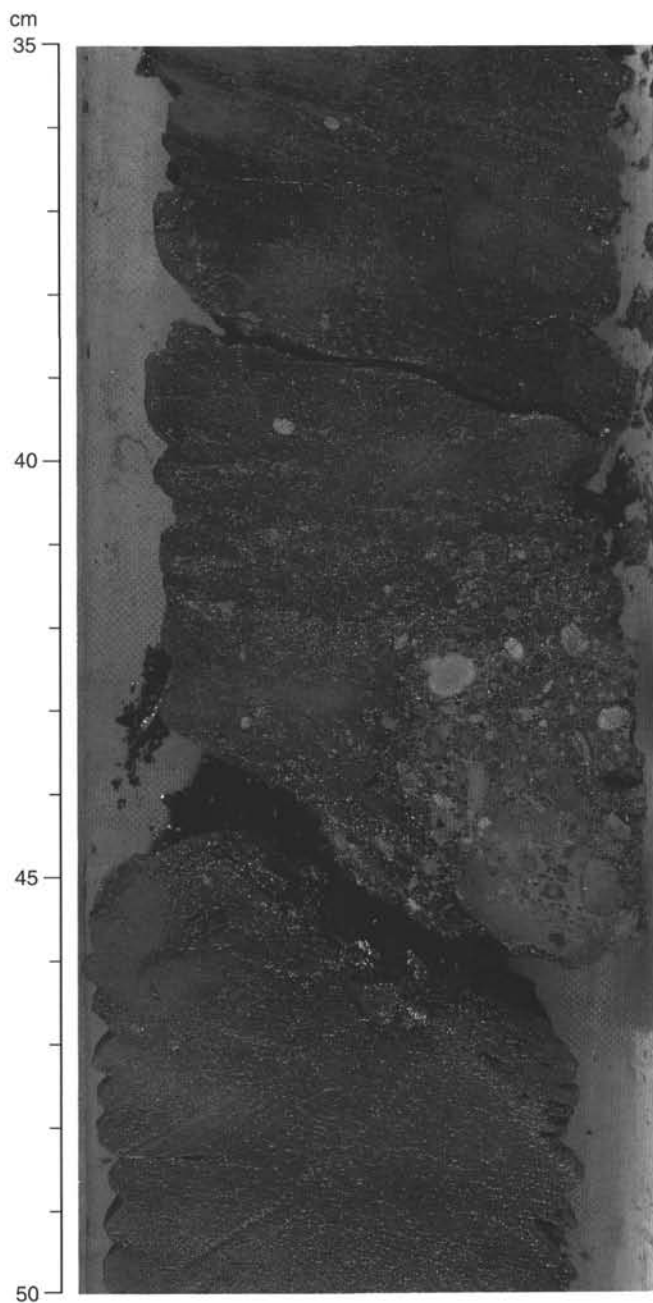


Figure 21. Section 159-959D-66R-4, 35–50 cm; phosphatic hardground in lithologic Unit III. Phosphate nodules show several generations of phosphatization.

Discussion

Lithologic Unit I comprises pelagic, calcareous sediment deposited in a basin that has been subjected to cyclic variations in the oxygen content of its bottom waters. Periodic stagnation of the bottom waters and decreased levels of oxygen gave rise to laminated intervals in Subunit IB when burrowing infauna were suppressed. These periods have alternated with those of more oxygenated bottom waters, during which a benthic community thrived and mixed the sediment. In addition, there was some variation in the input of the three primary components for this lithologic unit: nanofossils, foraminifers, and clay. Clay content decreased steadily from the late Miocene to the late Pliocene, but increased again during the Pleistocene. The pelagic rain

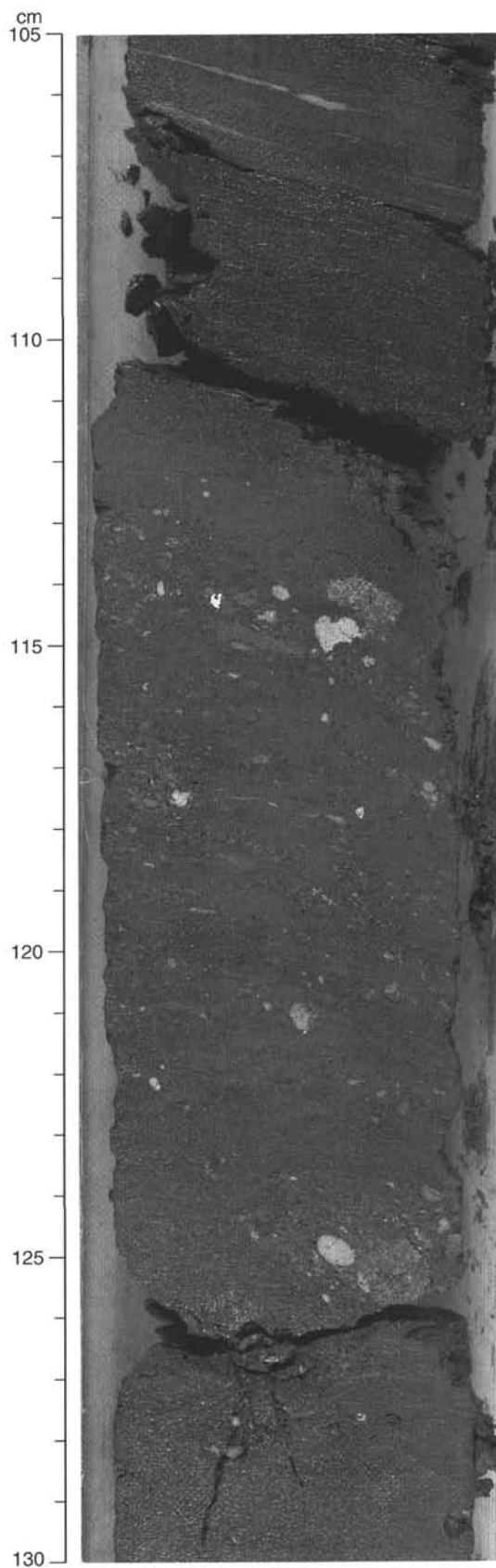


Figure 22. Section 159-959D-66R-6, 105–130 cm. Rip-up clasts from a phosphatic hardground near the base of lithologic Unit III are bedded in a matrix-supported conglomerate.

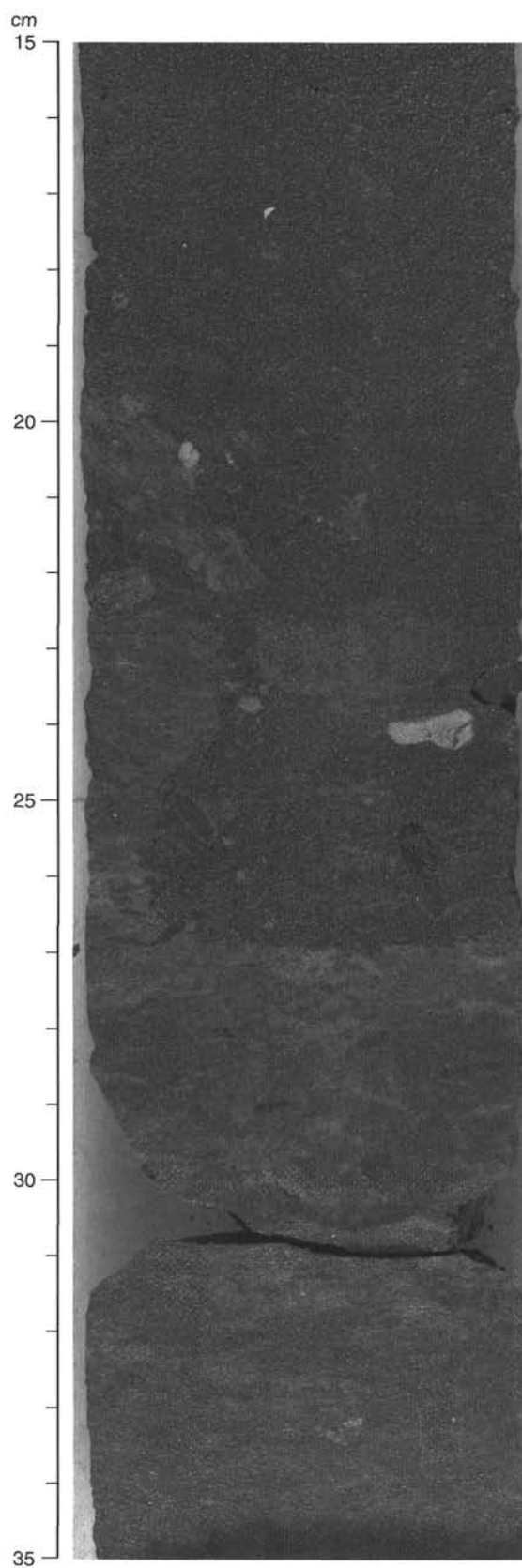


Figure 23. Section 159-959D-66R-CC, 15–35 cm. Black claystone of lithologic Unit III, Santonian in age, disconformably overlies quartz-sand-rich lower Coniacian sediment across a phosphatic hardground. Rip-up clasts of phosphate nodules have been incorporated into the overlying sediment.

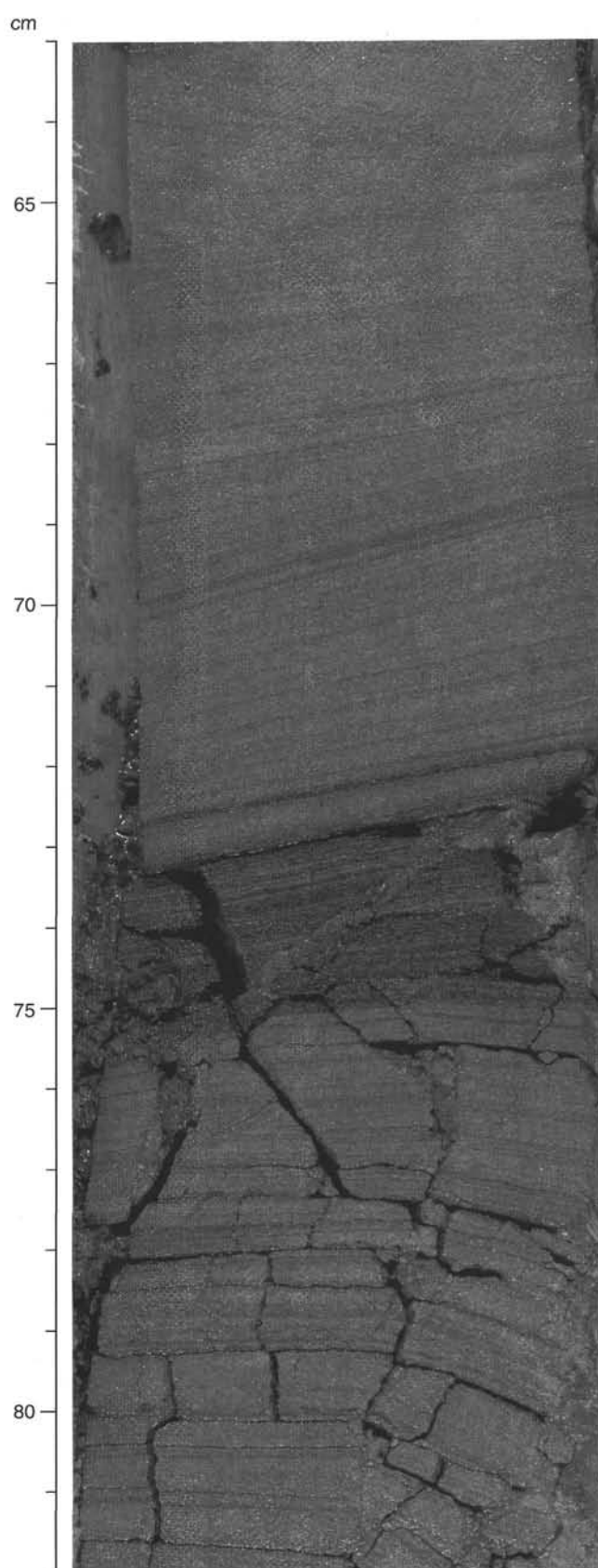


Figure 24. Section 159-959D-77R-2, 63–82 cm. Sandstone of lithologic Unit V shows parallel lamination and cross-lamination with foreset laminae at relatively low-angle crosscutting relationships.



Figure 25. Section 159-959D-74R-2, 34–57 cm. Sandstone of lithologic Unit V shows trough cross-bedding with curved erosional lower set contacts.

diminished enough to allow glauconitic hardgrounds to form, especially during the middle to late Miocene. In some cases these periods terminated in a spillover of oxidizing water into the area, as indicated by oxidized glauconitic laminae.

The lithologic sequence represented by lithologic Unit II reflects a time period of relatively high primary productivity. The occurrence of diatoms, and in particular their dominance, implies a general basinal setting, with an increased nutrient supply, causing these microfloras to dominate the planktonic community. The source of this high nutrient supply is unknown; it could reflect the influx of phosphates and nitrates from terrestrial systems through fluvial outflow, or it may be ocean-derived from upwelling of nutrient-rich bottom waters. The high abundance of plant debris throughout this interval is supportive of a terrestrial source; however, fluvial fluxes of organic nutrients are self-limiting, in that a balance remains between increased nutrient supply and decreased surface water salinity, which would ultimately limit diatom productivity.

An alternate source of the requisite nutrients may be through upwelling of deeper waters along the oceanward basin margin. The apparent cyclicity in diatom productivity that is recorded in the lithologic succession might represent periods of increased vs. decreased upwelling. Changes in the intensity and frequency of upwelling could reflect either climatic factors that might control both the direction and intensity of surface winds or changes in the stratification of surface waters. Implicit in this model is the lack of a physiographic barrier between the basin and the open ocean, a barrier that may have been developed in response to tectonic uplift of the CIGMR during earlier geologic periods.

The presence of a diverse benthic foraminifer assemblage, a *Zoo-phycos* trace fossil assemblage, and several authigenic minerals (barite, pyrite, dolomite, calcite, glauconite) in the dark gray to black claystones of Unit III is indicative of a deep-sea environment, which experienced hemipelagic sedimentation. Periods of high oxygen levels were accompanied by slight to moderate bioturbation by benthic faunas, while laminated intervals were deposited during periodic stagnation of the bottom waters and reduction in oxygen levels. We suspect a hiatus in the upper part of the unit, where upper Paleocene claystones with nannofossils are replaced by claystones barren of planktonic microfossils (Cores 159-959D-44R through 45). The palynological residues processed from core catchers in Cores 159-959D-44R, 46R, 49R, 51R, 54R, 56R, and 57R (see "Biostratigraphy" section, this chapter) yielded a Maastrichtian age for Cores 49R, 51R, and 54R; Cores 44R and 46R contain a Maastrichtian to early Tertiary assemblage and may be early Paleocene in age. The carbonate-bearing lowermost part of lithologic Unit II was probably deposited in the outer shelf, which is shallower than the deep basinal setting of the black claystones. This interval contains three phosphatic hardgrounds, the oldest of which marks a hiatus from the early Coniacian to the Santonian.

The palynological residues are also dominated by amorphous organic matter, and this is a reflection of high degradation of terrestrial and/or marine organic debris. Because the residues were oxidized, color cannot be used to speculate on the possible origins of the amorphous organic matter. Apart from a diagenetic overprint that is suspected to have affected the preservation of the palynomorphs and benthic foraminifers in the rocks, limited terrigenous input into the deep marine environment probably contributed to the small numbers of structured plant fragments and terrestrially derived palynomorphs preserved in the residues.

Lithologic Units IV and V are dominantly sand-bearing although they are interbedded with silt- and clay-rich sediments. A general downhole trend toward a coarser sediment and limestone succession indicates that the depositional setting shifted from shallower conditions during the late Albian to early Coniacian to a basinal setting during the late Coniacian (represented by lithologic Unit III). The limestones of lithologic Unit IV are indicative of reef-formation processes in a shallow shelf environment during the late Albian to Coni-

acian, but likely represent peri-platform deposits transported from shallow shelf settings.

Changes in the tectonic setting may have controlled major shifts in depositional environments, although most of the transportation of sand-sized grains was likely controlled by seasonal events such as major storms. In Unit V this is indicated by the deposition of thin, relatively well-sorted, laminated to cross-laminated sand beds in an environment that otherwise was dominated by deposition of fine-grained sediments.

BIOSTRATIGRAPHY

Introduction

Site 959 (3°37.70'N, 2°44.10'W; 2100 m water depth) is located on the landward edge of the CIGMR on the edge of the DIB. Biostratigraphic age assignments for Holes 959A–959C are illustrated in Figure 26. Biostratigraphic age assignments for Hole 959D are illustrated in Figure 27. Biostratigraphic control was provided by ship-board analyses of calcareous nannoplankton, planktonic foraminifers, silicoflagellates, and palynomorphs. The sequence apparently is complete from the upper Oligocene to the Holocene. A hiatus is probably present in the Paleocene. Additional hiatuses may also be present in the Cretaceous and Paleogene portions of the record, but the scarcity of age-diagnostic microfossils prevents construction of detailed sedimentation histories for much of the section below the upper Oligocene.

Calcareous Nannofossils

The core catcher of Core 159-959A-1H (9.1 mbsf) contains a middle Pleistocene assemblage of calcareous nannofossils including *Gephyrocapsa aperta*, *Gephyrocapsa oceanica*, *Gephyrocapsa caribbeanica*, and *Pontosphaera indoceanica*. This assemblage, in the absence of *Emiliania huxleyi*, indicates Subzone CN14b. Section 159-959A-2H-CC (18.6 mbsf) contains *Pseudoemiliania lacunosa*, *Pontosphaera indoceanica*, *Helicosphaera sellii*, *Gephyrocapsa caribbeanica*, and *Gephyrocapsa aperta* without *Gephyrocapsa oceanica*. There are trace amounts of *Discoaster brouweri* in this sample, although their very low abundance is indicative of reworking. This association indicates early Pleistocene Subzone CN13b. Calcareous nannofossils are abundant and well preserved in all of the Pleistocene samples examined.

Sample 159-959B-3H-CC (24.0 mbsf) contains *Calcidiscus macintyreii*, *P. lacunosa*, *H. sellii*, and common *Discoaster brouweri*, indicating late Pliocene Subzone CN12d. Sample 159-959A-3H-CC (28.1 mbsf) contains a similar assemblage with the addition of *Discoaster pentaradiatus*. This association indicates late Pliocene Subzone CN12c. Very rare specimens of *Sphenolithus neoabies* in this sample indicate trace amounts of reworking. Subzone CN12b was not observed in any core-catcher samples from the three holes. However, this subzone is of very short duration (<100 k.y. according to Berggren et al., 1985), so that its apparent absence is probably an artifact of sample spacing. Sample 159-959A-4H-CC (37.6 mbsf) contains *Discoaster tamalis*, *Discoaster surculus*, *D. pentaradiatus*, and *D. brouweri* without *Reticulofenestra pseudoumbilica* or sphenoliths.

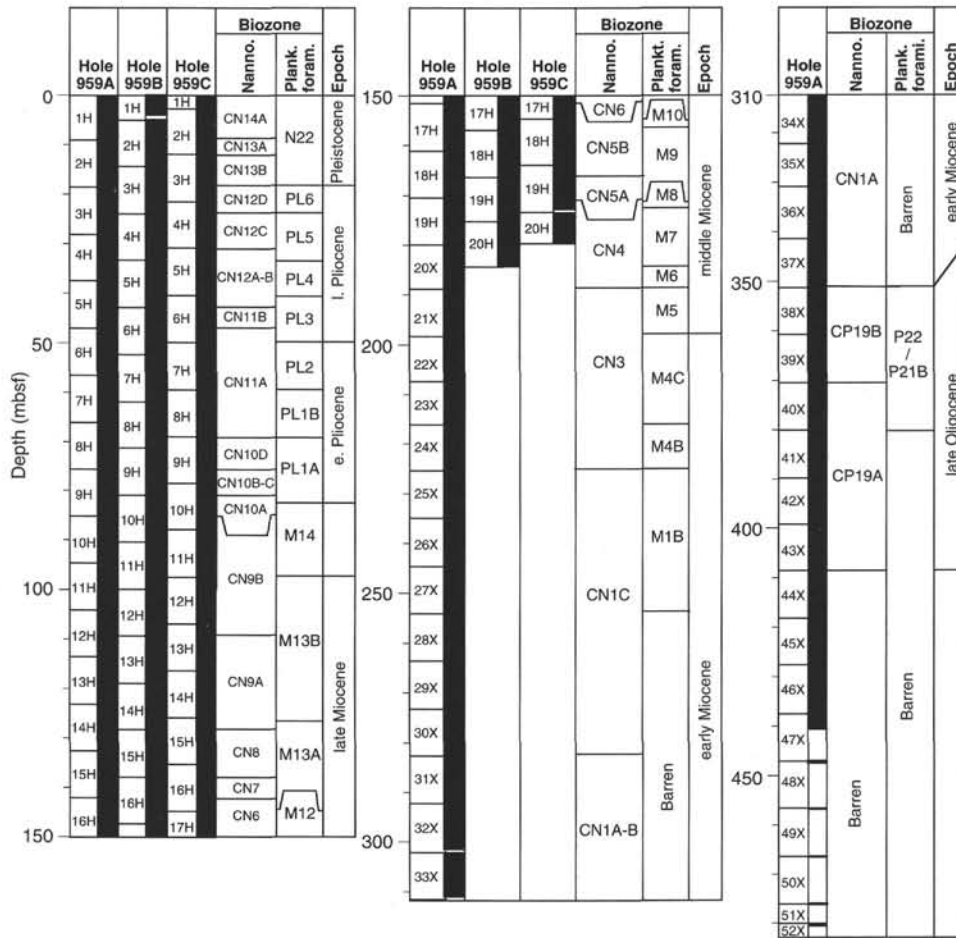


Figure 26. Biostratigraphic correlation of Holes 959A, 959B, and 959C.

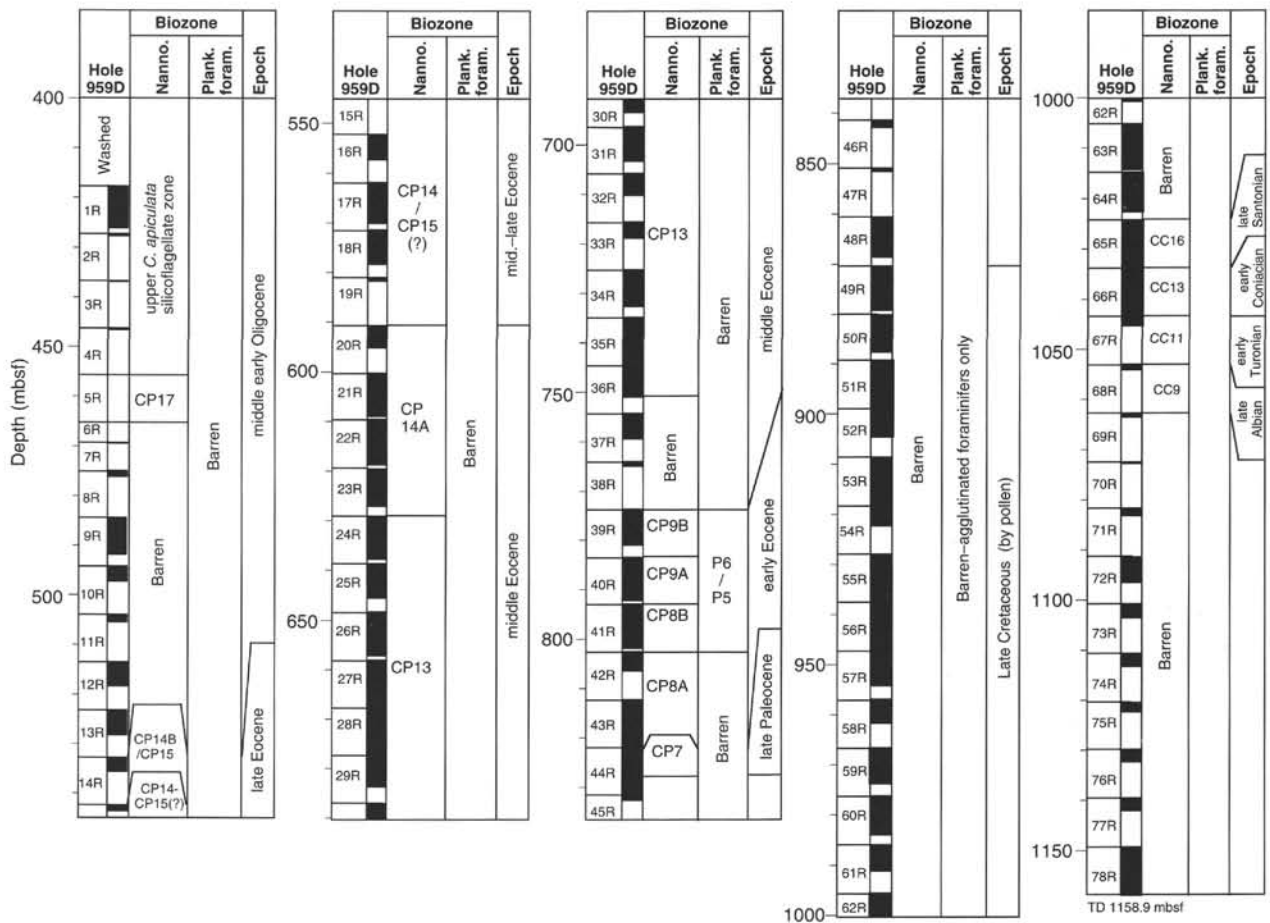


Figure 27. Biostratigraphic correlation of Hole 959D.

This association indicates late Pliocene Subzone CN12a. The absence of *Discoaster variabilis* and *Discoaster challengeri* from this assemblage indicates the upper part of Subzone CN12a.

This site contains a well-preserved and apparently complete record of the early Pliocene. Sample 159-959A-5H-CC (47.1 mbsf) contains *Discoaster tamalis*, *Sphenolithus neoabies*, *Sphenolithus abies*, and abundant *Discoaster asymmetricus*. The high abundance of *D. asymmetricus*, in concert with the presence of *D. tamalis*, indicates Subzone CN11b. It is interesting to note that *Reticulofenestra pseudoubilica* is absent from this assemblage. The presence of *S. abies* and *S. neoabies* without *R. pseudoubilica* corresponds to a period of approximately 300 k.y. at the end of Subzone CN11b, according to Berggren et al. (1985). Subzone CN11a is represented in Sample 159-959A-6H-CC (56.6 mbsf) by an assemblage containing *R. pseudoubilica*, *S. abies*, *S. neoabies*, and *Ceratolithus rugosus* without any *Amaurolithus* spp. *Discoaster asymmetricus* is present as rare specimens in this assemblage. Rare specimens of *Discoaster tamalis* suggest that this sample is at the top of Subzone CN11a. A similar assemblage belonging to Subzone CN11a occurs in Sample 159-959A-7H-CC (66.1 mbsf); however, this sample lacks *Discoaster tamalis*.

The middle early Pliocene Subzone CN10c is represented by sediment in Sample 159-959A-8H-CC (75.6 mbsf). This calcareous nanofossil assemblage includes *Amaurolithus delicatus*, *Amaurolithus tricorniculatus*, *Ceratolithus rugosus*, and rare *Discoaster asymmetricus*. The presence of *Discoaster asymmetricus* may indicate the *Amaurolithus delicatus* Subzone (CN10d) of Bukry (1981a). However, similarly rare specimens of asymmetrical five-rayed discoasters are known to occur below this stratigraphic level. As a result, we have

not adopted the use of this subzone for this preliminary work. Earliest Pliocene Subzone CN10b is present in Sample 159-959C-9H-CC (78.3 mbsf), as indicated by the presence of *Ceratolithus acutus* without *Ceratolithus rugosus* or *Triquetrorhabdulus rugosus*.

Subzone CN9b, from the late Miocene, is represented by the interval from Sample 159-959A-10H-CC through 11H-CC (94.6–104.1 mbsf), as indicated by the presence of *Discoaster quinquerramus*, *Amaurolithus primus*, *Amaurolithus delicatus*, and *Amaurolithus amplificus*. Calcareous nanofossils are abundant and well preserved throughout this interval. Samples 159-959A-12H-CC and 13H-CC (113.6–123.1 mbsf) contain *Discoaster berggrenii* and *D. quinquerramus* without any *Amaurolithus* spp. This is indicative of late Miocene Subzone CN9a. Zone CN8 is represented in Sample 159-959A-14H-CC (132.6 mbsf). Zone CN7 is represented in the interval from Sample 159-959A-15H-CC to 16H-CC (142.1–151.6 mbsf), as indicated by the presence of *Discoaster hamatus*, *Catinaster coalitus*, and *Catinaster mexicanus*.

Middle Miocene Subzone CN5b is represented in Sample 159-959A-17H-CC (161.1 mbsf), as indicated by the presence of *Discoaster kugleri*, *Discoaster exilis*, *Discoaster sanmiguelensis*, and *Calcidiscus macintyreii* without *Catinaster coalitus*. The presence of rare *Discoaster challengeri* in this sample suggests that it is from the upper part of this subzone. Sample 159-959A-18H-CC (170.6 mbsf) contains *Reticulofenestra pseudoubilica*, *Discoaster exilis*, *Discoaster braarudii*, and *Discoaster sanmiguelensis* without *Discoaster kugleri* or *Sphenolithus heteromorphus*. This association indicates middle middle Miocene Subzone CN5a. The interval from Samples 159-959A-19H-CC through 20X-CC (180.1–189.1 mbsf) contains *Sphenolithus heteromorphus*, *Coronocyclus nitescens*, *Discoaster*

druggii, and *Discoaster variabilis* without *Helicosphaera ampliapertura*. This assemblage is characteristic of early middle Miocene Zone CN4.

The interval from Samples 159-959A-21X-CC through 23X-CC (198.6–216.6 mbsf) contains *Helicosphaera ampliapertura*, *Sphenolithus heteromorphus*, and *Coronocyclus nitescens*, indicating late early Miocene Zone CN3. Preservation is relatively good through this interval, although nannofossil abundance is somewhat diluted by diatoms and radiolarians. The interval from Sample 159-959A-24X-CC through 26X-CC (225.8–245.1 mbsf) contains *Helicosphaera ampliapertura* and *Sphenolithus belemnos* without *Sphenolithus heteromorphus*. This association indicates early Miocene Zone CN2. Samples 159-959A-27X-CC through 30X-CC (254.8–283.7 mbsf) contain *Discoaster druggii*, *Helicosphaera ampliapertura*, *Discoaster deflandrei*, *Sphenolithus dissimilis*, *Triquetrorhabdulus carinatus*, and *Triquetrorhabdulus serratus* without *Sphenolithus belemnos* or *Sphenolithus delphix*. This association of species indicates Subzone CN1c from the early early Miocene. Calcareous nannofossil abundance is significantly lower in this interval than in the overlying lower Miocene section, with siliceous microfossils and clay composing most of the sediment.

The upper Oligocene sediments at Site 959 are dominated by siliceous microfossils, although calcareous nannofossils are usually present in sufficient quantities to permit biostratigraphic age determination. The interval from Sample 159-959A-31X-CC through 37X-CC (293.3–351.2 mbsf) contains *Cyclicargolithus abisectus*, *Reticulofenestra lockeri*, *Sphenolithus dissimilis*, and *Discoaster adamanus* without *Discoaster druggii*, *Dictyococcites bisectus*, or *Sphenolithus ciperoensis*. This association is characteristic of latest Oligocene Subzones CN1a and CN1b. Nannofossil preservation deteriorates downward through this interval, so that many of the intrazonal datums and abundance peaks documented by other workers (e.g., Fornaciari et al., 1990) cannot be recognized with confidence.

The interval from Sample 159-959A-38X through 42X-CC (360.8–399.2 mbsf) contains few, moderately preserved calcareous nannofossils including *Sphenolithus ciperoensis*, *Cyclicargolithus abisectus*, *Cyclicargolithus floridanus*, and *Discoaster deflandrei*. This assemblage is characteristic of late Oligocene Zone CP19. Preservation prevents confident identification of *Sphenolithus distentus*, especially as transitional forms between *S. distentus* and *S. ciperoensis* are known from sections with well-preserved nannofossils. As a result, division of this zone into its two subzones is not possible based solely on these core-catcher assemblages.

Core-catcher samples from the basal 53.0 m of Hole 959A (Samples 159-959A-45X-CC through 52X-CC; 427.7–480.7 mbsf) are barren of calcareous nannofossils. This is attributable in part to the sediment (clayey diatomite and massive claystone) and in part to the poor core recovery in this interval. Similar sediment and poor recovery characterize the depth-correlative part of Hole 959D (Sample 159-959D-1R-CC through 8R-CC; 417.8–484.6 mbsf). However, one sample from Section 159-959D-5R-CC (465.3 mbsf) does contain common, well-preserved nannofossils. This assemblage includes *Sphenolithus predistentus*, *Dictyococcites scrippsae*, *Cyclicargolithus floridanus*, and *Dictyococcites danicus* without *Sphenolithus distentus*, *Cyclicargolithus abisectus*, or *Reticulofenestra umbilica*. This assemblage is characteristic of middle early Oligocene Zone CP17. This age determination is in agreement with that derived from silicoflagellate biostratigraphy.

This sequence of barren core-catcher samples continues downward to Sample 159-959D-13R-CC (532.8 mbsf). Calcareous nannofossils are preserved again starting approximately at Sample 159-959D-14R-2, 71–72 cm (535.0 mbsf). This sample contains a poorly preserved assemblage that includes *Discoaster barbadiensis*, *Discoaster saipanensis*, *Discoaster nodifer*, *Discoaster tanii*, *Sphenolithus pseudoradians*, *Reticulofenestra umbilica*, *Dictyococcites scrippsae*, and *Dictyococcites bisectus* without *Discoaster bifax*,

Chiasmolithus grandis, or *Chiasmolithus solitus*. This association is usually characteristic of late Eocene Zone CP15. It is possible that the lack of chiasmoliths is a function of the poor preservation of this sample. However, in light of the generally good preservation and relatively high abundance of the discoasters, it is felt that the lack of *D. bifax* is a biostratigraphic, rather than preservational, phenomenon. As a result, this sample is formally placed in the late Eocene combined unit CP14b-CP15.

The interval from Samples 159-959D-14R-CC through 19R-CC (542.4–590.6 mbsf) contains sparse, poorly preserved assemblages with identifiable species of a generalized middle to late Eocene age. Abundance and preservation improve sufficiently in the interval from Samples 159-959D-20R-CC through 23R-CC (600.2–629.0 mbsf) to permit more precise biostratigraphic placement. Samples from this interval contain *Reticulofenestra umbilica*, *Reticulofenestra dictyoda*, *Chiasmolithus solitus*, *Chiasmolithus grandis*, *Sphenolithus obtusus*, and *Discoaster bifax*. This assemblage is characteristic of middle Eocene Subzone CP14a.

The interval from Samples 159-959D-24R-CC through 36R-CC (638.7–754.5 mbsf) consists of a sequence of porcellanite and clayey porcellanite that contains moderately to poorly preserved calcareous nannofossils. These assemblages include *Nannotetrina cristata*, *Reticulofenestra dictyoda*, *Discoaster strictus*, and *Sphenolithus furcatorithoides*, indicating early middle Eocene Zone CP13. The upper samples from this interval (Sections 159-959D-24R-CC through 26R-CC; 638.7–658.0 mbsf) contain *Discoaster bifax* and forms transitional to *Reticulofenestra umbilica*, indicating the upper part of Subzone CP13c. The lower samples, in Sections 159-959D-35R-CC through 36R-CC (744.9–754.5 mbsf) contain *Lophodolichus mochlophorus*, *Lophodolichus nascens*, and *Sphenolithus spiniger*, suggesting Subzone CP13a. Reworking is common throughout the entire Zone CP13 interval, with *Discoaster lodoensis*, *Discoaster keuperii*, *Tribrachiatus orthostylus*, and *Sphenolithus editus* being the most common forms. This suggests that sediments of Zone CP10 (early Eocene) are the source of the reworked material. Interestingly, the reworked material commonly is better preserved than the autochthonous nannofossils.

Core-catcher samples from Cores 159-959D-37R and 38R (764.5–773.8 mbsf) contain well-cemented porcellanite and chert that yield only sparse, poorly preserved calcareous nannofossils that are not age-diagnostic. Samples examined from within these two cores yielded similar, depauperate assemblages that indicate only an Eocene age.

Samples 159-959D-39R-CC through 41R-CC (783.5–802.6 mbsf) contain common but poorly preserved nannofossils that indicate an early Eocene age. Sample 159-959D-39R-CC (783.5 mbsf) contains *Tribrachiatus orthostylus*, *Sphenolithus conspicuus*, and *Discoaster binodosus* without *Tribrachiatus contortus* or *Discoaster lodoensis*. This association indicates Subzone CP9b. Sample 159-959D-40R-CC (793.0 mbsf) contains an older assemblage that includes *Tribrachiatus contortus*, *Discoaster multiradiatus*, *Discoaster lenticularis*, *Discoaster diastypus*, and *Sphenolithus anarrhopus* without *Fasciculithus* spp. This association indicates early Eocene Subzone CP9a. Sample 159-959D-41R-CC (802.6 mbsf) contains *Fasciculithus tympaniformis*, *Fasciculithus involutus*, *Fasciculithus alanii*, *Discoaster multiradiatus*, *Discoaster megastypus*, and *Rhomboaster bitrifida*, indicating earliest Eocene Subzone CP8b. *Campyosphaera eodela* could not confidently be identified in this sample due to the rather poor state of preservation; however, the co-occurrence of the previously mentioned taxa is unique to this subzone.

Samples 159-959D-42R-CC and 43R-CC (812.3–821.9 mbsf) contain *Discoaster multiradiatus*, *Discoaster megastypus*, *Fasciculithus involutus*, and *Fasciculithus tympaniformis* without *Campyosphaera eodela* or *Rhomboaster bitrifida*, indicating Subzone CP8a of late Paleocene age. Sample 159-959D-44R-3, 72–73 cm (825.6 mbsf) contains *Heliolithus kleinpellii*, *Heliolithus cantabrieae*, *Heli-*

olithus riedelii, *Cruciplacolithus frequens*, *Discoaster nobilis*, and *Discoaster megastypus* without *Discoaster multiradiatus*. This association indicates late Paleocene Zone CP7.

The interval from Sample 159-959D-44R-3, 90–91 cm, through Sample 159-959D-64R-CC (825.8–1024.1 mbsf) consists of black claystone within lithologic Unit III that is barren of calcareous nanofossils. Preliminary age determinations for this interval are based on palynology.

Sample 159-959D-65R-CC (1033.7 mbsf) contains common but poorly preserved nanofossils that include *Marthasterites furcatus*, *Lithastrinus grillii*, *Micula concava*, and *Reinhardtites anthophorus* without *Lithastrinus septenarius*, *Eprolithus floralis*, or *Aspidolithus parvus parvus*. In addition, rare specimens tentatively identified as *Calculites obscurus* were observed in this sample. With the exception of the rare *C. obscurus?* specimens, holococcoliths are absent from the assemblage, making use of their species for biostratigraphy impossible. Assuming that the tentatively identified specimens are, in fact, *C. obscurus*, the association of taxa indicates latest Santonian Zone CC17. However, if these specimens are not *C. obscurus*, then the zonal assignment would be late Santonian Zones CC15b–16. This latter interpretation is more consistent with the lack of *Aspidolithus parvus expansus*. Given this uncertainty, this sample is tentatively assigned to Zones CC15b–CC17, of late Santonian age.

Sample 159-959D-66R-2, 61–62 cm (1035.9 mbsf), contains a similar, albeit better preserved, assemblage as in Sample 159-959D-65R-CC. Even in this better preserved sample, however, holococcoliths are only poorly preserved and sparsely represented. As a result, Zones CC15 and CC16 cannot be resolved using the original zonal definitions. The lack of *Lithastrinus septenarius* in this sample indicates late Santonian Subzone CC15b or Zone CC16.

The interval from Samples 159-959D-66R-7, 19–20 cm, through 66R-CC (1042.9–1043.3 mbsf) contains a moderately preserved assemblage that includes *Marthasterites furcatus*, *Lithastrinus septenarius*, *Eprolithus floralis*, and *Eiffellithus eximius* but lacks *Micula decussata*. This association is characteristic of early Coniacian Subzone CC13b. A similar assemblage, albeit without *Lithastrinus septenarius*, occurs in Sample 159-959D-67R-2, 99–100 cm (1045.7 mbsf). The absence of *L. septenarius* in this sample indicates Subzone CC13a of late Turonian to early Coniacian age. This zonal assignment is corroborated by the rare occurrence of *Liliasterites atlanticus* in this sample.

Sample 159-959D-68R-1, 24–25 cm (1053.2 mbsf), contains an assemblage of calcareous nanofossils that includes *Quadrum gartneri*, *Microrhabdulus decoratus*, *Gartnerago nanum*, *Lithastrinus moratus*, and *Axopodorhabdus albianus*. The presence of *Q. gartneri* without *Eiffellithus eximius* indicates early to middle Turonian Zone CC11. However, the presence of rare *G. nanum* and *A. albianus* indicates that this sample is from the very base of this zone, yielding an early Turonian age.

Most of the samples examined from the interval from 159-959D-68R-CC through 78R-CC (1062.7–1158.9 mbsf) are barren of calcareous nanofossils. However, two samples do contain rare, poorly preserved nanofossils: 159-959D-69R-CC (1072.4 mbsf) and 159-959D-71R-1, 0–1 cm (1081.7 mbsf). These assemblages are dominated by *Watznaueria barnesae* but also contain *Prediscosphaera columnata*, *Eprolithus floralis*, *Rhagodiscus angustus*, *Axopodorhabdus albianus*, *Ellipsagelosphaera britannica*, *Tranolithus phacelosus*, and *Eiffellithus* sp. 1 of Perch-Nielsen (1985). The *Prediscosphaera columnata* are the small morphotype (<5 µm) that are restricted to Zone CC8 through Subzone CC9b. *Eiffellithus* sp. 1 of Perch-Nielsen (1985) is restricted to a narrow range of Subzones CC8a to CC9a. *Tranolithus phacelosus* has its first occurrence at the base of Subzone CC8b and continues through the Campanian. *Ellipsagelosphaera britannica* has its last occurrence at the top of Subzone CC9b. Based on the association of these taxa, these samples can be placed in Subzones CC8b to CC9a of late, but not latest, Albian age.

Planktonic Foraminifers

Planktonic foraminifers were studied most intensively in the Pleistocene to middle Miocene intervals of Holes 959A–959C. The lower Miocene and upper Oligocene interval was also studied in Hole 959A. In total, more than 160 samples from Site 959 were studied on the ship. Zonal assignments are summarized in Figures 26 and 27. Planktonic foraminifer data indicate an apparently continuous sequence at Site 959 from middle Miocene Zone M3 to the Holocene. Preservation of planktonic foraminifers is moderate to good through the Miocene to Holocene. Dissolution has led to extensive fragmentation of foraminifers throughout the upper Miocene to Holocene interval, although the foraminifers that remain unbroken are often abundant and well preserved, with glassy shells. Partial pyritization of foraminifers is common throughout this sequence. Preservation deteriorates in the middle Miocene to upper Oligocene with many samples entirely barren, but preservation is moderate to good in those samples in which foraminifers are present. Samples from the upper Oligocene and older sequence in Cores 159-959A-41X through 52X and throughout Hole 959D are barren of planktonic foraminifers, except in the lowest Eocene (Cores 159-959D-39R and 41R) and the Upper Cretaceous (Core 159-959D-65R).

The Pleistocene is recognized by the presence of *Globorotalia truncatulinoides*, which is used to identify Zone N22. Its ancestral form, *Globorotalia tosaensis*, has not been found. Foraminifers are abundant and moderately preserved with extensive fragmentation in the <150 µm fraction and dissolution of the interiors of thick-walled *Neogloboquadrina dutertrei* and *Globorotalia tumida*. Common taxa include *Globorotalia menardii*, *G. tumida*, *G. scitula*, *Pulleniatina obliquiloculata*, *Globigerinoides sacculifer*, *Neogloboquadrina pachyderma* (dextral), and *N. dutertrei*, in core catchers from Cores 159-959A-1H through 2H (9.1–18.6 mbsf), 159-959B-1H through 3H (5.0–24.0 mbsf), and 159-959C-1H through 3H (2.3–21.3 mbsf).

True morphotypes of *Globigerinoides fistulosus*, whose last occurrence approximates the Pleistocene/Pliocene boundary, are rare but have been found as high as Sample 159-959B-3H-CC (24.0 mbsf).

An apparently continuous record of the Pliocene was recovered from this site. Zone PL6 is differentiated in Sample 159-959B-3H-CC (24.0 mbsf) by the occurrence of *G. fistulosus* and *G. truncatulinoides*. Zone PL5 is recognized by the abundant occurrence of *G. miocenica* and *G. pertenuis* in Sample 159-959B-4-CC (33.5 mbsf), above the last occurrence of *G. multicamerata*, *Dentogloboquadrina altispira*, and *Sphaeroidinellopsis* spp. in Sample 159-959B-5H-CC (43.0 mbsf). *Globorotalia triangula* is rare in Zone PL5 as are *G. crassula*, *G. crassaformis*, and *Globigerina bulloides*. *Neogloboquadrina dutertrei*, *Globigerinoides ruber*, and *G. sacculifer* are common to abundant throughout Zones PL5 and PL6.

The last appearance of *D. altispira* and *G. multicamerata* in Sample 159-959C-5H-CC (40.3 mbsf) and the last appearance of *Sphaeroidinellopsis* spp. in Sample 959C-6H-CC (49.8 mbsf) identify Zone PL4 between these datums. Associated species in Zone PL4 include well-preserved *G. crassaformis*, *G. miocenica*, *G. triangula*, *G. sacculifer*, *G. obliquus*, and *G. multicamerata*. The same association was found in Sample 159-959A-4H-CC (37.6 mbsf). In Hole 959B, Zone PL4 was not recognized, but may be present between Sample 159-959B-4H-CC (33.5 mbsf; Zone PL5) and 159-959B-5H-CC (43.0 mbsf; Zone PL3). As at other Atlantic sites, *Pulleniatina obliquiloculata* and *G. tumida* are absent from the sequence representing middle Pliocene Zones PL5 and PL4.

Samples 159-959A-5H-CC (47.1 mbsf), 159-959B-5H-CC (43.0 mbsf) and 159-959C-6H-CC (49.8 mbsf) contain *Sphaeroidinellopsis kochi*, *S. paenedehiscens*, and *S. seminulina* in association with *G. multicamerata*, *G. miocenica*, and *N. acostaensis* and indicate Zone PL3. The assemblage is dominated by *G. sacculifer*, *G. multicamerata*, and *N. dutertrei*. Additional species characteristic of this zone include well-preserved *Globoquadrina venezuelana*, *G. tumida*, *G.*

plesiotumida, *N. dutertrei*, *Pulleniatina obliquiculata*, and *Sphaeroidinella dehiscens* (with a very small secondary aperture).

The last occurrence of *Globorotalia margaritae* in Sample 159-959A-6H-CC (56.6 mbsf) indicates the presence of Zone PL2 in the absence of *Globigerina nepenthes*. Associated species include abundant *G. tumida*, *D. altispira*, *G. venezuelana*, and the common occurrence of both *Pulleniatina primalis* and *S. kochi*. The zone has also been identified in Samples 159-959B-6H-CC (52.5 mbsf) and 159-959C-7H-CC (59.3 mbsf) and suggests that it spans the depth range of about 50 to 60 mbsf. *Globorotalia margaritae* is generally scarce in this zone, possibly because of extensive fragmentation of foraminifers in the <250- μ m sieve fraction.

Zone PL1 is marked by the last occurrence of *Globigerina nepenthes* in Sample 159-959C-8H-CC (68.8 mbsf). The last appearance of *Globorotalia cibaoensis* defines the top of Subzone PL1a. This species is present consistently in the lowermost Pliocene and upper Miocene between Samples 159-959B-8H-CC and 11H-CC (71.5–100.0 mbsf) and appears to have a reliable last occurrence. The next highest sample, 159-959B-7H-CC (62.0 mbsf), contains *G. crassaformis* and suggests the presence of Subzone PL1b. Foraminiferal assemblages are typically well preserved in Zone PL1 and are dominated by *G. venezuelana*, *G. plesiotumida*, *G. obliquus*, *G. sacculifer*, *G. menardii*, and *Sphaeroidinellopsis* spp.

The base of the Pliocene is marked by the first appearance of *Globorotalia tumida* between Samples 159-959B-10H-1, 59–61 cm, and 10H-3, 59–61 cm (81.6–84.6 mbsf). The first appearance of *S. dehiscens* with a very small secondary aperture has also been used to identify the Miocene/Pliocene boundary. *Sphaeroidinella dehiscens* was first documented in Sample 159-959B-9H-CC (81.0 mbsf) but may occur lower than this, as it is rare in the lowest Pliocene.

For most of the upper Miocene below Zone PL1, the age constraint provided by planktonic foraminifers is less rigorous. This is because fewer datums exist and were recognized, and because the datums that were found are less reliable. For example, the last occurrence of *Globorotalia linguaensis* (marking the base of Zone M14), and the first occurrences of *Globorotalia plesiotumida*, *Globigerinoides extremus*, and *Neogloboquadrina acostaensis* (the latter marking the base of Zone M13), are defined by gradual transition from other forms and are to some extent subjective.

The marker for the base of Zone M14, the last occurrence of *Globorotalia linguaensis*, is rare in the upper Miocene. The base of Zone M14 was provisionally identified by the first occurrence of keeled *G. margaritae*, which occurs in Samples 159-959A-10H-CC (94.6 mbsf) and 159-959C-11H-CC (97.3 mbsf). Core-catcher samples from equivalent depths in Hole 959B locate the first appearance of *G. margaritae* even more precisely. The transition from the varieties *G. margaritae primitiva* to *G. margaritae margaritae* (using the nomenclature of Cita, 1973) occurs between Samples 159-959B-11H-2, 59–61 cm, and 11H-3, 59–61 cm (92.6–94.1 mbsf). The varieties of *G. margaritae* are numerous and generally well preserved throughout the uppermost Miocene. Forms of *G. cibaoensis* transitional to *G. margaritae* persist down-section as far as 159-959B-17H-CC (157.0 mbsf). These transitional varieties have between four and four and a half chambers, like typical *G. cibaoensis*, but have a sharp peripheral margin with a poorly developed keel. They show variation from umbilically inflated forms similar to *G. cibaoensis* figured by Chaisson and Leckie (1993) from the western equatorial Pacific to biconvex forms reminiscent of the warm subtropical to temperate species *Globorotalia panda*, figured by Kennett and Srinivasan (1983).

The subdivision of Zone M13 was generally easy to identify using the first appearance of *G. plesiotumida* and *Globigerinoides extremus* to mark the base of Subzone M13b. Subzone M13b is recognized in Samples 159-959B-11H-3, 59–61 cm, through 13H-CC (94.1–119.0 mbsf). *Globorotalia plesiotumida* and *G. extremus* appear abruptly and morphological gradations to their ancestral forms are uncommon

in core-catcher samples. Both *G. plesiotumida* and *G. extremus* are common constituents of assemblages throughout Subzone M13b. They are associated with the common occurrence of *G. venezuelana*, *G. menardii*, *G. obliquus*, *G. sacculifer*, and the rare but consistent presence of *G. cibaoensis* and *N. acostaensis*. Both *G. juanai* and *Candeina nitida* are recorded in the same samples containing the first appearance of *G. plesiotumida*.

Foraminifer assemblages from Subzone M13a are typically strongly fragmented in the <250- μ m fraction, and dissolution has likely removed delicate forms such as *G. merotumida* and *G. obliquus*. It is possible that the base of Subzone M13b has been misidentified due to dissolution of its marker taxa. Subzone M13a is recognized from Samples 159-959B-14H-CC through 16H-CC (128.5–138.0 mbsf) by the common occurrence of *N. acostaensis* and *G. nepenthes* in the absence of members of the *Globorotalia mayeri* plexus. The lowest occurrence of Subzone M13a is in Sample 159-959C-16H-CC (144.8 mbsf). Transitional forms between *Globorotalia mesotumida* and *G. plesiotumida* are present in Samples 159-959B-14H-5, 59–61 cm (122.9 mbsf) and 159-959C-14H-CC (125.8 mbsf), but samples directly above and below these have been severely dissolved. Common constituents of this subzone include *G. venezuelana*, *G. sacculifer*, and *N. acostaensis* as well as the common occurrence of *G. nepenthes*, *G. menardii*, and *G. merotumida*.

Zone M12 is recognized in Samples 159-959B-16H-CC (147.5.0 mbsf) and 159-959C-17H-CC (154.3 mbsf) by the first occurrence of *G. aequilateralis* in the absence of *N. acostaensis*. Foraminifer populations are characterized by the abundant occurrence of *G. venezuelana*, *D. altispira*, and *G. menardii*. *Globorotalia linguaensis* is a common constituent of the >150- μ m sieve fraction.

Zone M11 was not identified at Site 959, but the condensed nature of the middle Miocene section suggests that this zone may be present between core catchers. Indeed, Zone M10, recognized by the presence of *Neogloboquadrina mayeri* before the first appearance of *G. nepenthes* (which indicates the base of Zone M11), has been identified only from Sample 159-959B-17H-CC (157.0 mbsf). This sample contains a partly dissolved assemblage characterized by common *G. trilobus*, *G. venezuelana*, and *G. menardii*. *Globorotalia "panda"*, as described above, has also been recognized in this sample.

The *Globorotalia fohsi* lineage provides a series of useful datums for the middle Miocene. The nearly full complement of morphotypes, including *G. fohsi robusta* and *G. fohsi lobata*, is present in Holes 959A through 959C. Middle Miocene datums, including the bases of Zones M9, M8, and M7, occur in succession from Samples 159-959C-18H-CC through 159-959C-20H-CC (163.8–179.6 mbsf). Preservation is highly variable throughout this interval, and vertically adjacent sections can yield both abundant, well-preserved foraminifers, as well as completely barren samples. Common species in this interval include *G. sacculifer*, *G. venezuelana*, and *G. mayeri* and its variants such as *G. siakensis*. Fohsellids have common to abundant occurrence in well-preserved samples in this succession, as do species such as *Globigerinella praesiphonifera*, *Globoquadrina dehiscens*, and *D. altispira*.

Only Hole 959A recovered the lower middle Miocene to lower Miocene interval. Preservation declines considerably in Zone M7, but many of the zone marker species are dissolution-resistant and permit all but the most dissolved samples to be zoned. The base of Zone M7 is recognized by the presence of *G. peripheroacuta*, *G. peripheroronda*, and *Orbulina suturalis* in Sample 159-959A-19H-CC (180.1 mbsf). *Globorotalia praemenardii* is also present. The first occurrence of *Orbulina suturalis*, the marker for the base of Zone M6, was noted in Sample 159-959A-20X-CC (189.1 mbsf) together with *G. archeomenardii*, *G. peripheroronda*, and *G. sicana*. We have not identified Zone M5 conclusively since neither *Praeorbulina glomerosa* nor *Orbulina suturalis* has been found in Sample 159-959A-21X-CC (198.6 mbsf). However, this sample does contain *G. archeomenardii*, which first appears in Zone M5. Sample 159-959A-21X-CC

is dominated by intermediate forms between *G. sicana* and *G. trilobus* as well as *G. dehiscens* and *G. peripheroronda*. The earliest representatives of *G. sicana* are found in Sample 159-959A-23X-CC (216.6 mbsf) and mark the lowest occurrence of Subzone M4c. This sample contains sparse, moderately preserved foraminifers such as *G. peripheroronda*, *G. trilobus*, and *G. birnageae*. The first appearance of *G. birnageae* in the next lowest sample (159-959A-24X-CC) identifies the base of Subzone M4b. A hiatus may be present below Sample 159-959A-24X-CC (Subzone M4b), since the next lowest sample (159-959A-25X-CC; 235.5 mbsf) contains *C. dissimilis* and *G. kugleri*, which are indicative of Subzone M1b. *Globorotalia kugleri* is represented by rare forms with a rounded, biconvex axial profile similar to *G. mendacis* described by Blow (1969). *Globorotalia kugleri mendacis* is distinguished from *G. birnageae* by possessing a larger number of chambers in the final whorl and the presence of a distinctive reticulate surface texture. Subzone M1b can be identified to as low as Sample 159-959A-27X-CC (254.8 mbsf) based on the presence of early forms of *G. triloba* and *G. dehiscens*. These initial specimens of *G. triloba* have the coarsely cancellate surface texture and morphology of the ancestral species *G. connecta*, but possess a small secondary aperture (Kennett and Srinivasan, 1983).

The core-catcher samples from 159-959A-28X through 37X (264.4–351.2 mbsf) contain radiolarian and diatom assemblages with sparse benthic foraminifer assemblages. No age-diagnostic planktonic foraminifers have been found in this interval, although Sample 159-959A-29X-CC (274.0 mbsf) does contain rare specimens of *G. mayeri*.

The only Oligocene assemblage was recorded from Samples 159-959A-38X-CC through 40X-CC (360.8–380.2 mbsf). *Globigerinella obesa*, together with *Globigerina praebulloides*, *Globigerina euapertura*, *G. ciperoensis*, and *G. angulifurcata*, indicates Zones P22 to P21b. Foraminifers are rare in these samples but they commonly are moderately well preserved.

The core-catcher samples from Cores 159-959A-41X to the bottom of Hole 959A (389.8–480.7 mbsf) are barren of planktonic foraminifers. So are the core-catcher samples from the top of Hole 959D to 159-959D-38R-CC and 40R-CC.

Samples 159-959D-39R-CC (783.5 mbsf) and 41R-CC (802.6 mbsf) provided a few specimens of *Acarinina primitiva* (late Paleocene to middle Eocene). These specimens are filled with sparry calcite, and most have been flattened. Below this, the core-catcher samples from Cores 159-959D-42R to the bottom of Hole 959D (Core 159-959D-78R; 812.3–1158.9 mbsf) are barren of planktonic foraminifers, except for a single specimen of *Globigerinelloides* in Sample 159-959D-65R-CC (1033.7 mbsf). This sample also contains a calcareous benthic foraminifer assemblage that stands in sharp contrast to the nearly exclusively agglutinated assemblages present from 195-959D-41R-CC through 59R-CC (802.6–976.1 mbsf).

Silicoflagellates

Core catchers from selected intervals in Holes 959A and 959D were examined for silicoflagellates to supplement age determinations based on calcareous planktonic fossils. Results are reported for silicoflagellate-bearing sediments in those intervals where calcareous microfossils were absent or too poorly preserved to be age-diagnostic.

Core-catcher samples from Sample 159-959A-27X-5, 23–25 cm, through 28X-CC (251.3–264.4 mbsf) contain common to few silicoflagellates that are generally well preserved. Assemblages include *Naviculopsis ponticula*, *Naviculopsis contraria*, *Naviculopsis obtusarica*, *Bachmannocena elliptica*, and common *Dictyocha hannai*. This association indicates early Miocene *N. ponticula* Zone. Other species in the assemblage include *Corbisema triacantha triacantha*, *Distephanus crux crux*, *Distephanus speculum speculum*, and *Distephanus speculum triommata*. Bukry (1981b) suggests that this silicoflagellate zone should correlate with calcareous nannofossil Zone

CN3, although examination of our material indicates a correlation with calcareous nannofossil Zone CN2 and the upper part of Subzone CN1c.

Core catchers from Cores 159-959A-29X through 31X (274.0–293.3 mbsf) contained few to common, well-preserved silicoflagellates including *Naviculopsis lata*, *Naviculopsis biapiculata*, *Distephanus triommata*, and *Dictyocha brevispina*. This assemblage indicates early Miocene *N. lata* Zone. Bukry (1981b) indicates a correlation of this zone with the lowest part of calcareous nannofossil Zone CN2, Subzone CN1c, and the upper part of Subzone CN1b. This is in general agreement with the preliminary results from Leg 159.

Samples from Sections 159-959A-32X-CC through 44X-CC (303.0–418.1 mbsf) contain *Bachmannocena apiculata*, *Distephanus crux crux*, *Naviculopsis biapiculata*, and *Corbisema triacantha triacantha* but lack *N. lata*, *Corbisema apiculata*, and *Corbisema hastata*. This association indicates the late Oligocene to early Miocene *N. biapiculata* Zone. Samples from Sections 159-959A-32X-CC and 33X-CC (303.0–312.6 mbsf) contain rare *Distephanus speculum haliomma*, indicating the latest Oligocene to earliest Miocene *D. speculum haliomma* Subzone. This is in agreement with the age determination based on calcareous nannofossils. It is uncertain if the lower boundary of this subzone represents an accurate placement, as the underlying samples from Sections 159-959A-34X-CC through 35X-CC (322.2–331.8 mbsf) contain only rare, generally poorly preserved silicoflagellates. The better preserved interval from Sections 159-959A-36X-CC through 44X-CC (341.5–418.1 mbsf) contains *N. biapiculata*, *B. apiculata*, and *Corbisema triacantha triacantha* without *Distephanus speculum haliomma* and *Distephanus speculum hemisphaericum*, indicating the late Oligocene *Corbisema triacantha mediana* Subzone. In addition, these assemblages include the diatom *Rocella vigilans* that occurs in abundance only in upper Oligocene sediments (Fenner, 1985). This late Oligocene age assignment is in agreement with the sparse nannofossil data available for this interval.

Sample 159-959A-45X-CC (427.7 mbsf) contains few, moderately preserved silicoflagellates including *Corbisema hastata globulosa*, *Corbisema triacantha mediana*, and *Naviculopsis biapiculata*. This assemblage indicates the late Eocene to early Oligocene *Corbisema apiculata* Zone. The presence of *Rocella vigilans* in this assemblage suggests the Oligocene portion of this zone. Samples from core catchers in Cores 159-959A-46X through 52H (437.4–480.7 mbsf) are barren of siliceous planktonic microfossils. However, core recovery degraded significantly in this interval (dropping to approximately 12%), with only chert and massive claystone barren of preserved siliceous microfossils recovered. This sequence was repeated in Hole 959D with recovery that included clayey diatomite.

The clayey diatomite in core catchers from Cores 159-959D-1R through 5R (427.3–465.3 mbsf) contains silicoflagellate assemblages that include *Corbisema hastata globulata* and *Corbisema triacantha mediana* without *Dictyocha hexacantha*. This association of species indicates the late Eocene to early Oligocene *Corbisema apiculata* Zone. Preservation and abundance degrade downward through this interval, as chert and claystone dominate the recovered material. No age-diagnostic siliceous microfossils were observed in the core catchers from Cores 159-959D-6R through 14R (469.3–542.4 mbsf). Attention shifted back to calcareous nannofossils with their return in Core 159-959D-14R (542.4 mbsf).

Palynology

The upper 43 cores in Hole 959D were dated using planktonic foraminifers, calcareous nannofossils, and silicoflagellates. The upper part of Core 159-959D-44R, which consists of alternating calcareous marl and black claystone, yields a nannofossil age of late Paleocene, but the lower black claystone interval (Sample 159-959D-44R-3, 90–91 cm, through 44R-CC; 825.8–831.6 mbsf) is barren of calcareous microfossils. Cores 159-959D-45R through 64R (black claystone)

are also barren of calcareous microfossils. Although some samples in the interval from Sections 159-959D-41R-CC through 59R-CC (802.6–976.1 mbsf) yielded a diverse agglutinated foraminifer assemblage of probable Late Cretaceous to early Eocene age, no more precise age determinations were possible in this interval without the use of palynology. Core-catcher samples from the following cores were processed for palynomorphs: 159-959D-44R (831.6 mbsf), 46R (850.9 mbsf), 49R (879.9 mbsf), 51R (898.8 mbsf), 53R (918.1 mbsf), 54R (927.8 mbsf), 56R (947.1 mbsf), and 57R (956.8 mbsf).

The residues from these samples yielded a sparse, poorly preserved pollen and spore assemblage. The identified forms include *Lygodiumsporites* sp., *Leiotriletes adriennis*, *Granulatisporites* sp., *Laevigatosporites* spp., *Inaperturopollenites* sp., *Taxodiaceapollenites* sp., *Araucariacites australis*, *Buttinia andreava*, *Proxapertites operculatus*, *Longapertites* spp., *Spinizonocolpites echinatus*, *Retimonocolpites* sp., *Clavatipollenites* sp., *Liliacidites* sp., *Foveotricolpites* sp., *Complexipollenites* sp., *Triporopollenites* sp., *Thompsonipollis?* sp., *Orbiculapollis?* sp., *Aquilapollenites* spp., *Echitripites trianguliformis?*, *Tricolporopollenites* spp., *Retitricolporites* sp., *Ephedripites* sp., *Ericipites* sp., and *Polyadapollenites* sp. Several dinoflagellate and acritarch cysts are also present, but were not identified. Other algal bodies include *Pilospora parva* and *Botryococcus*.

Four pollen species are diagnostic of the Late Cretaceous palaeo-palynological province (Germeraad et al., 1968; Traverse, 1988): *Buttinia andreava*, *Spinizonocolpites echinatus*, *Retitripites trianguliformis*, and *Proxapertites operculatus*. Whereas the last three species range into the early Tertiary, *Buttinia andreava* became extinct at the end of the Maastrichtian. Because this species was identified in Cores 159-959D-49R, 51R, and 54R, these cores cannot be younger than Maastrichtian. Cores 159-959D-44R and 46R contain a Cretaceous to early Tertiary assemblage and may be as young as early Paleocene. Although the boundary between the calcareous marl and the black claystone in Core 159-959D-44R is gradational, there may be a hiatus here, or in the missing sections of Core 159-959D-45R.

PALEOMAGNETISM

Investigations of magnetic properties at Site 959 included measurements of bulk susceptibility on the whole cores, and natural remanent magnetization (NRM) on the archive-half sections and selected discrete samples from working-half sections recovered by APC coring. NRMs were also measured on archive-half sections that preserved an intact structure when cored with the extended core barrel (XCB) and rotary core barrel (RCB). Stepwise demagnetization was conducted on APC sections, intact XCB sections, and selected RCB sections.

Bulk Susceptibility

Magnetic susceptibility measurements were made on whole cores from Holes 959A to 959D. These data, included in Site 959 Appendix B on the CD-ROM, provide a near-continuous shipboard record of the magnetic susceptibility with depth, although gaps occur between 440 and 480 mbsf and between 1060 and 1100 mbsf because of poor core recovery.

The susceptibility records of APC cores down to 179.6 mbsf in Holes 959A through 959C are similar (Fig. 28). Bulk susceptibility decreases from $\sim 20 \times 10^{-5}$ SI units in the upper part of the first core to $\sim 7 \times 10^{-5}$ SI units at ~ 10 mbsf. It then remains constant to a depth of 50 mbsf. Below this depth, susceptibility increases sharply to a value of $\sim 12 \times 10^{-5}$ SI units. This distinctive magnetic transition, which can be seen in measurements of both susceptibility and remanence (as described below), does not correspond to any obvious trend in lithology, chemistry, or physical properties. In the interval from 50

to 70 mbsf, susceptibility increases to $\sim 30 \times 10^{-5}$ SI units and then decreases to $\sim 20 \times 10^{-5}$ SI units at 95 mbsf. This may reflect a change to reducing conditions in the sediment, indicated by the occurrence of glauconite at, and below, 75 mbsf. Between 95 and 162 mbsf, bulk susceptibility increases gradually to a maximum of $\sim 45 \times 10^{-5}$ SI units. Below 162 mbsf, susceptibility drops over an interval of less than 3 m thick to a value of 15×10^{-5} SI units. This change in magnetic properties corresponds to an increase in clay content of the sediment, which may reflect a change in sedimentation rate. Below 180 mbsf, bulk susceptibility in Holes 959A and 959D, which ranges from 5 to 10×10^{-5} SI units, gradually decreases to ~ 0 SI units at a depth of 760 mbsf (Fig. 29), suggesting depletion of ferromagnetic minerals. Evidence of cyclicity is present within the susceptibility record at the 180 to 760 mbsf interval. This low susceptibility interval corresponds to the porcellanites, micrites, and clays of lithologic Unit II. From 760 to 960 mbsf, susceptibility progressively increases to a maximum value of $> 50 \times 10^{-5}$ SI units at a depth of 878 mbsf; it then decreases progressively to a minimum value at 960 mbsf, where it remains at an approximately constant susceptibility of $\sim 4 \times 10^{-5}$ SI units to 1050 mbsf. Below this depth, to the bottom of Hole 959D, the scatter in the data increases, with bulk susceptibility values falling between ~ 0 and 60×10^{-5} SI units. This interval corresponds to the lithologies of Units IV and V.

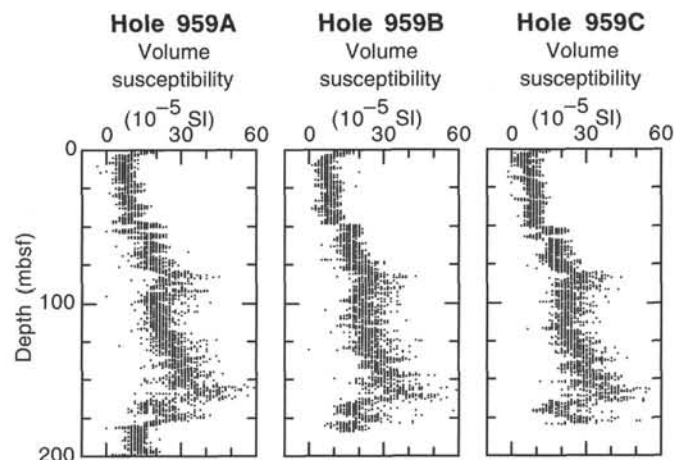


Figure 28. Bulk magnetic susceptibility vs. depth of upper sediments (<200 mbsf), Holes 959A (Cores 159-959A-1H through 21X), 959B, and 959C.

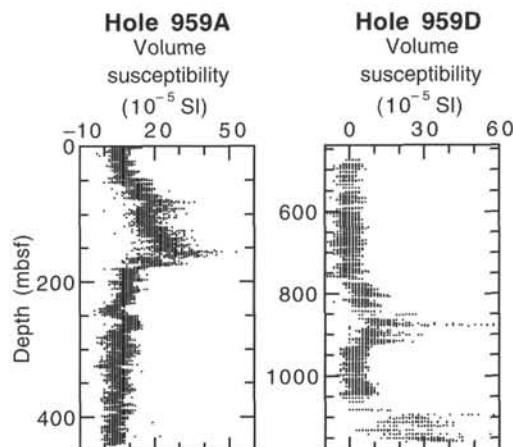


Figure 29. Bulk magnetic susceptibility vs. depth, Holes 959A and 959D. Note change in depth scale.

Core Orientation

Cores 159-959A-3H through 19H, 159-959B-3H through 20H, and 159-959C-3H through 20H were oriented using the Tensor orientation tool (Table 6). While the tool was in the measuring position in the monel nonmagnetic drill collar, the magnetometers in the tool recorded a field strength of $\sim 30 \times 10^3$ nT, similar to the Earth's field at the site. The directions of hole azimuth and inclination, as well as the position of the core within the barrel, typically varied by only a few degrees during the 5 min before the APC was "fired," providing a measure of confidence in the reliability of these measurements.

Remanent Magnetization

Measurements of remanent magnetization were made on core sections and discrete cubes from Holes 959A through 959D. The APC cores (159-959A-1H through 19H, 159-959B-1H through 20H, and 159-959C-1H through 20H) were all measured using the whole-core cryogenic (WCC) magnetometer, and demagnetized at 15 and 25 mT. Measurement of the XCB cores (159-959A-20X through 45X) was limited to NRM measurements. Individual sections of RCB cores, which appeared intact on visual inspection, were measured using the WCC magnetometer and, whenever sufficient NRM intensity was recorded, were demagnetized to 25 mT. These data are archived in Site 959 Appendix C on the CD-ROM.

Variations in the intensity of remanence with depth (Fig. 30) are similar to those of shipboard bulk susceptibility. The upper 10 m possesses a moderately high NRM intensity (~ 10 mA/m), which decreases to values between 0.1 and 1 mA/m in the interval from 10 to 50 mbsf. A sharp increase was noted at 50 mbsf, which corresponds to an increase in susceptibility, but not to any observed lithologic, chemical, or physical change. In the interval from ~ 50 to 160 mbsf, NRM intensity is constant and high, with values that range from 10 to 50 mA/m. Below 160 mbsf, NRM intensity is low (~ 1 mA/m), at the practical limit of sensitivity of the WCC magnetometer.

These measurements indicate that most of these rocks are either too weakly magnetized to obtain significant directional information; or, where they are strongly magnetized (NRM intensities > 5 mA/m, from ~ 50 to 170 mbsf), they are dominated by a remanence that varies systematically along the core (Fig. 31). In the latter case, the top of each core is more strongly magnetized (> 50 mA/m) than the bottom (< 10 mA/m) and the magnetization is directed downward at the top and upward at the bottom of each core. This core-related magnetization is probably a drilling-induced effect (Behrmann, Lewis,

Musgrave, et al., 1992), as it occurs irrespective of variations in lithology and degree of drilling disturbance. For example, the lower parts of some cores show clear evidence of "flow-in" as the core is pulled to the surface. The magnetic signature in these and in undisturbed cores is similar. The declination of the remanence in these cores is preferentially directed toward 000° in core coordinates (Fig. 32). Restoration of the declination to geographic coordinates (for those cores oriented by means of the Tensor tool) introduces a high degree of scatter to the data (Fig. 33). This enigmatic result may be caused by a radially symmetric magnetization in the core, as seen in the records of Leg 154 (Curry, Shackleton, Richter, et al., 1995). As with Leg 154, the resultant magnetization of a split half-core would be orthogonal to the cut face. We were unable to test this radial contamination on working-half cores before they were sampled.

Alternating field (AF) demagnetization at 25 mT is not sufficient to remove this drilling-induced effect. In some intervals, the magnetization on stepwise AF treatments follows a great circle trajectory in stereographic projection, which suggests that further cleaning may permit the isolation of a characteristic remanence.

In the intervals from ~ 15 to 50 mbsf and below ~ 170 mbsf, the intensity of remanence is low (mostly < 1 mA/m). In Holes 959B and 959C, the intensity and inclination of magnetization in these intervals show systematic, section-by-section variations (e.g., Core 159-959B-3H; Fig. 34), with intensities of ~ 1 mA/m at the top, and of ~ 0.1 mA/m at the bottom of each section. Inclinations steepen slightly from the top to the bottom of each section. At least some of this variation may be ascribed to the core liner, as a similar intensity and direction has been measured in empty liners. Previous estimates of the magnetization of empty core liners indicate intensities of ~ 0.1 mA/m (e.g., Mayer, Pisias, Janecek, et al., 1992), somewhat lower than those we have measured.

Approximately one discrete cube sample was taken per core from Holes 959A and 959D, and one per section from Hole 959B. Samples from Hole 959A were demagnetized to 80 mT, and those from Hole 959B to 25 mT. These samples were too weak to yield a reliable direction, so only the NRMs of samples from Hole 959D were measured on the WCC magnetometer.

Magnetostratigraphy

Because of the low intensity of magnetization and drilling-induced magnetization, it was impossible to determine the magnetostratigraphy for Site 959 on board ship, with the exception of the first few cores obtained in Hole 959A. In these cores, the NRM intensity is > 1 mA/m, and inclinations are shallow. The first two cores are not oriented, so magnetic reversals can only be recognized as a switch of polarity within an individual core. We have interpreted these apparent reversals (Fig. 35) in terms of the geomagnetic polarity time scale (Cande and Kent, 1992). We can identify reversals to the end of the Matuyama (2.6 Ma, Chron C2r), and tentatively the end of the Gauss (3.553 Ma, Chron C2An.3n) with some confidence, although reversals within the Gauss cannot be identified. The age vs. depth plot (Fig. 36) up to the end of the Matuyama is approximately linear, with a slope of ~ 7 m/Ma.

Magnetic Mineralogy

The nature of the carriers of the NRM has been investigated by isothermal remanent magnetization (IRM) acquisition experiments. Selected discrete samples from Hole 959A, which had previously been cleaned by static AF treatment to 80 mT, were subjected to direct fields up to 800 mT. In the interval from 0 to 162 mbsf, the samples saturate in fields less than 200 mT, suggesting that the primary carrier of the magnetization is magnetite or titanomagnetite. Below this depth, IRM acquisition experiments show a steep slope to 150 mT, and then a more gentle slope, with saturation occurring in fields

Table 6. Tensor tool orientations for cores from Site 959.

Leg, hole, and Core	MTF (°)	Leg, hole, and Core	MTF (°)	Leg, hole, and Core	MTF (°)
159-959A-		159-959B-		159-959C-	
3H	247	3H	224	3H	244
4H	164	4H	083	4H	054
5H	188	5H	087	5H	038
6H	039	6H	261	6H	346
7H	269	7H	267	7H	227
8H	037	8H	184	8H	103
9H	263	9H	269	9H	232
10H	213	10H	298	10H	292
11H	020	11H	032	11H	265
12H	211	12H	212	12H	102
13H	179	13H	031	13H	000
14H	169	14H	007	14H	291
15H	083	15H	156	15H	308
16H	065	16H	076	16H	214
17H	214	17H	043	17H	090
18H	113	18H	261	18H	074
19H	206	19H	266	19H	315
				20H	345

Note: The orientation parameter (MTF) is the angle in degrees between true north and the line marked on the center of the working half of the core.

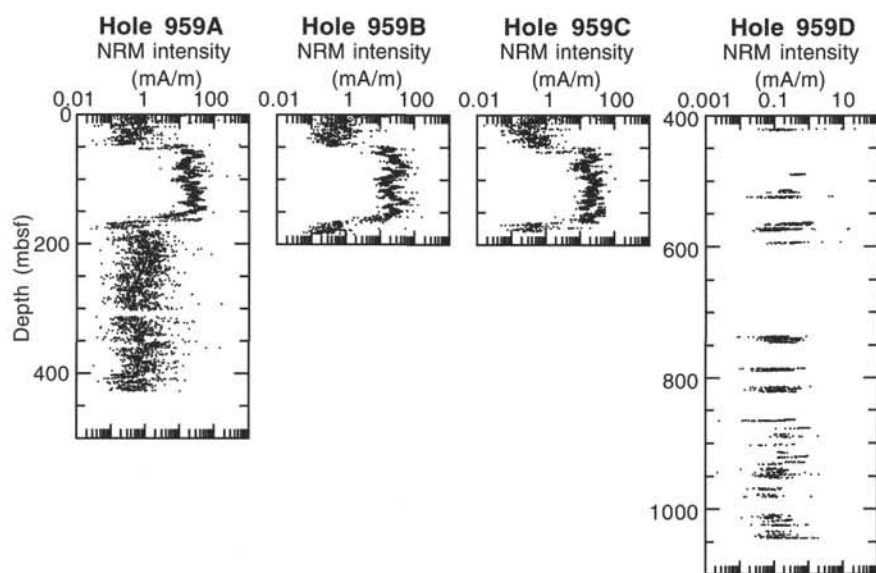


Figure 30. NRM intensity vs. depth, Holes 959A through 959D.

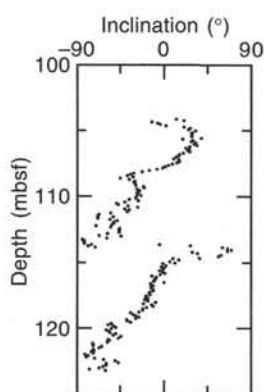


Figure 31. Inclination (at 25 mT demagnetization) for Cores 159-959A-12H and 13H, illustrating the nature of the drilling-induced remanence.

of 300–600 mT, which may indicate the presence of a higher coercivity mineral as well as the presence of magnetite or titanomagnetite.

SEDIMENTATION RATES

Sediment accumulation rates were calculated on the basis of preliminary biostratigraphic and paleomagnetic data from Site 959. In general, the Neogene appears to be continuous, although some intervals in the lower Miocene that are barren of calcareous microfossils may contain brief hiatuses. The Paleogene and Cretaceous sequences are more discontinuous. In addition, the lack of biostratigraphic control in most of the upper Eocene to Oligocene, lower Paleocene(?) to upper Santonian, and middle Cretaceous preclude the calculation of reliable sediment accumulation rates for these intervals. Given these uncertainties, sediment accumulation rates were calculated only for the Neogene and the interval from the upper Paleocene to the middle Eocene.

Sediment accumulation rates were calculated using the datum levels and ages reported in Table 7. In most cases, the depth of a given datum in the Neogene is known to within 1.5 m, although a few are known only within the distance between core-catcher samples. Depths for a given datum in the Paleogene are known only within the distance between core-catcher samples. This large sample spacing introduces significant uncertainties in the reported sediment accumulation rates for the lower Eocene and upper Paleocene.

The oldest interval for which reliable sediment accumulation rates can be calculated at Site 959 is the late Paleocene to early Eocene. Sediment accumulation during the late Paleocene occurred at rates of 10–13 m/m.y. These rates are typical for oligotrophic pelagic settings that are not directly influenced by clastic influx. Rates in the early Eocene were significantly reduced, as accumulation fell to 3–7 m/m.y. This slow rate of sediment accumulation, coupled with the poor preservation of nanofossils and the near total destruction of planktonic foraminifers, may indicate sporadic deposition and exposure of the sediment on the seafloor for extended periods of time.

A significant increase in the sediment accumulation rate occurred in the middle Eocene with the deposition of mixed siliceous and calcareous ooze (now porcellanite). The sediment accumulation rate for the interval from Cores 159-959D-24R-CC through 36R-CC (638.7–764.5 mbsf) was at least 21 m/m.y. This must be considered a minimum estimate, as neither the top nor the bottom of the defining biostratigraphic zone is well preserved.

The overlying upper Eocene and Oligocene section is either barren of calcareous microfossils or contains poorly preserved assemblages that are not age diagnostic. Although silicoflagellates aid in defining the age relationships in this interval, they are not correlated well enough to the chronostratigraphic time scale to provide reliable estimates of sediment accumulation rates. The same is true, albeit to a lesser extent, with the lowermost Miocene, where preservation of calcareous microfossils alternates with intervals of noncalcareous diatomite or claystone.

The return of well-preserved calcareous planktonic microfossils in the middle lower Miocene, and their persistence through the rest of the Neogene, permitted us to calculate more reliable sediment accumulation rates. The sediment accumulation rate curve is plotted for the Neogene in Figure 36.

Sediment accumulation rates during the middle early Miocene at Site 959 were high, with values of at least 22 m/m.y. This is certainly a minimum estimate, as substantial carbonate was removed by dissolution. The presence of both calcareous and siliceous microfossils in the sediments of this age also indicates that productivity was high. Sediment accumulation rates declined during the later part of the early Miocene to 9–10 m/m.y. This drop in sediment accumulation rates coincided with the disappearance of volumetrically important siliceous microfossil accumulation at the site. This suggests a return to low nutrient conditions in the overlying surface waters during the period of 8.5–18 Ma.

Sediment accumulation rates increased to approximately 25 m/m.y. during the middle late Miocene (8.4–7.3 Ma). This high rate of sediment accumulation was followed by a brief period of low sedi-

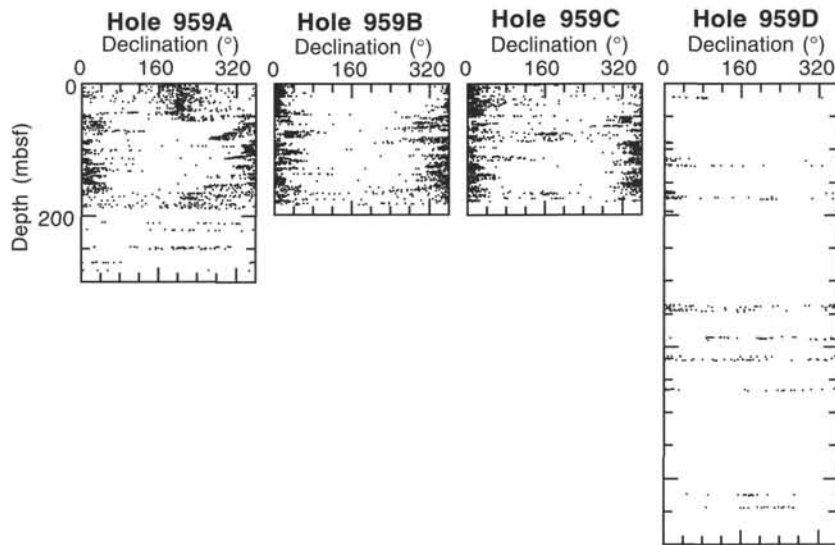


Figure 32. NRM declination before any reorientation (core coordinates), Holes 959A through 959D.

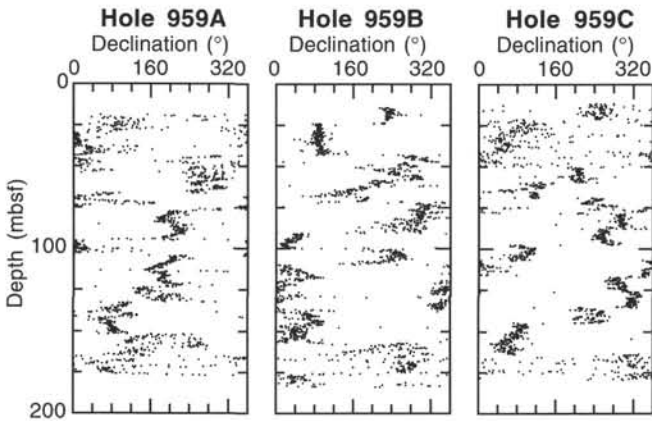


Figure 33. NRM declination of APC cores after reorientation using the Tensor tool (geographic coordinates), Holes 959A, 959B, and 959C.

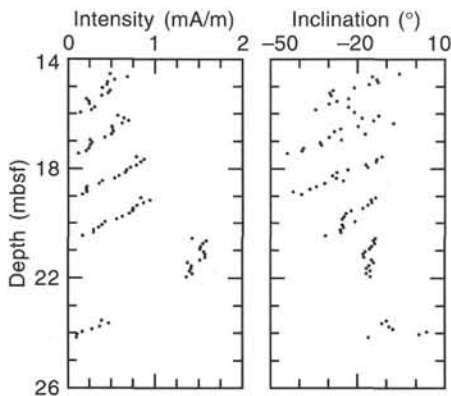


Figure 34. NRM intensity and inclination in Core 159-959B-3H.

ment accumulation (~4 m/m.y.) during the interval from approximately 7.3 to 6.5 Ma. Sediments deposited during this interval are notable for the paucity of well-preserved planktonic foraminifers, suggesting significant corrosion at or near the sediment/water interface. It is possible that this interval of apparently slow sediment ac-

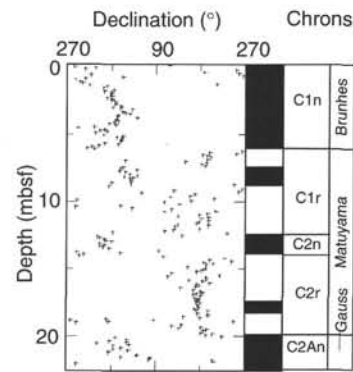


Figure 35. Preliminary magnetostratigraphic interpretation of the upper part of Hole 959A (0–22 mbsf, Cores 159-959A-1H through 3H). Note that the declinations for these cores are not absolute, and that they have been rotated by an arbitrary amount dictated by the interpretation.

cumulation actually incorporates a hiatus of short duration. Sediment accumulation rates returned to previous levels of approximately 23 m/m.y. during the late late Miocene and early Pliocene (6.5–4.4 Ma). Calcareous microfossil preservation improved concomitant with this increase in accumulation rates.

Sediment accumulation rates decreased to approximately 10–13 m/m.y. for the remainder of the Pliocene. Sediment accumulation rates for the Pleistocene are too poorly constrained to provide precise estimations, although it appears that similar low values persisted to the Holocene. Magnetostratigraphic age determinations for the upper Pliocene and Pleistocene are consistently younger than the biostratigraphic age determinations (see “Paleomagnetism” section, this chapter), although they yield a similar rate of sediment accumulation for the late Pliocene and Pleistocene. This consistent, but small, offset suggests that a miscorrelation of magnetostratigraphic reversals may be the source of this apparent discrepancy.

STRUCTURAL GEOLOGY

Structures observed and recorded at Site 959 include bedding planes, microfaults, and veins, and are described under these main

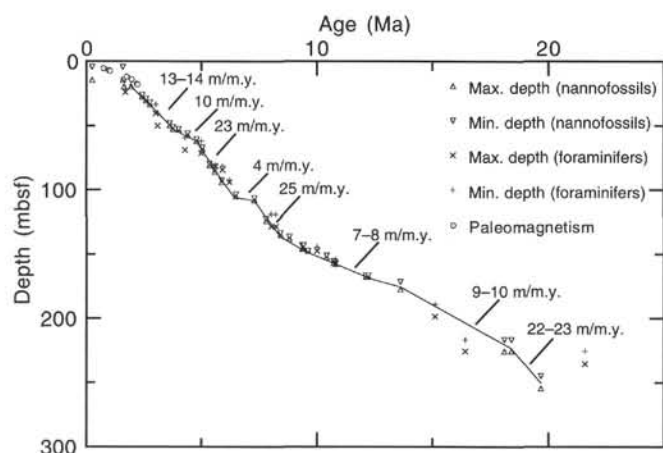


Figure 36. Graphic representation of sediment accumulation rates for the Neogene of Site 959.

headings. Structural measurements were taken from the core using temporary coordinates measured relative to the core liner, as described in the "Structural Geology" section of the "Explanatory Notes" chapter (this volume). Visual Core Description sheets and data tables are available on the CD-ROM at the back of the volume. Reorientation of the structures to geographic coordinates (i.e., relative to true north) was possible on cores recovered by APC through use of Tensor orientation tool data. Using this method, measurements made on Cores 159-959A-1H through 19H and all cores from Holes 959B and 959C were reoriented to geographic coordinates. The Tensor tool is not used during XCB and RCB drilling. Thus, the data from Cores 159-959A-20X through 52X (XCB) and from Hole 959D (RCB) can only be described in core coordinates until further detailed paleomagnetic and Formation MicroScanner (FMS) analysis has been conducted. The RCB drilling of Hole 959D caused rotation of individual blocks around a vertical axis within cores, forming drilling biscuits in a highly disturbed matrix. For this reason, most structural data from Hole 959D cannot be usefully analyzed until paleomagnetic and FMS data become available.

Bedding

The upper 274 m of Site 959 is characterized by a sequence of foraminifer-rich nannofossil oozes and chinks (spanning the Quaternary to lower Miocene). The oozes extend down to between 71.5 and 78.3 mbsf and contain few measurable structures. Extensive bioturbation has obliterated the primary bedding surfaces in many cases. In regions of less intense bioturbation the orientations of laminations were measured. Bedding dip values were plotted against depth for Holes 959A, 959B, and 959D (Fig. 37A, B, C). Bedding data are too scarce for this variation to be plotted for Hole 959C. In the interval between 0 and 47 mbsf of Hole 959A, the relatively high dips recorded are largely due to coring disturbance (Fig. 37A). The soft, easily deformed sediments are dragged down at the edges of the core, thus giving anomalously high values when apparent dips are measured (see "Explanatory Notes" chapter). Progressive consolidation of the sediments downhole allowed more accurate bedding orientations to be measured. Diatomite with clay and nannofossil chalk form the major lithology between 274 and 440 mbsf (lower Miocene to upper Oligocene). This interval, together with the lower part of the nannofossil chalk, was recovered by XCB coring. Rotation and fracturing of the cores produced biscuits and drilling slurry, making the measurement of structures difficult in many cases. Within the diatomite interval, bedding is defined mainly by green glauconitic laminations and abundant bedding-parallel burrows, especially *Zoophycos* traces.

Table 7. Biostratigraphic datums used to calculate sediment accumulation rates for Site 959.

Datum	Age (m.y.)	Maximum depth (mbsf)	Minimum depth (mbsf)
b <i>E. huxleyi</i>	0.26	14.6	4.8
Paleomag1	0.78	5.65	
Paleomag2	0.984	7.05	
Paleomag3	1.05	7.45	
t <i>C. macintyreii</i>	1.60	14.6	4.8
b <i>G. caribbeanica</i>	1.67	19.6	14.8
t <i>G. fistulosus</i>	1.70	24.0	21.3
t <i>G. fistulosus</i>	1.7	24	
Paleomag4	1.76	12.25	
t <i>D. brouweri</i>	1.95	19.6	14.8
t <i>D. brouweri</i>	1.95	24	
Paleomag5	1.98	14.15	
Paleomag6	2.2	17.45	
Paleomag7	2.23	18.15	
t <i>D. pentaradiatus</i>	2.44	27.6	26.1
t <i>D. surculus</i>	2.61	30.6	29.1
t <i>D. tamalis</i>	2.76	33.6	32.1
t <i>G. altispira</i>	3.00	40.3	33.5
t <i>G. multicamarata</i>	3.00	40.3	33.5
t <i>S. seminulina</i>	3.10	49.8	40.3
t <i>Sphenolithus</i>	3.62	49.6	48.1
t <i>R. pseudoumbilica</i>	3.77	52.6	51.1
b <i>D. tamalis</i>	4.01	52.8	52.5
t <i>G. nepenthes</i>	4.30	68.8	59.3
t <i>Amaurolithus</i>	4.39	57.6	56.1
b <i>D. asymmetricus</i>	4.79	62.1	60.6
t <i>G. ciaboensis</i>	5.00	71.5	62.0
b <i>C. rugosus</i>	5.04	68.6	67.1
b <i>C. acutus</i>	5.34	81.1	79.6
t <i>D. quinqueramus</i>	5.56	86.1	84.6
b <i>S. dehiscens</i>	5.60	81.6	81.0
t <i>A. amplificus</i>	5.88	94.1	92.6
b <i>G. tumida</i>	5.90	84.6	81.6
b <i>G. margaritae</i>	6.20	94.1	92.6
b <i>A. amplificus</i>	6.50	105.1	103.6
b <i>A. primus</i>	7.30	108.1	106.6
bc <i>D. surculus</i>	7.80	124.1	122.6
b <i>G. extremus</i>	8.00	128.5	119.0
b <i>G. pleisiotumida</i>	8.20	128.5	119.0
b <i>D. quinqueramus</i>	8.40	135.1	133.6
b <i>D. loeblichii</i>	8.80	138.1	136.6
t <i>C. calyculus</i>	9.36	146.1	143.1
t <i>D. hamatus</i>	9.40	146.1	143.1
b <i>D. neohamatus</i>	9.60	147.9	147.6
b <i>N. acostaensis</i>	10.00	147.5	144.8
b <i>D. hamatus</i>	10.40	152.6	151.1
b <i>C. coalitus</i>	10.70	157.1	155.6
t <i>C. miopelagicus</i>	10.80	157.6	157.3
b <i>G. nepenthes</i>	10.80	157.0	154.3
t <i>C. nitescens</i>	12.10	167.4	166.6
b <i>D. kugleri</i>	12.20	167.4	166.6
t <i>S. heteromorphus</i>	13.60	177.6	171.6
b <i>O. suturalis</i>	15.10	198.6	189.1
b <i>G. sicana</i>	16.40	225.8	216.6
b <i>S. heteromorphus</i>	18.10	225.6	216.6
t <i>S. belemnus</i>	18.40	225.8	216.6
b <i>S. belemnus</i>	19.70	255.0	245.0
t <i>G. kugleri</i>	21.60	235.5	225.6
t <i>G. kugleri</i>	21.60	235.5	225.6
t <i>Nannotetrina</i> spp.	41.90	638.7	629.0
b <i>Nannotetrina</i> spp.	47.80	764.5	754.5
b <i>D. lodoensis</i>	52.00	783.5	773.8
t <i>T. contortus</i>	53.30	793.0	783.5
b <i>T. contortus</i>	53.60	802.6	793.0
t <i>Fasciculithus</i> spp.	54.10	802.6	793.0
b <i>D. multiradiatus</i>	56.30	825.6	821.9
t <i>H. kleinpellii</i>	57.70	825.6	821.9
b <i>H. kleinpellii</i>	58.60		825.6

Note: b = bottom of occurrence, t = top of occurrence, and bc = bottom of common occurrence. Paleomag datums are explained in the "Paleomagnetism" section, this chapter.

Cores 159-959A-1H and 2H are Quaternary in age and display no sedimentary or structural features apart from gradational color changes. From Core 159-959A-3H, bedding is defined by colored layers in the sediment which are commonly severely distorted by coring. The first reasonably reliable dip measurements were obtained from Core 159-959A-6H. The dips are very low and are generally between 2° and 4° in Cores 159-959A-6H through 8H. These cores are

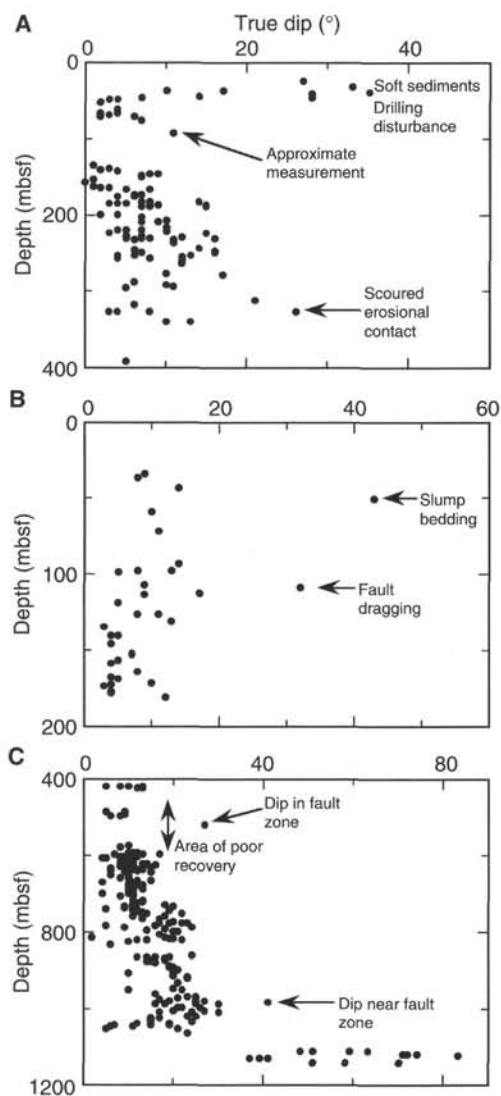


Figure 37. Variation of bedding dip with depth. **A.** Hole 959A. **B.** Hole 959B. **C.** Hole 959D. Dip values are calculated from two apparent dips.

still considerably affected by coring disturbance, and dips of 6° and 7° recorded in Core 159-959A-8H probably reflect this. The hinge of a slump fold was observed in the upper part of Section 159-959A-6H-5. However, slumping was not observed elsewhere and dips remain low (generally $<10^\circ$) throughout Hole 959A. Geographically oriented bedding data from Holes 959A and 959B were plotted on rose diagrams (Fig. 38). Despite the wide scatter of dip directions, there are clear maxima toward the north-northwest and northwest, respectively.

Hole 959D displays the best preserved structural features because of its greater depth and the more lithified nature of the sediments. Cores 159-959D-1R through 7R (417.8–475.0 mbsf) comprise diatomite with clay and radiolarians. Very few measurements were possible in this part of the hole because of poor recovery. Below the diatomite lies a thick sequence of porcellanite (475.0–812.3 mbsf). Bedding in the porcellanite is defined mainly by abundant bedding-parallel *Zoophycos* traces. Bedding dips are relatively shallow (generally $<12^\circ$) in the upper 180 m of the cored interval (417.8–600.0 mbsf) in Hole 959D. With increasing depth below 600 mbsf the amount of dip shows a gradual increase (Fig. 37C). The dip increases to values of 20° – 30° between 960 and 1000 mbsf. Laminated black claystones are the dominant lithology in this interval. Bedding is de-

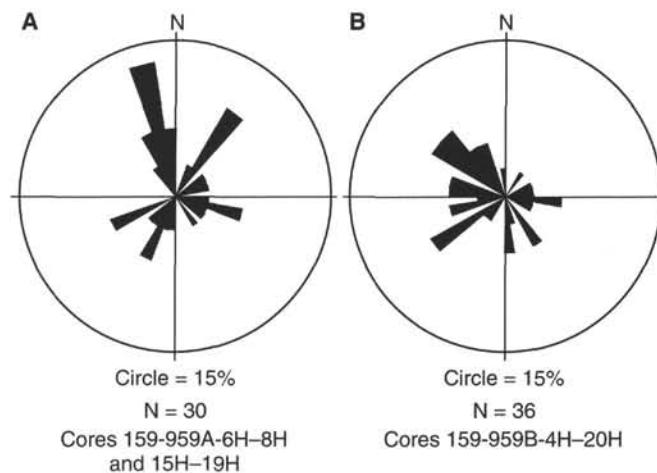


Figure 38. Rose diagrams showing dip directions of bedding in **(A)** Hole 959A and **(B)** Hole 959B. Data are in the geographic reference frame.

fined by streaky pyrite-rich laminations and thin lenses of pyrite. Pyrite nodules between 0.1 and 2 cm in diameter are a common feature of the black shales. Many of the pyrite nodules are lenticular, parallel the bedding, and display pressure shadows. Slight asymmetry and folding of the pressure shadows were observed in some examples. In thin section the pyrite within the pressure shadows appears as equant crystals that have clearly not been deformed. It thus appears as if original soft-sedimentary folds have been extensively recrystallized. An abrupt increase in bedding dip was noted in lithologic Unit V. The first bedding measurements were taken in Core 159-959D-74R (1112 mbsf). This core displays laminated, fine- to medium-grained buff sandstone with black silty claystone interbeds. Convolute bedding and cross-lamination are distinctive features. Bedding measurements were taken in regions of planar lamination and thus reflect horizontal bedding rather than dipping foresets. Core 159-959D-75R contains very steeply dipping beds (71° – 83°) of laminated buff sandstone intercalated with fissile black claystone. Cores 159-959D-76R and 77R also display steep bedding dips (up to 70°). The steep bedding dips recorded in the late Albian sandstones and claystones of lithologic Unit V reflect a phase of tectonic tilting that predated deposition of the overlying limestone (lithologic Subunit IVB) and early Coniacian–early Turonian calcareous sandstones (lithologic Subunit IVA).

Faults

Microfaults were first recorded in Core 159-959A-10H at a depth of 92 mbsf and occur within most of the cores below this level. They are generally normal, with offsets of 0.2–1 cm. In these upper parts of the sedimentary sequence it is unclear whether the microfaulting records sediment destabilization related to depositional and/or post-depositional events, or whether it is the result of coring disturbance. In many cases, faults are developed only in the center of the core and do not extend to the core edges. This phenomenon may reflect drilling-induced stresses. However, some faults do cut across the whole core width and do not appear to be caused by drilling. A fault that is clearly a primary feature occurs in Section 159-959A-18H-2. The fault is defined by a zone 1 cm wide that encloses lenses of sheared, laminated sediments. The fault has a dip of 59° and at least 5 cm of normal offset. Rare reverse faults with offsets up to 0.5 cm were also observed (e.g., Sections 159-959B-14H-2 and 159-959A-18H-2).

Listric and anastomosing faults, both reverse and normal, are present in Cores 159-959A-37X, 38X, and 39X. For example, a steeply dipping reverse fault with an offset of 20 cm is present in Section 159-959A-37X-1. Drag along the fault is evidenced by deformed *Chondrites* burrows as shown in Figure 39. The fault zone is anastomosing and contains lenses bound by thin seams of fine-grained gray

fault gouge. The fault planes themselves are undulose and display slickensides that indicate reverse motion. An anastomosing and bifurcating normal fault occurs in Section 159-959A-39X-3. As with the reverse fault described above, the fault planes are marked by thin seams of gray, fine-grained material. Anastomosing and bifurcating faults that enclose lenses of sheared material are also a common feature of Hole 959D. In Section 159-959D-12R-2 a series of curved faults up to 10 cm in length, with offsets up to 1 cm, form a conjugate set that is well defined by the displacement of pale laminations. On close examination, it can be seen that the microfaults have a localized effect. The fault planes are shiny, undulose, and display fine, slightly sinuous slickensides. A reverse microfault is associated with one of the normal faults. Figure 40 shows a good example of an anastomosing fault from Section 159-959D-43R-3. The fault runs approximately along the core axis and displays pale seams of fine-grained material and an enclosed lens of disturbed material. A younger, planar fault cuts the anastomosing fault, thus clearly indicating two phases of faulting. Although it is too early to date the faulting events,

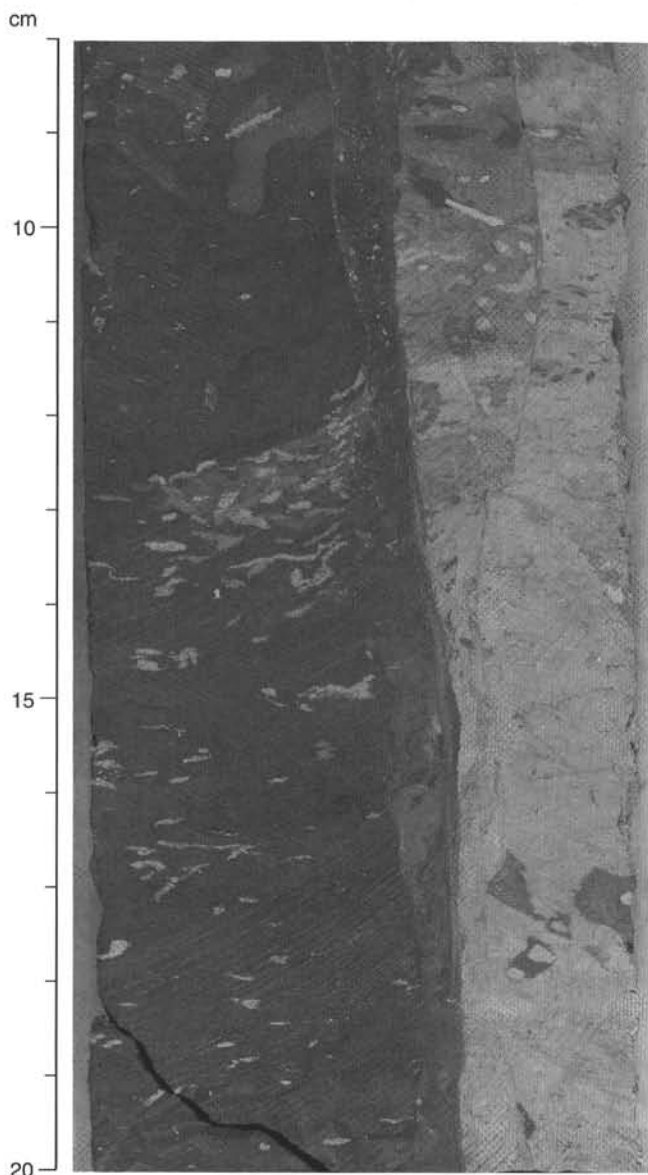


Figure 39. Anastomosing reverse fault in Section 159-959A-37R-1, 8–20 cm. Note the deformed *Chondrites* burrows and the thin seams of fine-grained material along the fault traces.

it appears that the anastomosing faults affect mainly the diatomites, porcellanites, and micrites of lithologic Unit II (lower Miocene–upper Paleocene). Anastomosing faults were not observed in the soft nannofossil oozes and chalks of lithologic Unit I (Pleistocene–lower Miocene), although the difference in lithification between lithologic Units I and II could account for this. Planar microfaults were observed throughout lithologic Units I and II.

Planar normal faults of the type shown in Figure 40 are a common feature at Site 959. Section 159-959A-39X-2 contains a series of normal microfaults that offset a *Zoophycos* trace (Fig. 41). With one exception, these faults are planar. The fault planes are not characterized by the presence of pale gray material and one is an open fracture. Slickensides indicate dip-slip motion. Figure 42A is a stereogram of normal fault planes measured in Cores 159-959A-15H through 19H. The data have been reoriented to geographic coordinates using Tensor orientation tool data. Several faults dip toward the north-northeast. Other faults dip southeast and southwest. A plot of reoriented normal faults from Hole 959B (Fig. 42B) also shows a north-northeast- to northeast-dipping set of faults. However, the most distinctive feature of the faults from Hole 959B is a conjugate set of faults that dip consistently to the southeast and northwest, although some faults also dip in a westerly direction.

Planar, normal faulting is also well developed in the porcellanites (Cores 159-959D-6R through 42R) and black claystones of Hole 959D (Cores 159-959D-43R through 66R). Figure 43 shows a planar, normal fault cutting streaky calcareous porcellanite. The clusters of pyrite crystals at the top of the photograph have formed along minor fractures. Normal faults from an apparently undisturbed core of black

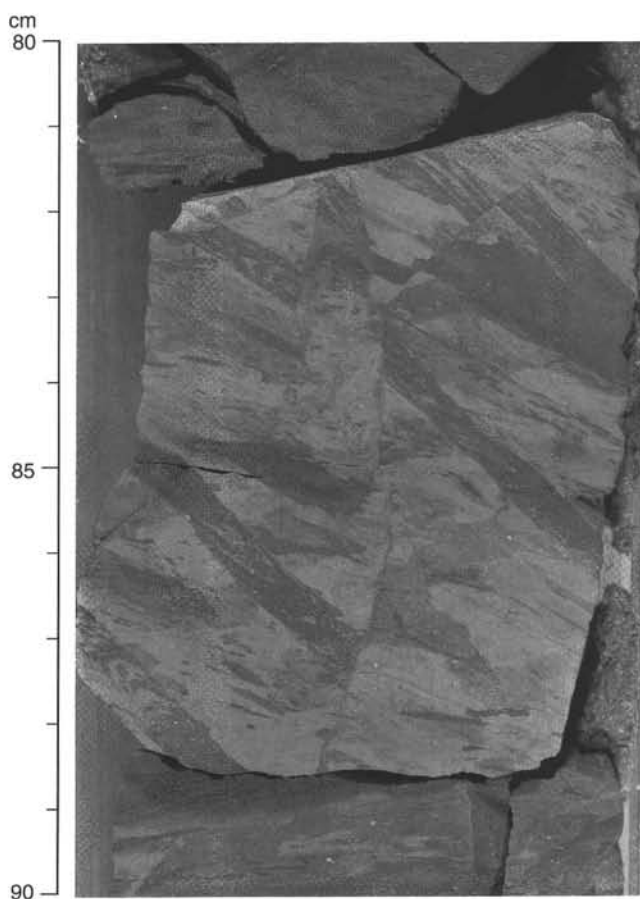


Figure 40. Anastomosing fault enclosing a lens of deformed sediments, cut by planar normal fault in Section 159-959D-43R-3, 80–90 cm.

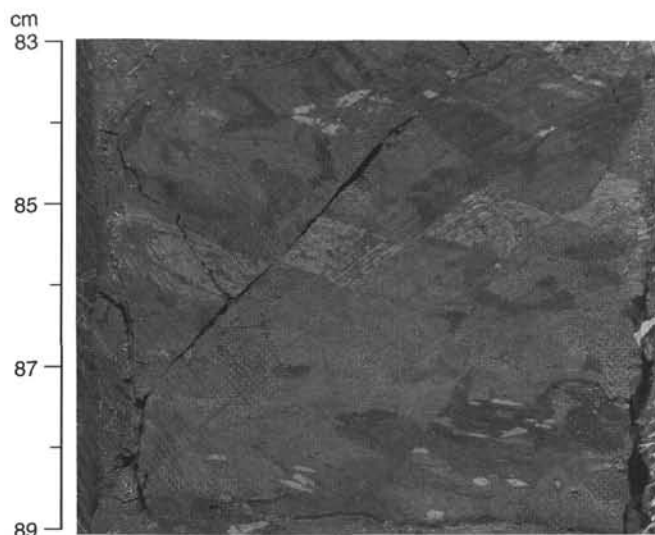


Figure 41. Series of planar normal faults in Section 159-959A-39R-2, 83–89 cm.

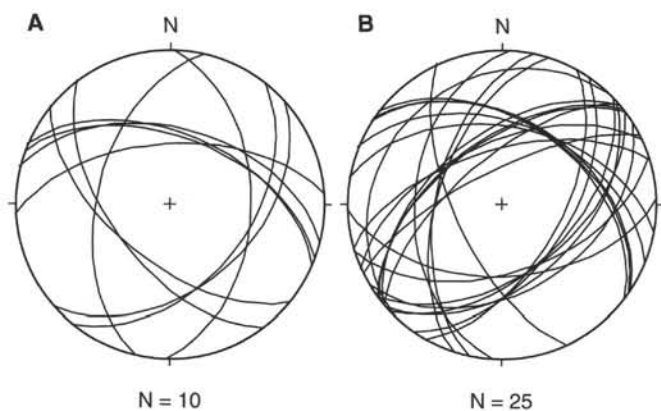


Figure 42. Stereographic projections of normal faults in (A) Cores 159-959A-15H through 19H, and (B) Hole 959B. Data are in the geographic reference frame.

claystones (Core 159-959D-57R) were plotted on a stereogram (Fig. 44). The average dip of the fault planes is 68° and the dip directions are predominantly east to southeast and west, in the core reference frame.

Veins

Several types of vein geometry and infills were observed in cores from Site 959. Vein fills include calcite, barite, pyrite, quartz, and dolomite, with minor amounts of gypsum, kaolinite, and siderite. Veins occur as tension gashes (including en échelon varieties), irregular veinlets, septarian-type vein networks, and along fault planes and fractures. Veins are relatively rare in levels above lithologic Subunit IIC, which may suggest a pre-late Eocene age for the majority of veins. However, it is also possible that veins may have been forming in lithologic Subunit IIC and below from late Eocene times onward.

A barite vein in Section 159-959D-52R-4 displays slickensided bounding surfaces. In a cross section across the core, the fabric is clearly oriented as a result of shearing (Fig. 45A). Within the vein, a round vug contains automorphic barite crystals.

Barite veins were also observed in association with an asymmetric microfold (Section 159-959D-66R-6). They occur as filled tension

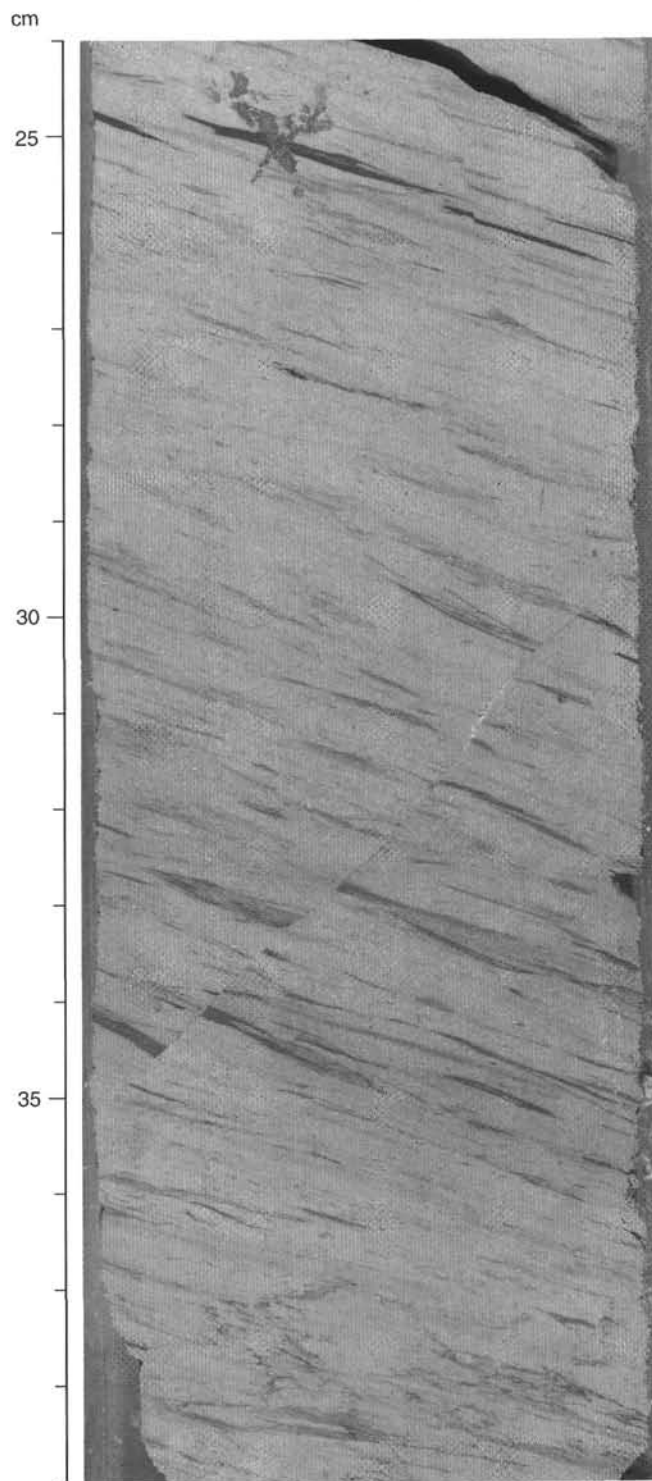


Figure 43. Normal fault in calcareous porcellanite (Section 159-959D-39R-3, 24–39 cm). Stylolitic seams can be seen at the bottom of the interval shown. At the top of the photograph, pyrite clusters have formed along small fractures.

gashes related to the bending of the fold hinge and along small normal faults in the releasing overstep of the fault trace. The small normal faults become parallel to bedding downward. In Section 159-959D-66R-7, the arrangement of two sigmoidal barite veinlets paral-

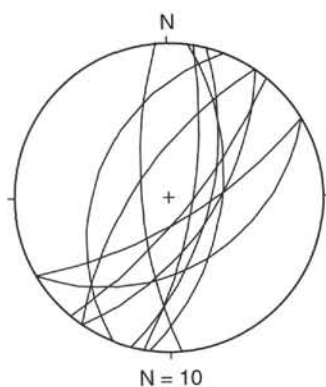


Figure 44. Stereographic projection of normal faults in Core 159-959D-57R. Data are in the core reference frame.

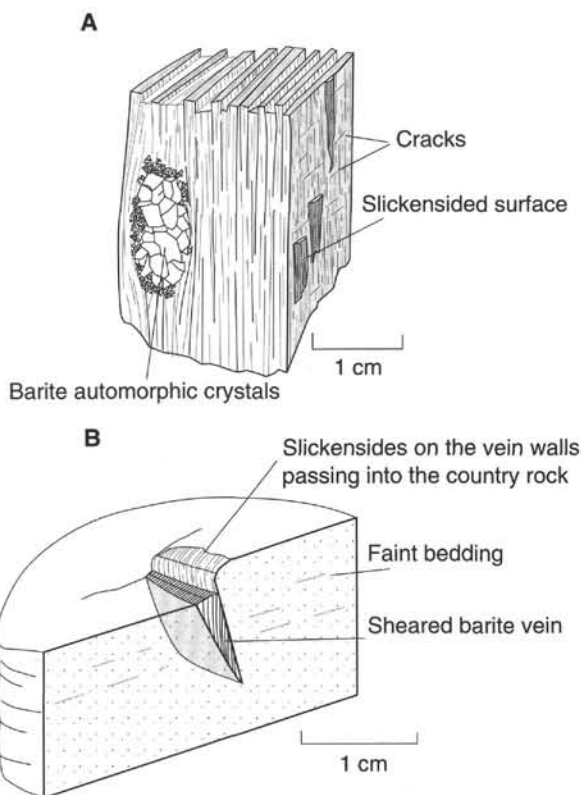


Figure 45. **A.** Barite mineralized fault in Core 159-959D-52R-4 (working half). **B.** Sketch of a sheared barite vein in Section 159-959D-56R-4.

parallel to the bedding is evidence for bedding plane slip. Vein formation is commonly related to tensional faults, and the geometrical characteristics described above are consistent with bedding plane slip acting to accommodate differential extension.

A steeply dipping, lens-shaped barite vein cuts a sandstone interval within black shales in Section 159-959D-56R-4. The vein surfaces are striated, and in a cross section of the core it can be seen that the vein is sheared. The striations on the vein surfaces curve to become parallel with the bedding surface (Fig. 45B).

In Section 159-959D-72R-2, thin veinlets of barite were formed at two different stages. An earlier, vertical veinlet is cut by two shallow-dipping lenticular veins.

Veins are relatively common in the porcellanites of lithologic Unit II. A vein in Section 159-959D-36R-4 displays a septarian arrangement and comprises translucent dark gray crystalline material

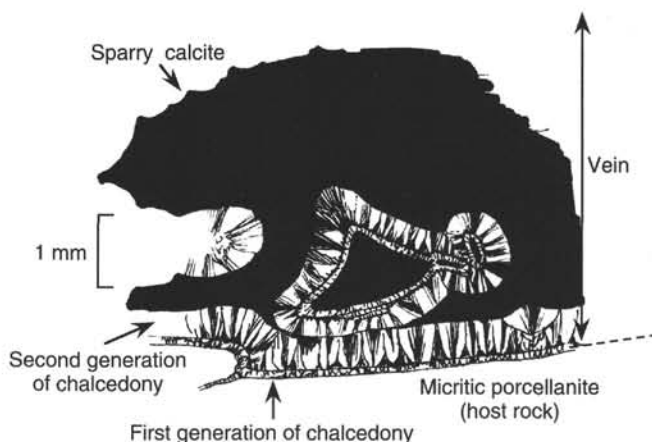


Figure 46. Detail from a thin section of a vein in Section 159-959D-36R-4, 126-127 cm (crossed polars). Two generations of chalcedony line the walls of the vein, and sparry calcite occupies the areas marked in black.

along the vein edges and opaque white material in the vein centers. Thin section study revealed the presence of at least three generations of vein fill (Fig. 46). Two earlier vein fills of gray chalcedony form concentric rinds around the edges of the vein cavity. Sparry calcite, the youngest vein fill, occupies the center of the vein. Septarian-type calcite veins also occur in the dark claystones in Section 159-959D-61R-1. En échelon tension gashes filled with calcite occur in the same section.

Thin thread-like veins of pyrite are a common feature of the black claystone interval (lithologic Unit III). They cross-cut laminations and may represent late-stage fracture fill.

Soft-sediment Deformation

Soft-sediment deformation observed at Site 959 can be divided into several main types that may be related to slope instabilities and possible coeval tectonic activity. These include faulting, slumping, and convolute bedding.

In the cores from Site 959 it was not easy to differentiate between faults formed in lithified rocks and faults generated in soft and semi-lithified sediments. Some of the anastomosing faults described above have localized effects and terminate within beds, suggesting formation while the sediments were relatively soft (e.g., Section 159-959D-12R-2). However, many also display shiny fault planes with slickensides, features suggestive of lithified (or at least partly lithified) conditions. In many cases further study, including detailed investigation of thin sections, is required. Other examples are more clear cut. A series of normal microfaults in Section 159-959D-73R-1 was probably formed by syn-sedimentary faulting. These faults are listric and their downward terminations cause slight distortion of the underlying laminations (Fig. 47).

The youngest evidence of slumping was observed in Section 159-959A-6H-5. Here, anomalously steep bedding and the hinge area of a slump fold were observed. Features that may be indicative of deformation in semilithified sediments were also observed in the dark, pyritic shales of Core 159-959D-61R. A small folded lens of gray shale that contains millimeter-size injections of dark shale is enclosed within a finely laminated sequence in Section 159-959D-61R-1. The most impressive soft-sediment deformation occurs in the deepest part of Hole 959D, in Cores 159-959D-73R through 77R (1100.8-1169.2 mbsf). Convolute bedding associated with cross-bedding occurs in Sections 159-959D-74R-2, 75R-1, and 77R-1 (e.g., Fig. 48). Slumped, coarse-grained sandstone beds were observed in Section 159-959D-76R-1, together with planar laminated beds and rip-up clasts of fine-grained silty sandstone. The age of these sediments is unknown but is at least Cenomanian-Albian or older.

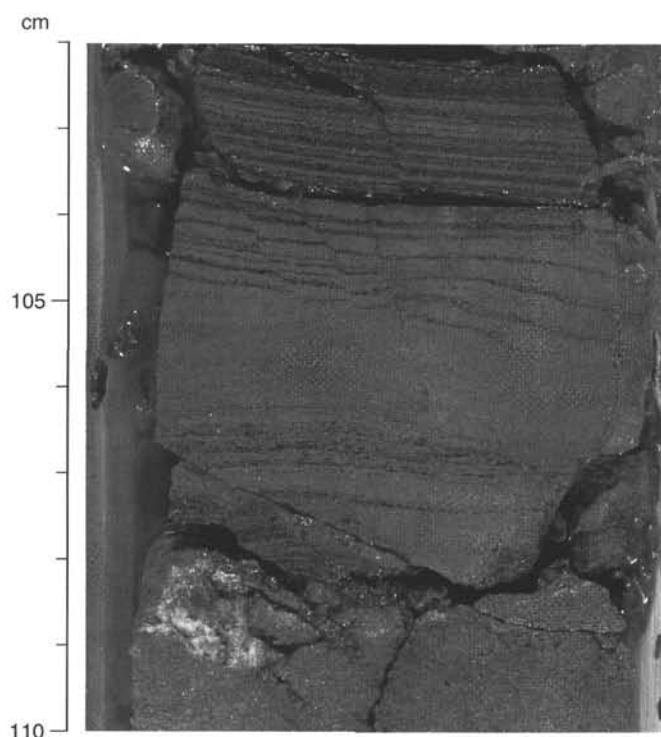


Figure 47. Series of syn-sedimentary normal faults in laminated sandstone (Section 159-959D-73R-1, 102–110 cm).

ORGANIC GEOCHEMISTRY

Introduction

At Site 959 real-time monitoring of volatile hydrocarbons, determination of inorganic carbon, total carbon, total nitrogen, and Rock-Eval measurements were performed (for methods see “Explanatory Notes” chapter, this volume). In addition, some headspace samples (Cores 159-959D-47R through 78R) were analyzed for their content and composition of organic carbon. Results of analyses of volatile hydrocarbons are discussed in the “Source Rock Geochemistry” section (this chapter).

Carbonate and Organic Carbon Records

At Site 959, carbonate and organic carbon, total nitrogen, and sulfur contents were measured on 302 samples. Sampling focused on APC cores recovered from Hole 959A. Sampling frequency ranged from one sample per section in the upper 150 mbsf (Cores 159-959A-1H through 16H) to three samples per core in the lower parts of Hole 959A (Cores 159-959A-17H through 51X). Holes 959B and 959C were sampled at lower frequency. In Hole 959D sampling focused on dark-colored sequences in Cores 159-959D-13R through 30R. The results of elemental analysis are summarized in Table 8 and presented in Figures 49 through 51.

Based on variations in organic carbon and carbonate carbon content, the sedimentary sequence from Holes 959A–959D can be divided into nine intervals (A to I).

Interval A (0–45 mbsf) covers the late Pliocene through Pleistocene, corresponding to the shallower part of lithologic Subunit IB and the entire Subunit IA (dark gray nannofossil-foraminifer oozes, see “Lithostratigraphy” section, this chapter). Organic and inorganic carbon records show large-amplitude, short-term fluctuations with



Figure 48. Convolute bedding in steeply dipping sandstone bed in Section 159-959D-75R-1, 30–56 cm. The sandstone is intercalated with fissile black claystone.

generally intermediate values for carbonate carbon (25–51 wt%) and low to very high contents for total organic carbon (0.2–1.4 wt% TOC; Fig. 49). In the upper 150 mbsf, organic and inorganic carbon contents are inversely correlated. Maximum total organic carbon (TOC) and minimum carbonate contents occur in Cores 159-959A-1H and 2H. This inverse correlation suggests enhanced carbonate dissolution associated with diagenetic degradation of labile organic matter. Similar variations in organic and inorganic carbon content were recorded from deposits of the Angola Basin (Müller et al., 1994) and the eastern equatorial Atlantic (deMenocal et al., 1993; Verardo and McIntyre, 1994). In these studies, large amplitude shifts in carbon contents are attributed to environmental changes during late Quaternary glacial-interglacial cycles. At these open-marine locations carbonate contents are high throughout the cores investigated (between 70 and 90 wt%), whereas TOC contents are generally intermediate to low (in general <1 wt%). In contrast, relatively low carbonate but very high TOC contents are recorded at Hole 959A, suggesting elevated dilution by terrestrial material. However, a continuous and rapid decrease in organic carbon is observed below 20 mbsf.

Interval B (45 to 150 mbsf) consists of nanofossil-foraminifer oozes and chalks interbedded with thin glauconite layers (see "Lithostratigraphy" section, this chapter) of late Miocene to early Pliocene age. The general downcore trend in diagenesis of organic matter, which is already obvious in interval A, continues in interval B, although rates of degradation seem to be lower below 95 mbsf (Fig. 49). TOC contents plateau at approximately 0.4 wt%. Although the inference of diminished rates of organic matter degradation is based on subtle decreases in organic carbon content, it is supported by lithologic and inorganic geochemical evidence (see "Inorganic Chemistry" and "Lithostratigraphy" sections, this chapter). A change in lithology from ooze to chalk, representing a diagenetic front, is recorded between 70 and 75 mbsf. A less steep increase in ammonium concentration below this front suggests diminished rates of organic matter degradation in the deeper sediments. In contrast to the organic carbon, carbonate contents are generally elevated throughout interval B. Maximum values exceeding 55 wt% CaCO₃ were measured in Sections 159-959A-8H-1 and 11H-3. This change in relative proportions of organic and carbonate carbon is probably related to various factors (i.e., a decrease in terrestrial dilution, an increase in carbonate flux rates, or a better preservation caused by limited oxidation of organic matter).

A sharp decrease in carbonate contents (10–20 wt%, Fig. 49) marks the upper part of interval C (155–240 mbsf), which coincides with the transition to bioturbated middle Miocene nanofossil chalks and clays. Carbonate content remains low to 180 mbsf. Below this level there is a sudden increase in carbonate content (25–50 wt%) with peak values up to 58 wt% (Section 159-959A-22X-3, Fig. 50). TOC contents in the upper part of interval C continue to decrease gradually as in interval B. Persistent long-term diagenesis is reflected by minimum TOC contents below 0.2 wt% in the bottom part of this interval. These low values are typical for modern pelagic sediments (Emerson and Hedges, 1988) and suggest maximum degradation of labile organic matter, resulting in the selective preservation of inert organic substances.

Interbeds of upper to middle Oligocene dark-colored organic-rich and carbonate-poor diatomites and light-colored organic-poor and carbonate-rich nanofossil chalks and clays (lithologic Subunit IIA) show a characteristic sawtooth pattern between 240 and 410 mbsf (interval D; Fig. 50). Organic carbon contents of diatomites always exceed 1.0 wt% with peak values of 4.2 wt% measured at 280 mbsf (Section 159-959A-31X-1). A first spike in TOC at 245 mbsf, however, is not related to diatomite but to light-colored nanofossil clay. Organic carbon content in background lithologies displays a continuous downcore increase, rising from minimum values below 0.1 wt% at 240 mbsf to 0.9 wt% at the bottom part of the interval. Carbonate contents remain at intermediate levels (25–40 wt%) down to 255 mbsf.

Below this level a conspicuous decrease to almost zero is obvious in diatomites followed by intermediate contents in nanofossil clays. The near absence of carbonate in diatomites indicates almost complete carbonate dissolution due to high pelagic flux rates at the time of deposition and subsequent oxidation of organic matter close to the sediment-water interface.

Interval E (410–560 mbsf) comprises different lithologic units: the lower section of the interbedded diatomites and nanofossil chalk (lithologic Subunit IIA), the middle Oligocene chert unit (lithologic Subunit IIB), and the upper part of the upper Eocene to the upper Paleocene porcellanite-micrite-clay unit (lithologic Subunit IIC) (Fig. 51). The upper part of interval E between 410 and 500 mbsf is characterized by elevated TOC that generally exceeds 2.5 wt%. Associated carbonate contents are extremely low (below 0.5 wt%). A downcore decrease in TOC is observed below 450 mbsf, although multiple spikes containing up to 4.7 wt% TOC (Section 159-959D-18R-3) demonstrate the persistence of organic-rich layers in lithologic Subunit IIC. Carbonate remains at minimum levels throughout interval E except for slightly enhanced contents at 420 mbsf (Section 159-959D-1R-3).

Carbon contents below 15 wt% and in general elevated amounts of TOC (around 1 wt%) characterize the upper Eocene to upper Paleocene part of interval F (560–825 mbsf; Fig. 51). Slightly higher carbonate values, reaching 30 wt%, were measured in two sections between 660 and 700 mbsf and at 825 mbsf (Section 159-959D-44R-2). Organic carbon contents drop to low values around 0.2 wt% below about 750 mbsf. Above this level high TOC contents and reduced carbonate contents suggest either selective diagenetic dissolution of carbonate and enhanced organic matter preservation or persistent elevated paleoproductivity throughout the late Eocene.

The beginning of interval G (825–1040 mbsf) is marked by a distinct change in lithology to black claystones and minor black marls of late Paleocene to early Coniacian age. Background TOC contents vary between 0.2 and 1.6 wt% in these deposits. Hydrocarbon-rich black shales with peak contents in organic carbon of 5.45 wt% occur in this interval. Average values, however, are in the range of 2.2–3.1 wt% TOC. Carbonate is absent in this lithology.

Interval H (1040–1085 mbsf) comprises two lithologic subunits: the Coniacian to lower Turonian sandy carbonate unit (lithologic Subunit IVA) and the barren limestone unit (lithologic Subunit IVB). Interestingly, both lithologic units bear an almost identical carbon pattern (Fig. 51). TOC contents are very low (<0.4 wt%) throughout the sequence. In contrast, carbonate contents reach the highest values in all cores from Holes 959A through 959D. Values range from 58 to 83 wt% (Cores 159-959D-67R through 71R).

At the base of Hole 959D TOC-rich sandstones and conglomerates of late Albian age were recovered. A drastic change in organic and carbonate carbon contents marks the transition to interval I (1085 mbsf to 1158 mbsf [TD]; Fig. 51). TOC contents are generally very high, exceeding 2.5 wt%. Carbonate is almost absent in this lithology.

Composition of Organic Matter

The type of sedimentary organic matter (OM) in Holes 959A–959D was characterized using organic carbon: total nitrogen ratios (C/N) and Rock-Eval pyrolysis data (hydrogen index and T_{max}). Results are summarized in Tables 8 and 9 and are presented in Figures 49 through 52.

The application of C/N ratios for qualitative estimation of the relative proportions of marine and terrigenous organic matter in marine sediments is based on the different elemental composition of marine and terrestrial biomass. As nitrogen is fixed mainly in proteins and these biopolymers are enriched in marine biomass, C/N ratios of marine zoo- and phytoplankton are low, averaging between 5 and 8, whereas higher land plants have ratios between 20 and 200 (Emerson

Table 8. Summary of elemental analysis of sediments at Site 959.

Core, section, interval (cm)	Depth (mbsf)	Inorg-C (wt%)	CaCO ₃ (wt%)	Tot-C (wt%)	Org-C (wt%)	TN (wt%)	C/N	Core, section, interval (cm)	Depth (mbsf)	Inorg-C (wt%)	CaCO ₃ (wt%)	Tot-C (wt%)	Org-C (wt%)	TN (wt%)	C/N
159-959A-								14H-CC, 20-21		4.91	40.90				
1H-1, 79-80	0.80	5.30	44.15	6.26	1.01	0.11	9.0	15H-2, 80-81	134.91	3.52	29.32	3.71	0.19	0.05	4.1
1H-2, 14-15	1.65	5.45	45.40	5.59	0.23	0.06	4.2	15H-3, 80-81	136.41	4.11	34.24	4.45	0.34	0.05	7.1
1H-3, 93-94	3.94	4.43	36.90	5.59	1.00	0.09	11.1	15H-4, 114-115	138.25	4.60	38.32	4.92	0.32	0.04	8.4
1H-4, 77-78	5.28	5.81	48.40	7.16	1.34	0.11	11.8	15H-5, 80-81	139.41	5.46	45.48	5.75	0.29	0.04	7.7
1H-5, 74-75	6.75	4.23	35.24	5.54	1.11	0.10	10.9	15H-6, 26-27	140.37	4.36	36.32	4.65	0.29	0.04	7.5
1H-6, 77-78	8.28	4.90	40.82	6.08	1.08	0.09	12.0	15H-7, 50-51	142.11	4.13	34.40	4.50	0.37	0.05	7.8
2H-1, 113-114	10.24	6.06	50.48	7.14	0.93	0.08	11.7	15H-CC, 20-21		4.12	34.32				
2H-2, 80-81	11.41	3.50	29.16	4.42	0.92	0.09	10.1	16H-1, 72-73	142.83	4.39	36.57	4.69	0.30	0.04	8.0
2H-3, 82-83	12.93	5.21	43.40	6.41	0.99	0.09	10.9	16H-2, 80-81	144.41	3.63	30.24	3.82	0.19	0.04	5.1
2H-4, 80-81	14.41	3.44	28.66	4.73	1.17	0.11	10.3	16H-3, 73-74	145.84	4.53	37.73	4.79	0.26	0.04	6.9
2H-5, 56-57	15.67	2.93	24.41	4.34	1.39	0.14	10.3	16H-4, 80-81	147.41	3.96	32.99	4.30	0.34	0.04	9.0
2H-6, 80-81	17.41	5.49	45.73	6.84	1.24	0.10	12.2	16H-5, 77-78	148.88	5.50	45.81	5.78	0.28	0.03	9.9
2H-7, 60-61	18.71	3.45	28.74	4.69	1.17	0.11	10.4	16H-6, 80-81	150.41	3.99	33.24	4.21	0.22	0.04	5.9
3H-1, 57-58	19.18	3.53	29.40	4.84	1.25	0.12	10.0	16H-7, 47-48	151.58	4.77	39.73	5.03	0.26	0.03	9.0
3H-2, 79-80	20.90	4.69	39.07	5.72	0.94	0.10	9.3	17H-1, 66-67	152.27	4.55	37.90	4.80	0.25	0.04	6.6
3H-3, 50-51	22.11	4.02	33.49	5.00	0.96	0.09	10.6	17H-3, 64-65	155.25	3.02	25.15	3.37	0.35	0.03	12.3
3H-4, 79-80	23.90	4.32	35.99	5.36	0.99	0.11	8.7	17H-5, 70-71	158.31	1.22	10.16	1.46	0.24	0.05	5.1
3H-5, 30-31	24.91	4.69	39.07	5.34	0.71	0.08	9.0	18H-1, 51-52	161.62	2.21	18.41	2.50	0.29	0.05	6.1
3H-6, 78-79	26.89	4.57	38.07	5.52	0.95	0.10	9.3	18H-3, 53-54	164.64	2.13	17.74	2.28	0.15	0.04	4.0
3H-7, 52-53	28.13	4.83	40.23	5.50	0.69	0.09	7.6	18H-5, 109-110	168.20	3.64	30.32	3.84	0.20	0.15	1.3
4H-1, 80-81	28.91	4.79	39.90	5.28	0.54	0.07	8.0	19H-1, 116-117	172.07	2.77	23.07	2.87	0.10	0.05	2.1
4H-1, 116-117	29.27	5.41	45.07					19H-3, 8-9	173.99	0.07	0.58	0.23	0.16	0.04	4.1
4H-2, 80-81	30.41	5.37	44.73	6.53	0.88	0.09	9.7	19H-4, 130-131	176.71	3.10	25.82				
4H-3, 81-82	31.92	5.71	47.56	6.15	0.44	0.06	7.7	20X-2, 23-24	181.84	6.03	50.23	6.27	0.24		
4H-4, 80-81	33.41	5.19	43.23	5.90	0.66	0.07	9.7	20X-3, 105-106	184.16	5.34	44.48	5.52	0.18		
4H-5, 95-96	35.06	4.63	38.57	5.62	0.79	0.09	8.8	20X-5, 113-114	187.24	5.53	46.06	5.54	0.01	0.04	0.2
4H-6, 82-83	36.43	3.50	29.16	4.30	0.80	0.10	7.9	21X-1, 126-127	190.37	3.52	29.32	3.64	0.12	0.04	3.0
4H-7, 60-61	37.71	4.60	38.32	5.37	0.76	0.09	8.4	21X-2, 80-81	191.41	4.19	34.90	4.52	0.33		
5H-1, 77-78	38.38	3.80	31.65	4.55	0.75	0.09	8.3	21X-3, 87-88	192.98	4.85	40.40	5.09	0.24	0.04	6.0
5H-2, 80-81	39.91	4.59	38.23	5.53	0.76	0.09	8.4	21X-4, 86-87	194.47	4.15	34.57	4.33	0.18		
5H-3, 76-77	41.37	5.15	42.90	5.96	0.74	0.08	9.4	21X-5, 96-97	196.07	5.03	41.90	5.28	0.25	0.05	5.0
5H-4, 80-81	42.91	4.37	36.40	4.93	0.55	0.08	7.0	21X-6, 72-73	197.33	3.02	25.16	3.30	0.28		
5H-5, 80-81	44.41	5.65	47.06	6.33	0.58	0.07	8.6	21X-7, 30-31	198.41	3.07	25.57	3.34	0.27		
5H-6, 80-81	45.91	6.15	51.23	7.12	0.76	0.08	9.6	22X-1, 125-126	199.86	5.36	44.65	5.51	0.15	0.04	3.7
5H-7, 70-71	47.31	4.96	41.32	5.91	0.95	0.09	10.5	22X-2, 78-79	200.89	4.82	40.15				
6H-1, 76-77	47.87	5.85	48.73	6.43	0.55	0.07	8.1	22X-3, 73-74	202.34	7.00	58.31	7.14	0.14	0.04	3.5
6H-2, 80-81	49.41	5.91	49.23	6.53	0.62	0.07	8.8	22X-4, 72-73	203.83	2.97	24.74				
6H-3, 72-73	50.83	5.42	45.15	6.13	0.71	0.07	10.1	22X-5, 55-56	205.16	4.50	37.49	4.73	0.23	0.04	5.8
6H-4, 80-81	52.41	5.98	49.81	6.59	0.61	0.06	10.2	22X-6, 81-82	206.92	3.35	27.91				
6H-5, 73-74	53.84	6.10	50.81	6.82	0.72	0.07	10.3	23X-1, 59-60	208.20	3.08	25.66	3.27	0.19	0.04	4.8
6H-6, 80-81	55.41	5.56	46.31	6.21	0.65	0.06	10.9	23X-3, 70-71	211.31	3.75	31.24				
6H-7, 62-63	56.73	5.66	47.15	6.30	0.64	0.07	9.2	23X-5, 117-118	214.78	2.05	17.08	2.11	0.06	0.05	1.2
7H-1, 89-90	57.50	5.45	45.40	6.12	0.67	0.07	9.6	24X-1, 67-68	217.28	3.47	28.91				
7H-2, 80-81	58.91	5.81	48.40	6.38	0.57			24X-3, 29-30	219.90	5.49	45.73	5.77	0.28	0.04	7.7
7H-3, 89-90	60.50	4.83	40.23	5.33	0.50	0.06	8.4	25X-1, 110-111	226.91	4.52	37.65	4.70	0.18		
7H-4, 80-81	61.91	5.25	43.73	5.75	0.50	0.06	8.4	25X-2, 80-81	228.11	5.30	44.15	5.40	0.10	0.04	2.9
7H-5, 119-120	63.80	5.98	49.81	6.51	0.53	0.06	8.8	25X-3, 102-103	229.83	4.46	37.15	4.61	0.15		
7H-6, 80-81	64.91	5.49	45.73	5.90	0.41	0.00		25X-4, 71-72	231.02	4.74	39.48	4.92	0.18	0.04	5.0
7H-7, 40-41	66.01	5.47	45.57	5.93	0.46	0.05	9.1	25X-5, 87-89	232.68	4.03	33.57	4.18	0.15		
7H-CC, 20-21		4.67	38.90	5.25	0.58			25X-6, 75-77	234.06	3.46	28.82	3.69	0.23	0.05	5.0
8H-1, 80-81	66.91	6.65	55.39	7.03	0.38	0.05	7.6	26X-1, 62-63	236.13	4.76	39.65				
8H-2, 80-81	68.41	6.45	53.73	7.03	0.58	0.06	9.6	26X-7, 30-31	244.81	3.82	31.82	5.20	1.38	5.93	0.2
8H-3, 90-91	70.01	6.04	50.31	6.55	0.51			27X-2, 85-86	247.46	4.94	41.15	5.04	0.10	0.04	2.8
8H-4, 80-81	71.41	5.64	46.98	6.26	0.62	0.06	10.4	27X-3, 10-11	248.21	3.00	24.99	4.45	1.45	0.13	11.5
8H-5, 95-96	73.06	5.82	48.48	6.42	0.60	0.05	11.9	27X-3, 80-81	248.91	4.84	40.32	5.02	0.18	0.05	4.0
8H-6, 80-81	74.41	4.38	36.49	5.12	0.74	0.07	10.6	27X-5, 137-138	252.48	2.39	19.91	3.04	0.65	0.07	9.0
8H-7, 60-61	75.71	5.60	46.65	6.16	0.56	0.06	9.3	28X-1, 96-97	255.77	3.84	31.99	4.00	0.16	0.05	3.5
9H-1, 106-107	76.67	5.50	45.81	5.74	0.24	0.05	4.9	28X-2, 73-74	257.04	0.24	2.00	1.86	1.62	0.14	11.2
9H-2, 80-81	77.91	5.11	42.57	5.46	0.35	0.04	8.7	28X-3, 83-84	258.64	1.35	11.25	1.69	0.34	0.05	6.2
9H-3, 105-106	79.66	4.41	36.74	4.89	0.48			28X-6, 53-54	262.84	1.95	16.24	3.34	1.39	0.13	11.1
9H-4, 81-82	80.92	4.62	38.48	5.24	0.62			29X-2, 54-55	266.45	2.96	24.66	3.29	0.33	0.05	6.2
9H-5, 96-97	82.57	4.14	34.49	4.65	0.51			29X-3, 145-146	268.86	0.67	5.58	1.23	0.56	0.07	7.8
9H-6, 80-81	83.91	5.90	49.15	6.24	0.34			30X-1, 124-126	275.25	0.44	3.67	2.59	2.15	0.16	13.2
10H-1, 72-73	85.83	5.85	48.73	6.19	0.34			30X-3, 11-13	277.12	4.79	39.90	4.96	0.17		
10H-3, 82-83	88.93	6.12	50.98	6.51	0.39			30X-4, 42-44	278.93	2.40	19.99	2.80	0.40	0.06	6.3
10H-5, 68-69	91.79	5.37	44.73	5.72	0.35			30X-5, 140-143	281.42	0.37	3.08	1.28	0.91	0.09	10.1
11H-1, 80-81	95.41	5.92	49.31	6.22	0.30			31X-1, 15-16	283.86	0.08	0.67	4.31	4.23	0.31	13.8
11H-2, 83-84	96.94	6.32	52.65	6.75	0.43			31X-2, 82-83	286.03	2.68	22.32	3.03	0.35	0.09	3.9
11H-3, 66-67	98.27	6.77	56.39	7.18	0.41			31X-3, 12-13	286.83	2.43	20.24	3.11	0.68	0.08	8.4
11H-4, 84-85	99.95	6.01	50.06	6.50	0.49			31X-4, 90-91	289.11	2.66	22.16	2.95	0.29	0.05	6.4
11H-5, 44-55	101.10	5.21	43.40	5.52	0.31			31X-5, 79-80	290.50	0.12	1.00	2.37	2.25	0.18	12.5
11H-6, 84-85	102.95	5.95	49.56	6.32	0.37			31X-6, 70-72	291.91	0.42	3.50	1.08	0.66	0.08	8.2
13H-1, 116-117	114.77	4.80	39.98	5.15	0.35	0.05	7.0	32X-1, 48-49	293.79	0.05	0.42	2.30	2.25	0.18	12.5
13H-2, 80-81	115.91	6.65	55.39	7.07	0.42	0.05	8.4	32X-2, 79-80	295.60	0.04	0.33				

Table 8 (continued).

Core, section, interval (cm)	Depth (mbsf)	Inorg-C (wt%)	CaCO ₃ (wt%)	Tot-C (wt%)	Org-C (wt%)	TN (wt%)	C/N	Core, section, interval (cm)	Depth (mbsf)	Inorg-C (wt%)	CaCO ₃ (wt%)	Tot-C (wt%)	Org-C (wt%)	TN (wt%)	C/N
35X-5, 22-23	328.43	1.53	12.74	1.99	0.46	0.06	7.6	11R-1, 59-60	504.40	0.11	0.9	1.72	1.61	0.13	12.4
36X-1, 23-24	332.04	0.30	2.50	0.82	0.52	0.07	7.0	12R-1, 31-33	513.92	0.08	0.7	1.96	1.88	0.14	13.4
36X-2, 59-60	333.90	2.20	18.33	2.86	0.66	0.07	9.3	12R-2, 107-108	516.18	0.06	0.5	1.47	1.41	0.11	12.8
36X-3, 26-27	335.07	0.96	8.00	1.94	0.98	0.09	10.4	13R-1, 48-50	523.69	0.04	0.3	1.89	1.85	0.12	15.4
36X-4, 66-67	336.97	0.79	6.58	1.66	0.87	0.09	10.2	13R-1, 65-66	523.86	0.05	0.4	2.98	2.93	0.19	15.4
36X-6, 145-146	340.76	2.93	24.41	3.59	0.66	0.07	9.4	13R-3, 90-91	527.11	0.06	0.5	1.44	1.38	0.10	13.8
36X-7, 40-41	341.21	3.32	27.66	4.47	1.15	0.09	12.4	14R-1, 102-103	533.83	0.03	0.2	2.61	2.58	0.18	14.3
37X-1, 29-31	341.80	3.59	29.90	4.01	0.42	0.06	7.2	16R-1, 34-35	552.45	0.09	0.7	2.95	2.86	0.19	15.1
37X-2, 79-80	343.80	0.21	1.75	0.95	0.74	0.07	10.6	17R-1, 80-81	562.61	0.31	2.6	1.03	0.72	0.07	10.3
37X-3, 44-45	344.95	1.14	9.50	1.98	0.84	0.08	10.0	17R-1, 119-121	563.00	2.20	18.3	5.79	3.59	0.23	15.6
37X-4, 79-80	346.80	3.17	26.41	3.87	0.70	0.06	12.1	17R-3, 57-58	565.38	1.65	13.7	2.15	0.50	0.05	10.0
37X-5, 40-42	347.91	5.60	46.65	6.19	0.59	0.04	13.8	18R-3, 109-110	575.50	3.30	27.5	4.31	1.01	0.08	12.6
37X-6, 77-78	349.78	1.73	14.41	2.51	0.78	0.11	7.3	18R-5, 10-11	577.51	0.07	0.6	4.79	4.72	0.34	13.9
37X-7, 39-40	350.90	1.69	14.08	2.61	0.92	0.10	9.6	21R-1, 65-66	600.86	0.41	3.4	1.35	0.95	0.08	11.8
38X-1, 94-95	352.15	0.68	5.66	1.81	1.13	0.11	10.3	21R-3, 33-34	603.54	0.31	2.6	1.78	1.49	0.11	13.4
38X-4, 74-75	356.45	0.76	6.33	1.93	1.17	0.11	10.3	21R-5, 77-78	606.98	1.11	9.2	2.24	1.15	0.09	12.6
38X-5, 119-120	358.40	4.37	36.40	4.75	0.38	0.06	6.8	23R-3, 48-50	622.79	1.83	15.2	2.67	0.87	0.07	12.0
39X-2, 60-61	362.91	0.63	5.25	2.97	2.34	0.18	13.3	23R-5, 12-14	625.43	1.23	10.2	1.81	0.60	0.06	9.7
39X-3, 52-54	364.33	0.72	6.00	3.86	3.14	0.23	13.9	27R-2, 21-22	659.72	1.30	10.8	2.13	0.83	0.07	11.9
39X-3, 109-110	364.90	1.33	11.08	1.93	0.60	0.10	5.9	27R-4, 28-29	662.79	2.81	23.4	3.30	0.49	0.05	9.8
39X-5, 33-34	367.14	0.27	2.25	1.48	1.21	0.17	7.0	27R-6, 10-13	665.62	1.57	13.1	2.70	1.13	0.09	12.6
41X-1, 82-83	381.03	1.85	15.41	2.62	0.77	0.08	9.6	28R-1, 33-35	667.94	2.01	16.7	3.08	1.07	0.08	13.4
41X-2, 80-81	382.51	3.47	28.91	3.92	0.45	0.05	8.2	28R-3, 6-8	670.67	2.41	20.1	2.93	0.52	0.05	10.4
41X-3, 80-81	384.01	0.31	2.58	2.14	1.83	0.20	9.2	28R-5, 96-98	674.57	3.50	29.2	4.16	0.66	0.06	11.0
41X-4, 81-82	385.52	0.41	3.42	1.37	0.96	0.13	7.2	29R-1, 60-61	677.81	2.16	18.0	2.66	0.50	0.05	10.0
41X-5, 76-77	386.97	2.07	17.24	2.52	0.45	0.06	7.6	29R-3, 27-28	680.48	1.13	9.4	2.01	0.88	0.07	12.6
41X-6, 77-78	388.48	0.92	7.66	1.76	0.84	0.13	6.4	29R-5, 33-34	683.54	2.72	22.7	3.29	0.57	0.05	11.4
41X-7, 40-41	389.61	0.09	0.75	0.95	0.86	0.09	9.7	30R-1, 56-57	687.47	2.11	17.6	3.14	1.03	0.08	12.9
42X-1, 18-19	389.99	0.07	0.58	1.00	0.93	0.14	6.6	30R-3, 74-75	690.65	2.01	16.7	3.05	1.07	0.08	13.0
42X-2, 79-80	392.10	3.26	27.16	4.01	0.75	0.12	6.4	31R-5, 16-17	693.07	2.73	22.7	3.79	1.10	0.08	13.3
42X-3, 68-69	393.49	0.19	1.58	1.42	1.23	0.11	11.0	34R-4, 100-101	731.01	0.62	5.2	1.57	0.97	0.08	11.9
42X-4, 77-78	395.08	0.15	1.25	1.09	0.94	0.09	10.6	37R-3, 53-54	758.04	1.16	9.7				
42X-5, 37-38	396.18	4.20	34.99	5.24	1.04	0.10	10.9	42R-2, 0-5	804.13	0.06	0.5	0.12	0.06	0.02	2.4
42X-6, 78-79	398.09	3.23	26.91	4.53	1.30	0.10	13.1	44R-2, 129-131	824.70	3.77	31.4	3.83	0.10	0.02	3.0
43X-1, 33-34	399.54	1.70	14.16	2.45	0.75	0.08	9.0	47R-1, 0-5	850.93	0.09	0.7	1.65	1.56	0.03	48.4
43X-3, 48-49	402.69	0.25	2.08	1.02	0.77	0.09	8.8	48R-1, 13-14	860.74	0.31	2.6	1.11	0.81	0.04	20.0
43X-5, 31-32	405.52	0.78	6.50	1.65	0.87	0.09	9.7	48R-5, 49-50	867.10	0.08	0.7	0.41	0.33	0.03	11.0
44X-1, 92-93	409.43	0.05	0.42	0.93	0.88	0.09	10.3	49R-1, 84-86	871.05	0.07	0.6	0.26	0.19	0.03	6.3
44X-3, 48-49	411.99	0.04	0.33	2.07	2.03	0.15	13.6	49R-3, 0-5	873.23	0.07	0.6	0.75	0.68	0.04	15.8
44X-5, 58-59	415.09	0.04	0.33	2.80	2.76	0.20	13.9	49R-5, 40-41	876.61	0.70	5.8	2.00	1.32	0.04	32.5
45X-3, 118-119	422.29	0.46	3.83	2.31	1.85	0.14	12.9	53R-CC, 0-5		0.05	0.4	1.40	1.35	0.04	30.3
45X-5, 83-84	424.94	0.47	3.92	2.72	2.25	0.16	13.7	56R-1, 118-119	938.59	0.04	0.3	1.68	1.66	0.07	23.4
46X-1, 84-85	428.55	0.03	0.25	2.66	2.63	0.18	14.6	57R-3, 51-52	940.92	0.04	0.3	1.34	1.31	0.05	26.0
46X-2, 87-88	430.08	0.04	0.33	2.14	2.10	0.16	13.4	56R-4, 125-126	943.16	0.03	0.2	3.09	3.09	0.13	23.5
46X-3, 138-139	432.09	0.04	0.33	2.29	2.25	0.16	13.8	57R-5, 40-41	953.51	0.04	0.3	1.50	1.48	0.07	20.9
46X-4, 79-80	433.00	0.04	0.33	4.22	4.18	0.27	15.5	58R-4, 57-58	961.88	0.04	0.3	1.04	1.01	0.05	20.0
46X-5, 41-42	434.12	0.04	0.33	3.18	3.14	0.21	14.9	60R-3, 0-5	979.13	0.04	0.3	0.70	0.66	0.05	14.3
46X-6, 80-81	436.01	0.04	0.33	3.24	3.20	0.22	14.8	61R-2, 0-5	987.33	0.12	1.0	0.70	0.58	0.03	16.6
47X-1, 75-76	438.16	0.04	0.33	4.19	4.15	0.26	15.8	64R-1, 107-108	1015.78	0.16	1.3	2.71	2.58	0.11	23.2
47X-2, 88-89	439.79	0.04	0.33	4.23	4.19	0.26	16.3	64R-3, 120-121	1018.91	0.05	0.4	2.18	2.15	0.09	23.7
49X-CC, 30-31		0.03	0.25	4.90	4.87	0.29	17.1	65R-3, 63-64	1027.74	0.67	5.6	7.86	5.45	0.21	27.3
50X-CC, 24-25		0.04	0.33	2.45	2.41	0.13	18.3	67R-1, 39-41	1043.70	9.91	82.6				
51X-CC, 23-24		0.04	0.33	4.26	4.22	0.24	17.8	68R-1, 0-5	1053.03	8.71	72.6	9.11	0.40	0.03	11.9
159-959D-								69R-1, 0-5	1062.73	6.99	58.2				
1R-1, 75-76	418.56	0.17	1.4	1.73	1.56	0.15	10.4	71R-1, 0-5	1081.73	9.20	76.6	9.31	0.21	0.03	7.2
1R-3, 77-79	421.58	1.18	9.8	3.43	2.25	0.18	12.5	72R-2, 0-5	1092.73	0.28	2.3	1.42	1.14	0.23	5.0
1R-5, 62-63	424.43	0.09	0.7	2.37	2.28	0.19	12.0	73R-2, 0-5	1102.33	0.40	3.3	3.03	2.63	0.12	21.8
2R-1, 21-22	427.52	0.11	0.9	3.99	3.88	0.27	14.4	74R-2, 0-5	1112.03	0.21	1.7	1.98	1.77	0.03	52.7
3R-CC, 2-3		0.07	0.6	2.58	2.51	0.18	13.9	75R-1, 0-5	1120.23	0.16	1.3	2.89	2.73	0.16	17.3
4R-1, 30-31	446.71	0.08	0.7	3.58	3.50	0.23	15.2	78R-3, 0-5	1152.23	0.33	2.7	2.96	2.63	0.21	12.6
5R-CC, 2-3		2.91	24.2	3.66	0.75	0.09	8.3								
7R-CC, 7-8		0.10	0.8	2.59	2.49	0.19	13.1								
9R-5, 116-117	491.77	0.27	2.2	2.43	2.16	0.17	12.7								
10R-3, 11-12	497.32	0.16	1.3	2.98	2.82	0.19	14.8								

Note: Inorg-C = inorganic carbon, CaCO₃ = carbonate, Tot-C = total carbon, Org-C = total organic carbon, TN = total nitrogen, and C/N = organic carbon/total nitrogen ratios.

and Hedges, 1988). However, when using C/N ratios of TOC-poor deposits, inorganic nitrogen fixed as ammonium to clay minerals has to be considered, because it may constitute a substantial proportion of the total nitrogen content (Müller, 1977). Data obtained by Rock-Eval pyrolysis provide further information on the origin and stage of thermal maturity of organic matter in marine sediments (Espitalié et al., 1977; Tissot and Welte, 1984). Increased hydrogen indices (HI, in milligrams hydrocarbon per gram organic carbon) above 200 indicate higher proportions of marine organic matter. In immature sediments, organic matter dominated by marine compounds produces HI values of 200 to 400, whereas values below 100 suggest increased proportions of terrestrial organic matter (e.g., Stein, 1991). Very low values below 50, however, indicate dominantly oxidized organic matter either of marine or terrestrial source. The second parameter obtained by Rock-Eval pyrolysis, T_{max}, provides information on the thermal maturity of the organic matter. Values below 410°–420°C indicate immature organic matter corresponding to lower brown coal

stage (vitrinite reflectance 0.3–0.5 %Rm), whereas T_{max} values between 420° and 500°C mark thermally mature to overmature organic matter (1.6–1.8 %Rm, bituminous hard coal stage; Tissot and Welte, 1984). Limitations of Rock-Eval pyrolysis due to mineral matrix adsorption of organic matter have to be considered when applied to TOC-lean samples (Katz, 1983; Peters, 1986).

C/N ratios vary between 4 and 12 in TOC-rich samples of interval A (0–45 mbsf), indicating a mixture of marine and terrestrial organic matter (Fig. 49). Slightly higher proportions of terrestrial organic matter, however, are interpreted from consistently elevated C/N values above 10 between 9 and 19 mbsf, which correlate with peak TOC contents during the Pleistocene. This is also suggested by low HI values between 30 and 70 mgHC/gTOC throughout this interval (Fig. 52). Some contribution of inert organic matter might explain the very low HI values below 50 mgHC/gTOC, especially in TOC-rich samples. T_{max} values, however, remain below 410°C, indicating immature organic matter to be the major source. Plant debris detected in

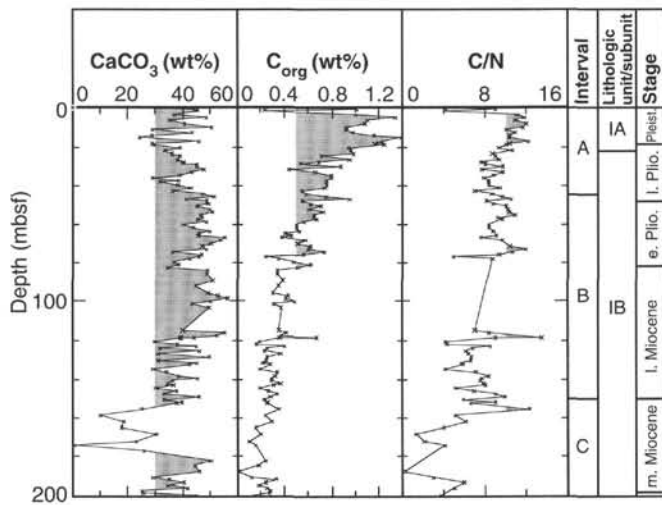


Figure 49. Carbonate content, total organic carbon content, and C/N ratios in sediments between 0 and 200 mbsf at Site 959. Intervals distinguished on the basis of carbonate and organic carbon records, lithologic units (see "Lithostratigraphy" section, this chapter), and preliminary stratigraphic stages are indicated.

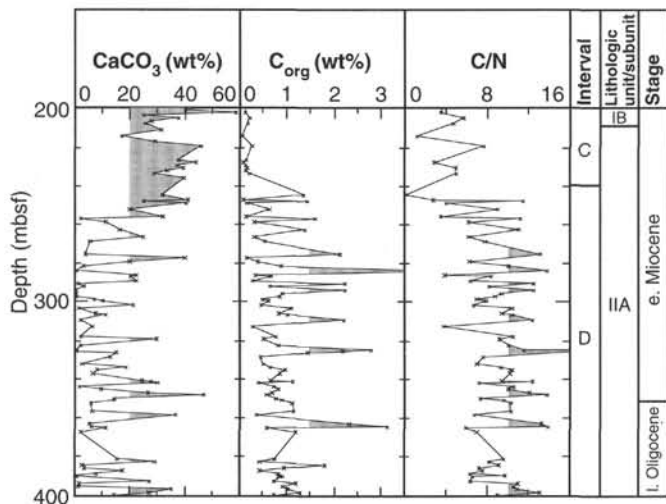


Figure 50. Carbonate content, total organic carbon content, and C/N ratios in sediments between 200 and 400 mbsf at Site 959. Intervals distinguished on the basis of carbonate and organic carbon records, lithologic units (see "Lithostratigraphy" section, this chapter), and preliminary stratigraphic stages are indicated.

smear slides ranges from traces to 5 vol%, thus supporting these geochemical results. Amorphous organic matter (AOM), probably derived from marine organic matter, was not encountered (see "Lithostratigraphy" section, this chapter). Preliminary organic geochemical and sedimentological results do not imply large amplitude fluctuations in productivity during late Quaternary glacial-interglacial cycles at Site 959.

Decreasing TOC contents down to baseline values of 0.2 wt% in interval B (45–155 mbsf) have no major effect on C/N ratios, which display a variable but discernible downcore decrease (4–14; Fig. 49). Interpreting the lower C/N ratios as evidence of higher proportions of marine organic matter below 120 mbsf does not seem reasonable considering analytical limitations for TOC-lean samples (see discussion above) and results of Rock-Eval analysis. HI values below 40 mgHC/g

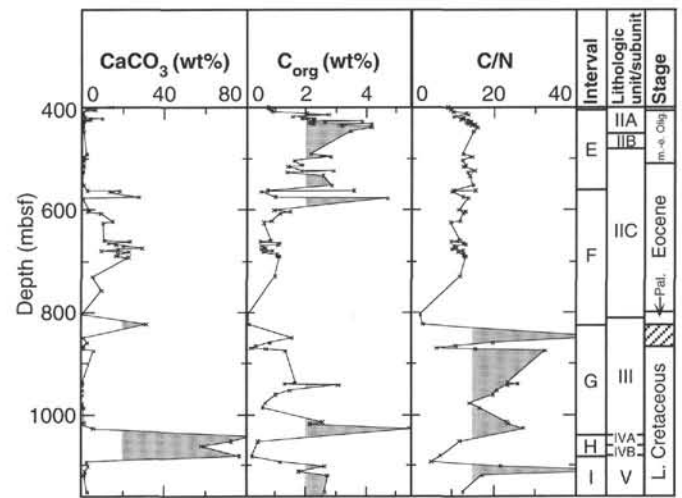


Figure 51. Carbonate content, total organic carbon content, and C/N ratios in sediments between 400 and 1160 mbsf at Site 959. Intervals distinguished on the basis of carbonate and organic carbon records, lithologic units (see "Lithostratigraphy" section, this chapter), and preliminary stratigraphic stages are indicated. Hatched area marks sediment section barren of microfossils or foraminifers.

gTOC suggest a relative enrichment of hydrogen-poor, inert, organic matter with depth because of selective diagenetic degradation of labile organic substances. T_{max} values below 410°C persist through interval B, similar to interval A (Fig. 52).

Ongoing oxidation of organic matter finally leads to minimum organic and nitrogen contents between 155 and 240 mbsf (interval C; Figs. 49, 50). Due to extremely low TOC values, C/N ratios are not interpreted as source indicators.

Changes in organic matter composition in intervals D and E (240–560 mbsf) are recorded by large amplitude variations in C/N and HI records (Figs. 50, 52). The organic character of TOC-rich diatomites and porcellanites probably is dominated by elevated proportions of marine organic matter, demonstrated by high HI values ranging from 140 mgHC/gTOC in the upper part of the interval to 370 mgHC/gTOC in deeper parts of the section. Maximum HI values of 575 mgHC/gTOC were measured in a diatomite at 275 mbsf (Section 159-959A-30X-1). However, porcellanites in general show higher HI values than diatomites (Fig. 52). Pyrolysis data are supported by results from smear slide analysis, which show distinctly elevated abundances of AOM up to 25 vol% in diatomites and porcellanites (see "Lithostratigraphy" section, this chapter). In contrast, a coincident pronounced increase in C/N ratios averaging 11–16 indicates a substantial supply of terrestrial organic matter. Input of allochthonous material during periods of diatomite deposition probably caused higher nutrient supply, which might have triggered enhanced primary production. Thermal maturity of organic matter in diatomites and porcellanites is at an immature to low maturity level, as documented by T_{max} values between 395° and 420°C. Interbedded organic-poor nannofossil chinks have C/N ratios and low HI values similar to the immature stage as discussed above.

Minor changes in the organic character are recorded in interval F (560–825 mbsf). Elevated TOC contents of about 1 wt% and high HI values between 255 and 325 mgHC/gTOC are correlated to C/N ratios between 10 and 15 (Figs. 51, 52). Amorphous organic matter (AOM) remains at low levels below 5 vol%, except for one pronounced spike at 610 mbsf (see results from smear-slide analysis, this volume) suggesting reduced proportions of marine organic matter compared to the upper units.

Table 9. Summary of total organic carbon (Org-C), obtained from elemental analysis, and of T_{max} , S_1 , S_2 , S_3 , hydrogen index (HI) values, and oxygen index (OI) values derived from Rock-Eval pyrolysis in sediments at Site 959.

Core, section, interval (cm)	Org-C (wt%)	T_{max} (°C)	S_1 (mgHC/gRock)	S_2 (mgHC/gRock)	S_3 (mgHC/gRock)	HI (mgHC/gTOC)	OI (mgHC/gTOC)
159-959A-							
1H-1, 79-80	1.01	397	0.09	0.68	5.90	67	582
1H-2, 14-15	0.23	373	0.04	0.08	3.45	33	1469
1H-3, 93-94	1.00	387	0.06	0.29	4.40	29	439
1H-4, 77-78	1.34	406	0.14	0.96	5.32	72	397
1H-5, 74-75	1.11	389	0.11	0.46	5.53	42	500
1H-6, 77-78	1.08	394	0.08	0.51	4.71	47	435
2H-1, 113-114	0.93	390	0.05	0.31	4.45	33	480
2H-2, 80-81	0.92	391	0.08	0.41	4.57	45	499
2H-3, 82-83	0.99	389	0.06	0.39	4.50	39	456
2H-4, 80-81	1.17	392	0.07	0.47	4.79	40	411
2H-5, 56-57	1.39	396	0.13	0.84	5.02	60	361
2H-6, 80-81	1.24	400	0.08	0.73	4.10	59	331
2H-7, 60-61	1.17	389	0.13	0.69	4.89	59	418
3H-1, 57-58	1.25	401	0.07	0.70	4.01	56	321
3H-2, 79-80	0.94	394	0.06	0.55	4.21	58	446
3H-3, 50-51	0.96	393	0.05	0.41	4.01	43	416
3H-4, 79-80	0.99	396	0.08	0.65	4.47	65	453
3H-6, 78-79	0.95	398	0.06	0.47	5.92	49	623
4H-2, 80-81	0.88	396	0.06	0.45	6.60	51	754
4H-5, 95-96	0.79	386	0.05	0.49	0.35	62	45
4H-6, 82-83	0.80	390	0.04	0.29	1.03	36	129
5H-1, 77-78	0.75	388	0.06	0.33	1.91	43	254
5H-2, 80-81	0.76	387	0.03	0.20	15.14	26	1992
5H-6, 80-81	0.76	387	0.04	0.20	5.53	26	731
5H-7, 70-71	0.95	385	0.06	0.31	6.91	32	726
6H-3, 72-73	0.71	381	0.04	0.20	0.99	28	139
6H-5, 73-74	0.72	386	0.04	0.24	6.24	33	862
6H-6, 80-81	0.65	383	0.05	0.16	1.32	24	202
7H-1, 89-90	0.67	406	0.05	0.27	1.45	40	217
8H-6, 80-81	0.74	385	0.04	0.27	1.50	37	203
13H-7, 30-31	0.40	380	0.03	0.09	1.20	23	297
16H-5, 77-78	0.28	378	0.02	0.07	2.08	24	739
26X-7, 30-31	1.38	404	0.06	0.65	2.08	47	151
28X-2, 73-74	1.62	420	0.12	2.15	1.14	133	70
28X-6, 53-54	1.39	409	0.11	1.62	13.40	117	962
30X-1, 124-126	2.15	418	1.01	12.15	7.43	566	346
31X-1, 15-16	4.23	404	0.04	0.25	0.90	6	21
31X-5, 79-80	2.25	419	0.16	4.10	4.45	182	197
32X-1, 48-49	2.25	409	0.14	3.01	0.08	134	4
32X-4, 80-81	0.50	401	0.05	0.29	3.71	57	737
33X-5, 34-35	2.23	412	0.16	0.50	2.35	22	105
35X-3, 84-85	1.46	412	0.08	1.94	0.38	133	26
35X-5, 22-23	0.46	415	0.12	2.24	0.31	167	23
36X-2, 59-60	0.66	404	0.06	0.52	1.80	79	272
39X-2, 60-61	2.34	419	0.15	4.36	1.71	187	73
39X-3, 52-54	3.14	415	0.19	6.40	0.72	204	23
39X-3, 109-110	0.60	407	0.27	7.76	7.61	264	259
44X-5, 58-59	2.76	419	0.10	8.88	0.41	322	15
46X-4, 79-80	4.18	409	0.31	12.46	9.51	298	227
47X-1, 75-76	4.15	413	0.32	13.39	5.00	323	120
47X-2, 88-89	4.19	413	0.35	13.94	0.42	333	10
159-959D-							
2R-1, 21-22	3.88	416	0.26	11.12	1.46	286	38
4R-1, 30-31	3.50	408	0.32	11.53	1.20	329	34
9R-5, 116-117	2.16	408	0.17	7.48	0.82	347	38
10R-3, 11-12	2.82	401	0.32	10.01	0.91	355	32
12R-1, 31-33	1.88	405	0.17	6.94	0.67	369	35
13R-1, 65-66	2.93	395	0.45	11.00	0.78	376	27
14R-1, 102-103	2.58	397	0.27	8.83	0.68	342	26
16R-1, 34-35	2.86	405	0.22	7.68	0.89	269	31
17R-1, 119-121	3.59	416	0.15	11.60	1.85	323	52
18R-5, 10-11	4.72	403	0.31	15.32	1.02	325	22
21R-3, 33-34	1.49	411	0.11	4.17	0.88	280	59
21R-5, 77-78	1.15	407	0.09	3.74	1.57	325	136
27R-6, 10-13	1.13	410	0.11	3.78	1.67	334	148
30R-3, 74-75	1.07	412	0.08	2.74	1.61	256	151
47R-1, 0-5	1.56	441	0.02	0.45	0.49	29	31
49R-3, 0-5	0.68	449	0.01	1.24	0.33	182	49
53R-CC, 0-5	1.35	411	0.02	1.69	0.20	125	15
60R-3, 0-5	0.66	408	0.03	1.55	0.09	236	13
61R-2, 0-5	0.58	405	0.04	1.19	0.05	206	9
64R-3, 120-121	2.15	414	0.10	5.46	0.37	254	17
65R-3, 63-64	5.45	420	0.16	19.06	1.24	350	23
68R-1, 0-5	0.40	417	0.01	1.50	0.25	375	63
71R-1, 0-5	0.21	411	0.02	0.70	0.32	330	150
72R-2, 0-5	1.14	419	0.09	0.80	0.00	70	0
73R-2, 0-5	2.63	465	0.07	1.43	1.27	54	48
74R-2, 0-5	1.77	483	0.00	0.21	0.93	12	53
75R-1, 0-5	2.73	470	0.08	0.95	0.49	35	18
78R-3, 0-5	2.63	385	0.02	0.25	0.84	10	32

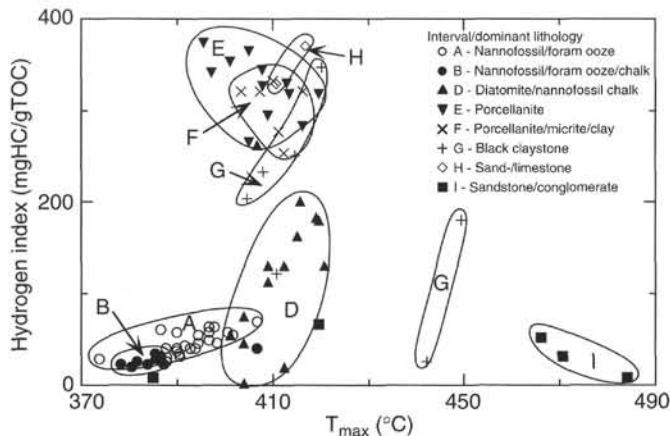


Figure 52. Hydrogen index values vs. T_{max} values of different sediment types at Site 959. Intervals distinguished on the basis of carbonate and organic carbon records, and corresponding dominant lithologies (see "Lithostratigraphy" section, this chapter). Hydrogen index values between 0 and 50 mgHC/gTOC suggest elevated proportions of inert organic matter, between 50 and 150 mgHC/gTOC dominant terrestrial with minor contents of marine organic matter, and above 200 mgHC/gTOC dominant marine organic matter. T_{max} values below 410°–420°C are characteristic of thermally immature organic matter, values between 420° and 460°C of mature organic matter, and values above 460°C of overmature organic matter.

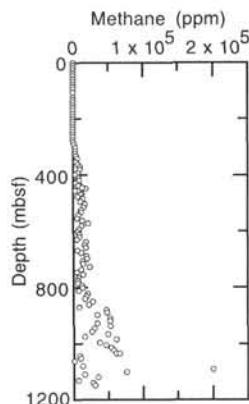


Figure 53. Variations in methane concentrations (in ppm) with depth for Hole 959D.

Black shales in interval G (825–1040 mbsf) provide distinct C/N, HI, and T_{max} records that reflect large amounts of mixed terrestrial and marine organic matter (Figs. 51, 52). C/N ratios are in the range of 5–50, with average values above 20, evidence of the presence of terrestrial organic matter. However, elevated HI values between 110 and 220 mgHC/gTOC and high amounts of AOM indicate significant proportions of marine organic matter. T_{max} values average around 410°C, documenting low thermal maturity of organic matter.

Sandstones and limestones between 1040 and 1085 mbsf (interval H) have intermediate to low TOC contents (below 0.4 wt%) and low C/N ratios (below 5; Fig. 51). Despite the low amount of organic matter, Rock-Eval pyrolysis results derived from one sample (Section 159-959D-68R-1) show high HI (200 mgHC/gTOC) and T_{max} (417°C) values demonstrating small amounts of hydrogen-rich organic matter of low thermal maturity in the sandstone facies (Fig. 52). These results may be related to the occurrence of AOM reported from smear slide analysis.

Below 1085 mbsf (interval I) sandstones are characterized by sharply increased TOC contents (up to 2.7 wt%). These unexpected

high values correlate with a drastic drop in HI to values below 60 mgHC/gTOC (Core 159-959D-72R and below) and a sudden increase in T_{max} up to 480°C (Core 159-959D-73R and below; Fig. 52). This dramatic change in organic parameters is also reflected by steeply increasing amounts of volatile hydrocarbons. Methane (C_1) to ethane (C_{2+}) ratios display a sudden drop from ratios above 120 to values between 75 and 26 below 1085 mbsf (Section 159-959D-72R-2 and below; for further discussion see "Source Rock Geochemistry" section below).

SOURCE ROCK GEOCHEMISTRY

At Site 959 real-time monitoring of volatile hydrocarbons, determination of inorganic carbon, totals of nitrogen, carbon, and sulfur, as well as Rock-Eval measurements were performed (for methods, see "Organic Geochemistry" section, "Explanatory Notes" chapter, this volume).

Volatile Hydrocarbons

As part of the shipboard safety and pollution monitoring program, volatile hydrocarbon concentrations were monitored routinely throughout the sediment column in Holes 959A–959D. Standard ODP headspace sampling techniques were used to measure methane, ethane, and heavier hydrocarbons. Potential hydrocarbon source rocks (organic-rich black shales) were given special attention, particularly in Hole 959D, where greatest depths of penetration were attained.

Figure 53 and Table 10 illustrate the concentration of methane in parts per million (ppm) starting at about 400 meters below seafloor (mbsf) in Hole 959D and continuing to total depth (1158.9 mbsf). Methane content remains consistently low until 880–1040 mbsf, where methane concentrations range from 30,000 to 70,000 ppm. This interval closely corresponds to the section where black shales were penetrated. Methane concentrations approaching 20% (182,467 ppm) were encountered at 1092.7 mbsf. This sample is considered anomalous in that subsequent measurements at greater depths yielded lower, more "normal" methane readings in what could be considered background concentrations.

Ethane (C_2) and heavier hydrocarbons up to and including hexane (C_6) were also recorded in Hole 959D. The plot of C_1/C_{2+} in the deeper part of Hole 959D is presented in Figure 54. The presence of these heavier hydrocarbon fractions suggests that elevated geothermal gradients were responsible for thermal maturation of the organic matter in the vicinity of this site at some time in the geologic past. Low present-day temperatures preclude current hydrocarbon generation.

INORGANIC GEOCHEMISTRY

Interstitial waters extracted from 33 whole-round samples from Site 959 were analyzed. Samples were taken from every core in the first 70 mbsf of Hole 959B to document early diagenetic changes associated with microbial degradation of labile organic matter. From 70 to 815 mbsf, one interstitial water sample was taken every third core in Holes 959A and 959D, provided recovery exceeded 20%. No interstitial water samples were taken below 815 mbsf (159-959D-43R-3, 135–150 cm), because the volume of pore fluid recovered from the overlying sediments had diminished to <2 mL/15 cm³ whole-round sample. The combined data from Holes 959A, 959B, and 959D are shown in Figures 55 through 57. The data do not show abrupt shifts in concentration at the boundaries between holes. Based on the smooth character of these composite profiles, we interpret them as a single coherent record of depth variations in interstitial water composition. The data from the interstitial water analyses are given in Table 11.

Table 10. Methane concentration, Holes 959A and 959D.

Hole	Depth (mbsf)	C ₁ /C ₂₊	Methane (ppm)	Hole	Depth (mbsf)	C ₁ /C ₂₊	Methane (ppm)
959A	0		44		533	1254	11287
	9		3		542	1372	8230
	19		3		552	1332	5326
	28		2		562	1306	13063
	38		3		571	693	21470
	47		3		581	1139	12526
	57		3		591	882	8819
	66		3		600	998	6985
	76		3		610	854	8541
	85		3		619	903	9029
	95		3		629	791	4746
	95		3		639	826	18162
	104		3		648	723	15911
	123		3		658	661	17836
	133		3		668	589	5891
	142		3		677	507	11159
	152		3		687	550	18715
	161		3		697	524	19396
	171		3		706	583	13413
	180		3		716	641	14103
	189		3		726	488	23435
	199		3		735	589	11789
	208		3		745	409	5311
	217		3		755	589	14141
	226		3		764	490	7834
	236		3		774	607	6679
	245		4		784	640	6400
	255		27		793	539	11864
	264		208		803	495	12869
	274		364		812	500	7501
	284		548		822	489	20546
	293		1144		832	391	18770
	303		3298		841	405	17424
	313		2790		851	337	27664
	322		2967		861	316	22781
	332		3752		870	243	8757
	342		5676		880	231	47883
	351		3716		889	271	48476
	361	3272	6543		899	203	34534
	371	20	9332		909	204	53124
	380		9217		918	180	53007
	390	2145	6434		928	177	34192
	399	241	3377		937	130	53384
	409	1862	7447		947	158	29313
	418	862	6031		957	158	26581
	428	787	7870		967	293	49306
	437	995	9953		976	242	15961
	447	1365	17742		986	261	61800
					995	165	37729
959D					1005	118	46318
	418	1100	8803		1015	186	54230
	428	1779	3558		1024	67	57148
	437	975	7803		1034	75	61346
	446	972	13603		1034	65	66049
	456	2772	2772		1043	32	8796
	465	2007	12044		1053	46	10433
	469	2103	10515		1063	103	1641
	475	1832	7327		1082	53	13351
	485	1986	13899		1091	67	200000
	494	2674	10694		1101	37	76293
	504	2165	17318		1111	85	16380
	514	2159	15114		1120	23	35684
	523	1857	11143		1130	47	7283
					1140	26	28230
					1149	26	30749

Note: C₁ = methane. C₂₊ = ethane and higher hydrocarbons.

Chloride concentrations are similar to seawater values throughout the Site 959 profile. A subtle increase in chloride concentration of approximately 1.5% over the 800-m interval is discernible in the data. This increase exceeds the analytical uncertainty of the chloride titration by a factor of approximately 2. The similarity of interstitial water chloride concentrations to ambient seawater chloride concentrations indicates that compositional variations within the pore fluids are governed by in situ diagenetic reactions rather than by mixing distinct fluids.

Microbially Mediated Organic Matter Degradation

Over the first 200 m of the sediment column, microbially mediated oxidation of sedimentary organic matter exerts the dominant con-

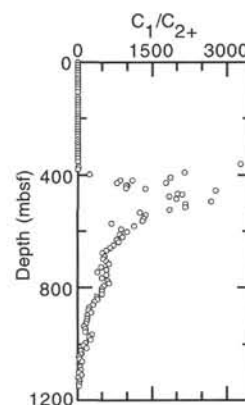


Figure 54. Variations in C₁/C₂₊ ratios with depth for Hole 959D. Samples plotted as C₁/C₂₊ = 0 correspond to samples in which C₁ and/or C₂₊ measurements were below detection limit.

trol on the composition of interstitial waters. As shallow as 30 mbsf, pore-fluid sulfate drops to concentrations 10% lower than ambient sea water, indicating ongoing sulfate reduction within the sediment pile (Fig. 55A). The onset of sulfate reduction above 30 mbsf requires that dissolved oxygen in the sediment has been quantitatively consumed by this depth and that iron and manganese are subject to reduction to their soluble divalent states. This latter point is evidenced by the maximum in dissolved Mn concentration near 10 mbsf (Fig. 56B) and a local maximum in dissolved Fe concentrations near 40 mbsf (Table 11). Interstitial water sulfate concentrations drop to zero between 250 and 300 mbsf. As expected, the zone of complete sulfate reduction coincides with the onset of microbially mediated methanogenesis, marked by an abrupt increase in head space methane concentrations (Fig. 55B). The gradual decrease in pore-water sulfate concentrations over the first 250 mbsf is suggestive of a broad sulfate reduction zone (pore-water) with diffusive resupply of sulfate from the overlying waters.

Active organic matter degradation is also evidenced by the rapid increase in interstitial water ammonium concentrations over the first 70 mbsf (Fig. 55D), with concentrations approaching 2000 μM. Below 100 mbsf, the rate of increase in pore-water ammonium decreases significantly, likely reflecting a diminished rate of organic matter degradation as the available pool of labile organic matter is consumed. Maximum ammonium concentrations (~4000 μM) occur near 500 mbsf. These high ammonium concentrations coincide with elevated organic carbon concentrations (see "Organic Geochemistry" section, this chapter), and higher organic carbon contents of squeeze cakes resulting from interstitial water extraction (Table 12). Below 600 mbsf, interstitial water ammonium concentrations begin to decrease with increasing depth. Such a reversal suggests that the rate of ammonium uptake, presumably by clay minerals, exceeds the rate of ammonium production by organic matter degradation at depth in the sediment.

Oxidation of buried organic carbon also plays an important role in regulating the carbonate chemistry of the pore fluids. A marked drop in the pH of pore water in the first 30 mbsf is consistent with the production of carbonic acid via oxic degradation of organic carbon. Below this depth, the stoichiometry of sulfate reduction requires that the rate of production of bicarbonate ions be twice the rate of sulfate reduction. At 100 mbsf, nearly 50% of the initially available sulfate has been consumed. However, total alkalinity remains low over this depth interval and begins to increase rapidly below 100 mbsf. One explanation for this decoupling of the sulfate and alkalinity profiles is carbonate precipitation in the shallow portions of the core. Additional evidence supporting this interpretation is given in the discussion of carbonate diagenesis below.

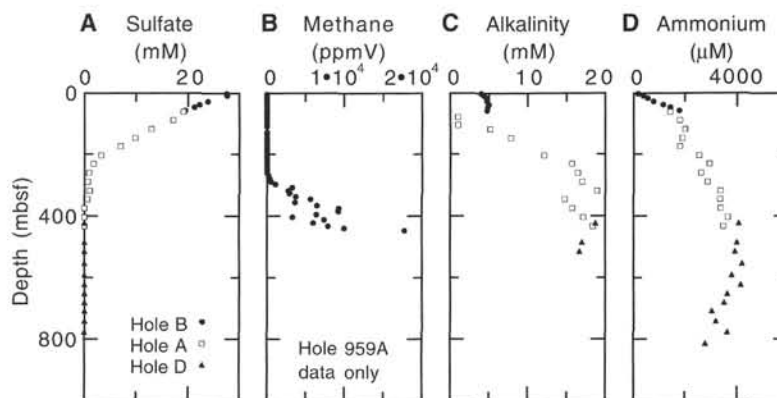


Figure 55. Interstitial water concentrations for (A) sulfate, (B) methane, (C) alkalinity, and (D) ammonium plotted vs. depth in the sediment at Site 959.

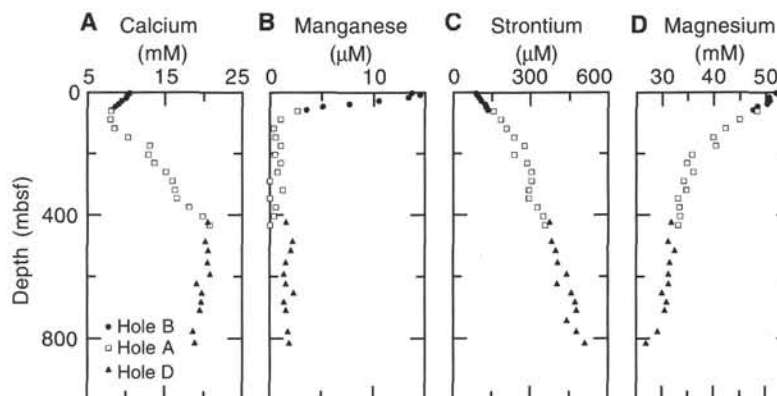


Figure 56. Interstitial water concentrations for (A) calcium, (B) manganese, (C) strontium, and (D) magnesium plotted vs. depth in the sediment at Site 959.

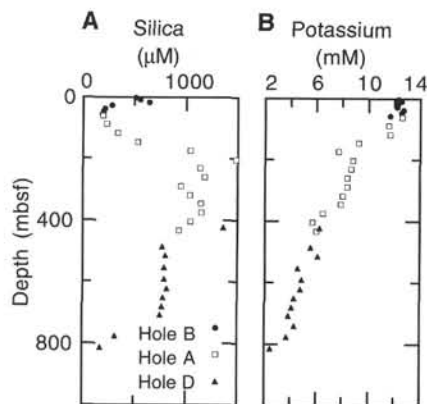


Figure 57. Interstitial water concentrations for (A) silica and (B) potassium plotted vs. depth in the sediment at Site 959.

Carbonate Diagenesis

Concentrations of dissolved calcium are depleted relative to present seawater values over the uppermost 150 mbsf of the section, corresponding to the Pleistocene to late Miocene portion of the sedimentary record, and are enriched relative to seawater below this level (Fig. 56A). The lowest measured calcium concentration (~8.01 mM) occurs at ~80 mbsf, just below the lithologic transition from nanno-

fossil foraminifer ooze to nannofossil foraminifer chalk (at ~75 mbsf, see "Lithostratigraphy" section, this chapter). Below this level, dissolved calcium concentrations increase downhole to nearly 21 mM at ~430 mbsf. This profile, together with the low alkalinity values above 100 mbsf (Fig. 55C), indicates a sink for dissolved calcium that is likely related to the precipitation of calcium carbonate in an active diagenetic front within the chalk (Sayles and Manheim, 1975). Dissolved manganese, which decreases exponentially from 10 mbsf to below background levels (1 μM) at 80 mbsf (Fig. 56B), may be precipitated in association with the carbonate (Hartmann, 1964; Hartmann et al., 1976). The increase in dissolved calcium concentrations from 200 to 430 mbsf within the chalk and interbedded diatomite and chalk units suggests dissolution of calcium carbonate. Below the chert units at ~430 mbsf, dissolved calcium concentrations are high but decrease gradually.

The gradual increase in interstitial water strontium concentration with depth is likely the result of dissolution-reprecipitation processes (i.e., recrystallization) in the calcium carbonate (Fig. 56C). Biogenic calcites have higher Sr concentrations than inorganically precipitated calcites. As biogenic calcite dissolves and reprecipitates during diagenetic alteration, the strontium concentration of pore water increases (Gieskes, 1981; Baker et al., 1982). At Site 959, the steepest gradient occurs in the upper 200 mbsf, where strontium concentrations increase by 50 μM , indicating a diffusive flux of dissolved strontium out of the sediment into the overlying water. Below this level, strontium concentrations are nearly invariant to ~350 mbsf, in the same interval that interstitial calcium concentrations appear to level. Below 350 mbsf, strontium concentrations increase gradually, probably reflecting continuing recrystallization of calcium carbonate

Table 11. Interstitial water analyses for Holes 959A, 959B, and 959D at Site 959.

Core, section, interval (cm)	Depth (mbsf)	IW vol (mL)	pH	Alkalinity (mM)	Salinity (g/kg)	Ca (mM)	Mg (mM)	Sr (μ M)	Cl (mM)	SO ₄ (mM)	NH ₄ (μ M)	SiO ₂ (μ M)	K (mM)	Mn (μ M)	Fe (mM)
159-959B-															
1H-2, 145-150	2.975	35	7.7	4.1	35.0	10.4	52.1	89	557	27.5	195	515	12.3	13.7	3.1
2H-3, 145-150	9.45	35	7.5	4.3	34.0	10.2	52.6	94	560	27.6	377	554	12.6	14.5	2.2
3H-3, 145-150	18.95	22	7.2	4.7	34.5	10.0	50.6	100	565		558	643	12.3	13.4	1.6
4H-3, 145-150	28.45	15	7.2	4.8		9.5	50.8	108	563	23.9	774	285	12.2	10.5	6.0
5H-3, 145-150	37.95	20	7.5	5.0	34.0	9.0	50.2	123	563	22.3	1154	213	12.7	7.7	28.4
6H-3, 145-150	47.45	32	7.5	4.9	34.0	8.6	48.4	128	558	21.3	1417	200	12.5	5.1	8.0
7H-3, 145-150	56.95	28	7.4	4.8	34.0	8.2	47.7	136	561	19.6	1767	187	11.6	3.6	7.0
159-959A-															
7H-3, 145-150	61.05	60	7.3	1.7	34.5	8.1	48.4	159	563	19.2	1422	194	12.6	2.7	33.5
10H-3, 145-150	89.55	45	7.4	1.7	34.0	8.0	45.0	185	566	17.2	1796	233	11.6	0.4	11.2
13H-3, 145-150	118.05	30	7.3	5.2	33.5	8.5	42.3	208	560	13.0	1989	340	11.6	0.6	9.0
16H-3, 140-150	146.50	42	7.1	7.8	33.5	10.2	40.0	238	562	9.9	1897	528	9.2	0.0	49.4
19H-3, 140-150	175.00	10			33.0	13.1	40.4	276	560	7.0	1806	1043	7.7	1.1	3.3
22X-3, 140-150	203.00	32	6.9	12.1	33.0	12.9	35.9	237	558	3.3	2544	1484	8.8	0.5	26.3
25X-3, 140-150	230.20	55	6.9	15.7	33.0	13.6	34.9	286	563	1.8	2939	1137	8.7	0.0	33.1
28X-3, 140-150	259.20	18	7.0	16.4	32.5	15.1	36.1	303	562	0.9	2625	1180	8.4	0.0	3.2
31X-3, 140-150	288.10	32	7.7	17.0	33.5	16.0	34.2	305	560	0.7	2878	953	8.4	0.0	7.2
34X-4, 140-150	317.00	54	7.5	18.9	34.0	16.3	34.8	295	563	1.0	3364	1038	8.0	0.0	14.4
37X-3, 140-150	345.90	32	7.1	14.8	33.0	16.6	33.1	293	557	0.7	3374	1145	7.9	0.0	68.7
40X-3, 140-150	374.90	41	6.8	15.8	33.0	18.1	33.4	327	564	0.0	3380	1152	6.5		
43X-3, 140-150	403.60	28	6.7	17.2	33.5	19.9	33.5	350	573	0.0		1045	5.7		29.3
46X-3, 140-150	432.10	34	6.7	18.4	33.5	20.8	33.1	356	570	0.0		936	6.0		70.4
159-959D-															
1R-3, 140-150	422.20	46	6.6	18.8	33.0	20.6	31.8	374	12	0.0	4087	1361	6.3	1.6	
9R-1, 140-150	486.00	20	6.6	17.0	33.0	20.2	31.1	380	570	0.0	4013	773	5.6	2.2	
12R-1, 140-150	515.00	14	7.5	16.7		20.7	32.5	398	572	0.0	3940	807	6.1	2.1	
16R-1, 140-150	553.50	10			32.5	20.5	31.5	405	563	0.0	4213	790	4.6	1.6	
20R-1, 140-150	592.00	13			35.0	20.9	31.3	441	572	0.0	3803	790	4.8	1.4	
23R-3, 140-150	623.70	6				19.2	31.3	404	569	0.0	4150	815	4.7	1.6	
26R-2, 140-150	651.20	6			32.5	19.8	30.0	459	574	0.0	3646	782	4.3	2.3	
29R-2, 140-150	680.10	6				19.7	30.8	473	567	0.0	3520	773	4.1	1.4	
32R-1, 135-150	707.55	7			32.0	19.5	30.5	477	569	0.0	3048	756	3.9	1.6	
35R-1, 135-150	741.05	1						441		0.0	3205		4.3		
39R-2, 135-150	776.65	9			32.0	18.6	29.2	478	567	0.0	3635	320	3.7	1.8	
43R-3, 135-150	816.65					18.9	26.9	509			2806	177	2.5	1.9	

Table 12. Summary of elemental analysis of sediments squeezed for interstitial water samples at Site 959.

Core, section, interval (cm)	Depth (mbsf)	Inorg-C	CaCO ₃	Tot-C	Org-C	TN
159-959B-						
1H-2, 145-150		4.46	37.2	5.54	1.08	0.10
2H-3, 145-150	9.45	4.12	34.3	5.20	1.08	0.14
3H-3, 145-150	18.95	3.77	31.4	5.03	1.26	0.13
4H-3, 145-150	28.45	6.24	52.0	6.91	0.67	0.08
5H-3, 145-150	37.95	3.92	32.7	4.65	0.73	0.13
6H-3, 145-150	47.45	5.84	48.6	6.31	0.47	0.06
7H-3, 145-150	56.95	5.50	45.8	5.98	0.48	0.06
159-959A-						
7H-3, 145-150	61.05	5.40	45.0	6.03	0.63	0.07
10H-3, 145-150	89.55	6.57	54.7	7.29	0.72	0.05
13H-3, 145-150	118.05	6.42	53.5	6.63	0.21	0.04
16H-3, 145-150	146.5	3.79	31.6	4.03	0.24	0.04
19H-3, 140-150	175	0.65	5.4	1.27	0.62	0.06
22X-3, 140-150	203	4.08	34.0	4.47	0.39	0.05
25X-3, 140-150	230.2	1.37	11.4	2.29	0.92	0.09
28X-3, 140-150	259.2	0.29	2.4	0.72	0.43	0.08
31X-3, 140-150	288.1	1.18	9.8	1.61	0.43	0.08
34X-3, 140-150	317	0.17	1.4	1.56	0.39	0.14
37X-3, 140-150	345.9	3.18	31.7	4.37	0.56	0.08
40X-3, 140-150	374.9	5.50	45.8	5.82	0.32	0.05
43X-3, 140-150	403.6	1.77	14.7	2.39	0.62	0.08
46X-3, 140-150	432.1	0.05	0.4	2.15	2.30	0.23
159-959D-						
1R-3, 140-150	422.2	0.43	3.6	2.36	1.93	0.21
9R-1, 140-150	486	0.03	0.2	4.65	4.62	0.29
12R-1, 140-150	515	0.03	0.2	2.5	2.47	0.21
16R-1, 140-150	553.5	0.36	3.0	1.40	1.04	0.08
20R-1, 140-150	592	0.38	3.2	1.43	1.05	0.08
23R-3, 140-150	623.7	2.49	20.7	3.13	0.64	0.05
26R-2, 140-150	651.2	2.08	17.3	2.79	0.71	0.06
29R-2, 140-150	680.1	1.09	9.1	2.46	1.37	0.09
35R-4, 135-150	741.05	4.61	38.4	4.88	0.27	0.00

Note: Inorg-C = inorganic carbon, CaCO₃ = carbonate, Tot-C = total carbon, Org-C = total organic carbon, and TN = total nitrogen.

in nanofossil chalk and micrite at depth in the lower Tertiary–Upper Cretaceous part of the section (see “Lithostratigraphy” section, this chapter).

The dissolved magnesium profile exhibits a trend of decreasing concentrations with depth (Fig. 56D). From near-seawater values in the uppermost sample, concentrations decrease by ~33% over the next 200 mbsf. The gradient is significantly lower in the interval from 200 to ~780 mbsf, where concentrations decline gradually from 37 to 29 mM. There are several possible explanations for the measured magnesium pattern. Magnesium decreases more rapidly than calcium increases from 90 to ~200 mbsf. This is strongly suggestive of the formation of dolomite by calcite replacement in this interval at present. In fact, dolomite rhombs, whose formation is usually inhibited by the presence of dissolved sulfate in deep-sea sites (Baker and Kastner, 1981), are observed throughout the sedimentary column as shallow as 95 mbsf at Site 959 (see barrel sheets in the back part of this volume). Furthermore, the transformation of biogenic opal to chert and porcellanite from 430 to 812 mbsf also would have taken up dissolved magnesium (Kastner et al., 1977; Donnelly and Merrill, 1977).

Silica, Potassium, and Iron Profiles

Interstitial water silica concentrations appear to reflect lithologic changes in the sediment pile (Fig. 57A). In the uppermost 25 mbsf of the sediment, silica concentrations increase rapidly to nearly 700 μ M and drop to a broad minimum near 60 mbsf. The local maximum in the silica profile probably results from dissolution of trace amounts of biogenic silica in the first three cores of Hole 959B (see smear slide descriptions). Based on smear-slide analyses the portion of the core exhibiting the minimum in dissolved silica concentrations is nearly devoid of biogenic silica. From the minimum in the silica profile, concentrations increase abruptly near 200 mbsf to slightly greater than 1000 μ M, coinciding with a shift to a diatom-bearing

lithology. These silica concentrations are similar to the solubility limit of opal-A (Kastner, 1979). Silica concentrations remain high and variable down to approximately 480 mbsf, where they stabilize at concentrations of approximately 800 μM to a depth of approximately 700 mbsf. The upper boundary of this portion of the profile corresponds to a transition from diatomites to porcellanites. The deepest pore-fluid samples exhibit a rapid decrease in silica concentration, indicative of diffusion of silica into the black claystones underlying the porcellanites.

Potassium concentrations in the pore fluids exhibit a systematic decrease with depth (Fig. 57B). In the first 20 mbsf, potassium concentrations are slightly elevated relative to seawater (approximately 12 mM vs. 10.44 mM in seawater). Below 200 mbsf, potassium exhibits a nearly linear decrease corresponding to removal of more than 80% of the initial potassium content. Uptake of potassium has been attributed to several different processes at previous DSDP and ODP sites, including authigenic potassium feldspar formation (Kastner, 1976), potassium removal associated with oceanic crustal alteration (Gieskes, 1983), and, most commonly, uptake by clay minerals. However, it is unclear if this potassium removal in association with clay minerals is the result of reversible ion exchange processes or incorporation of potassium into inter-layer sites of fine-grained authigenic clay minerals. Given that glauconite and zeolite have been observed in smear slides (see "Lithostratigraphy" section, this chapter), attributing the gradual potassium decrease to authigenic clay mineral formation seems most reasonable.

Concentrations of dissolved iron were measured in samples from the top 430 mbsf of Site 959. Below this depth the volumes of interstitial water recovered from the whole round samples were not adequate for iron analyses. The iron profile exhibits several local minima and maxima. Although it is impossible to preclude oxidative artifacts in the iron data, there was no clear evidence of artifacts, such as precipitation of iron oxyhydroxides in pore-water samples. If the variations in dissolved iron are in fact representative of interstitial water dissolved iron concentrations, the large amplitude of concentration variations, which show no systematic depth trend, requires active iron redistribution over discrete portions of the sediment column. In light of the fact that the sediments from Site 959 contain several authigenic iron minerals, including pyrite, glauconite, and siderite (see "Lithostratigraphy" section, this chapter), it is reasonable to suggest that ongoing redistribution of iron may be occurring within the sediment pile.

In summary, results from interstitial water analyses were obtained for the upper 820 mbsf of Site 959. Organic matter degradation exerts the dominant control on pore-water chemistry in the upper 200 mbsf of the sediment column, as indicated by decreasing sulfate concentrations, and systematic increases in ammonium concentrations and alkalinity with increasing depth. Methanogenesis is evident, beginning at the base of the sulfate-reducing zone, 250–300 mbsf, down to the bottom of the hole. Profiles of calcium, magnesium, manganese, and alkalinity indicate carbonate precipitation within the zone of sulfate reduction. Carbonate dissolution and recrystallization is suggested by strontium, calcium, and alkalinity trends below 150 mbsf. Dissolved silica concentrations reflect lithologic changes with high concentrations associated with sediments rich in biogenic silica, and low concentrations in portions of the section with lesser silica contents. Uptake of potassium by clay minerals is likely to be responsible for a systematic decrease in pore-fluid potassium concentrations with increasing depth in the sediment.

PHYSICAL PROPERTIES

Measurements on whole cores taken at Site 959 were made with the magnetic susceptibility meter, gamma-ray attenuation porosity evaluator (GRAPE), *P*-wave Logger (PWL), and Natural Gamma

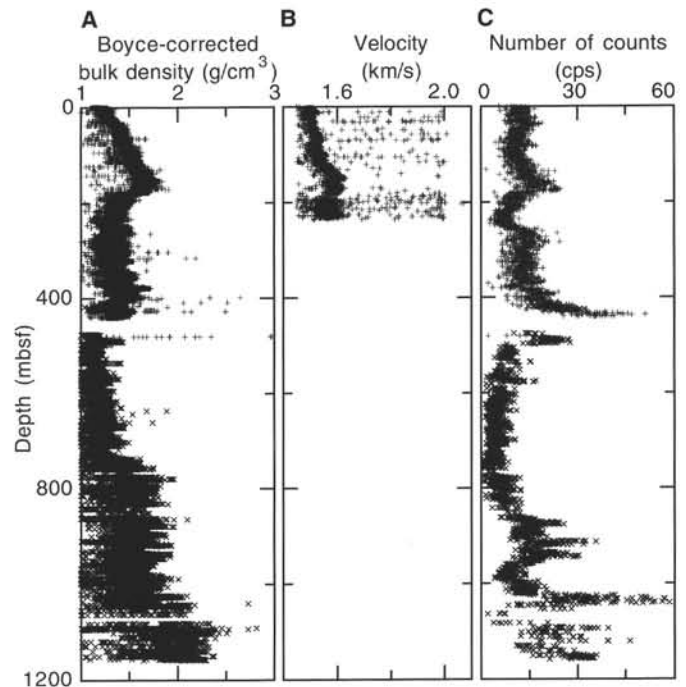


Figure 58. Results from MST measurements at Holes 959A and 959D. **A.** Boyce-corrected density, results from the GRAPE. **B.** Horizontal *P*-wave velocity, results from the PWL. **C.** Total number of counts, results from the NGR. Plus signs = Hole 959A, "x" symbols = Hole 959D.

Radiation (NGR) tool. Both full-space and half-space thermal conductivity measurements were made. Index properties were calculated from wet and dry masses and wet and dry volumes. Compressional (*P*) wave velocity, shear strength, and electrical resistivity were measured on split cores. Descriptions of the experimental methods are provided in the "Physical Properties" section of the "Explanatory Notes" chapter (this volume). All tables presented and all MST data are available on the CD-ROM in the back of this volume.

Multisensor Track

All four sensors (magnetic susceptibility, GRAPE, PWL, and NGR) on the MST were used on APC and XCB cores at Holes 959A (0–240 mbsf), 959B, and 959C. At Hole 959D, only magnetic susceptibility, GRAPE, and NGR were used because of the reduced diameter of the cores.

Magnetic susceptibility was measured at 5-cm intervals in all cores collected at Site 959. The results are discussed in the "Paleomagnetism" section (this chapter).

GRAPE density values were edited and Boyce-corrected, and only the maximum bulk density values were taken into consideration. Figure 58A shows the variation of Boyce-corrected bulk density with depth at Holes 959A and 959D. Values from Holes 959B and 959C are not included in Figure 58A; they are, however, similar in magnitude to those of Hole 959A. The density increases from about 1.3 to 1.8 g/cm^3 in the upper 155 m of Hole 959A. Shifts to lower values (about 1.5 g/cm^3) occur at 175 and 450 mbsf and shifts to higher densities occur below 750 and 1050 mbsf.

Horizontal *P*-wave velocity was measured from 0 to 240 mbsf at Hole 959A and on all sections at Holes 959B and 959C. No measurements were made in Hole 959D because of the nature of the cores recovered (no contact between core and liner). Figure 58B shows the variation of horizontal *P*-wave velocity with depth at Hole 959A after editing. The values from Holes 959B and 959C are similar in magni-

tude to those of Hole 959A and are therefore not included. The majority of velocity values are smaller than 1.62 km/s. Higher values may reflect increases in velocity in layers with, for example, pyrite and/or glauconite. They may, however, also be artificial values caused by liner effects (i.e., the *P*-wave travels through the liner) and edge effects (i.e., the *P*-wave travels through the double thickness of liner).

Natural gamma radiation was measured with a 10-s-long counting period at all holes. The quality of data is less sensitive to changes in the core diameter than with the GRAPE and PWL; thus, no editing of the data was needed. The background variation values for the total number of counts (8.74 cps) were subtracted from subsequent measurements. Figure 58C shows the downhole variation for the total number of counts at Holes 959A and 959D only, as the values from Holes 959B and 959C are similar in magnitude to those at Hole 959A. The downhole trend for the total number of counts changes with depth. Generally, the total number of counts is less than 15 cps, although zones of higher values (>20 cps) exist. Higher values were observed between 150 and 175 mbsf, 375 and 500 mbsf, and in three zones below 850 mbsf (870–950, 1020–1050, and below 1090 mbsf). The other counting channels are not reported here, but they show similar trends with smaller values.

Thermal Conductivity

Thermal conductivity data were collected in four sections per core at Holes 959A and 959B in full-space configuration. No measurements were made in Hole 959C because of time constraints. Measurements were resumed in Hole 959D: twice per core for the full-space method, and once or twice per core for the half-space method (below Core 159-959D-34R).

The thermal conductivity data have a scattered distribution with depth and high error, partially caused by technical problems with the equipment but also by drilling disturbances, cracks and fractures in the sediments, and water in the liner. Thus, after careful consideration, the corrections for in situ pressure and temperature were not applied as they are considered to be significantly smaller than the possible errors in the measurements. The majority of the thermal conductivity values in the upper 700 mbsf at Site 959 range between 0.8 and 1.4 $\text{Wm}^{-1}\text{C}^{-1}$ (Table 13; Fig. 59). Generally, thermal conductivity increases gradually with depth as the sediments become more lithified. A local maximum in thermal conductivity, with values higher than 1.4 $\text{Wm}^{-1}\text{C}^{-1}$, occurred between 125 and 165 mbsf. Thermal conductivity values are larger in magnitude and more scattered below 700 mbsf, compared to those above. These higher values are probably caused by higher quartz content in these cores.

Index Properties

Index properties, measured on every second section at Holes 959A, 959B, and 959D, were determined using gravimetric methods. Three procedures for wet volume determination were used: the constant-volume syringe in soft sediments; volume calculated directly from cube dimensions in well-lithified sediment; and direct measurements in the pycnometer for other sediment types. The pycnometer was also used for dry volume determinations.

Offsets and changes in the slope and magnitude of index properties can be correlated with changes in age and lithology (Table 14; Fig. 60). There is an abrupt change in most index properties in the upper 150 m. Values of water content (wet and dry), porosity, and void ratio increase, whereas density (bulk and dry) decreases between 155 and 230 mbsf. A shift to a wider scatter in values occurs between about 230 and 450 mbsf. An increase in scatter was observed in values for all index properties. Below this depth, index properties values display normal trends, i.e., water content (wet and dry), porosity, and void ratio decrease and density (bulk and dry) increases with depth.

Table 13. Thermal conductivity data at Site 959.

Core, section, interval (cm)	Depth (mbsf)	Lithologic unit	Thermal conductivity ($\text{Wm}^{-1}\text{C}^{-1}$)
159-959A-			
2H-1, 75	9.85	IA	1.02
2H-3, 75	12.85	IA	0.92
2H-5, 75	15.85	IA	1.01
2H-7, 30	18.40	IA	0.86
3H-1, 75	19.35	IA	1.09
3H-3, 75	22.35	IA	0.98
3H-5, 75	25.35	IB	1.11
4H-1, 75	28.85	IB	1.08
4H-3, 75	31.85	IB	1.31
4H-5, 75	34.85	IB	1.05
4H-7, 30	37.40	IB	0.95
5H-1, 75	38.35	IB	1.17
5H-3, 75	41.35	IB	1.04
5H-5, 75	44.35	IB	1.03
5H-7, 30	46.90	IB	0.93

Only a part of this table is reproduced here. The entire table appears on the CD-ROM (back pocket).

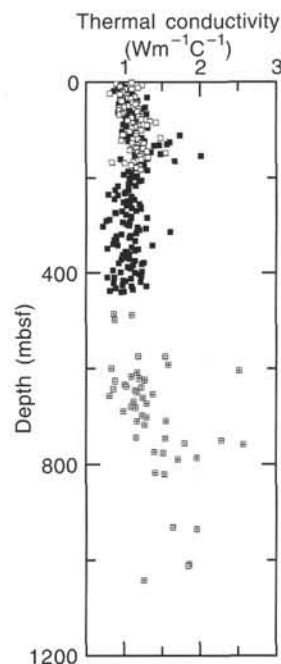


Figure 59. Thermal conductivity variation with depth at Site 959. Solid squares = Hole 959A, open squares = Hole 959B, divided squares = Hole 959D.

A change in the magnitude of all index properties except in solids-grain density was observed at about 750 mbsf. Water content (wet and dry) and porosity values decrease by more than 10%, void ratio decreases by 0.4, and density values (bulk and dry) increase by at least 0.2 g/cm^3 . Fewer measurements were made below 1000 mbsf. Those that were taken reveal a somewhat wider scatter of points. Water content (wet and dry), porosity, and void ratio are lower whereas density (bulk, solids-grain, and dry) values are higher.

Velocimetry

Discrete measurements of *P*-wave velocity were made at Holes 959A, 959B, and 959D close to the location of samples for index properties measurements in soft sediments and on the same sample in

Table 14. Index properties data at Site 959.

Core, section, interval (cm)	Depth (mbsf)	Lithologic unit	Water content		Density			Porosity (%)	Void ratio (1)
			Total wet mass (%)	Mass of solids (%)	Wet bulk (g/cm ³)	Solids-grain (g/cm ³)	Dry (g/cm ³)		
159-959A-									
1H-1, 75	0.75	IA	54.95	121.96	1.40	2.67	0.63	75.18	3.18
1H-3, 95	3.95	IA	52.56	110.77	1.45	2.72	0.69	74.22	2.94
1H-5, 76	6.76	IA	55.57	125.07	1.42	2.66	0.63	76.92	3.25
2H-1, 110	10.20	IA	57.08	132.98	1.38	2.70	0.59	76.83	3.50
2H-3, 79	12.89	IA	55.32	123.80	1.41	2.66	0.63	75.96	3.22
2H-5, 58	15.68	IA	59.06	144.23	1.37	2.78	0.56	78.70	3.92
3H-1, 55	19.15	IA	56.56	130.20	1.40	2.68	0.61	77.37	3.41
3H-3, 48	22.08	IA	52.02	108.44	1.46	2.65	0.70	74.05	2.80
3H-5, 27	24.87	IB	51.12	104.58	1.46	2.66	0.71	72.73	2.72
4H-1, 114	29.24	IB	48.91	95.75	1.50	2.67	0.77	71.73	2.50
4H-3, 88	31.98	IB	47.81	91.60	1.52	2.68	0.79	71.03	2.40
4H-5, 75	34.85	IB	46.19	85.85	1.53	2.62	0.83	69.10	2.19
5H-1, 73	38.33	IB	47.56	90.69	1.59	2.82	0.83	73.71	2.50
5H-3, 74	41.34	IB	46.81	88.00	1.57	2.76	0.83	71.64	2.37
5H-5, 75	44.35	IB	44.94	81.62	1.61	2.76	0.89	70.52	2.20

Only a part of this table is reproduced here. The entire table appears on the CD-ROM (back pocket).

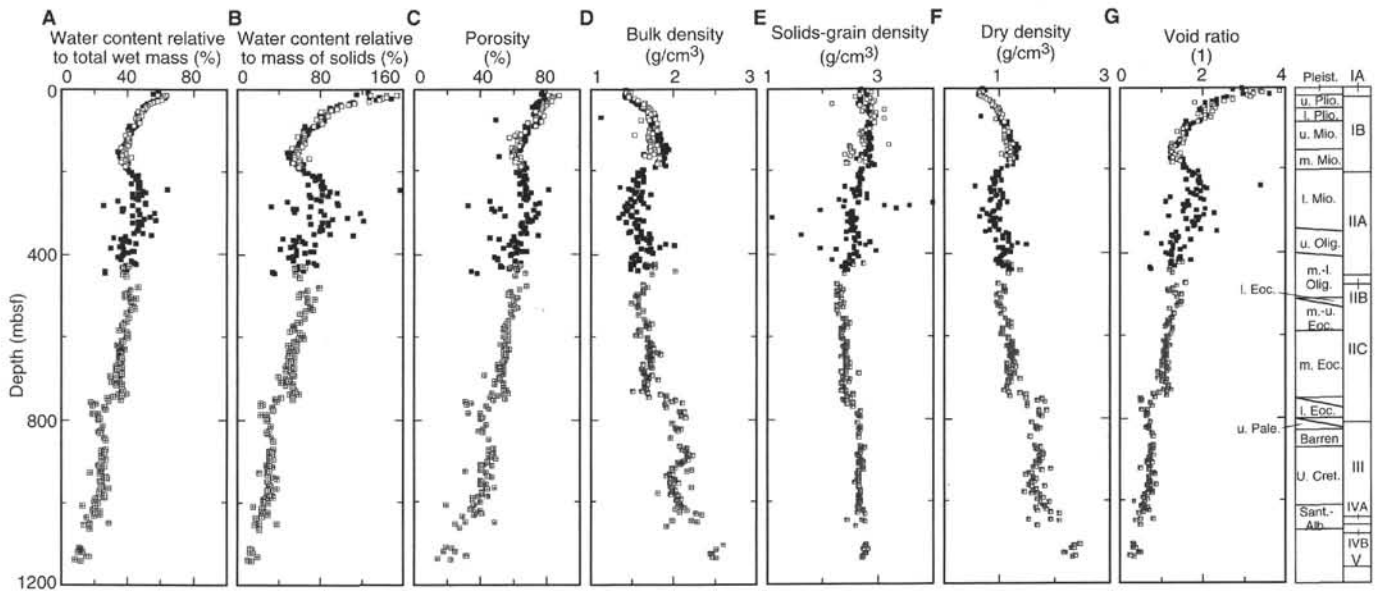


Figure 60. Index property variations with depth at Site 959. Solid squares = Hole 959A, open squares = Hole 959B, divided squares = Hole 959D.

lithified ones (i.e., once every second section). The sampling frequency was increased to once every section in cores without PWL measurements at Hole 959A (i.e., all XCB cores).

Both vertical and horizontal uncorrected *P*-wave velocities increase gradually from about 1.5 km/s near the seafloor to about 2.0 km/s at 745 mbsf (Table 15; Fig. 61). Below 748 mbsf, velocities shift to higher and more scattered values. The horizontal velocities are generally slightly higher than the vertical ones, as shown by positive anisotropy values (Fig. 61C). The anisotropy appears to increase slightly with depth. This indicates that pore spaces affecting horizontal velocities are closed more rapidly than pore spaces affecting vertical velocities (Carlson and Christensen, 1977).

Table 15 further shows *P*-wave velocities corrected to in situ depths. Curve-fit equations were derived for in situ velocity values of seawater and porosity values for Hole 959A, 959B, and 959D using linear, exponential, and power functions in KaleidaGraph 3.0.4. The curve fit between equations and data is very good (>0.99) for in situ seawater velocity at Holes 959A, 959B, and 959D. The curve fit between equations and data for porosity is not as good: the best curve fit (0.91) was obtained for Hole 959D, whereas the poorest fit (0.68) was obtained at Hole 959A. In the upper 173 m of Hole 959A and 167

m of Hole 959B, values of corrected velocity are smaller than those of uncorrected ones. This may be related to the fact that the soft sediment becomes slightly more compacted during measurements with DSV 3, but also to inaccuracies in the curve-fit equations for porosity.

Undrained Shear Strength

Undrained shear strength was measured with two methods, vane shear and penetrometer. At Holes 959A and 959B, reliable vane shear measurements were made down to depths of 80 and 66 mbsf, respectively. Overlapping vane shear and penetrometer measurements were made on adjacent pieces of the core face at Hole 959A. Both techniques show similar downhole trends of undrained shear strength, but the results from the penetrometer measurements are consistently lower than those from the vane shear at Site 959 (Table 16; Fig. 62). Vane shear measurements terminated at 82 mbsf at Hole 959A as the sediment was brittle below this depth and produced incorrect values of undrained shear strength.

Shear strength values at Hole 959A agree well with those of Hole 959B, and the shear strength decreases linearly from the seafloor to

Table 15. Uncorrected and corrected P-wave velocity data in vertical and horizontal directions and anisotropy data at Site 959.

Core, section, interval (cm)	Depth (mbsf)	Lithologic unit	Uncorrected velocity			Anisotropy		Corrected velocity			DSV
			Vert (km/s)	Hor 1 (km/s)	Hor 2 (km/s)	Hor 1 (1)	Hor 2 (1)	Vert (km/s)	Hor 1 (km/s)	Hor 2 (km/s)	
159-959A-											
1H-1, 67.2	0.67	IA	—	1.569	—	—	—	—	1.542	—	3
1H-1, 76.1	0.76	IA	1.522	—	—	—	—	1.497	—	—	1
1H-3, 87.7	3.88	IA	—	1.547	—	—	—	—	1.522	—	3
1H-3, 94.4	3.94	IA	1.525	—	—	—	—	1.500	—	—	1
1H-5, 69.4	6.69	IA	—	1.544	—	—	—	—	1.519	—	3
1H-5, 74.8	6.75	IA	1.523	—	—	—	—	1.499	—	—	1
2H-1, 102	10.12	IA	—	1.589	—	—	—	—	1.563	—	3
2H-3, 65.9	12.76	IA	—	1.575	—	—	—	—	1.550	—	3
2H-3, 78.3	12.88	IA	1.548	—	—	—	—	1.524	—	—	1
2H-5, 45.4	15.55	IA	—	1.559	—	—	—	—	1.535	—	3
2H-5, 56.6	15.67	IA	1.533	—	—	—	—	1.510	—	—	1
3H-1, 46.9	19.07	IA	—	1.545	—	—	—	—	1.522	—	3
3H-1, 53.9	19.14	IA	1.525	—	—	—	—	1.503	—	—	1
3H-3, 36.8	21.97	IA	—	1.543	—	—	—	—	1.521	—	3
3H-5, 26.5	24.86	IB	1.535	—	—	—	—	1.514	—	—	1

Only a part of this table is reproduced here. The entire table appears on the CD-ROM (back pocket)

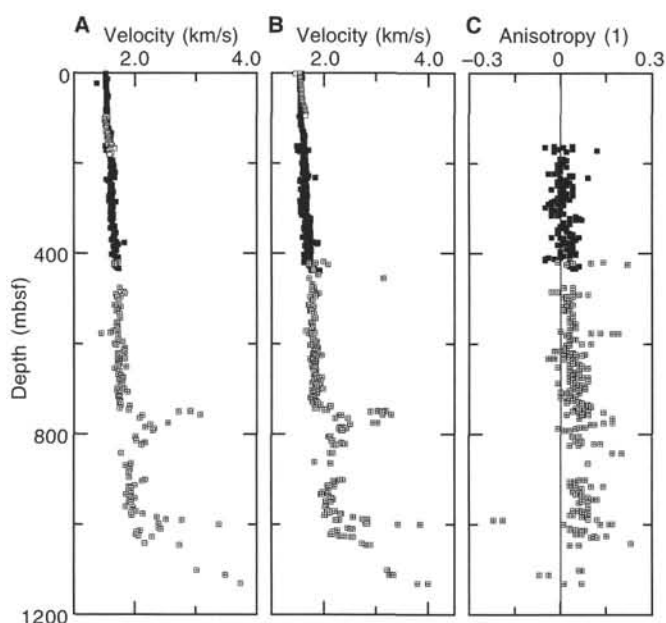


Figure 61. Results of discrete velocity measurements vs. depth at Site 959. A. P-wave velocity in vertical direction. B. P-wave velocity in horizontal direction. C. Anisotropy. Solid squares = Hole 959A, open squares = Hole 959B, divided squares = Hole 959D.

about 100 mbsf. There is a gradual increase in shear strength values with depth below 100 mbsf, which reflects the increasing stiffness of the sediments. Since there are no sharp offsets in undrained shear strength values with depth, sediments at Holes 959A and 959B are apparently only affected by compaction (normal consolidation).

Electrical Resistivity

Resistance in vertical and horizontal directions was measured three times per core in the upper 225 m of Hole 959A and through the entire section in Hole 959B, and six times per core from 250 mbsf to total depth at Hole 959A. Sediments in Hole 959D were too stiff and fractured for a meaningful result to be attained if the resistance probe was inserted. Maximum values of resistance were attained directly from the display of the Wayne Kerr Precision Component Analyzer. Resistivity was calculated by multiplying resistance with the cell constant value, which is 0.00114 m.

Table 16. Undrained shear strength data at Site 959.

Core, section, interval (cm)	Depth (mbsf)	Lithologic unit	Shear strength	
			Vane shear (kPa)	Penetrometer (kPa)
159-959A-				
1H-1, 84.3	0.84	IA	3.70	—
1H-3, 101.9	4.02	IA	8.80	—
1H-5, 80.2	6.80	IA	10.00	—
2H-1, 117.1	10.27	IA	18.80	—
2H-3, 85.6	12.96	IA	19.10	—
2H-5, 71.9	15.82	IA	20.90	—
3H-1, 62.7	19.23	IA	15.60	—
3H-3, 58.4	22.18	IA	20.60	—
3H-5, 41.3	25.01	IB	24.10	—
4H-1, 110	29.20	IB	17.10	—
4H-3, 85.2	31.95	IB	20.20	—
4H-5, 84.1	34.94	IB	27.90	—
5H-1, 87.9	38.48	IB	26.30	—
5H-3, 77.1	41.37	IB	114.80	—
5H-3, 77	41.37	IB	—	19.62

Only a part of this table is reproduced here. The entire table appears on the CD-ROM (back pocket).

At Hole 959A, vertical and horizontal resistivities increase from about 0.1 Ω m near the seafloor to about 0.4 Ω m at 64 mbsf (Table 17; Fig. 63A). Only the upper 135 m at Hole 959B was measured, but a similar downhole trend of the resistivity compared to Hole 959A was observed (Fig. 63B). Resistivity values are fairly constant below 64 mbsf, and generally range between 0.15 and 0.30 Ω m. There is a small increase in the magnitudes below 415 mbsf, and maximum resistivity, 0.51 Ω m, was measured at 440 mbsf.

The formation factor was calculated using a pore-water resistance of 161 Ω . No correlation between the porosity of different lithologies and corresponding formation factor was made, but values of porosity are presented in Table 17.

Comparison Between Continuous and Discrete Measurements

Bulk density was determined by continuous measurements using the GRAPE and by discrete measurements using gravimetric methods at Holes 959A, 959B, and 959D. Both methods show similar trends of bulk density variation with depth, but the results from continuous measurements are consistently lower than the discrete ones (Fig. 64A). This difference in bulk density is expected because it was determined using two different methods. However, the discrepancy between continuous and discrete bulk density values becomes greater

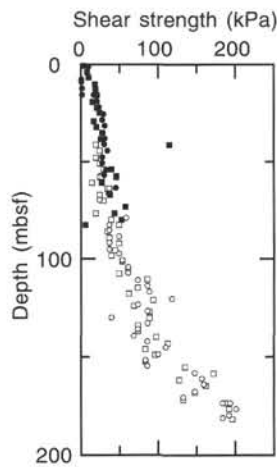


Figure 62. Undrained shear strength variation with depth at Holes 959A and 959B. Squares = Hole 959A, circles = Hole 959B, solid symbols = vane shear data, open symbols = penetrometer data.

Table 17. Electrical resistivity and formation factor data at Site 959

Core, section, interval (cm)	Depth (mbsf)	Lithologic unit	Resistivity		Formation factor		Porosity (%)
			Vert (Ω m)	Hor (Ω m)	Vert (1)	Hor (1)	
159-959A-							
1H-1, 74	0.74	IA	0.17	0.10	0.94	0.52	75.20
2H-1, 108	10.18	IA	0.11	0.11	0.59	0.59	76.80
2H-3, 77	12.87	IA	0.10	0.05	0.54	0.30	76.00
2H-5, 54	15.64	IA	0.08	0.07	0.42	0.40	78.70
3H-1, 60	19.20	IA	0.09	0.09	0.51	0.47	77.40
3H-3, 46	22.06	IA	0.12	0.12	0.67	0.66	74.10
3H-5, 25	24.85	IB	0.13	0.13	0.72	0.70	72.70
4H-1, 101	29.11	IB	0.15	0.14	0.80	0.74	71.70
4H-3, 72	31.82	IB	0.11	0.09	0.62	0.49	71.00
4H-5, 69	34.79	IB	0.10	0.09	0.52	0.52	69.10
5H-1, 71	38.31	IB	0.20	0.17	1.12	0.94	73.70
5H-3, 74	41.34	IB	0.21	0.21	1.13	1.16	71.60
5H-5, 72	44.32	IB	0.22	0.21	1.20	1.15	70.50
6H-1, 73	47.83	IB	0.12	0.23	0.66	1.26	71.20
6H-3, 74	50.84	IB	0.33	0.25	1.78	1.37	70.60

Note: Vert = vertical direction (parallel to core axis), Hor = horizontal direction (perpendicular to cut core axis).

Only a part of this table is reproduced here. The entire table appears on the CD-ROM (back pocket).

with depth. This additional difference is probably related to variation in the core diameter. Best correspondence between continuous and discrete measurements was obtained between 150 and 450 mbsf.

Horizontal *P*-wave velocity was determined with continuous measurements using the PWL and from discrete measurements on cubes using DSV 3 at Holes 959A and 959B. There is only a 100-m interval at Hole 959A that has both types of measurements (Fig. 64B). The data show a fairly good correlation between the continuous and discrete velocity measurements. Discrepancies in magnitude between the two data sets are probably related to the fact that only well-lithified sediments were tested in DSV 3, whereas the entire section was tested in the PWL.

Summary

The physical properties data at Site 959 are heterogeneous, reflecting variations in consolidation, age, and lithology. There are three large discontinuities at Site 959 that can be seen in several phys-

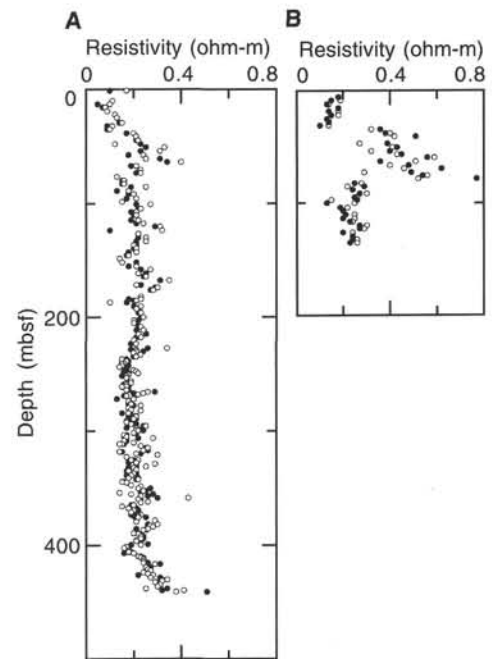


Figure 63. Electrical resistivity variation with depth at Site 959. A. Hole 959A. B. Hole 959B. Open circles = vertical resistivity, solid circles = horizontal resistivity.

ical properties measurements. The upper discontinuity occurs at 150 mbsf (Figs. 58–62) and corresponds to the boundary between the upper and middle Miocene, but with no apparent change in lithology (see “Lithostratigraphy” section, this chapter). The middle discontinuity occurs across an interval without measurements (446–469 mbsf; Figs. 58–60). It coincides with a change in the lithology (from nanofossil chalk and clay to chert), age, and tectonic deformation. The scatter in the values of the index properties is generally narrow below 469 mbsf (Fig. 60). This might reflect the onset of the tectonic deformation (i.e., dewatering of sediments) and/or show that only a few small-scale heterogeneities exist in the sediments at Site 959. The lower discontinuity at 750 mbsf is the most clearly marked (Figs. 58–61); it occurs in an interval of unknown age and with no obvious change in lithology.

DOWNHOLE MEASUREMENTS

Logging Operations and Log Quality

The Quad, Formation MicroScanner (FMS), and Geochemical Tool String (GLT) were successfully deployed at Hole 959D in the lower part of the hole (395–1081 mbsf), but poor borehole conditions prevented logging in the upper segment (above 395 mbsf). Sea-state conditions were mild and the wireline heave compensator was employed during most of the logging. Despite the attempted use of the side-entry sub, borehole blockage prevented all three tool strings from reaching total depth (1158.9 mbsf). After an initial delay in getting the tool strings down the hole, logging operations in the bottom section of the hole went smoothly. A lower (1078 to 521 mbsf) and upper (545–395 mbsf) main log and a repeat (1081–994.9 mbsf) log were run with the Quad combination tool string at 900 ft/hr, and both standard mode (recorded at 15 cm sampling) and high-resolution (2.5 cm and 5.08 cm sampling) data were recorded. The FMS tool string was run next at 1800 ft/hr over the interval 936.8 to 546.9 mbsf (main) and then at 1600 ft/hr over the interval 932 to 655.1 mbsf (repeat). The last tool string run was the GLT, which was run over the

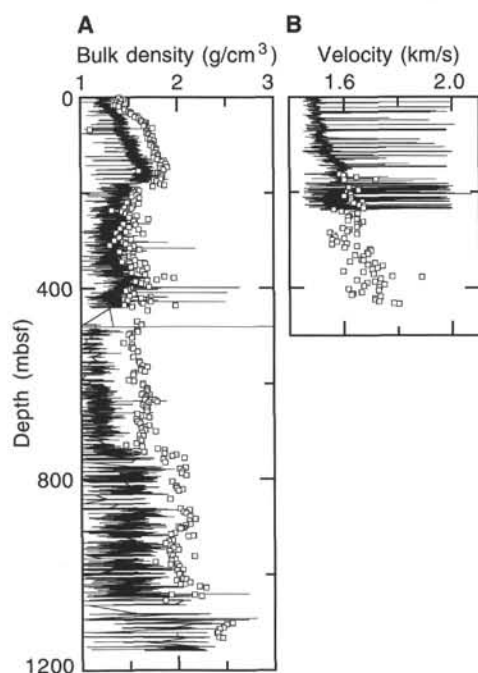


Figure 64. Comparison between continuous and discrete measurements. **A.** Boyce-corrected bulk density and gravimetric bulk density variation vs. depth at Holes 959A and 959D. **B.** Horizontal *P*-wave velocity variation with depth at Hole 959A, measured from the PWL and DSV 3. Lines correspond to continuous measurements, and open squares correspond to discrete measurements.

Table 18. Summary of logging operations at Hole 959D.

Hole	Tool string	Tool string components	Depth (mbsf)
959D	Quad	DITE/HLDT/CNT-G/SDT/NGTC/TLT DITE/HLDT/CNT-G/SDT/NGTC DITE/HLDT/CNT-G/SDT/NGTC	Main (top): 545–395 Repeat: 1081–995.9 Main (bot): 1078–521
959D	FMS	FMS/GPIT/NGTC	Main: 936.8–546.9 Repeat: 932–655.1
959D	GLT	GSTA/ACTC/CNT-G/NGTC	Main: 928.7–528 Repeat: 898–794

Notes: DITE = Dual Induction Resistivity Tool; HLDT = High Temperature Lithodensity Tool; CNT-G = Compensated Neutron Porosity Tool; SDT = Sonic Digital Tool (Array); NGTC = Natural Gamma-Ray Tool; TLT = Lamont-Doherty Temperature Tool; FMS = Formation MicroScanner; GPIT = General Purpose Incliner Tool; GLT = Geochemical Tool String; GSTA = Gamma-Ray Spectrometry Tool; ACTC = Aluminum Clay Tool.

interval 928.7 to 528 mbsf at 500 ft/hr (main) with a short repeat over the interval 898 to 794 mbsf. A summary of logging operations is presented in Table 18.

Data Processing

Data from all three tool strings appear to be of generally excellent quality despite intermittent borehole washout, especially near the top (405–425 mbsf) and bottom (1025–1045 mbsf) of the logged interval where the Quad caliper measured 17 and 14.5 in., respectively. The increase in borehole diameter caused slight deterioration of the density and velocity data from the Quad tool string (see processed logs at the end of chapter). Where washout prevents the density tool from maintaining close contact with the borehole wall, the tool is forced to measure a combination of seawater and formation density, resulting in anomalous low densities that should be interpreted with caution.

The same type of behavior can be observed with the photoelectric effect log, which uses the same measurement principle. Borehole size variations also induce “cycle skipping” in the sonic velocity log, as a result of the receivers picking incorrect first arrival times used in velocity calculation. This log, however, can be improved with post-cruise processing of the full-waveform sonic data. Comparison of the density, photoelectric effect, and velocity logs with the caliper log (Fig. 65) illustrates the effects of borehole diameter variability on these log measurements. The resistivity and gamma-ray logs are relatively unaffected by borehole washout. Generally, the width of Hole 959D varies between 10 and 12 in., well within the limits of all three tool strings.

Selected Quad logs for Hole 959D are shown in Figure 65. Data from this tool string were linearly depth-shifted by +3.7 m to match the core natural gamma-ray data for comparison purposes, but will undergo more precise depth-shifting during post-cruise processing. Preliminary shipboard processing of FMS data was performed using Schlumberger’s GeoFrame software. The images were enhanced by histogram equalization after undergoing depth and voltage corrections and were then used to determine the dip and azimuth of faults and sedimentary bedding. Because of a bug in the computation of true dips and azimuths, those data were computed independently using apparent dips and azimuths, diameter (from caliper 1), deviation, and azimuth of the hole (Fig. 66). Complete reprocessing of the FMS data will be performed post-cruise. Geochemical data will also undergo extensive onshore processing to convert the relative concentrations of Si, Ca, Fe, S, H, and Cl and wet weight percentages of K, U, Th, and Al to dry weight percentages and to determine Gd and Ti (see “Downhole Measurements” section, “Explanatory Notes” chapter, this volume).

Comparison of Core and Log Physical Property Measurements

Bulk density, natural gamma ray, and *P*-wave velocity were measured both in the core and by logs. The natural gamma-ray data for the core and log at Hole 959D (Fig. 67) demonstrate good correspondence where recovery is high, with slight offsets where recovery drops. These offsets are attributable to the difficulty in pin-pointing the location of the core within the cored interval where recovery is low. Core measurements were made at 15-cm intervals with background variation for each counting channel subtracted (see “Physical Properties” section, this chapter). Bulk density measurements from the core are consistent with those obtained by logging throughout the logged interval (Fig. 68). The sonic log was originally recorded in transit time or slowness ($\mu\text{s}/\text{ft}$) and has been manually corrected for “cycle skipping.” The velocity log was obtained from the corrected transit time data; a comparison is shown in Figure 69 with *P*-wave core data, which were edited and corrected to in situ *P*-wave velocities (see “Physical Properties” section, this chapter). Good agreement can be observed between the log data and both the horizontal and vertical *P*-wave velocities measured in the core.

Log Interpretation and Lithology

The natural gamma-ray, density, porosity, velocity, resistivity, and caliper logs provide confirmation of most of the major lithologic unit boundaries derived from core descriptions (Fig. 65). The boundary separating Subunit IIA, described as diatomite interbedded with nannofossil chalk and clay (see “Lithostratigraphy” section, this chapter), from Subunit IIB, comprising black chert and claystone, is apparent on the natural gamma-ray log, which shows a short-term increase in uranium, and on the caliper curve, which indicates an abrupt decrease in borehole diameter and improved borehole conditions downhole. The velocity log increases from 1.5 to about 1.8 km/s, but this increase is suspect because of the change in borehole conditions that may have affected the data quality.

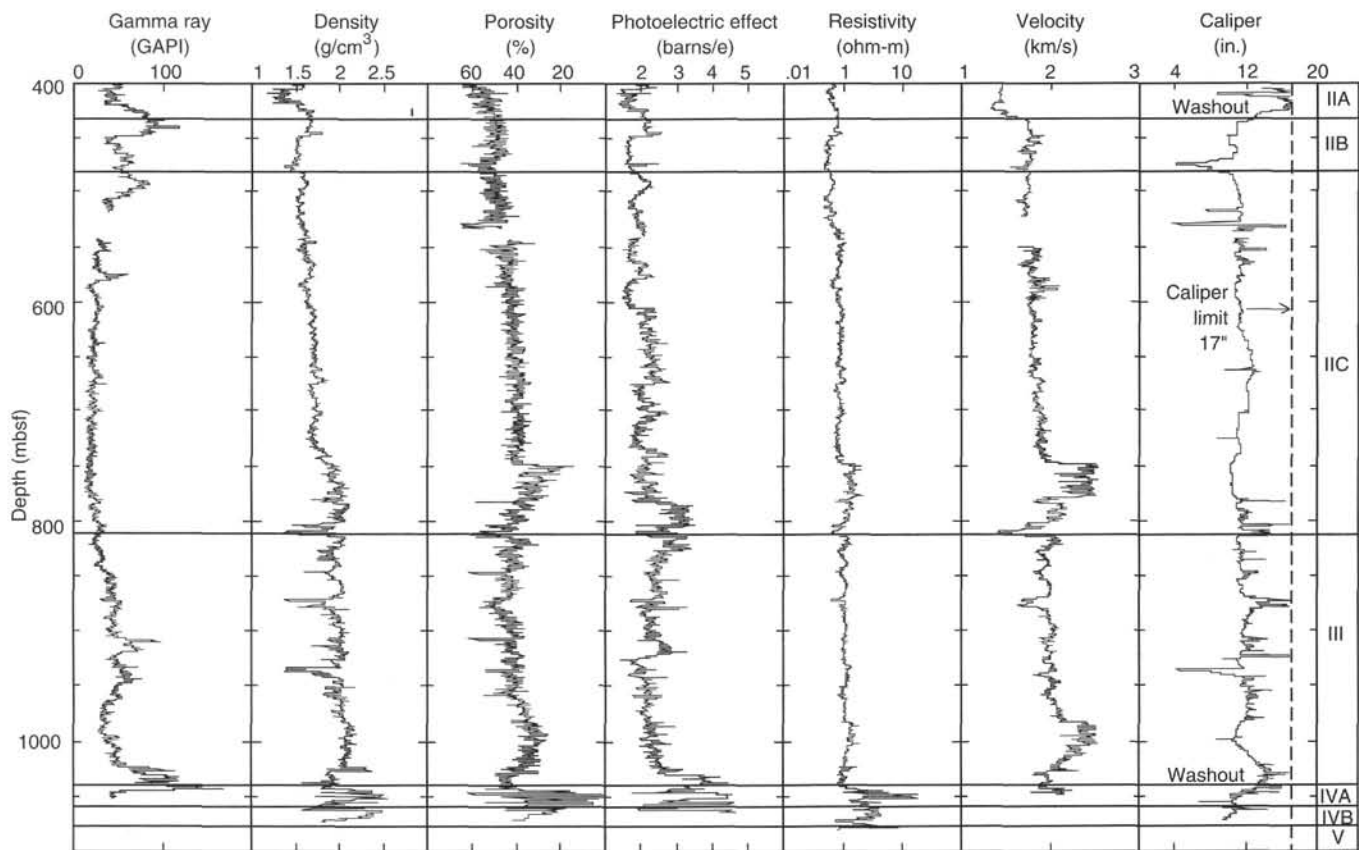


Figure 65. Summary of selected log data from Hole 959D. Lithologic units are shown at the right of the diagram (see "Lithostratigraphy" section, this chapter).

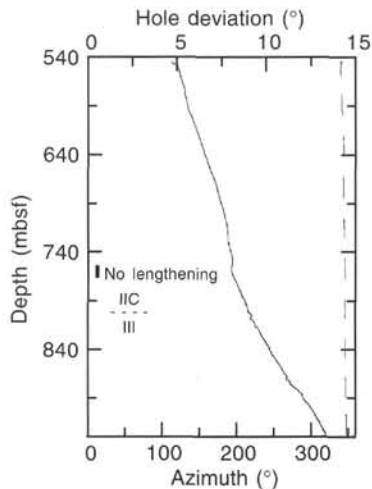


Figure 66. Deviation (dashed line) and azimuth (solid line) of Hole 959D in the interval logged by the FMS tool. Deviation and azimuth are by reference to the vertical and north, respectively. (The Subunit IIC/Unit III boundary is indicated). No lengthening of the hole between 760 and 770 mbsf was noted (cf., Fig. 73).

The change from chert to porcellanite defining the Subunit IIB/IIC boundary (484.6 mbsf) causes an increase in the density log and corresponding decrease in the porosity, but the velocity and resistivity logs exhibit little or no change.

Throughout most of Subunit IIC, described as porcellanite, micrite, and clay, increased rigidity and carbonate content result in a

slow but steady increase in density and velocity (and decrease in porosity), but no real change in resistivity. On the FMS images, the interval between 540 and 714 mbsf appears to consist of 30- to 50-cm-thick beds. The boundaries between the beds do not exhibit sharp contrasts in resistivity, and the numerous burrows seen in the cores appear as spots in the FMS images (Fig. 70). Between 714 and 788 mbsf, the beds appear finely laminated, with 2- to 20-cm-thick beds defined by well-defined contrasts in resistivity (Fig. 71). In this interval the bioturbation seems to decrease downhole on the FMS images. At approximately 750 mbsf, a sharp increase in resistivity and velocity logs occurs together with an abrupt reduction in the porosity log, which may result from the increased micritization and reduction in clay observed in the core (see "Lithostratigraphy" section, this chapter). The Gamma-ray Spectrometry Tool (GST) component of the geochemical tool string indicates a relative increase in silica at this depth. The reappearance of chert, in Core 159-959D-40R, near the base of Subunit IIC, coincides with a significant drop in the velocity log and a relative increase in calcium in the GST. The bedding previously visible in the FMS images cannot be seen past 788 mbsf. Near 810 mbsf, the contact between Subunit IIC and Unit III is hidden on the FMS images by numerous faults and breakouts. Below this contact, the bedding is poorly defined in FMS images because of low resistivity contrasts between the sedimentary layers, bioturbation, and numerous small breakouts that affect the quality of the images.

The top of Unit III, comprising black claystone and claystone with nanfossils, is clearly defined in the density, photoelectric, resistivity, and velocity logs, all of which show a short-lived decrease. This boundary also marks the onset of a steady climb in total natural gamma radiation measured by the Natural Gamma-ray Tool (NGT). The increase in gamma radiation peaks at about 910 mbsf, after which the levels begin to steadily decrease until about 990 mbsf. At 985 mbsf, the velocity, density, and resistivity logs all exhibit sharp increases as

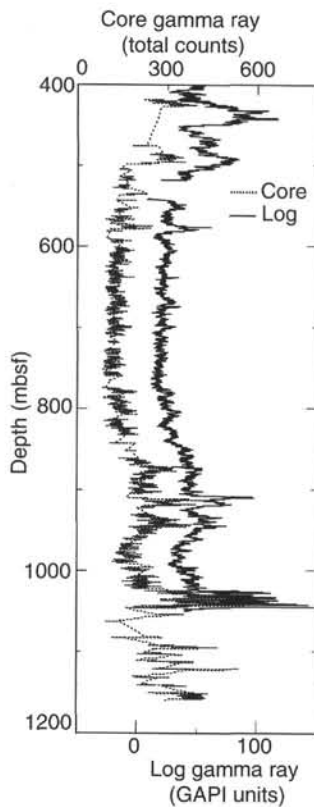


Figure 67. Comparison of core and log natural gamma-ray activity.

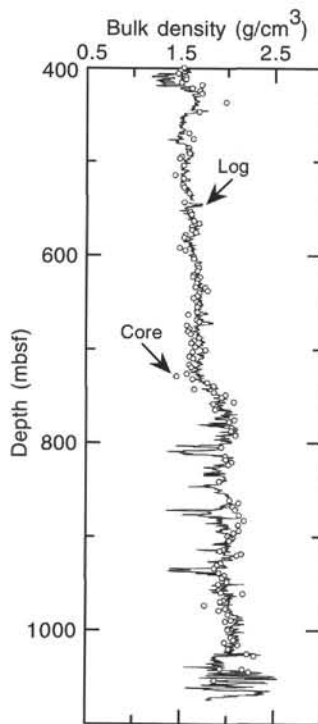


Figure 68. Comparison of core and log bulk density.

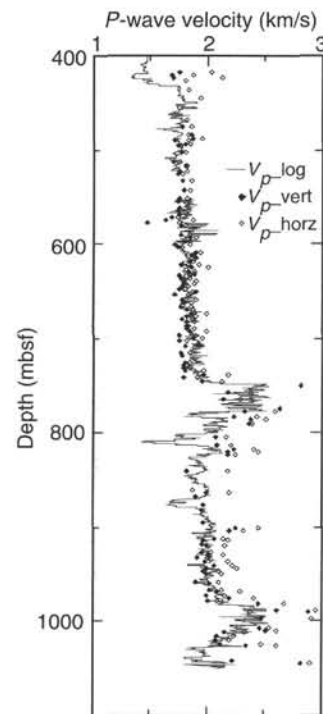


Figure 69. Comparison of core and log P -wave velocity.

the porosity log drops. Toward the base of Unit III, as the gamma-ray and porosity logs show higher levels, the density, resistivity, and velocity all drop again. The caliper log indicates a tendency toward borehole washout as the carbonate-bearing lithologies reappear. At approximately 1040 mbsf, the phosphatic nodules found in Section 159-959D-66R-4 may be the cause of the high uranium reading evident in the computed gamma-ray log.

The Unit III/IV boundary is the most clearly defined boundary visible in the logs, causing significant rises in density, resistivity, and velocity and a downward shift in porosity as the nanofossil claystones at the base of Unit III give way to the calcareous sandstone in Subunit IVA.

Structural Measurements with FMS Images

The FMS images indicate that the hole is dipping north for the logged interval, with the azimuth changing from 340° at 544 mbsf to 347° at 929 mbsf (Fig. 66). Hole deviation increases within the same interval from 4.7° to 13° with an interruption just above 760 mbsf, below which deviation grows.

Above 872 mbsf, caliper 1, which has about the same azimuth as the hole, measures the maximum width of the hole and caliper 2 measures the minimum (Fig. 72). Below 882 mbsf, the tool is rotated and the position of the calipers is switched. Because caliper 2 displays a relatively constant hole diameter, the widths recorded by caliper 1 approximate the variation in hole elongation (maximum width/minimum width). Figure 73 shows the lengthening of the hole at the points where one of the calipers has the same azimuth as the borehole, which is supposed to be the elongated direction (i.e., $N345^\circ$). Between 540 and 590 mbsf, the elongation is fairly constant (1.05) but it increases to 1.22 at 650 mbsf. Within this interval, the calipers show oscillations in the hole size with a wavelength of 10 m, which are probably related to drilling-induced washout rather than to contrasts in the sediment's strength. From 650 to 770 mbsf, the lengthening of the hole decreases by steps: 1.2 between 650 and 690 mbsf,

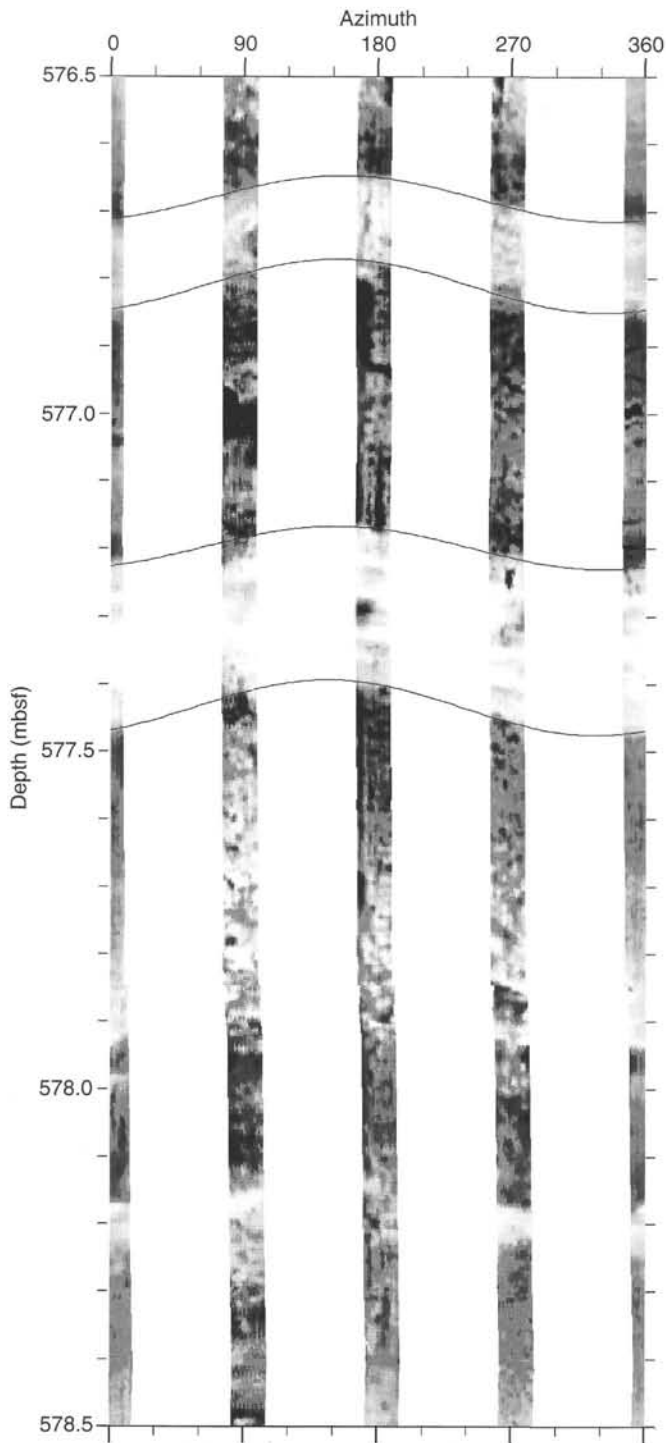


Figure 70. FMS image of bioturbated Subunit IIC. Horizontal scale is azimuth in degrees by reference to north. The sinusoids follow the trace of the intersection between bedding and borehole.

1.1 between 710 and 745 mbsf, and 1.0 (no elongation) between 750 and 770 mbsf. At 780 mbsf, the hole is locally elongated perpendicular to its azimuth. Below this depth, the average lengthening of the hole is 1.1, but can reach 1.26 to 1.3. These increases in borehole size are probably related to breakouts, as they are not cylindrical but occur only in the elongated direction.

The dip and azimuth of the sedimentary bedding were measured in the FMS images between 550 and 860 mbsf, with most of the mea-

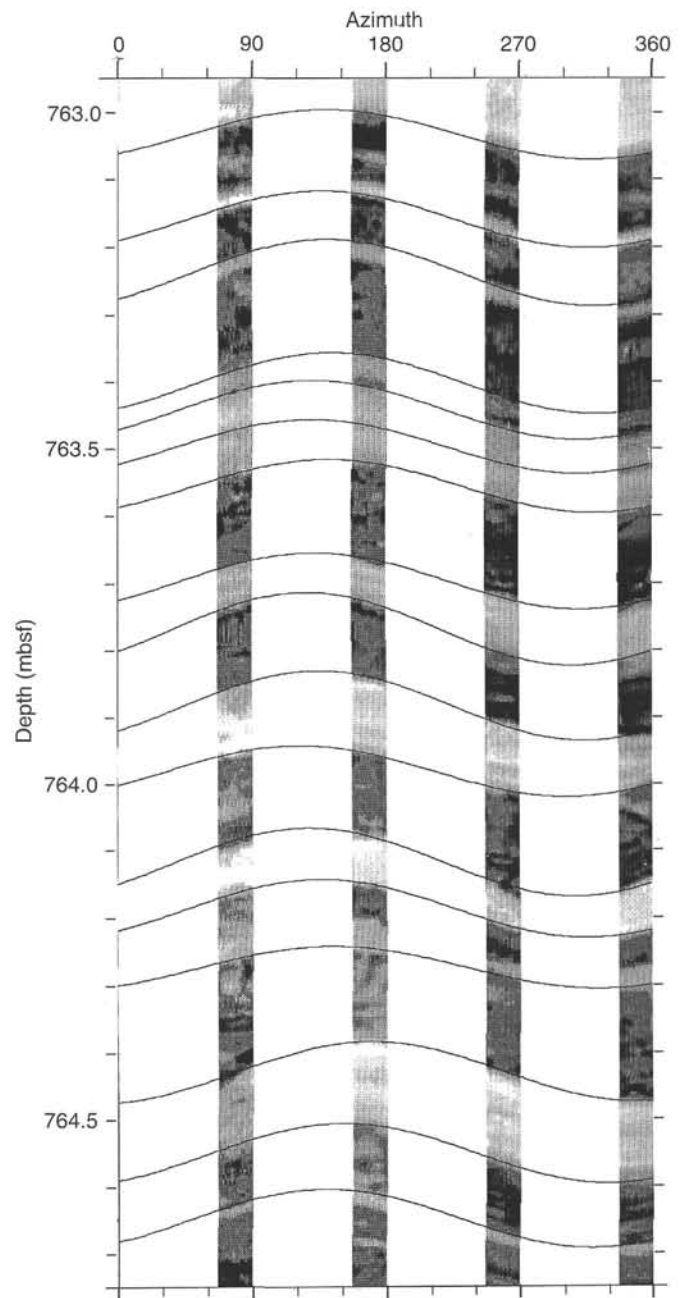


Figure 71. FMS image of the lower part of Subunit IIC. Same conventions as for Figure 70.

surements between 714 and 780 mbsf in the well-layered lower part of Subunit IIC (Fig. 74). The azimuth of the bedding is quite constant at about 320° (northwest; Fig. 75) and the average dip of the bedding increases with depth from 5° at 550 mbsf to 14° at 860 mbsf. But both azimuths and dips exhibit important variations about their average values that cannot be ascribed to measurement resolution: $\pm 30^\circ$ for azimuths, $\pm 5^\circ$ for dips. Moreover, the variations of dips and azimuths appear to be correlated (Fig. 76) and it may be possible to retrieve the rotation axis from a series of measurements made at a meter scale.

Two kinds of fractures can be observed on the FMS images: sub-vertical breakouts (conductive, open fractures) and dipping faults (resistive, sealed). Resistive fractures in the logged interval are mostly normal faults and veins filled by calcite (see "Structural Geology"

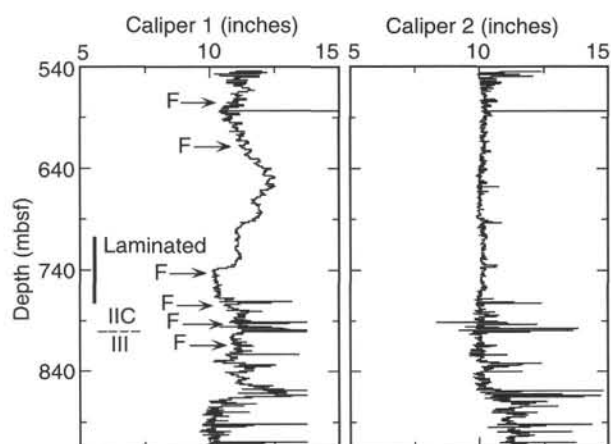


Figure 72. Width of Hole 959D as measured by calipers 1 and 2 in the interval logged by the FMS tool. Fault zones (F) observed on FMS images, the Subunit IIC/Unit III boundary, and the laminated unit are indicated.

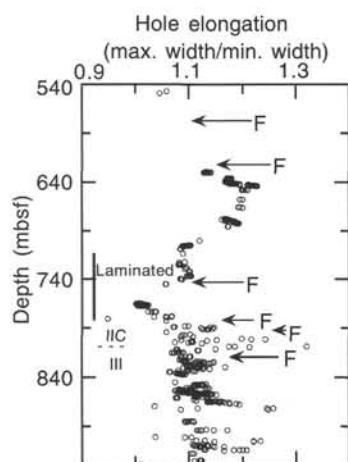


Figure 73. Elongation of Hole 959D. The hole lengthening equals the maximum width divided by the minimum width. The elongated axis is supposed to fit with the azimuth of the hole, and the measurements of the calipers are used only when one caliper has the azimuth of the hole. Same conventions as for Figure 72.

section, this chapter). The fracturing is localized in a few faulted zones, less than 10 m thick, at 575, 620, 745, 780, 795, and 820 mbsf (Fig. 77). The faulted zones between 745 and 820 mbsf can be correlated with important changes in log density (Fig. 68), log velocity (Fig. 69), and core measurements (see "Physical Properties" section, this chapter). A peculiar characteristic of all the fault zones is the dispersion of dip (from 20° to 70°) and azimuth (all directions) of the fault planes (Fig. 77). Low-dipping normal faults and dispersion of azimuths prevent a correlation between faulting and paleo-stresses. These faults are possibly related to gravity-driven sliding during lithification of the sediment, which may also explain the observed rotations of bedding.

Breakouts can be seen as a vertical conductive line in most of the logged FMS section, occurring mainly on the southern wall of the hole (Fig. 78). Some of them are disposed in an échelon pattern. Between 540 and 700 mbsf, breakouts are numerous, but only slightly increase the size of the hole; below 790 mbsf, the increase in hole size can be related to N345° open fractures. Breakout occurrence depends on the type of sediments (no breakouts appear in the well-lay-

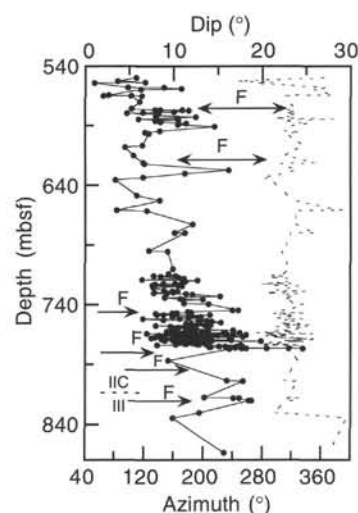


Figure 74. True dips (by reference to horizontal) (solid line) and azimuths (by reference to north) (dotted line) of sedimentary beds logged by the FMS in Hole 959D. The dots on the dip line show the location of measurements. F indicates a fault zone observed on FMS images, and IIC and III show the boundary between lithologic units.

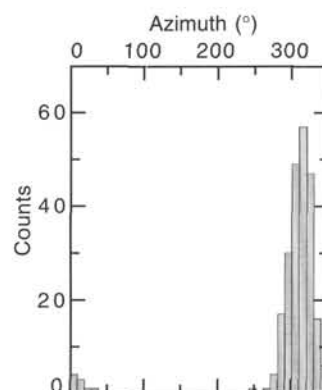


Figure 75. Azimuth of the bedding in 10° increments between 550 and 860 mbsf. Total count of 248.

ered sediment between 714 and 788 mbsf) and the strikes are most likely related to the present state of stress (S-Max = east-northeast-west-southwest and S-Min = north-northwest-south-southeast). As Site 959 is on a plateau close to a steep continental slope, one can expect the orientation of principal stresses to be linked to the strike of the continental slope, which dips south-southeast 5 miles south of this location. The sudden changes in hole elongation cannot be related to changes in lithology in the cores or FMS images, but appear to be limited by sealed fault zones. Two hypotheses can be proposed: either the strength of the sediments changes (but above 750 mbsf, there is no evidence of this from physical measurements), or the faulted zones act as stress screens, isolating several layers in which the regional stresses have the same orientation but change in intensity.

Borehole Temperature

The Lamont-Doherty Temperature Logging Tool (TLT) was run at the bottom of the Quad tool string for the upper logged interval (395–545 mbsf) in Hole 959D. Because of poor borehole conditions, it was replaced by a "hole finder" to enable greater depth to be

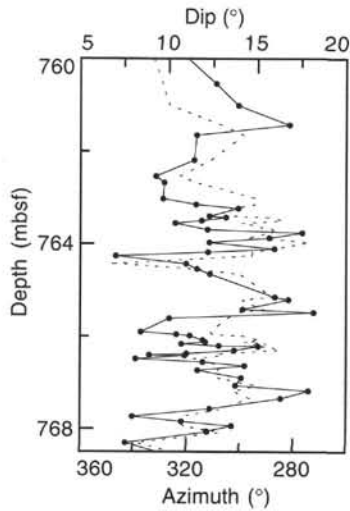


Figure 76. Variations of dip (solid line) and azimuth (dotted line) of the bedding between 760 and 768.5 mbsf.

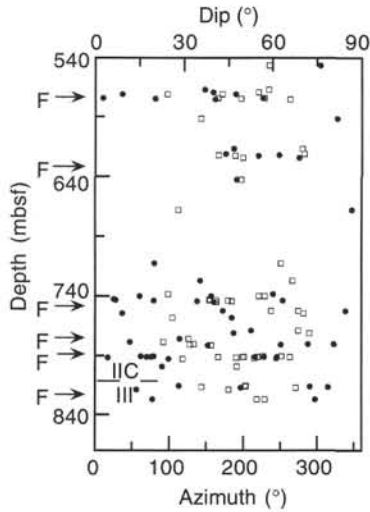


Figure 77. True dips (by reference to horizontal) (open squares) and azimuths (by reference to north) (solid circles) of fault planes logged by the FMS in Hole 959D. F indicates a faulted zone, and IIC and III show the boundary between lithologic units.

reached by the tool string in the lower section. The temperatures measured (Fig. 79) predominantly reflect the seawater temperature in the borehole, rather than the true formation temperature. The formation cools during drilling operations because of drilling fluid circulation and temperatures begin to rebound only after drilling has ceased. The depths were calculated from the pressures recorded by the tool.

An equilibrium thermal profile for this run is difficult to obtain because of fluid circulation during hole conditioning immediately before logging. The recorded maximum temperature, 22.5°C at 540 mbsf, can be considered a minimum estimate of equilibrium temperature. Temperature patterns in the uplog can be an evidence of thermal lags caused by mud clogging; downlog temperatures are less affected by this phenomenon. The temperatures increase approximately linearly between the base of the pipe and the bottom of the hole.

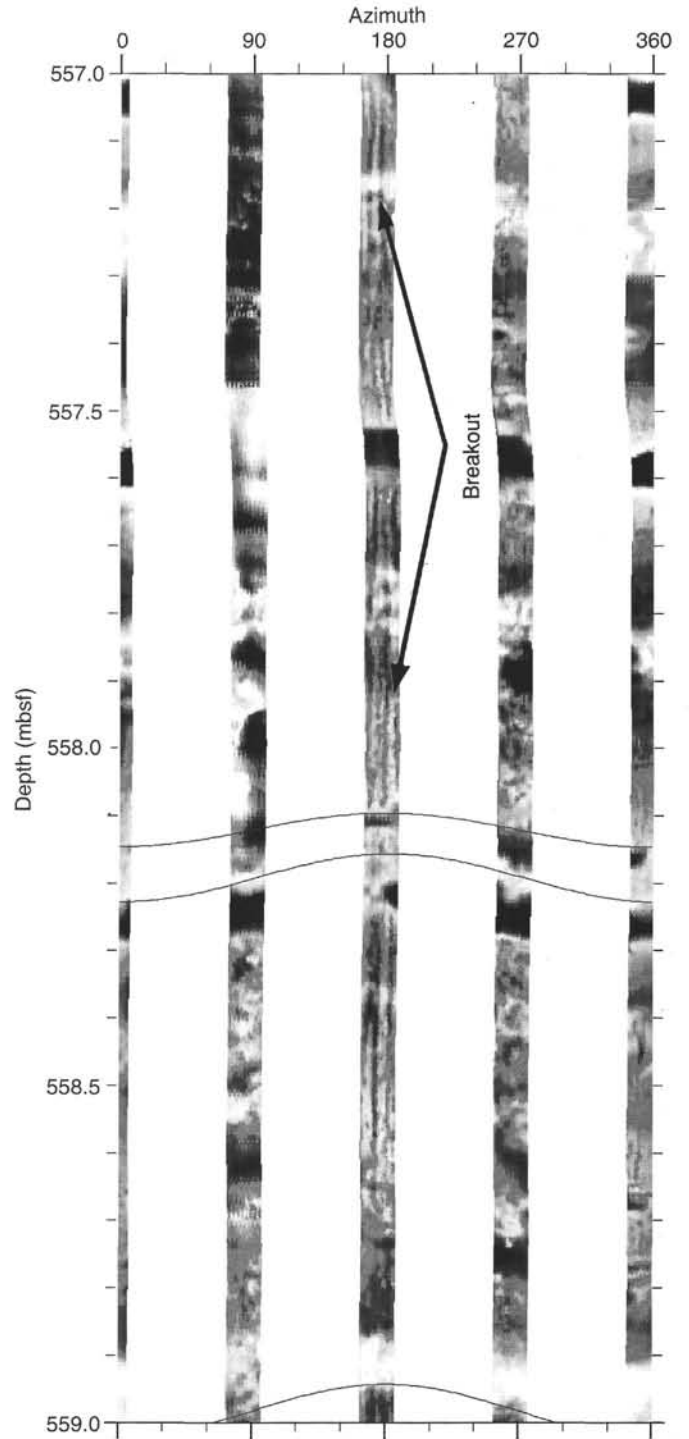


Figure 78. FMS image of the upper part of Subunit IIC. The dark vertical lines on the pad oriented southward (180°) are breakouts. Same conventions as for Figure 70.

Synthetic Seismogram

A log-derived synthetic seismogram was created using a symmetrical ricker wavelet with a negative polarity peak and assuming a variable density along the logged interval between 550 and 1050 mbsf. The sonic and density data within this interval were used to create an impedance log that was convolved with the wavelet to produce the synthetic seismogram. The result (Fig. 80) agrees well with the

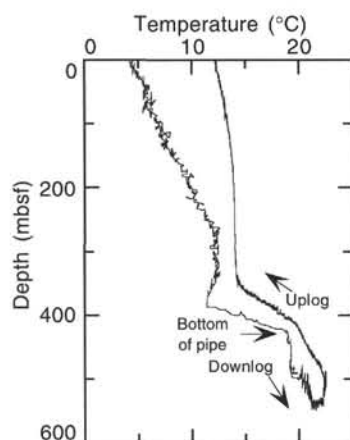


Figure 79. Borehole fluid temperature from the temperature logging tool, which was run during the upper pass of the Quad combination tool string in Hole 959D. Maximum temperature was 22.5°C at 540 mbsf.

seismic data and increases the precision of time/depth conversion. Some of the logged horizons are easily identifiable in the seismic section; the high-velocity, relatively high-density, and low-porosity level at approximately 750–800 mbsf corresponds with a strong, laterally consistent reflector at about 3.7 s. The low velocity and low density values at 1030 mbsf can be correlated with the event at 4.0 s on the seismic section. The logging data provide significant additional detail on the thickness and character of the depositional units. On the seismic section, Units I and II coincide with the upper seismic unit that is dominated by largely continuous reflectors. Unit III corresponds with an area of the seismic section where reflectivity decreases. High-amplitude, laterally continuous reflectors coincide with the Unit III/IV boundary at 3.7 s.

REFERENCES

- Baker, P.A., Gieskes, J.M., and Elderfield, H., 1982. Diagenesis of carbonates in deep-sea sediments: evidence from $\text{Sr}^{2+}/\text{Ca}^{2+}$ ratios and interstitial dissolved Sr^{2+} data. *J. Sediment. Petrol.*, 52:71–82.
- Baker, P.A., and Kastner, M., 1981. Constraints on the formation of sedimentary dolomite. *Science*, 213:215–216.
- Basile, C., Mascle, J., Popoff, M., Bouillin, J.P., and Mascle, G., 1993. The Côte d'Ivoire-Ghana transform margin: a marginal ridge structure deduced from seismic data. *Tectonophysics*, 222:1–19.
- Behrmann, J.H., Lewis, S.D., Musgrave, R.J., et al., 1992. *Proc. ODP, Init. Repts.*, 141: College Station, TX (Ocean Drilling Program).
- Berggren, W.A., Kent, D.V., and Van Couvering, J.A., 1985. The Neogene, Part 2. Neogene geochronology and chronostratigraphy. In Snelling, N.J. (Ed.), *The Chronology of the Geological Record*. Geol. Soc. London Mem., 10:211–260.
- Blow, W.H., 1969. Late middle Eocene to Recent planktonic foraminiferal biostratigraphy. In Brönnimann, P., and Renz, H.H. (Eds.), *Proc. First Int. Conf. Planktonic Microfossils, Geneva, 1967*: Leiden (E.J. Brill), 1:199–422.
- Bukry, D., 1981a. Pacific coast coccolith stratigraphy between Point Conception and Cabo Corrientes, Deep Sea Drilling Project Leg 63. In Yeats, R.S., Haq, B.U., et al., *Init. Repts. DSDP*, 63: Washington (U.S. Govt. Printing Office), 445–471.
- , 1981b. Synthesis of silicoflagellate stratigraphy for Maestrichtian to Quaternary marine sediments. In Warme, T.E., Douglas, R.C., and Winterer, E.L. (Eds.), *The Deep Sea Drilling Project: A Decade of Progress*. Spec. Publ.—Soc. Econ. Paleontol. Mineral., 32:433–444.
- Cande, S.C., and Kent, D.V., 1992. A new geomagnetic polarity time scale for the Late Cretaceous and Cenozoic. *J. Geophys. Res.*, 97:13917–13951.
- Carlson, R.L., and Christensen, N.I., 1977. Velocity anisotropy and physical properties of deep-sea sediments from the western South Atlantic. In
- Supko, P.R., Perch-Nielsen, K., et al., *Init. Repts. DSDP*, 39: Washington (U.S. Govt. Printing Office), 555–559.
- Chaisson, W.P., and Leckie, R.M., 1993. High-resolution Neogene planktonic foraminifer biostratigraphy of Site 806, Ontong Java Plateau (western equatorial Pacific). In Berger, W.H., Kroenke, L.W., Mayer, L.A., et al., *Proc. ODP, Sci. Results*, 130: College Station, TX (Ocean Drilling Program), 137–178.
- Cita, M.B., 1973. Pliocene biostratigraphy and chronostratigraphy. In Ryan, W.B.F., Hsü, K.J., et al. *Init. Repts. DSDP*, 13: Washington (U.S. Govt. Printing Office), 1343–1379.
- Curry, W.B., Shackleton, N.J., Richter, C., et al., 1995. *Proc. ODP, Init. Repts.*, 154: College Station, TX (Ocean Drilling Program).
- Donnelly, T.W., and Merrill, L., 1977. The scavenging of magnesium and other chemical species by biogenic opal in deep-sea sediments. *Chem. Geol.*, 19:167–186.
- Fenner, J., 1985. Late Cretaceous to Oligocene planktic diatoms. In Bolli, H.M., Saunders, J.B., and Perch-Nielsen, K. (Eds.), *Plankton Stratigraphy*: Cambridge (Cambridge Univ. Press), 713–762.
- Fornaciari, E., Raffi, I., Rio, D., Villa, G., Backman, J., and Olafsson, G., 1990. Quantitative distribution patterns of Oligocene and Miocene calcareous nannofossils from the western equatorial Indian Ocean. In Duncan, R.A., Backman, J., Peterson, L.C., et al., *Proc. ODP, Sci. Results*, 115: College Station, TX (Ocean Drilling Program), 237–254.
- Germeraad, J.H., Hopping, C.A., and Müller, J., 1968. Palynology of Tertiary sediments from tropical areas. *Rev. Palaeobot. Palynol.*, 6:189–348.
- Gieskes, J.M., 1981. Deep-sea drilling interstitial water studies: implications for chemical alteration of the oceanic crust, layers I and II. In Warme, J.E., Douglas, R.G., and Winterer, E.L. (Eds.), *The Deep Sea Drilling Project: A Decade of Progress*. Spec. Publ.—Soc. Econ. Paleontol. Mineral., 32:149–167.
- , 1983. The chemistry of interstitial waters of deep-sea sediments: interpretation of deep-sea drilling data. In Riley, J.P., and Chester, R. (Eds.), *Chemical Oceanography* (Vol. 8): London (Academic Press), 222–269.
- Hartmann, M., 1964. Zur Geochemie von Mangan und Eisen in der Ostsee. *Meyniana*, 14:3–20.
- Hartmann, M., Mueller, P.J., Suess, E., and van der Weijden, D.H., 1976. Chemistry of late Quaternary sediments and their interstitial waters from

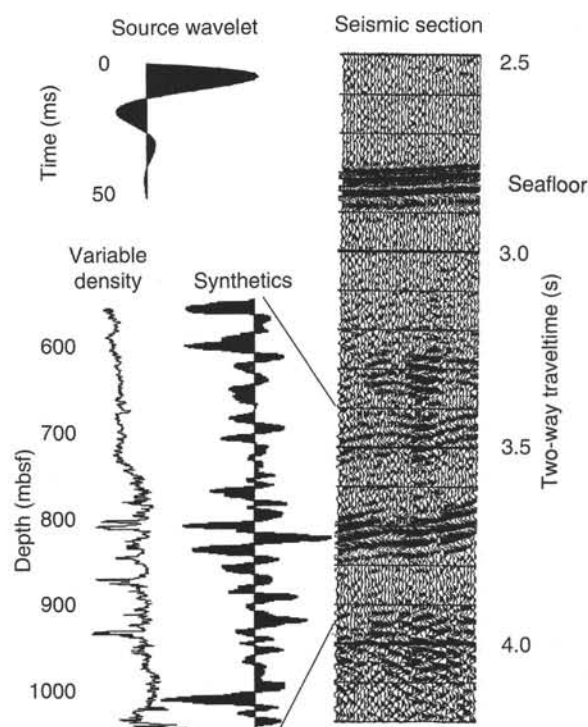


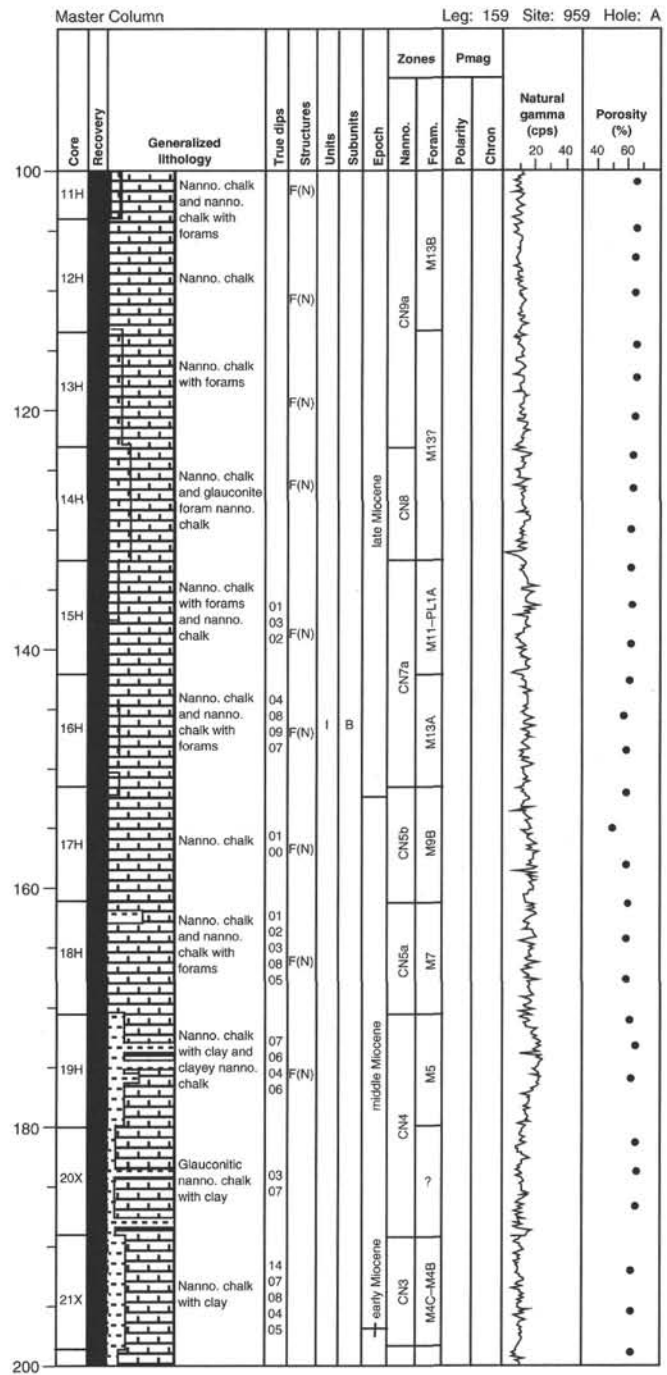
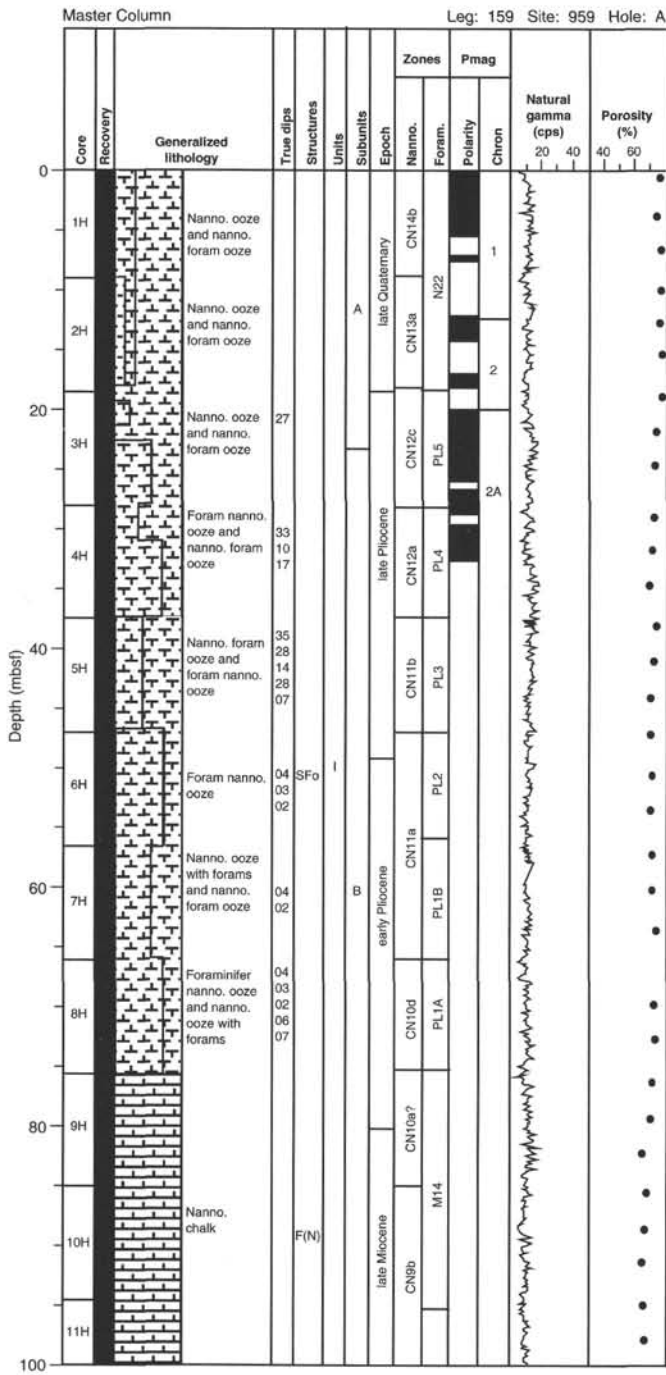
Figure 80. Comparison of seismic line with synthetic seismogram generated by convolving the source wavelet with an impedance curve based on the log-based velocity and density curves for Hole 959D.

- the N.W. African continental margin. *"Meteor" Forschungsergeb. Reihe C*, 24:1-67.
- Kastner, M., 1976. Diagenesis of basal sediments and basalts of Sites 322 and 323, Leg 35, Bellinghausen Abyssal Plain. In Hollister, C.D., Craddock, C., et al., *Init. Repts. DSDP*, 35: Washington (U.S. Govt. Printing Office), 513-527.
- , 1979. Silica polymorphs. In Burns, R.G. (Ed.), *Marine Minerals*. Mineral. Soc. Am., Rev. Mineral., 6:99-111.
- Kastner, M., Keene, J.B., and Gieskes, J.M., 1977. Diagenesis of siliceous oozes. I. Chemical controls on the rate of opal-A to opal-CT transformation—an experimental study. *Geochim. Cosmochim. Acta*, 41:1041-1059.
- Kennett, J.P., and Srinivasan, M.S., 1983. *Neogene Planktonic Foraminifera: A Phylogenetic Atlas*: Stroudsburg, PA (Hutchinson Ross).
- Masclé, J., Auroux, C., and the Shipboard Scientific Team, 1989. Les marges continentales transformantes ouest-africaines (Guinée, Côte d'Ivoire-Ghana) et la zone de fracture de la Romanche: Campagne Equamarge II (Février-Mars 1988). *Campagnes Océanographiques Françaises*, 8: Brest (IFREMER).
- Masclé, J., Basile, C., Pontoise, B., and Sage, F., 1995. The Côte d'Ivoire-Ghana transform margin: an example of an ocean-continent transform boundary. In Banda, E., Talwani, M., and Thorne, M. (Eds.), *Rifted Ocean-Continent Boundaries*, NATO ASI Ser.: Dordrecht (Kluwer), 327-339.
- Masclé, J., and Blarez, E., 1987. Evidence for transform margin evolution from the Côte d'Ivoire-Ghana continental margin. *Nature*, 326:378-381.
- Masclé, J., Guiraud, M., Basile, C., Benkhelil, J., Bouillin, J.P., Cousin, M., and Masclé, G., 1993. La marge transformante de Côte d'Ivoire-Ghana: premiers résultats de la campagne Equanaute (Juin 1992). *C. R. Acad. Sci. Ser. 2*, 316:1255-1261.
- Masclé, J., and the Scientific Party, 1994. Les marges continentales transformantes ouest-africaines—Côte d'Ivoire, Ghana, Guinée. *Série Repères Océan*, 5: Brest (IFREMER).
- Mayer, L., Pisias, N., Janecek, T., et al., 1992. *Proc. ODP, Init. Repts.*, 138: College Station, TX (Ocean Drilling Program).
- Perch-Nielsen, K., 1985. Mesozoic calcareous nannofossils. In Bolli, H.M., Saunders, J.B., and Perch-Nielsen, K. (Eds.), *Plankton Stratigraphy*: Cambridge (Cambridge Univ. Press), 329-426.
- Sage, F., 1994. Structure crustale d'une marge transformante et du domaine océanique adjacent: exemple de la marge de Côte d'Ivoire-Ghana [Ph.D. thesis]. Univ. Pierre et Marie Curie, Paris.
- Sayles, F.L., and Manheim, F.T., 1975. Interstitial solutions and diagenesis in deeply buried marine sediments: results from the Deep Sea Drilling Project. *Geochim. Cosmochim. Acta*, 39:103-128.
- Traverse, A., 1988. *Paleopalynology*: Boston (Unwyn Hyman).

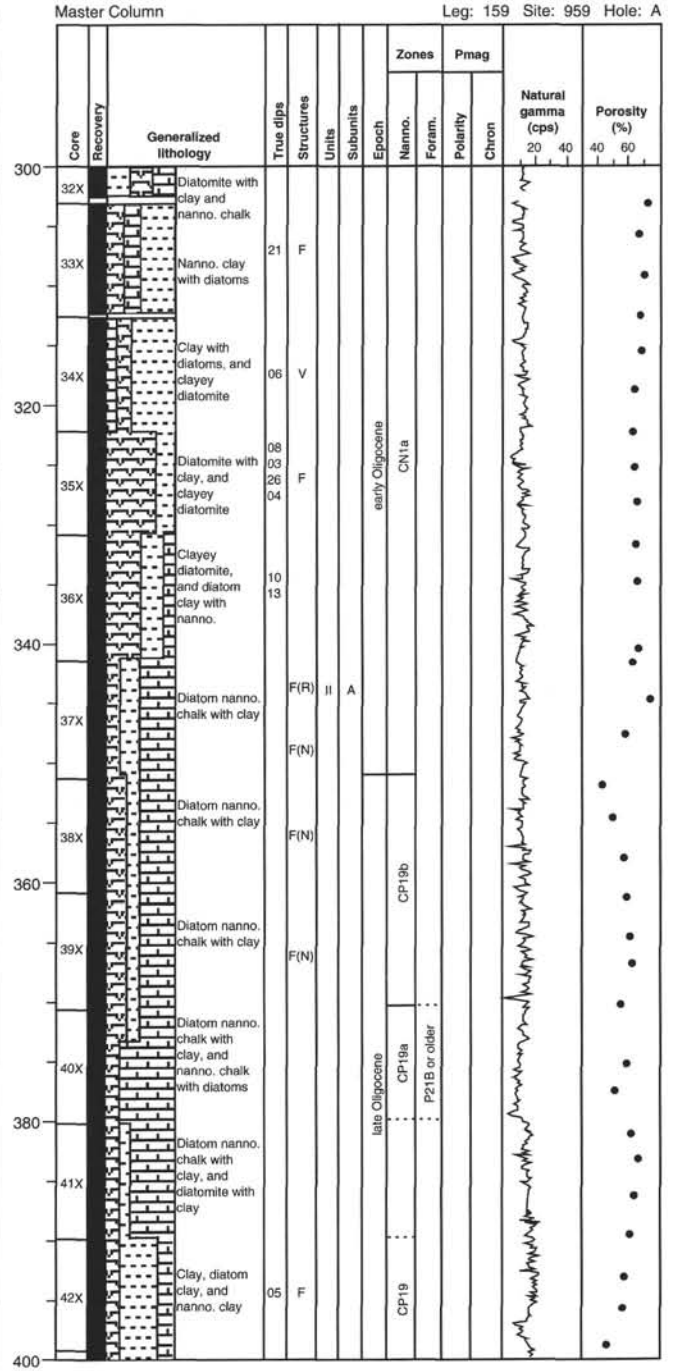
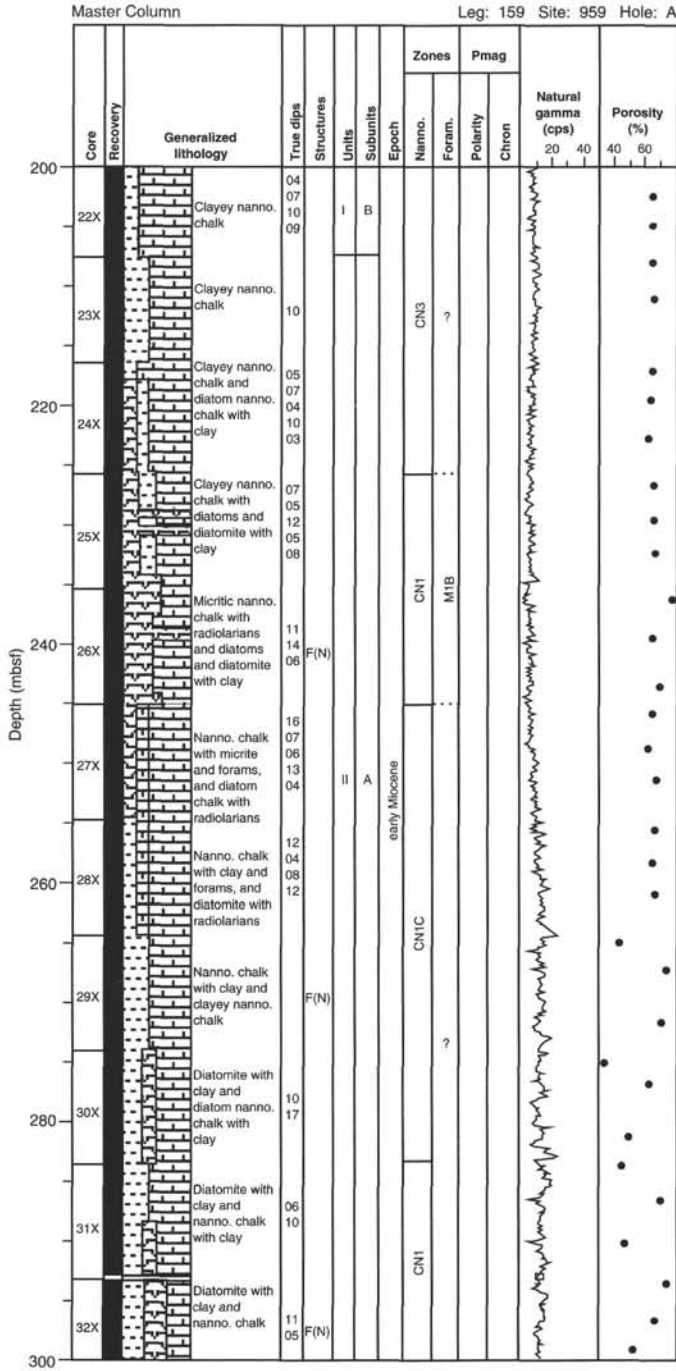
Ms 159IR-105

NOTE: For all sites drilled, core-description forms ("barrel sheets") and core photographs can be found in Section 4, beginning on page 317. Smear-slide data can be found in Section 5, beginning on page 587. Scanned structural VCDs, structural data spreadsheets, and selected scanned microstructures are included on the CD-ROM in the back of this volume. Also presented on the CD-ROM are all processed logs (including FMS, dipmeter, BRG temperature, high-resolution density, and neutron data), sonic waveforms, and explanatory text.

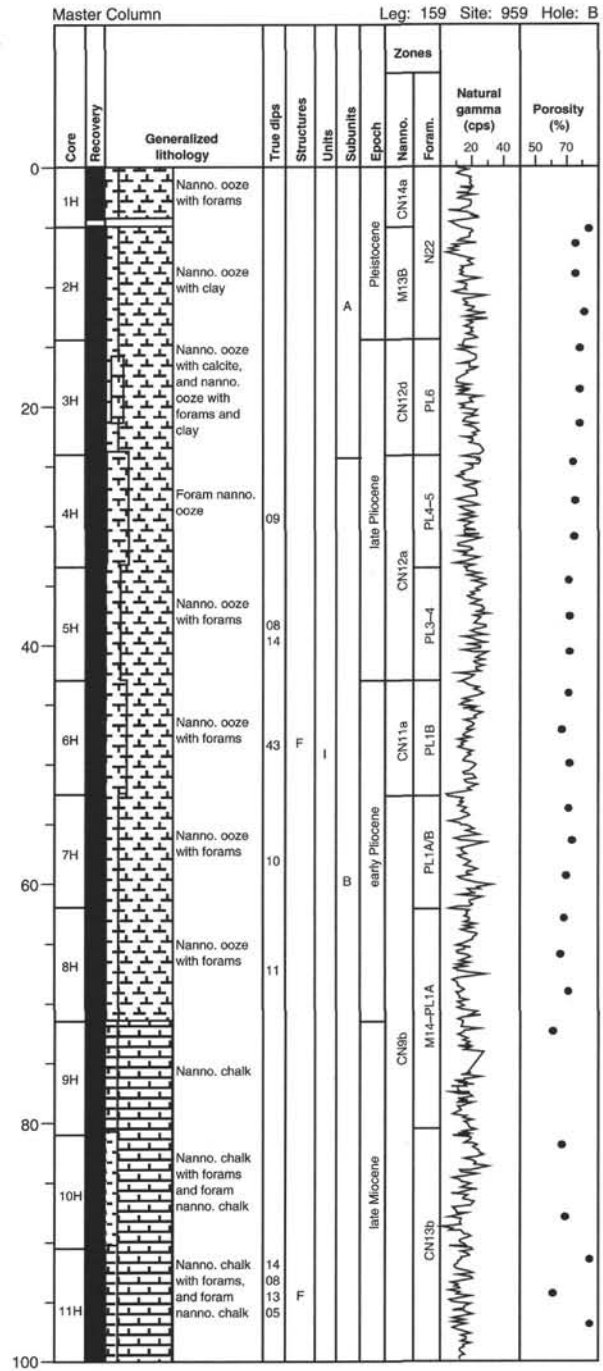
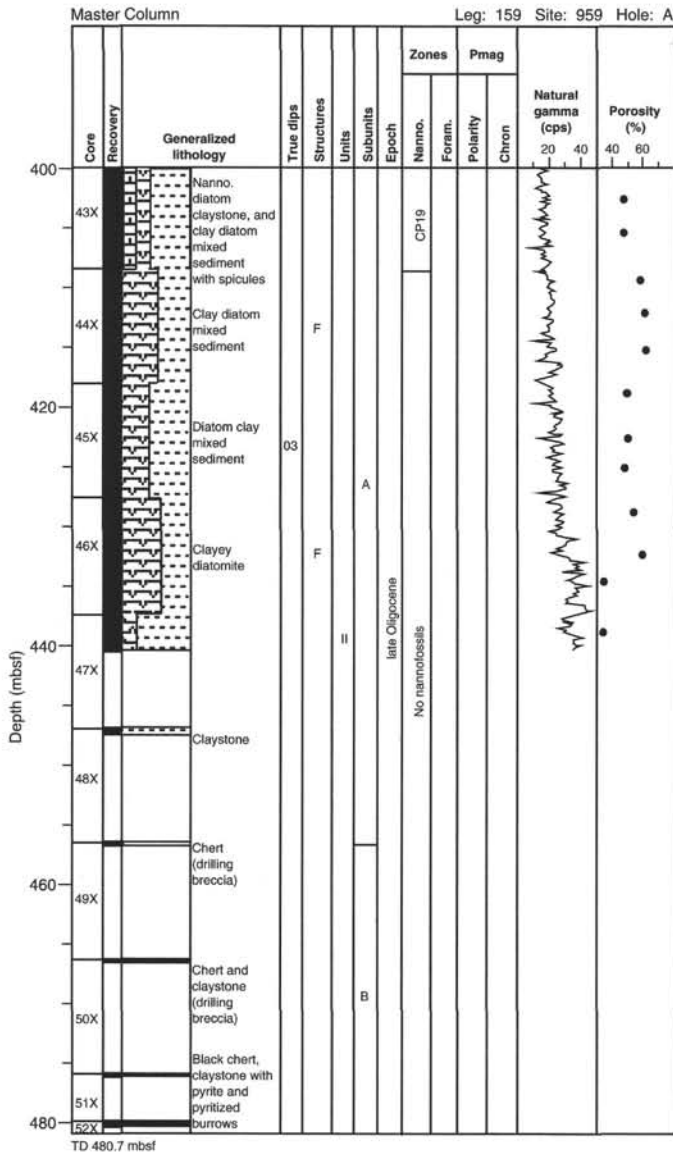
APPENDIX A
Site 959 Master Column



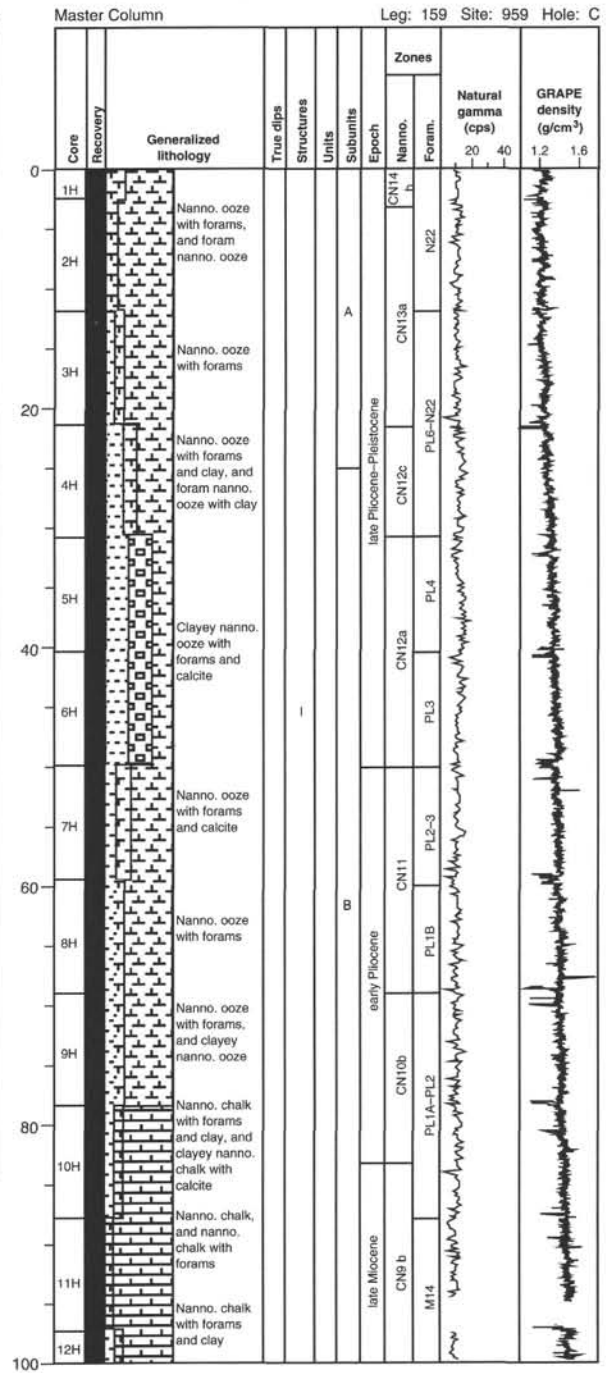
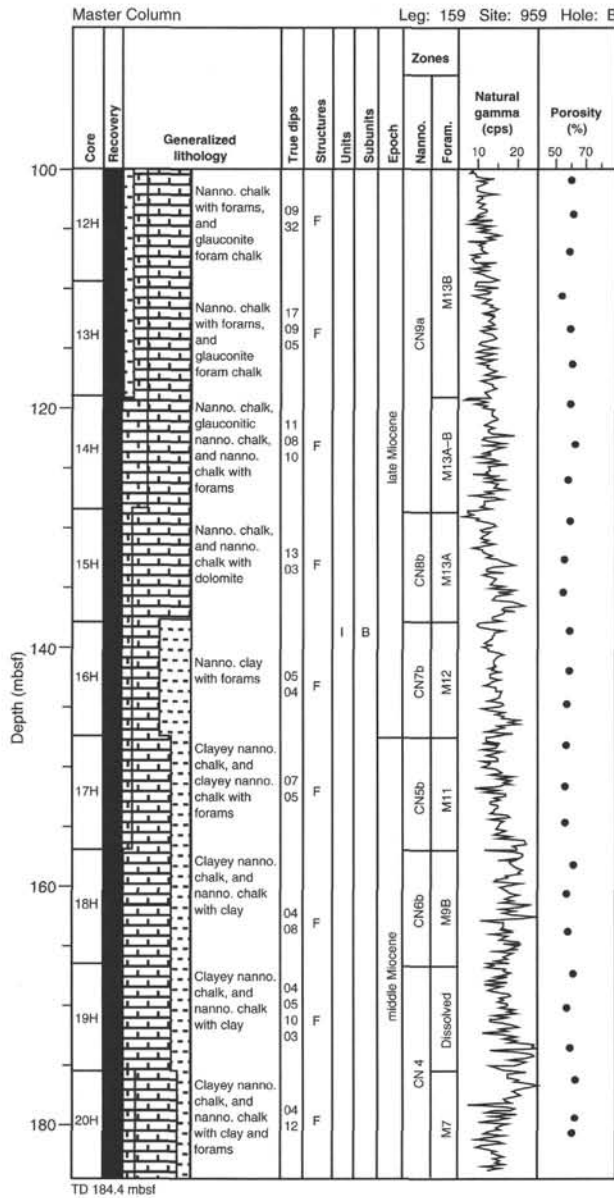
Appendix A (continued).



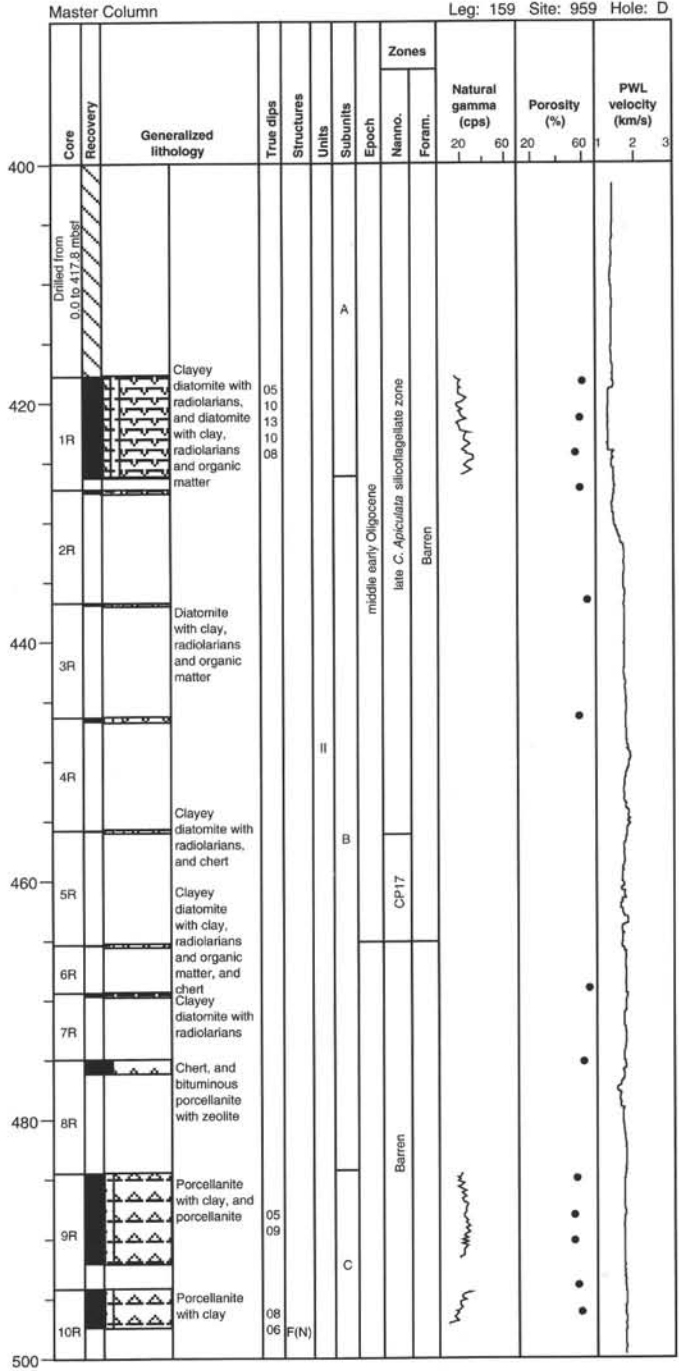
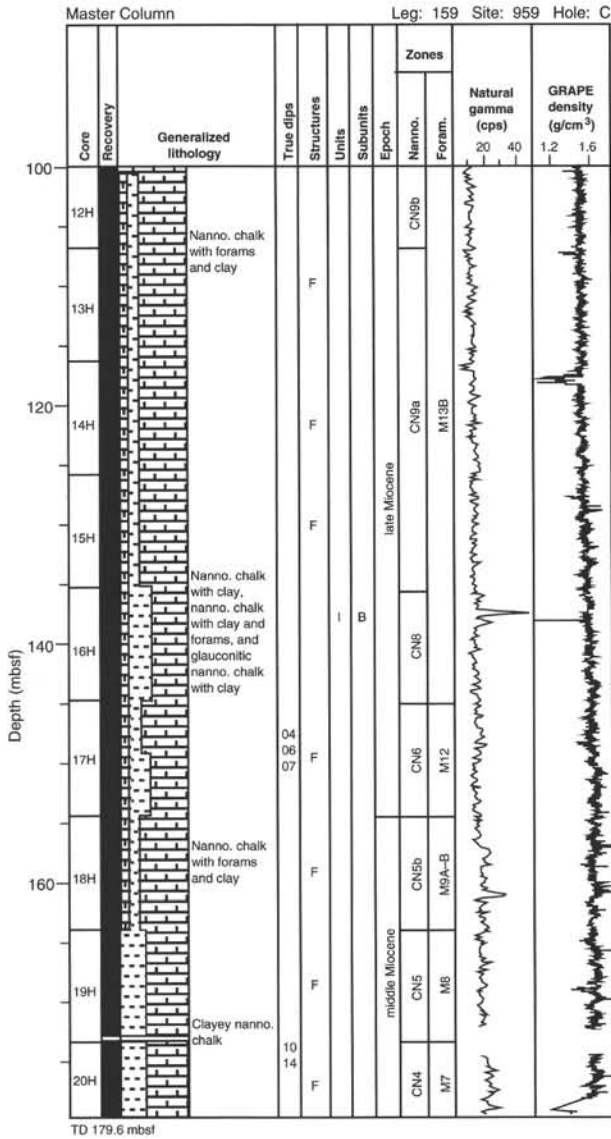
Appendix A (continued).



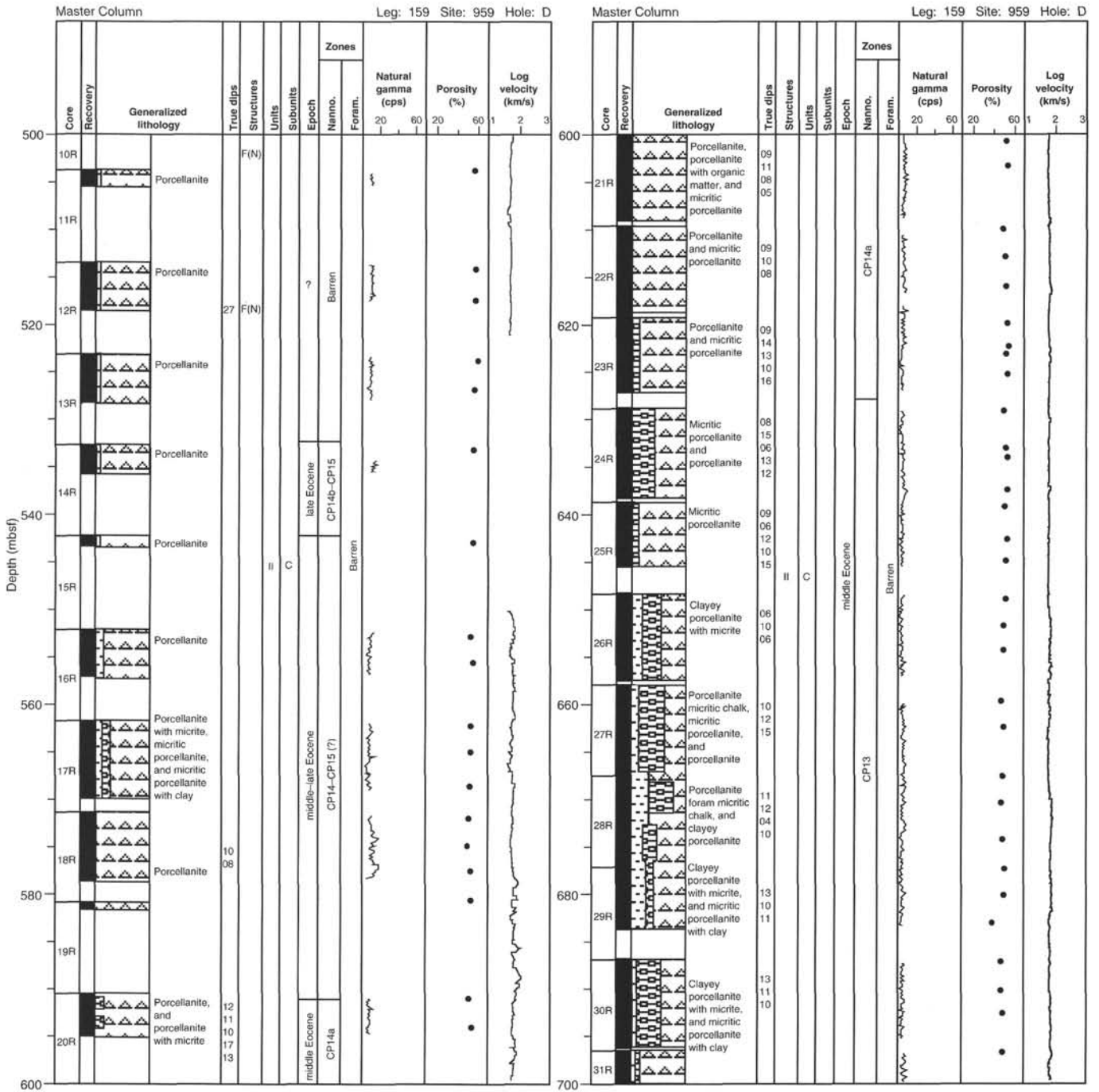
Appendix A (continued).



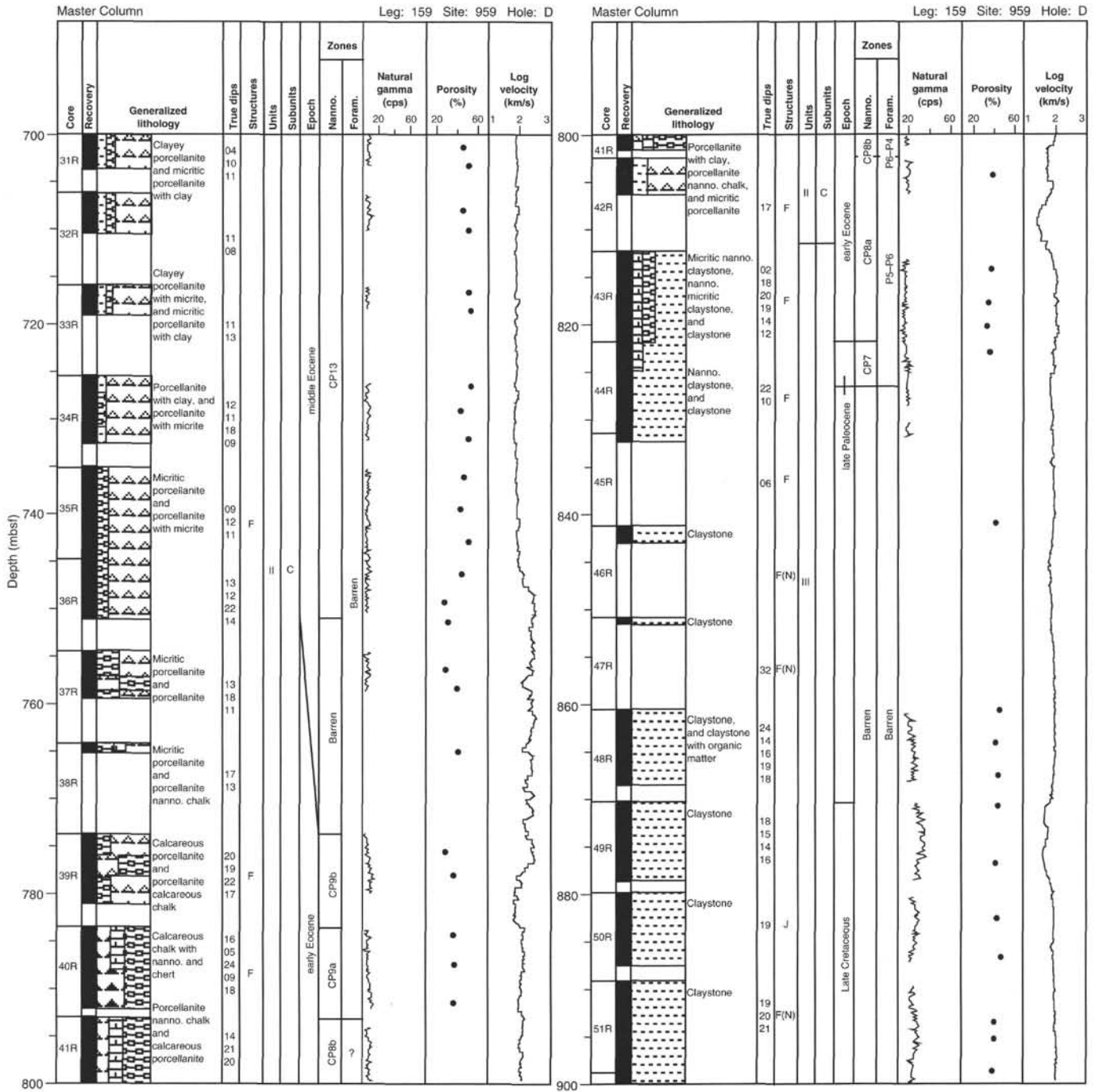
Appendix A (continued).



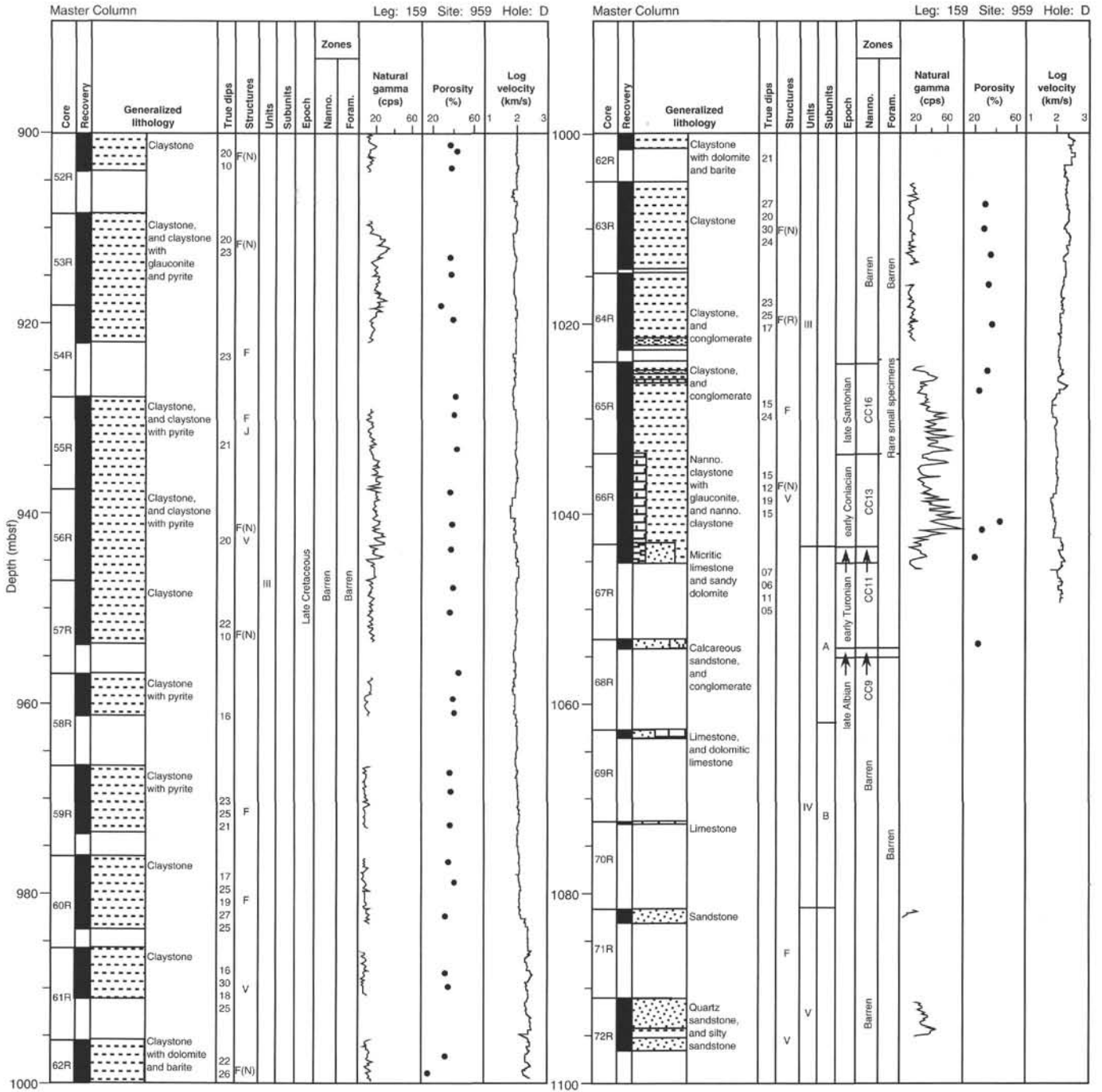
Appendix A (continued).



Appendix A (continued).



Appendix A (continued).



SHORE-BASED LOG PROCESSING HOLE 959D

Bottom felt: 2102 mbrf (used for depth shift to seafloor)

Total penetration: 1158.9 mbsf

Total core recovered: 429.03 m (57.9%)

Logging Runs

Logging string 1: DIT/SDT/HLDT/CNTG/NGT

Logging string 2: FMS/GPIT/NGT

Logging string 3: ACT/GST/NGT

Wireline heave compensator was used to counter ship heave resulting from the mild sea conditions.

Bottom-hole Assembly

The following bottom-hole assembly, drill pipe or casing depths are as they appear on the logs after differential depth shift (see "Depth Shift" section) and depth shift to the seafloor. As such, there might be a discrepancy with the original depths given by the drillers on board. Possible reasons for depth discrepancies are ship heave, use of wireline heave compensator, and drill string and/or wireline stretch.

DIT/SDT/HLDT/CNTG/NGT: Bottom-hole assembly at ~392 mbsf.

FMS/GPIT/NGT: Did not reach bottom-hole assembly.

ACT/GST/NGT: Bottom-hole assembly at ~545 mbsf.

Processing

Depth shift: Reference run for depth shift: DIT/SDT/HLDT/CNTG/NGT. All original logs have been interactively depth shifted with reference to NGT from DIT/SDT/HLDT/CNTG/NGT run, and to the seafloor (-2102 m).

Gamma-ray processing: NGT data have been processed to correct for borehole size and type of drilling fluid.

Acoustic data processing: The sonic logs have been processed to eliminate some of the noise and cycle skipping experienced during the recording.

Geochemical processing: (For detailed explanation of the processing please refer to the "Explanatory Notes" chapter, this volume,

or to the geochem.doc file on the enclosed CD-ROM). The elemental yields recorded by the GST tool represent the relative contribution of only some of the rock-forming elements (iron, calcium, chlorine, silica, sulfur, hydrogen, gadolinium, and titanium—the last two computed during geochemical processing) to the total spectrum. Because other rock-forming elements are present in the formation (such as aluminum, potassium, etc.), caution is recommended in using the yields to infer lithologic changes. Instead, ratios (see acronyms.doc on CD-ROM) are more appropriate to determine changes in the macroscopic properties of the formation. A list of oxide factors used in geochemical processing includes the following:

SiO₂ = 2.139

CaCO₃ = 2.497

FeO* = 1.358

TiO₂ = 1.668

K₂O = 1.205

Al₂O₃ = 1.889

FeO* computed using an oxide factor that assumes a 50:50 combination of Fe₂O₃ and FeO factors.

Quality Control

Data recorded through bottom-hole assembly, such as the NGT above 492 mbsf, should be used qualitatively only because of the attenuation on the incoming signal.

Hole diameter was recorded by the hydraulic caliper on the HLDT tool (CALI), and the caliper on the FMS string (C1 and C2).

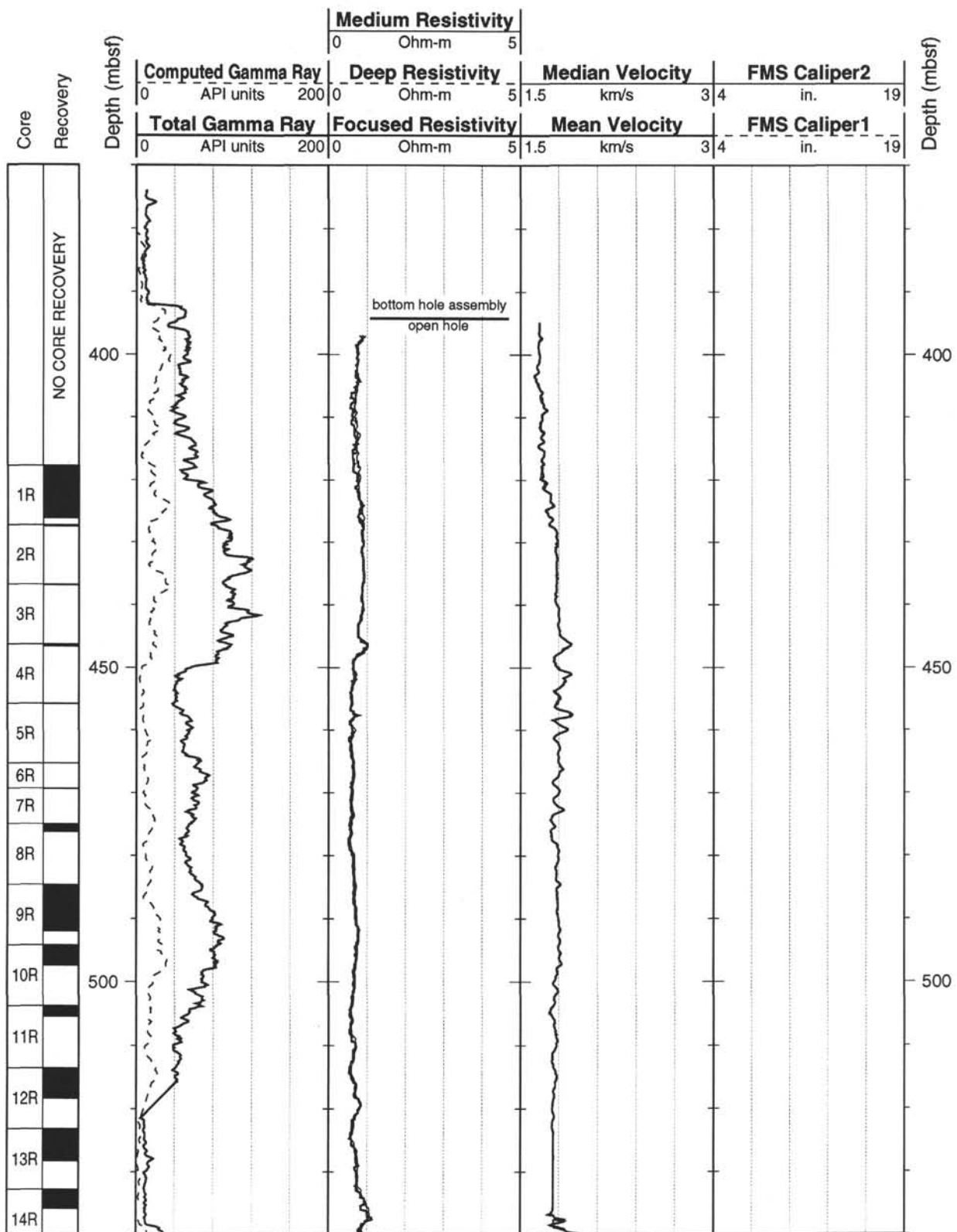
FACT = quality control curve in geochemical processing. Accuracy of the estimates is inversely proportional to the magnitude of the curve.

Details of standard shore-based processing procedures are found in the "Explanatory Notes" chapter, this volume. For further information about the logs, please contact:

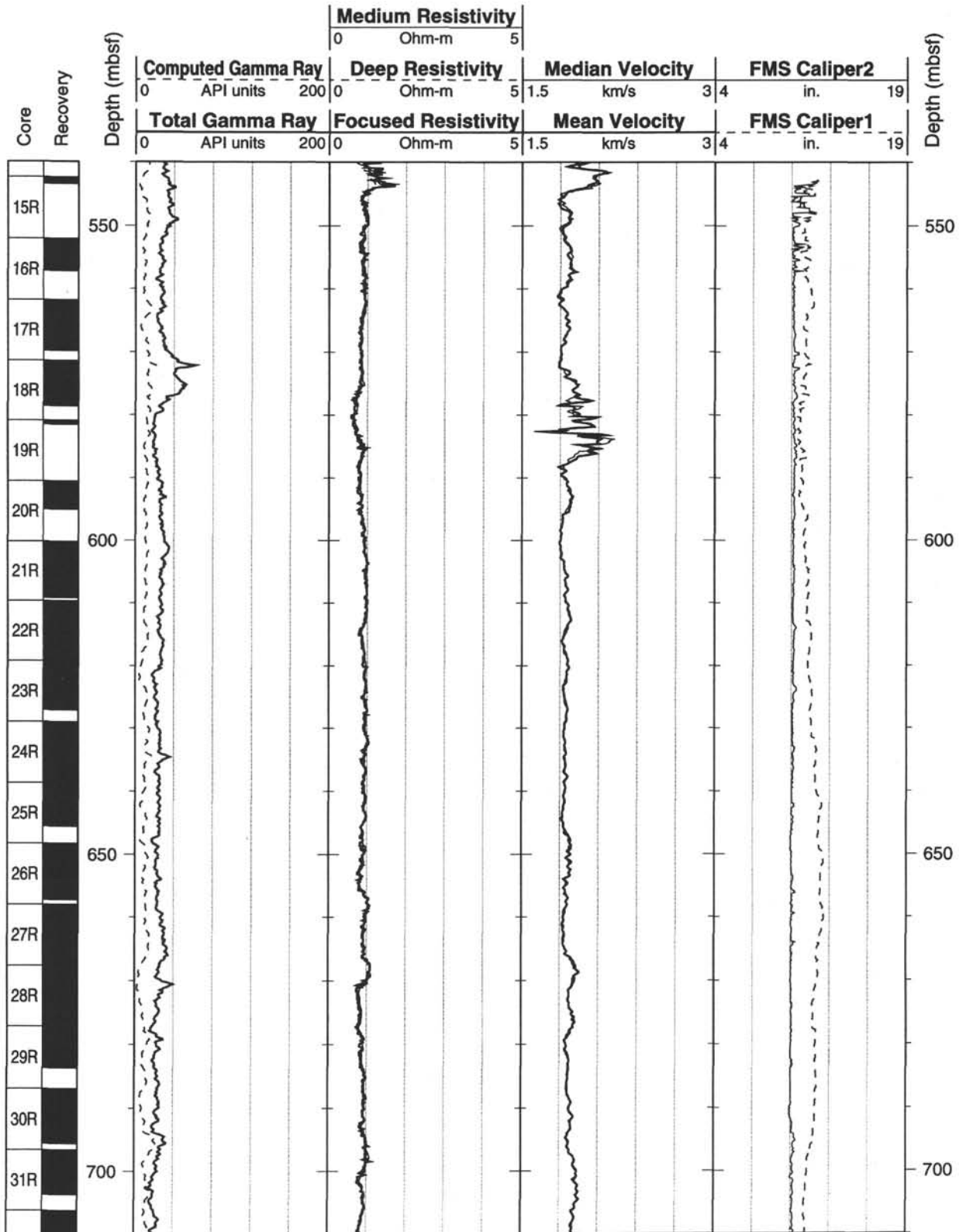
Cristina Broglia
Phone: 914-365-8343
Fax: 914-365-3182
email: chris@ldeo.columbia.edu

Elizabeth Pratson
Phone: 914-365-8313
Fax: 914-365-3182
email: beth@ldeo.columbia.edu

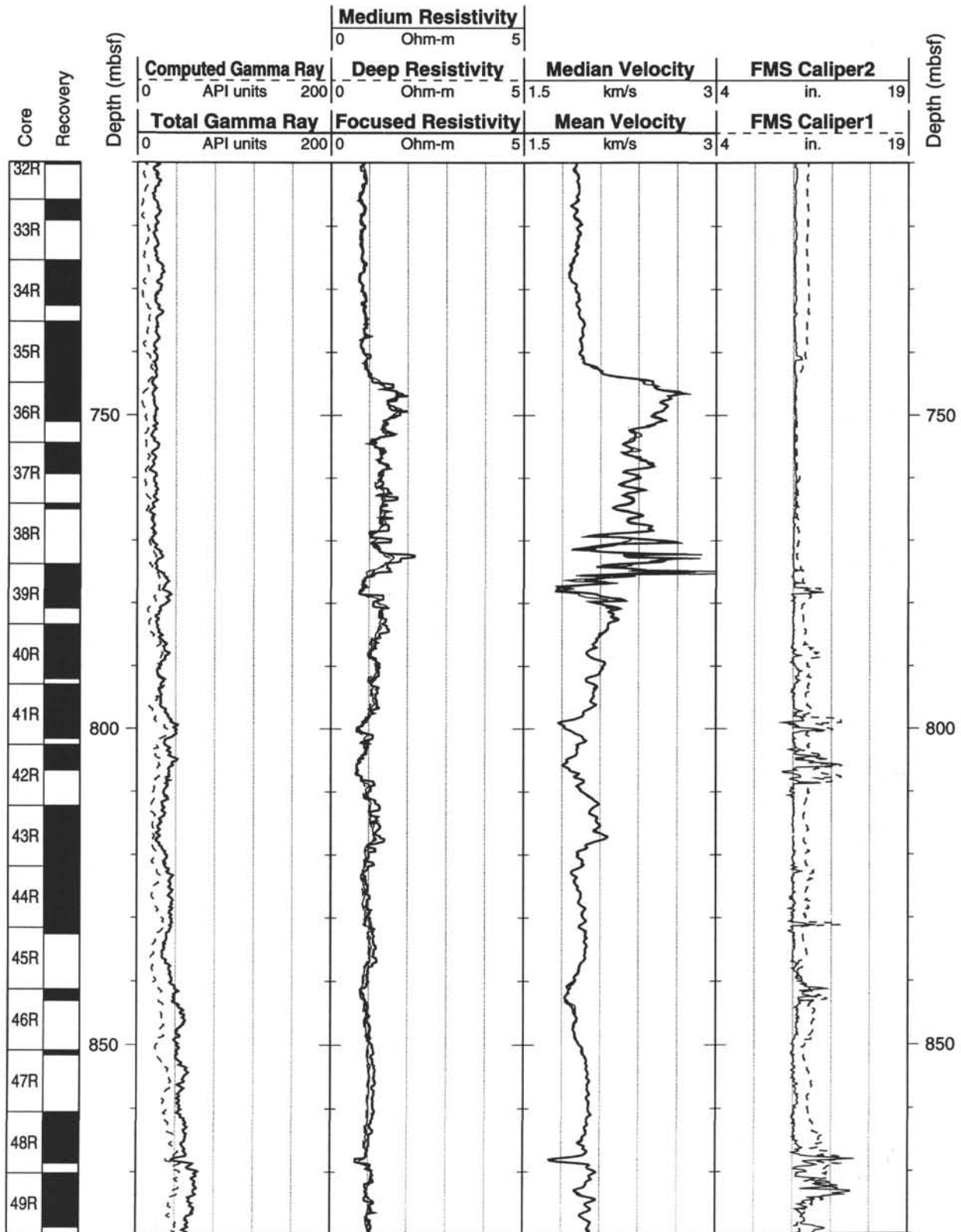
Hole 959D: Natural Gamma Ray-Resistivity-Sonic Logging Data



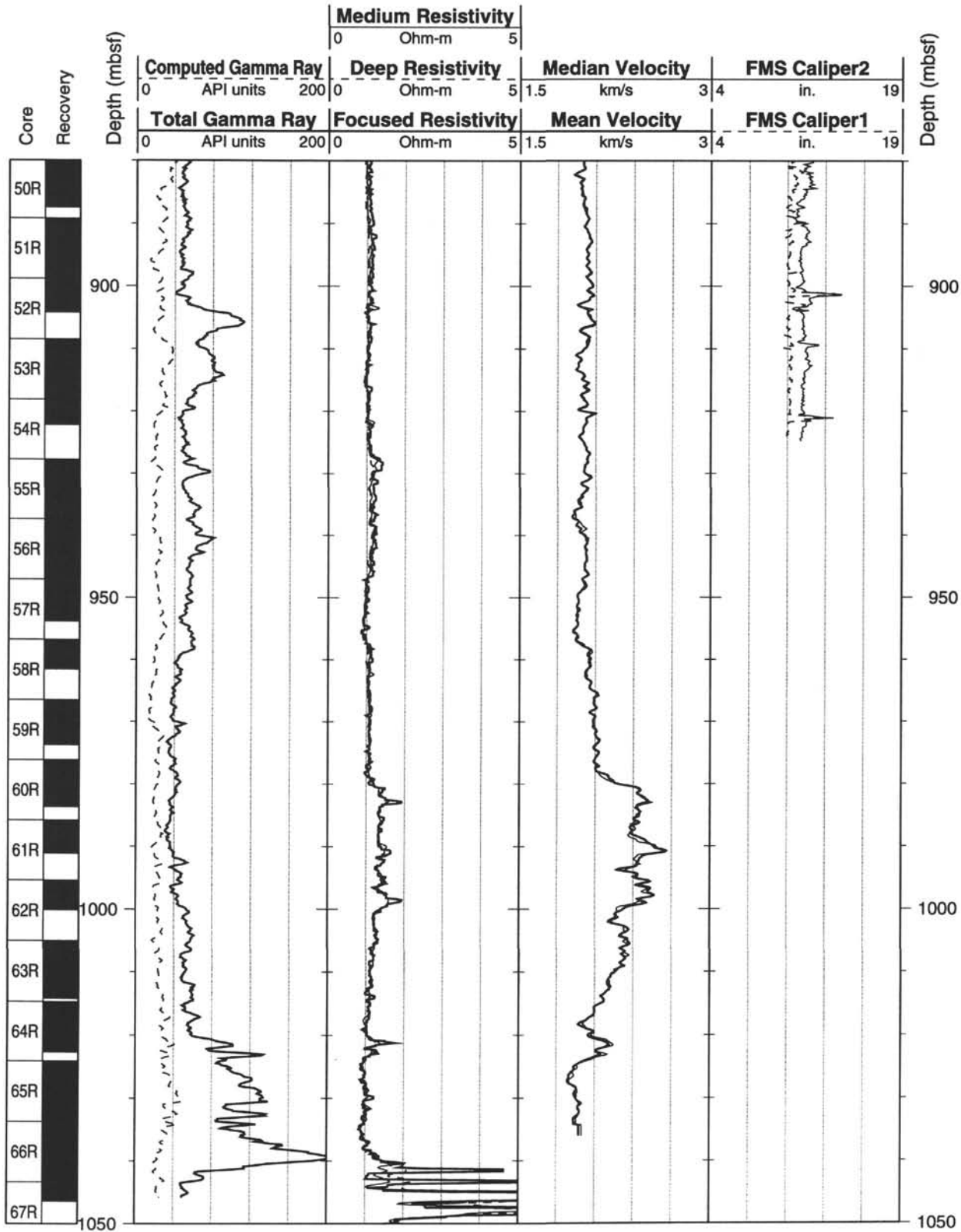
Hole 959D: Natural Gamma Ray-Resistivity-Sonic Logging Data (cont.)



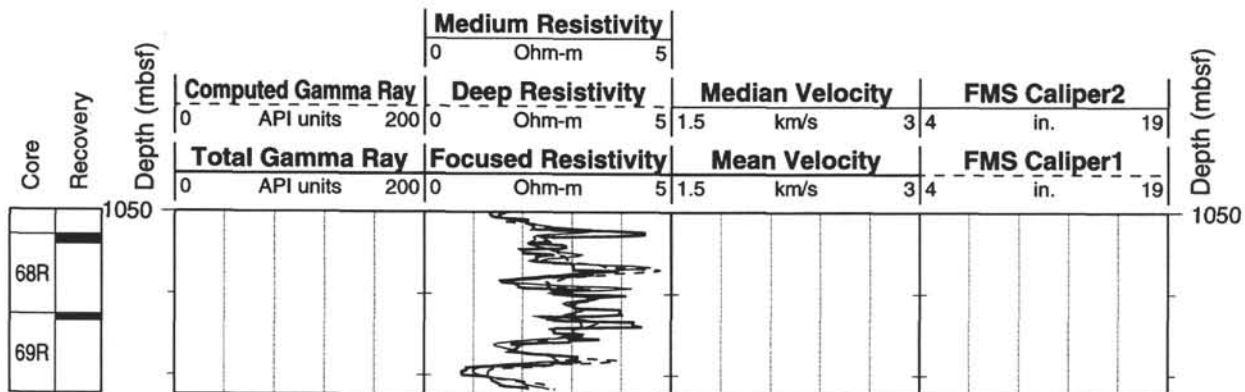
Hole 959D: Natural Gamma Ray-Resistivity-Sonic Logging Data (cont.)



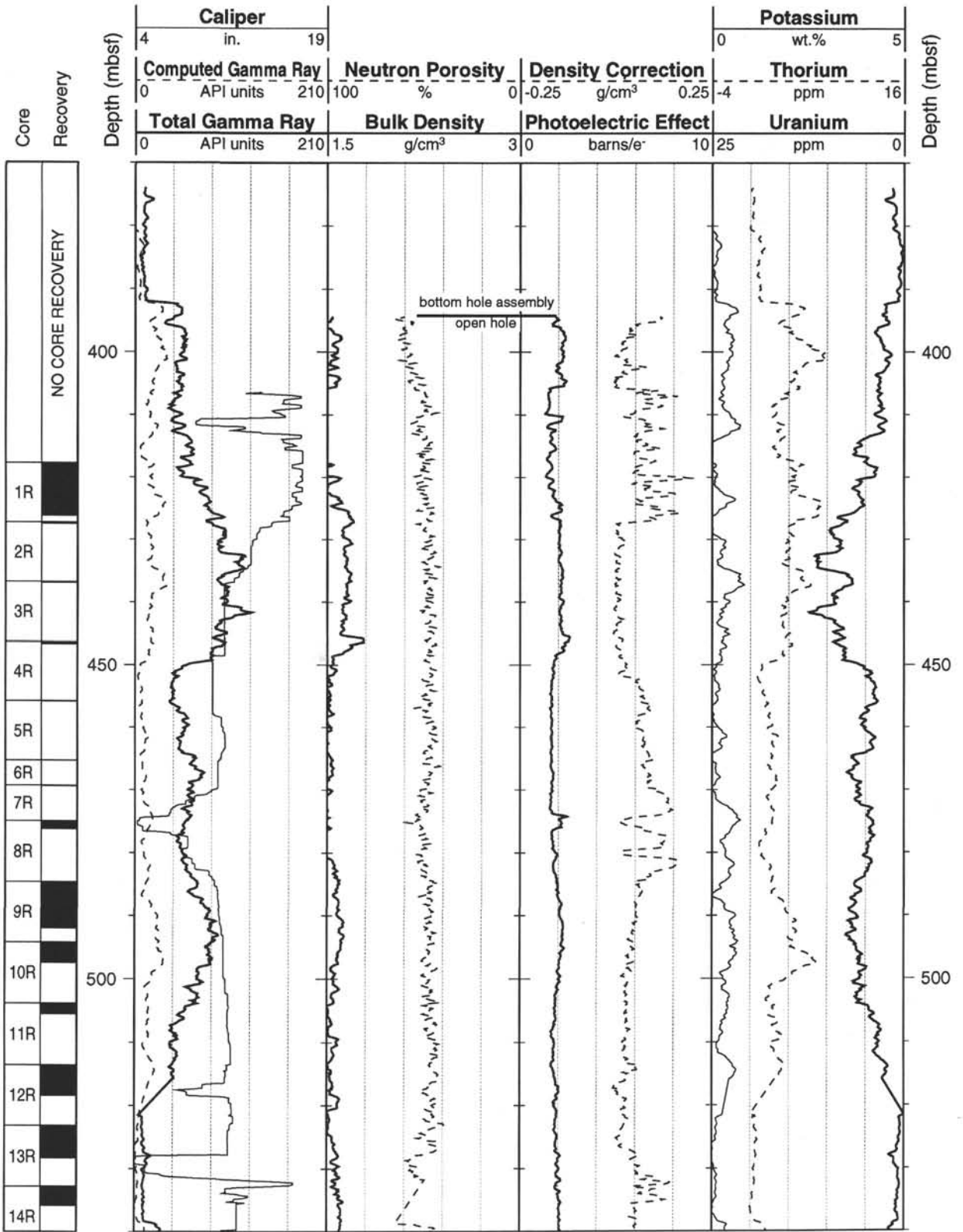
Hole 959D: Natural Gamma Ray-Resistivity-Sonic Logging Data (cont.)



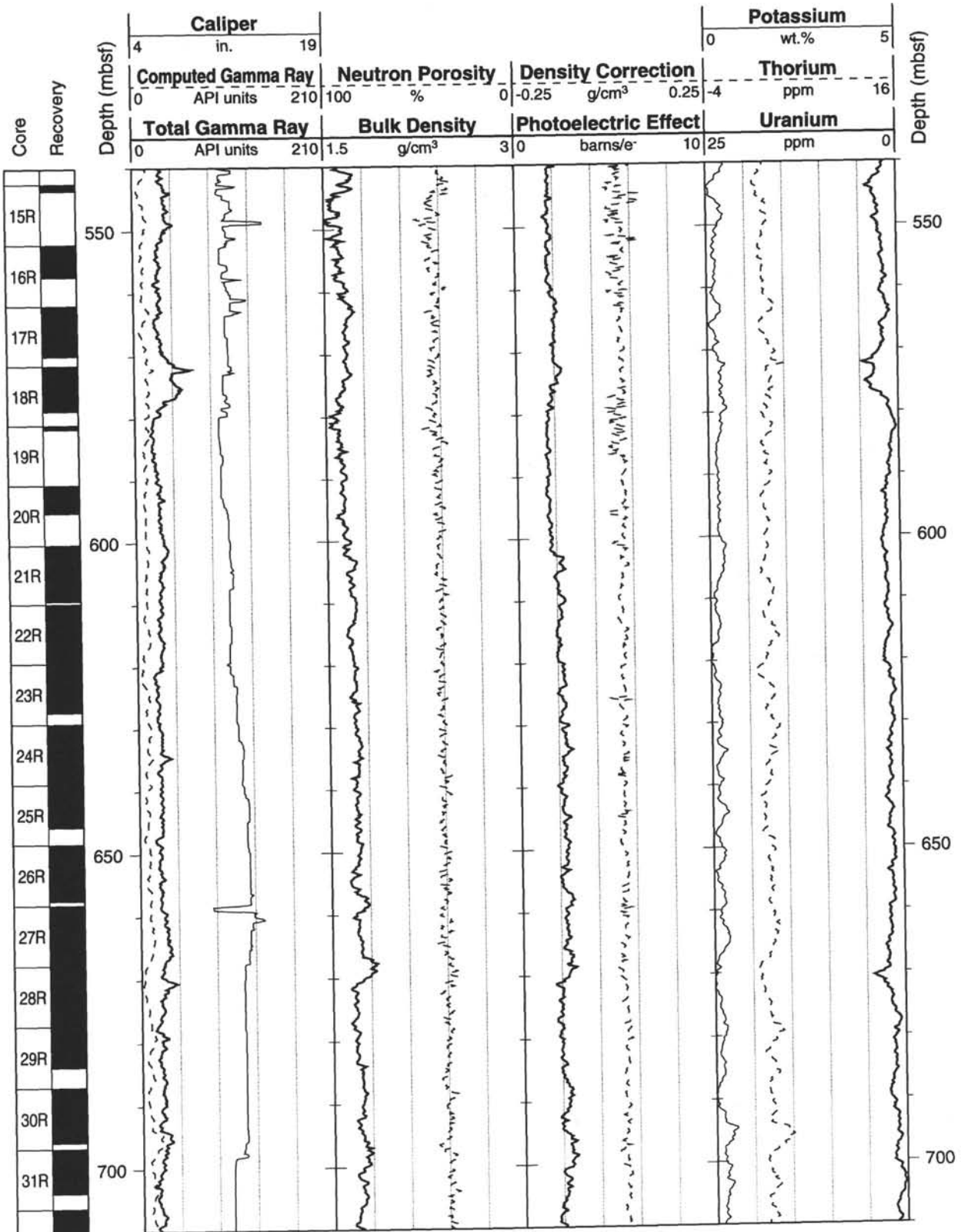
Hole 959D: Natural Gamma Ray-Resistivity-Sonic Logging Data (cont.)



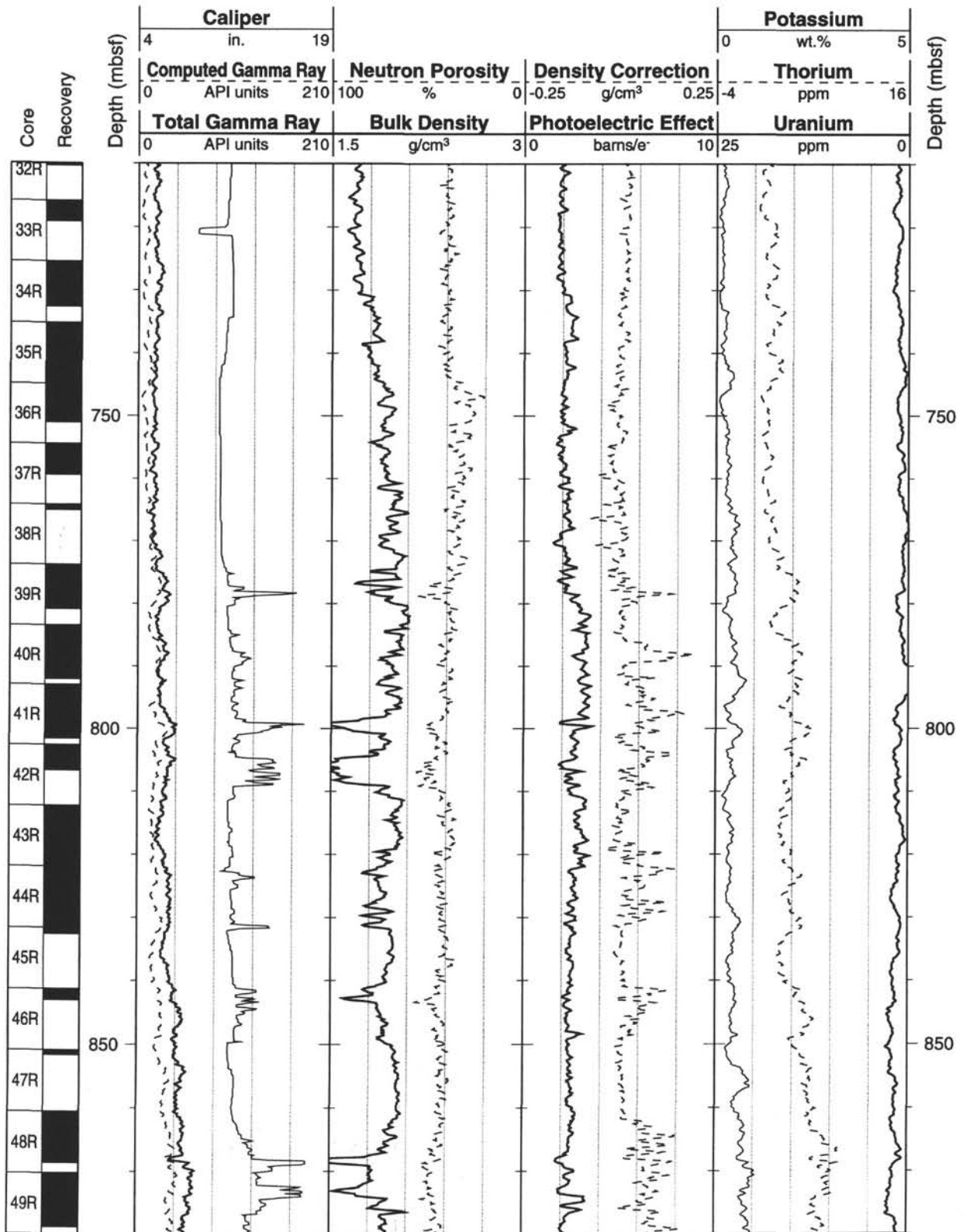
Hole 959D: Natural Gamma Ray-Density-Porosity Logging Data



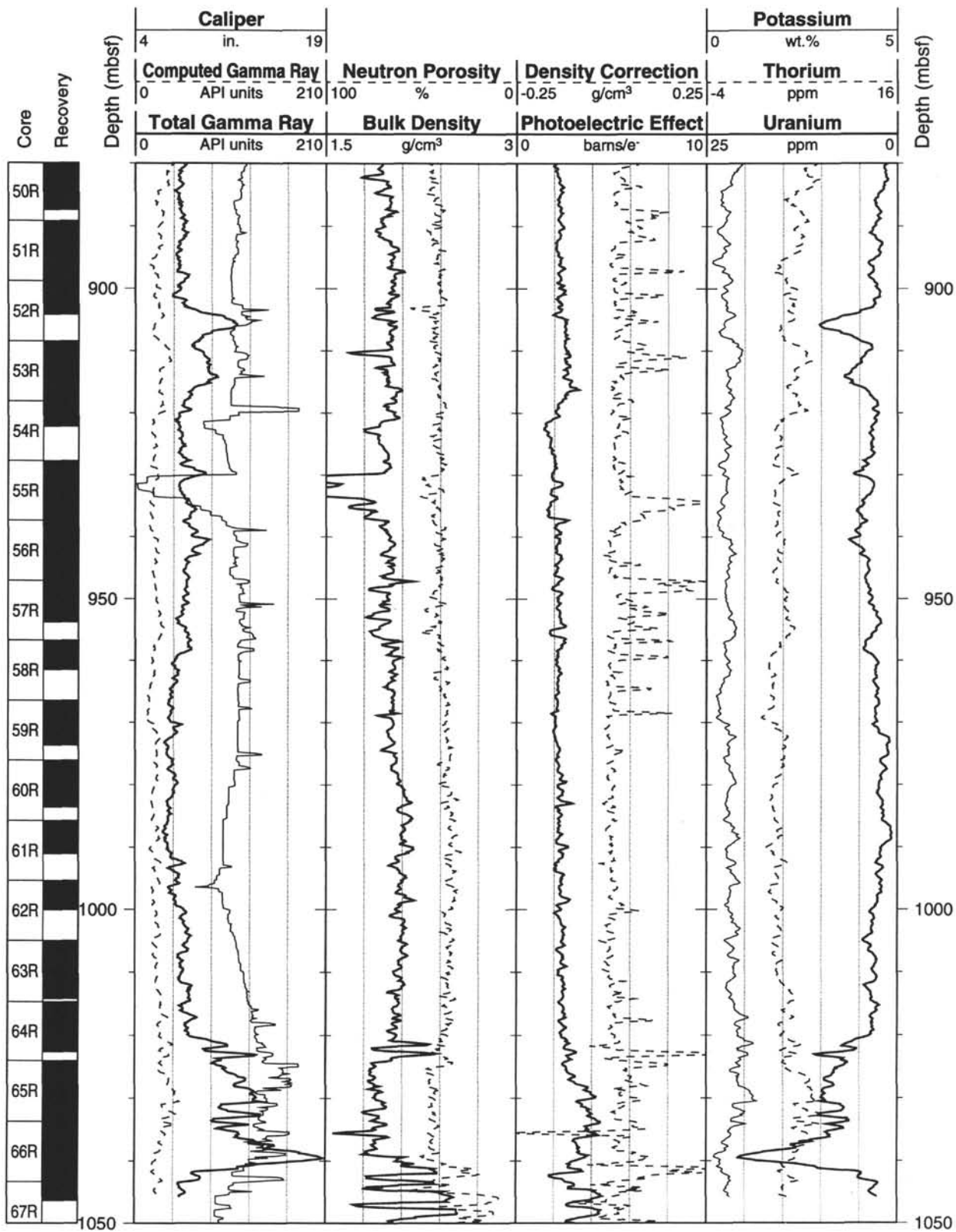
Hole 959D: Natural Gamma Ray-Density-Porosity Logging Data (cont.)



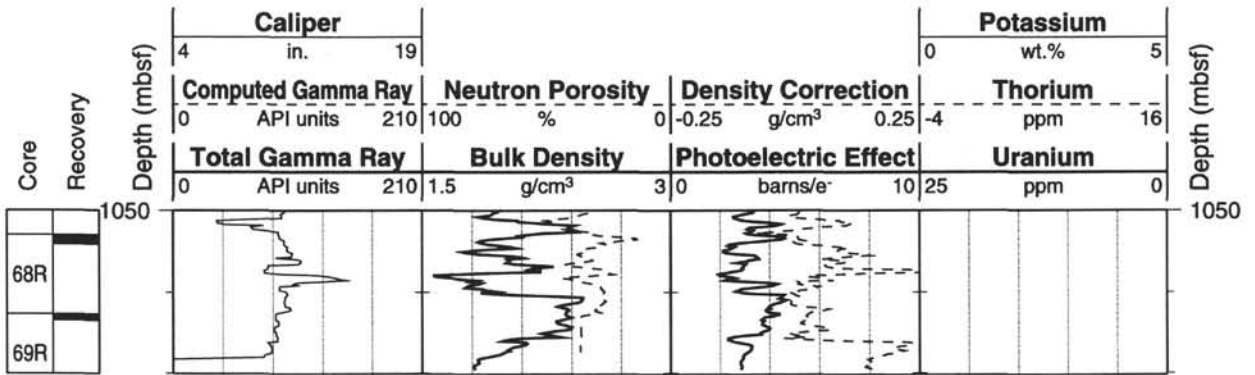
Hole 959D: Natural Gamma Ray-Density-Porosity Logging Data (cont.)



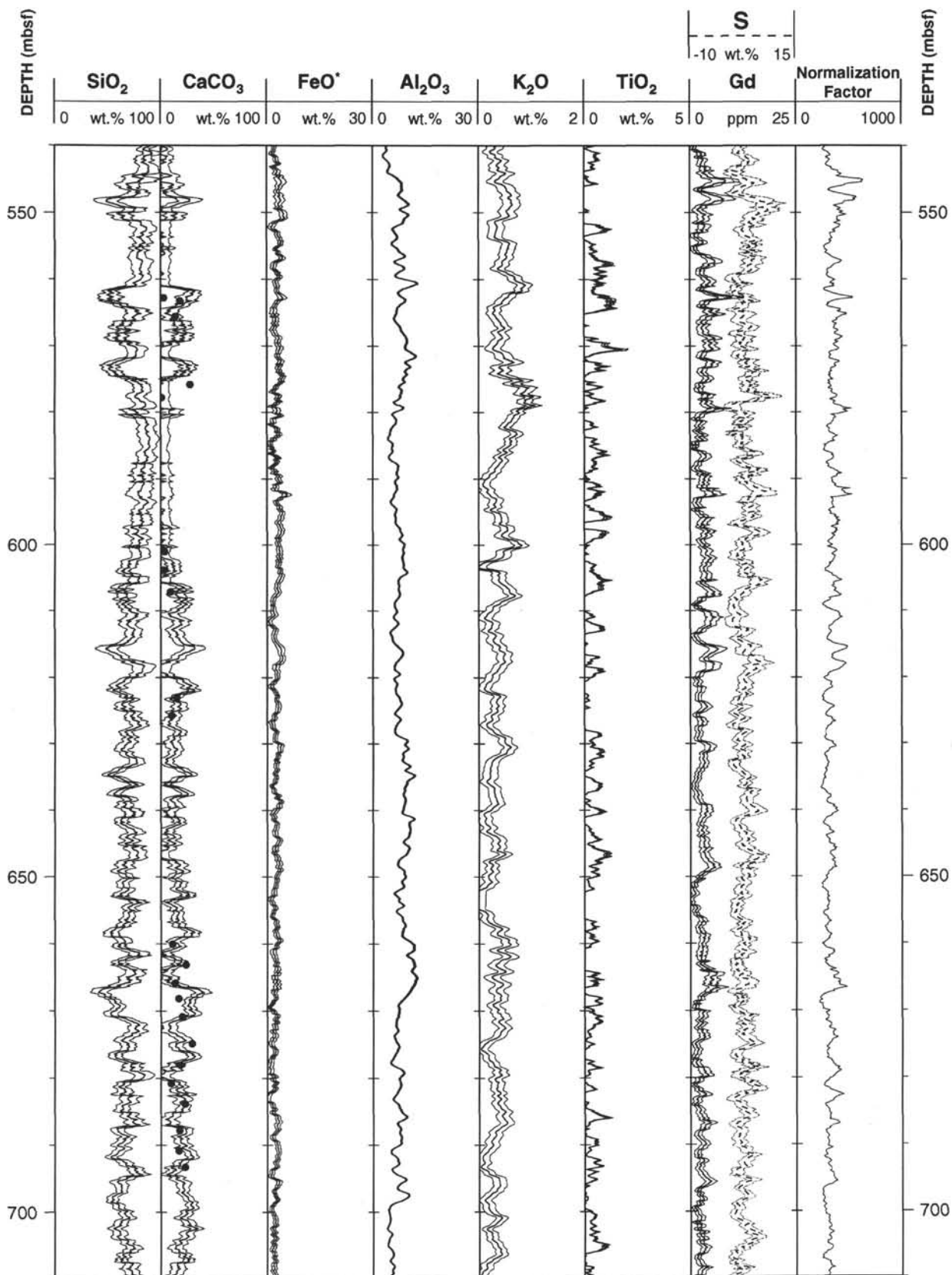
Hole 959D: Natural Gamma Ray-Density-Porosity Logging Data (cont.)



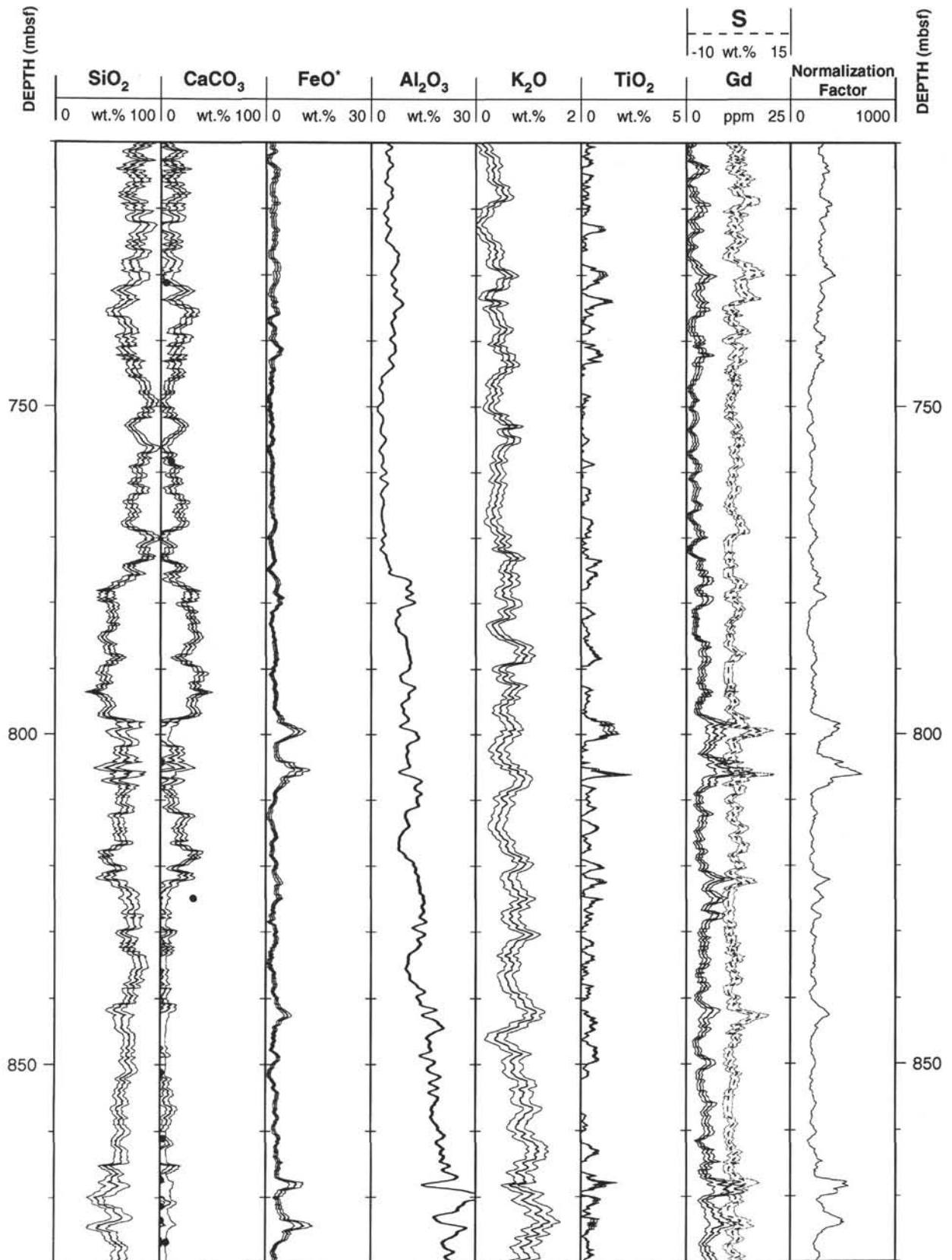
Hole 959D: Natural Gamma Ray-Density-Porosity Logging Data (cont.)



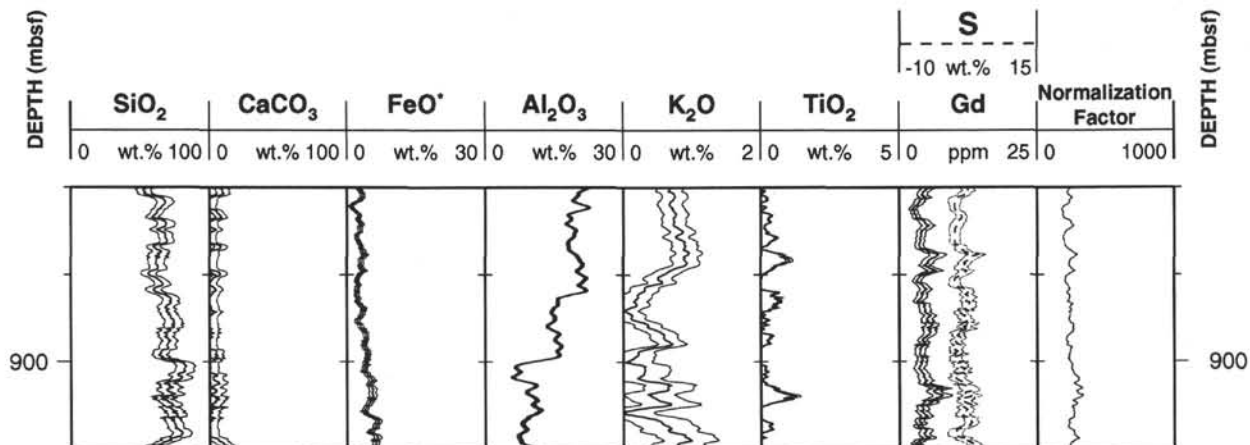
Hole 959D: Geochemical Logging Data



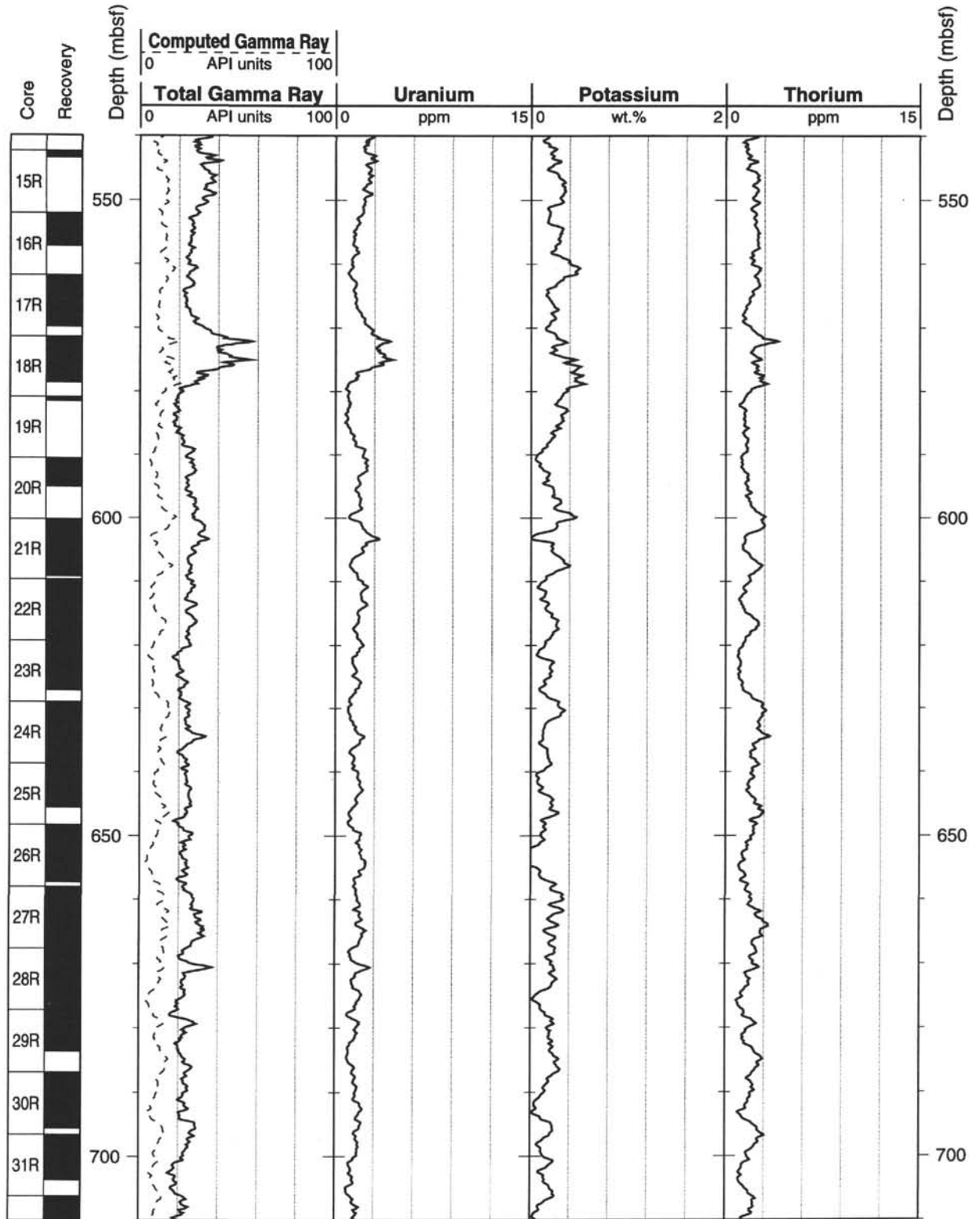
Hole 959D: Geochemical Logging Data (cont.)



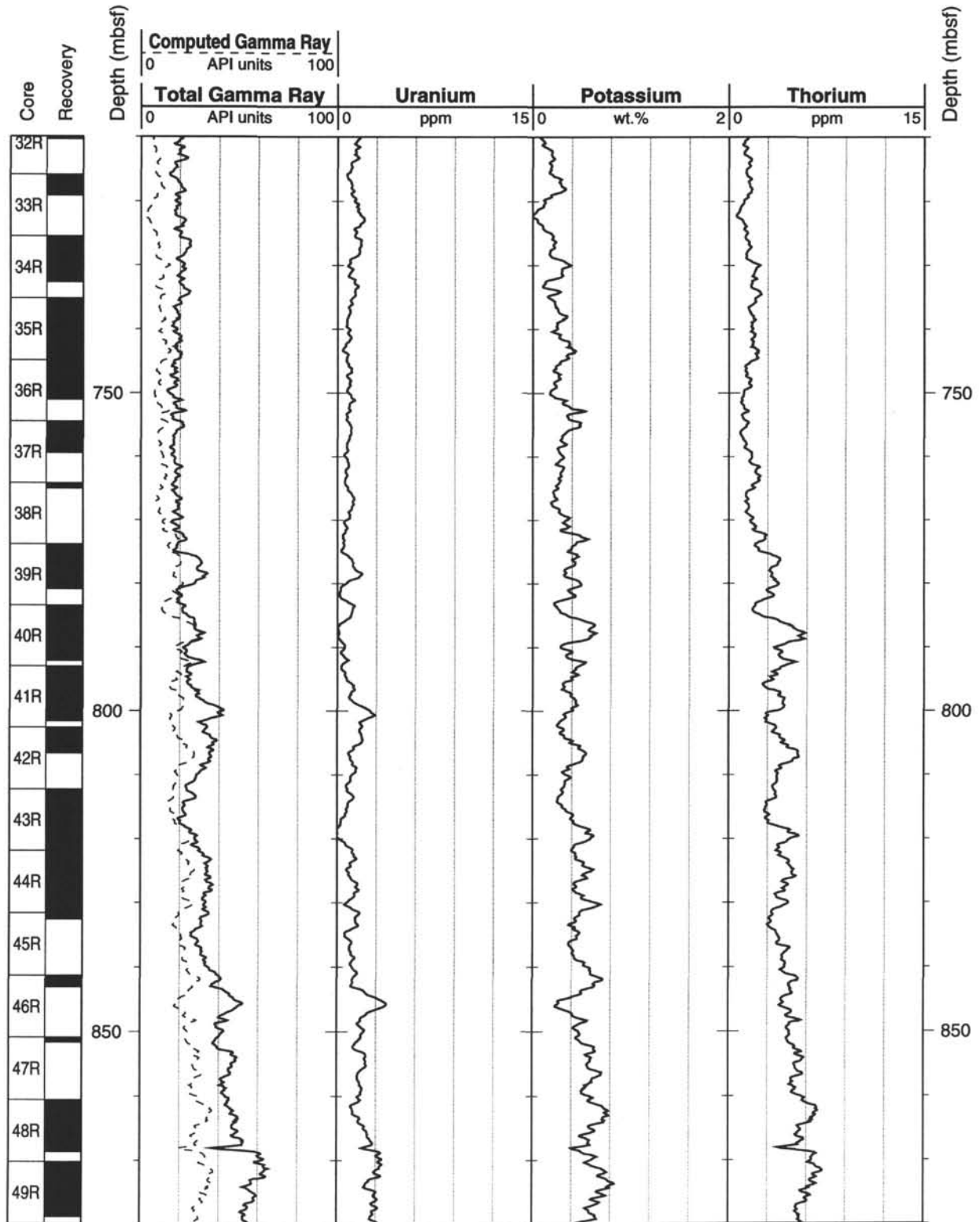
Hole 959D: Geochemical Logging Data (cont.)



Hole 959D: Natural Gamma Ray Logging Data



Hole 959D: Natural Gamma Ray Logging Data (cont.)



Hole 959D: Natural Gamma Ray Logging Data (cont.)

